Interphases in Polymer-Metal Adhesive Joints

Interphasen in Polymer-Metall-Klebungen

Dissertation
zur Erlangung des Grades
des Doktors der Ingenieurwissenschaften
der Naturwissenschaftlich-Technischen Fakultät
der Universität des Saarlandes

vorgelegt von

Dipl.-Ing. Ludovic Krogh

Saarbrücken, 2021

Tag des Kolloquiums:	10. Dezember 2021
Dekan:	Prof. Dr. Jörn Eric Walter
Berichterstatter:	Prof. Dr. Wulff Possart Prof. Dr.-Ing. Stefan Diebels Prof. Dr.-Ing. Alexander Lion
Akad. Mitglied:	Dr. -Ing. Frank Aubertin
Vorsitz:	Prof. Dr. Ralf Busch

Abstract

The prediction of mechanical deformation behaviour and durability of adhesively bonded joints under duty conditions is one of the most important issues for engineering since it is a key parameter for design and health evaluation of adhesively bonded structures.

Due to the viscoelastic nature of polymers, the mechanical behaviour of metal adhesive joints depends on temperature and deformation rate or time. Moreover, it happens that their mechanical response is also influenced by the adhesive thickness. This effect can be attributed to interphases which form between the adhesive and the substrates. Hence for a complete description of the thermomechanical behaviour of adhesive joints at small deformation, the theory of linear viscoelasticity is utilised to calculate the effective linear viscoelastic functions of adhesive joints. Metal-polyurethane adhesive joints with different adhesive thicknesses have been characterised by isothermal shear tests at constant shear rates, creep and stress relaxation experiments as well as dynamic mechanical analysis in a broad temperature range. The bond line thickness dependence of their mechanical response is interpreted as proof for a mechanical interphase of considerable thickness between the polyurethane adhesive and the metal substrate. To investigate the characteristics of the observed interphase, different methods of the scanning differential calorimetry and the dielectric spectroscopy have also been applied.

Zusammenfassung

Die Vorhersage des mechanischen Verformungsverhaltens und der Beständigkeit von Klebungen unter unterschiedlichsten Betriebsbedingungen ist eines der wichtigsten Themen für die Ingenieurswissenschaften. Es handelt sich hierbei um Schlüsselparameter für die Konstruktion und die Überwachung von geklebten Strukturen.

Aufgrund der viskoelastischen Natur von Polymeren hängt das mechanische Verhalten von Metallklebungen von der Temperatur und der Verformungsrate oder -zeit ab. Darüber hinaus kommt es vor, dass das mechanische Verhalten auch von der Klebschichtdicke beeinflusst wird. Dieser Effekt kann auf Interphasen zurückgeführt werden, die sich in der Klebung ausbilden. Zur Beschreibung des thermomechanischen Verhaltens von Klebungen bei kleinen Verformungen wird die Theorie der linearen Viskoelastizität verwendet, um die effektiven linear viskoelastischen Funktionen zu berechnen. Metall-Polyurethan-Klebungen mit unterschiedlichen Klebschichtdicken wurden durch isotherme Scherversuche mit konstanten Scherraten, durch Kriech- und Spannungsrelaxationsexperimente sowie durch dynamisch-mechanische Analysen in einem breiten Temperaturbereich charakterisiert. Die Abhängigkeit der mechanischen Antwort von der Klebschichtdicke wird als Beweis für eine mechanische Interphase mit beträchtlichem Ausmaß zwischen dem Polyurethan-Klebstoff und dem Metallsubstrat interpretiert. Um die Natur der beobachteten Interphase weitergehend zu charakterisieren, wurden die Auswirkungen der Interphase auf die kalorischen und dielektrischen Eigenschaften bestimmt.

Résumé

La prédiction du comportement de déformation mécanique et de la durabilité des assemblages collés dans des conditions de service est l'une des questions les plus importantes pour l'ingénierie, car elle constitue un paramètre clé pour la conception et le contrôle des structures collées.

En raison de la nature viscoélastique des polymères, le comportement mécanique des assemblages métalliques collés dépend de la température et de la vitesse ou du temps de déformation. En outre, il arrive que leur réponse mécanique soit également influencée par l'épaisseur de l'adhésif. Cet effet peut être attribué à l'interphase qui se forme entre l'adhésif et le substrat. Par conséquent, pour une description complète du comportement thermomécanique des assemblages collés à faible déformation, la théorie de la viscoélasticité linéaire est utilisée pour calculer les fonctions viscoélastiques linéaires effectives de tels assemblages. Des assemblages collés de type métal-polyuréthane de différentes épaisseurs ont été caractérisés par des essais isothermes de cisaillement à vitesse de déformation constante, des expériences de fluage et de relaxation des contraintes ainsi que des analyses mécaniques dynamiques dans une large gamme de température. La dépendance de leur réponse mécanique en fonction de l'épaisseur d'adhésif est interprétée comme étant la preuve d'une interphase mécanique d'une épaisseur considérable entre l'adhésif polyuréthane et le substrat métallique. Pour étudier les caractéristiques de l'interphase observée, différentes méthodes de calorimétrie différentielle à balayage et de spectroscopie diélectrique ont également été appliquées.

Resumen

La predicción del comportamiento de la deformación mecánica y de la durabilidad de las uniones adhesivas en condiciones de servicio es uno de los retos más importantes para la ingeniería, ya que es un parámetro clave para el diseño y el control de las estructuras unidas con adhesivos.

Debido a la naturaleza viscoelástica de los polímeros, el comportamiento mecánico de los ensamblajes metálicos unidos con adhesivos depende de la temperatura y la velocidad de deformación o del tiempo. Además, su respuesta mecánica también puede verse influida por el grosor del adhesivo. Este efecto puede atribuirse a las interfases que se forman entre el adhesivo y los sustratos. Por lo tanto, para una completa descripción del comportamiento termomecánico de las uniones adhesivas en deformaciones pequeñas, se utiliza la teoría de la viscoelasticidad lineal para calcular las funciones viscoelásticas lineales efectivas de dichas uniones. Las uniones metal-poliuretano de diversos espesores se han caracterizado mediante ensayos de cizallamiento isotérmico a velocidad de tensión constante, experimentos de fluencia y relajación de tensiones y análisis mecánicos dinámicos en una amplia gama de temperaturas. La relación de dependencia entre la respuesta mecánica y el espesor del adhesivo se interpreta como prueba de una interfase mecánica de considerable espesor entre el adhesivo de poliuretano y el sustrato metálico. Para estudiar las características de la interfase observada, se ha aplicado la misma estrategia utilizando diferentes métodos de calorimetría diferencial de barrido y espectroscopía dieléctrica.

Danksagung

Die vorliegende Dissertation entstand an der Universität des Saarlandes am Lehrstuhl für Adhäsion und Interphasen in Polymeren (LAIP) unter der Leitung und Betreuung von Univ.-Prof. Dr. rer. nat. habil. Wulff Possart. Ich möchte mich an dieser Stelle bei all jenen bedanken, die mich bei der Anfertigung dieser Arbeit so kräftig unterstützt haben.

Mein besonderer Dank gilt Herrn Univ.-Prof. Dr. rer. nat. habil. Wulff Possart für die herzliche Aufnahme an seinem Lehrstuhl, die vielen anregenden Diskussionen sowie die stete und engagierte Unterstützung. Insbesondere zolle ich ihm ein hohes Maß an Anerkennung, weil er jederzeit bei Rückfragen zur Verfügung stand und wir gemeinsam interessante Lösungswege erarbeitet haben. Die Verantwortung und die Freiheiten, die er mir während meiner Zeit am LAIP gewährt hat, haben mich wertvolle Erfahrungen sammeln lassen. Ich danke Herrn Prof. Possart herzlich für sein Vertrauen, seine Geduld und sein Verständnis!

Bei Herrn Univ.-Prof. Dr.-Ing. habil. Stefan Diebels (Professur für Technische Mechanik) bedanke ich mich vielmals für seine fachlich qualifizierte Unterstützung und seine Diskussionsbereitschaft sowie für die Übernahme des Koreferats.

Für die Bereitschaft zur Berichterstattung sowie die interessanten Anregungen bedanke ich mich bei Herrn Univ.-Prof. Dr.-Ing. habil. Alexander Lion (Universität der Bundeswehr, München).

Herrn Prof. Dr. Dr. h. c. Jan Kristian Krüger danke ich sehr für die Unterstützung bei wissenschaftlichen Fragestellungen und seine wertvollen Anregungen.

Mein weiterer Dank gilt Herrn Dr. rer. nat. Jürgen E. K. Schawe und der Firma Mettler-Toledo AG (Schwerzenbach, Schweiz) für die sehr gute Zusammenarbeit und für die Bereitstellung von Ressourcen zur dynamisch mechanischen Charakterisierung von Klebungen.

Herrn Prof. Dr. rer. nat. habil. Christoph Schick (Universität Rostock) und seinen Mitarbeitern danke ich sehr für die großzügige und freundliche Unterstützung bei der Charakterisierung der kalorischen Eigenschaften von Klebungen.

Weiteren Dank schulde ich allen Mitarbeiterinnen und Mitarbeitern des Lehrstuhls für Adhäsion und Interphasen in Polymeren für ihre Hilfsbereitschaft in wissenschaftlichen und technischen Fragen, die gute Zusammenarbeit und das freundliche Arbeitsklima: Dr. Maëlenn Aufray, Dr.-Ing. Carsten Wehlack, Dr.-Ing. Andreas Meiser, Prof. Dr.-Ing. Jan Gaukler, Dipl.-Chem. Christophe Nies, Dipl.-Chem. Frank Fug, M.Sc. Ernesto Jesus Huacuja Sanchez, Dr.-Ing. Ana Lucia Penagos Palencia, Dipl.-Ing. Léo Depollier, M.Sc. Maren Weidner.

Weiterhin danke ich Herrn Dr.-Ing. Thomas Helfen, Frau Dipl.-Ing. Amandine Roth, Herrn Dipl.-Ing Léo Depollier, Frau Dipl.-Ing. Elise Bosset, Herrn Dr.-Ing. Michael Schwarz, Herrn M.Sc. Christian Schmitt und Herrn M.Sc. Adrien Schmitt, die mit ihren von mir betreuten Studien-, Diplom- und/oder Masterarbeiten einen wichtigen Teil zu den Ergebnissen dieser Dissertation beigetragen haben.

Den Herren Peter Kohl, Werner Rauber und Jürgen Klesen möchte ich für ihre Unterstützung bei technischen Problemen aller Art sowie für die geniale und teils unkonventionelle Umsetzung von ausgefallenen Ideen danken.

Für die Hilfe bei den administrativen Tätigkeiten sowie die freundliche Arbeitsatmosphäre danke ich unseren Sekretärinnen Frau Beate Epstein und Frau Alice Goldschmidt.

Ich danke ebenfalls Frau Dr.-Ing Johann Lacava und Herrn Dr.-Ing. Brice Raillard sowie Frau M.Sc. Maren Weidner für ihre außerordentliche Unterstützung und ihre Geduld, insbesondere während der Stunden, die sie mit dem Korrekturlesen dieser Arbeit verbrachten.

Herzlich danken möchte ich ebenfalls meinen Freunden und meiner Familie für die Unterstützung während meines Studiums und meiner Doktorarbeit.

Merci beaucoup à toutes et à tous pour votre soutien pendant ces années!

Zu guter Letzt bedanke ich mich bei Maren, die mit viel Geduld und Rücksicht, vor allem aber mit Liebe und seelisch-moralischer Fürsorge, maßgeblich zum Gelingen dieser Arbeit beigetragen hat.

Contents

1. Introduction

1.1. Motivation

The use of adhesives to join materials is not a recent technique as it was already used during the Middle Palaeolithic. However, during the past decades, the popularity of adhesive bonding is growing in every manufacturing industry and even in the medical branch driven by a range of interrelated benefits. Whether in cars, trains, planes, wind wheels or microchips, adhesive bonding is more and more introduced as a complement to or instead of conventional joining techniques such as welding, soldering or riveting.

In contrast to point fixing such as spot-welding which creates localised stress peaks under load, adhesive joining spreads the stress of the bond across a wider area, allowing more of the material to contribute to energy adsorption and improving for example the crash performance. It enables also the use of lightweight and hybrid structures which can be difficult or impossible to weld: different materials, such as composite and aluminium, can be joined with adhesives. Under the pressure of the economic and environmental requirements of the recent years, the implementation of adhesive bonding to design more complex hybrid structures appears to be the better alternative to achieve a significant reduction in weight. Nevertheless, comprehension of the processes and mechanisms which determine the properties of adhesive joints is necessary to fully exploit the potential of adhesive joining. This requires a fundamental understanding of the processes that influence and change structure and chemistry in the adhesive, namely the adhesion phenomena.

The adhesion mechanisms become effective when the adhesive in a fluid state is brought into contact with the substrate (solid material). The solidification of the adhesive forms an *interface* where physical intermolecular interactions (Van der Waals forces), chemical bonds of any form or electrostatic attractions are responsible for the adhesion between the two materials. This means that mechanical force can be transferred across this interface.

Generally, any adhesive bonding mechanism immobilises adhesive molecules at the contact to the substrate (adherend). However, the adhesive interactions trigger also some trend to the demixing of adhesive components and to preferential orientation of adhesive molecules in the region at the contact. Hence, they strongly affect the formation of chemical and morphological structures as well as the molecular mobility in the underlying region of the adhesive during solidification. As a result, gradients of the structure and the properties appear in the adhesive layer, forming property-specific *interphases*. The characteristics of these interphases depend on the combination of adhesive and adherend surface condition and the nature of the involved adhesion processes. The interphase properties can differ significantly from the behaviour of the bulk adhesive.

The formation of interphases creates inhomogeneity in adhesive bonds resulting in gradients of physical and/or chemical properties. These latter are usually correlated to processes such as selective adsorption, segregation or phase separation of polymer components, orientation effects, steric hindrance or curing shrinkage. Consequently, as illustrated in Figure 1-1 for a given adhesive/substrate combination, the behaviour of the adhesive joint should depend on the adhesive layer thickness d_p. It is obvious that the influence of the interphases (red regions) is growing when the thickness of the joint is reduced whereas bulk properties (blue region) dominate in thick adhesive layers.

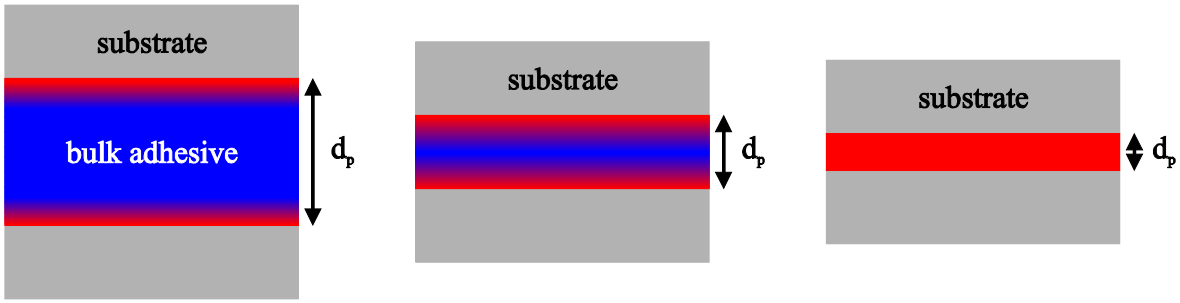

Figure 1-1: Schematic illustration of the influence of interphases (red regions) in adhesive joints, depending on the adhesive layer thickness d_p (according to [1]).

In a similar way, all these considerations also apply to material composites. In this case, interphases form between the matrix and the filler material. Hence, in comparison with sandwich-structured composites, additional factors can influence the formation of interphases: e.g. fraction, geometry, size distribution and dispersion of the fillers.

In brief, the existence of interphases, regardless of their nature, attests that the effect of adhesion is not restricted to the adhesive-substrate interface. Therefore, the influence of interphases must be considered for a realistic description and estimation of the technical performance of adhesive joints.

1.2. State of the art

1.2.1. Interphases in polymer-metal adhesive joints

The materials testing conducted for many decades has shown that the knowledge about the fundamental adhesion phenomena is an essential issue for the understanding of the properties of adhesive joints and other material compounds [2, 3]. Nevertheless, due to the complexity of the physicochemical processes responsible for the adhesion and their strong dependence on the chemical nature of the adhesive and the metal surfaces, the comprehension of adhesive bonding remains up to now rudimentary. In this context, several works have dealt with the formation of interphases in polymer adhesives on metal substrates, reporting concentration gradients of the chemical composition in the adhesive at the contact with different metal substrates [4-13].

However, quantitative measurements of such chemical gradients are, in many cases, difficult to perform and a sufficient local resolution is hard to achieve. Wehlack et al. show differences in reaction kinetics and chemical conversion of reactive groups between polyurethane bulk adhesive and adhesive in contact with metal layer on the scale of some hundred nanometres [10, 11, 13-17]. In epoxy adhesives, many contributions report the formation of organometallic complexes, catalytic effects of metallic ions as well as a preferential adsorption of monomers at the contact region between the adhesive and the metal substrate [5, 6, 8, 18-20]. To mention just one of these, Meiser et al. identify, using infrared microscopy, spatial variations in the chemical structure – i.e. *chemical interphases* – in epoxy adhesives at the contact with different metals (Cu, Al) for distances of up to a few microns, whereas *morphological interphases* - i.e. modifications of the adhesive microstructure and presence of anisotropy – extend up to 50 µm [8, 18].

As the result, chemical structure and corresponding network morphology differ in that chemical interphase from the polymer bulk revealed in form of noticeable variations in the degree of cross-linking [9, 19, 21-23] and the glass transition [24-35], even for crosslinked polymers considered once as homogeneous. Thermal and hydrothermal ageing of these polymers are also strongly affected by the interphases [21, 35-41]. Since chemical structure and mechanical properties are directly related, the mechanical behaviour of that region also differs from the bulk [8, 9, 23, 31, 42-44]. For a given combination of adhesive and substrate, the bond line thickness rules the volume ratio of interphase and remaining bulk region. Indeed, such thickness dependence was reported for the mechanical moduli of selected polymer-metal combinations in the literature [9, 25, 45-51].

These results lead to the conclusion that interphases can generally affect the properties of adhesive joints in a different manner, yielding the extent of these interphases different for each property.

Considering the crucial role played by mechanical properties of interphase for engineering applications, the local measurement of mechanical properties in adhesive joints is in the focus of interest. As for the identification of chemical gradients, most publications which deal with spatial variation of mechanical behaviour concern epoxy adhesives. *Mechanical interphases* – i.e. gradients in the mechanical properties – are identified in adhesive joints in the same order of magnitude as for the chemical gradients. For example, stiffer interphases of about 2-4 µm width have been identified in two epoxies in contact to copper using the scanning force microscopy-based force modulation microscopy [52, 53]. Nanoindentation appears as well to be predestined for the characterisation of interphases. Numerical simulations have shown that this technique is sensitive enough to detect gradients in the mechanical properties across the front surfaces of adhesive layers with a sufficient resolution [54-57]. Therefore, stiffer interphases of about 1-2 µm have been detected in epoxy-aluminium adhesive joints [8], whereas softer interphases with comparable scale have been measured for the same epoxy adhesive but in contact with copper [1, 8]. However indentation measurements on elastomers or ductile polymers are strongly influenced or even distorted in the vicinity of the metal substrate [1, 57]. That is why simulations of the experiments have to be used to discern the effects of interphases from the contributions of the stiffer substrates which dominate the measurements [57]. In addition, the viscoelastic nature of polymers complicates both experiments and simulations, making the result analysis complex [54-57].

Spatial variations in the mechanical behaviour of adhesive joints have also been experimentally observed using microscopy techniques to record the surface deformation of adhesive joints during shear tests. Markers are applied with the focused ion beam (FIB) technique and used to track the deformation with digital light microscope [58, 59] or scanning electron microscope (SEM) [57]. However, the results obtained with scanning electron microscope show that the inhomogeneity in the shear deformation across the adhesive layer thickness occurs first at inelastic deformations. Therefore no conclusion can be drawn on possible elastic stiffness gradients [57]. Moreover, the local characterisation of mechanical interphases in elastomers or ductile polymers still presents a particular difficult challenge. Numerical simulations have shown that the spatial resolution of the contemporary experimental methods used in [57] is not sufficient to detect local variations of mechanical properties in elastomeric polyurethane – metal adhesive joints.

Besides the formation of chemical and mechanical interphases, internal stresses arise in the adhesive as it shrinks during polymerisation and vitrification. Krüger et al. conclude from Brillouin spectroscopy results on internal stresses in the contact region between the adhesive and the substrate, which extend up to about 200 µm [42, 60]. Mechanical modelling reveals the influence of these internal stresses on the formation of mechanical interphases in adhesive joints due to polymerisation shrinkage [61-66]. The effect of these residual stresses gives a new dimension to the definition of mechanical interphases that are henceforth not only the direct consequence of the formation of chemical interphases. The confinement of the polymer layer which is directly attached to the substrate surface – i.e. responsible for the adhesion – impacts greatly the mechanical properties of the polymer network.

1.2.2. **Modelling of mechanical behaviour of polymers – a brief discussion**

Numerous models attempt to describe the mechanical behaviour of polymers in the rubbery state [67]. Whether the models are based on a phenomenological approach [68, 69] or on the molecular theory [70, 71], the polymer network is considered as a hyperelastic isotropic continuum. The hyperplastic models can predict the nonlinear stress-strain behaviour exhibited by the elastomers in their rubbery state at finite deformations. The deformation mechanisms are then assumed to be ideally elastic, i.e. non-dissipative and reversible. On this last point, two remarks can be formulated:

i. In practice, however, all processes involving atomic motion are dissipative. Since deformation processes in polymers are based on molecular relaxation processes, a part of both absorbed and released deformation works (energies) by the polymer is dissipated, contributing to the entropy production. Therefore, even if the macroscopical relaxation processes cannot be measured on the experimental timescale, deformation processes are, from a thermodynamic point of view, always irreversible.

ii. In case of the investigated hyperelastic polymer, if the external load is released, the original deformation is invertible. The polymer network returns in its original state. The word “invertible” has been deliberately chosen here to point out the difference between the thermodynamic meaning and the mechanics meaning of the word “reversible”. Nevertheless, the term “reversible” is widely accepted and used to refer to such a mechanical behaviour.

Since the present work follows the footsteps of the works of Johlitz [72] and Batal [1], the following discussion rely on the same modelling strategy: to predict the (relaxed) elastic properties of a similar polyurethane adhesive to that investigated in this work, the Mooney-Rivlin model has been implemented [47, 72]. The polyurethane adhesive layer is considered as an isotropic and incompressible continuum. A comparison with the experimental results shows that the adhesive can be considered as a neo-Hookean material (a special case of the Mooney-Rivlin solid) in the measured strain range.

The model presented by Johlitz has not been discussed for the energy elastic range of the polyurethane adhesive due to the lack of experimental data. In the energy elastic range of the polymers, invertible deformations occur in a small strain range. Polymers behave then almost linear elastic and their stress-strain relationship can be described by the Hooke’s law. In this case, the deformation mechanisms are here also assumed to be ideally elastic, i.e. non-dissipative.

In the transition region, relaxation processes cannot be neglected anymore, and the relaxation times increase with decreasing temperature. Due to these viscoelastic effects, dynamic contributions are added to the equilibrium modulus, inducing the increase of the measured modulus of the material with decreasing temperature. The different contributions to the modulus cannot be experimentally isolated.

To model the viscoelastic behaviour of a polyurethane adhesive similar to the one used in this work, Johlitz suggests splitting the expression of the free energy function in equilibrium and non-equilibrium parts [73]. The resulting stress and strain tensors are then also divided into two parts: one purely elastic to describe the relaxed properties of the polymer and one inelastic to describe its time-dependent properties. The incompressible neo-Hookean material models were chosen for the corresponding constitutive equations because of the good agreement between the modelled results and the experimental ones. The detailed description of this model can be found in [72].

1.3. Aim of this work

The prediction of mechanical deformation behaviour, strength and durability of adhesively bonded joints under duty conditions is one of the key parameters for design and health evaluation of adhesively bonded structures. The consideration of the influence of interphases, which can play a decisive role in the properties of adhesive bonds, is therefore necessary for the engineering of adhesively bonded structures. To grasp this challenge and to better understand the occurring mechanisms, only metal-polymer-metal sandwich composites are considered in this work to investigate the influence of interphases on the properties of adhesive joints.

The major part of this work focuses on the detection and identification of mechanical interphases in juvenile metal-polyurethane adhesive joints. In such adhesive joints the local variations of the mechanical properties cannot be (accurately enough) detected [57]. A way to circumvent this issue is to consider the adhesive bond line as a homogeneous continuum and to measure the effective properties of the whole adhesive layer. All the parameters thus measured are then mean values over the whole polymer volume. As illustrated in Figure 1-1, if those effective mechanical properties depend on the adhesive bond line thickness, d_P, this evidences the existence of interphases in such adhesive joints. This strategy has been already successfully applied by Johlitz [72] and Batal [1]. Using the same approach, this work intends to develop a method for the characterisation of the mechanical behaviour of adhesive bonds considering their temperature and adhesive thickness dependences. The data collected can then, in future works, be implemented in a numerical model similar to the one developed by Johlitz [72] in order to optimise it.

Besides to its use in mechanical testing the consideration of the effective properties of the whole adhesive layer has also been applied in this work to identify interphases using calorimetric and dielectric methods. This intends to gain a broader insight of the definition of interphase and its influence on further properties of the adhesive.

1.4. Outline of this work

One of the major challenges of this work is to detect and quantify the influence of interphases on the mechanical behaviour of adhesive joints. As presented in chapter 2, polymers exhibit complex mechanical properties depending on time and temperature. It is also necessary to design equipment that is sensitive and precise enough to characterise these effects. The investigated materials, the designed experimental set-ups as well as the preliminary tests to ensure the reliability and accuracy of the results are presented in chapter 3.

To interpret the results of the mechanical testing presented in chapter 4, a strategy similar to that developed by Johlitz in [72] has been used to attempt to separate the relaxed elastic properties from the viscoelastic ones: The relaxed elastic properties (equilibrium moduli) of the polymer and their temperature dependence can be extrapolated from the entropy elasticity to the transition region. The linear increase of the equilibrium modulus with increasing temperature is then assumed to be valid in the transition region. The relaxation/retardation time spectra, obtained using the analytical solution of a one-dimensional constitutive model (see section 2.4), describe the viscoelastic properties.

To determine whether mechanical interphases can be detected by other experimental methods, dynamic mechanical analysis has also been used to investigate adhesive joints with lower bond line thickness range. Since the influence of interphases is not limited to mechanical properties only, other methods of investigation (calorimetry and dielectric spectroscopy) are also presented in chapter 5. These investigations intend to improve the understanding of the extent of interphase effects and their possible influences on the caloric and dielectric properties of adhesive joints.

2. Basics of polymer mechanics

The major focus of this work is the identification of mechanical interphases in adhesive joints by measuring the effective mechanical properties as a function of thickness of the whole adhesive layer. Damage mechanisms and plastic deformation are not in the scope of this work, as it only deals with invertible deformation[1]. All the mechanical tests presented in this work are performed in the linear viscoelastic region of the adhesive. This means that for infinitesimal strain and strain rate, the time-dependent stress-strain relations – i.e. the constitutive equations – in the different experiments can be described by linear differential equations with constant coefficients. As described by L. Boltzmann, it implies that the responses of the specimen after successive arbitrary perturbation steps are linear superpositions of the individual responses [74]. According to this definition, if the shear stress due to a shear strain $\gamma_i(t)$ is $T_{12}(\gamma_i)$ and that due to another strain $\gamma_j(t)$ is $T_{12}(\gamma_j)$, then the shear stress due to the both shear strains is:

$$T_{12}(\gamma_i + \gamma_j) = T_{12}(\gamma_i) + T_{12}(\gamma_j) \tag{2.1}$$

This principle is experimentally verified for the investigated polymer in section 3.4.2.5.

Since mechanical tests are used as probes to detect interphases in adhesive joints, fundamentals on polymers mechanics are therefore necessary to interpret the results presented in section 4. As the mechanical behaviour of a polymer is directly related to its molecular structure, the following discussion is focussed on the type of polymer used in this work: amorphous polymer networks.

2.1. Phenomenological description of the thermomechanical behaviour

In polymer networks, the crosslinked macromolecular polymer chains form a three-dimensional network. The crosslinking prevents viscous flow and restricts the maximum possible deformation of the network without damage. In such macromolecular materials different interatomic interactions coexist. The combination of strong intramolecular covalent bonds and weak intermolecular bonds imparts differences in the mobility of the macromolecules as a whole and of their segments. The arrangements of the polymer chains or segments, which can move relative to one another, can be altered under the action of temperature and/or external stress or deformation. These processes of reestablishment of equilibrium are called stress relaxation phenomena, if the polymer is submitted to external deformation and strain retardation phenomena if the sample is subjected to external loads. Hence, the relaxation/retardation phe-

[1] The term “invertible deformation” has been deliberately chosen here instead of “reversible deformation” to point out that although the polymer returns in its initial state without external load or deformation, some energy is dissipated during this process.

nomena lead to a dependence on time and temperature of the mechanical properties of polymer networks. Such time-dependent mechanical response is called viscoelastic.

The involved material rearrangements – i.e. relaxation or retardation phenomena – always require a finite time. However, when these phenomena cannot be identified at a given temperature within the experimental timescale whether they are too slow or too fast, the mechanical response is usually interpreted as being "elastic". Thus, the notion of elasticity in polymers is directly related to the experimental conditions (timescale and measuring temperature).

To illustrate the viscoelastic response of amorphous polymer networks, the influence of time and temperature on their mechanical properties is separately discussed considering different shear experiments.

2.1.1. **Time dependence**

As the relaxation/retardation phenomena in polymers subjected to external load or deformation originate from molecular motions, they necessarily depend on time. To illustrate these phenomena, a shear stress relaxation experiment is considered. At constant temperature, T, an amorphous crosslinked polymer sample is subjected, at a constant shear rate, $\dot{\gamma} = \frac{d\gamma}{dt}$, to a constant shear strain, γ_0. At a time t_0 the deformation is maintained constant and the resulting shear stress $T_{12}(t)$ is monitored as a function of time as shown in Figure 2-1. After a defined time t_e the externally applied shear strain γ_0 is then removed allowing the sample to relax into its initial state. This experiment is repeated at different temperatures: $T_1 < T_2 < T_3$.

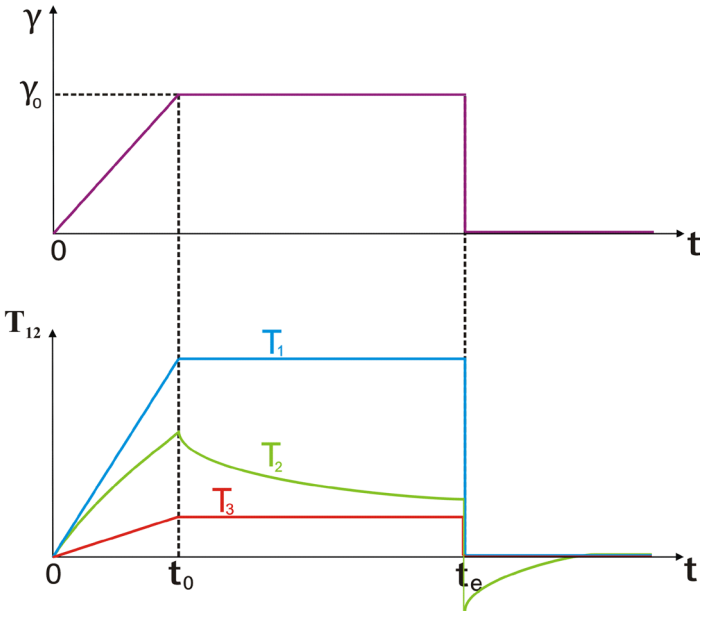

Figure 2-1: Shear stress relaxation experiments performed at different temperatures: $T_1 < T_2 < T_3$.

In the example illustrated in Figure 2-1, the time dependence of the mechanical response of a polymer network can be also identified at the measuring temperature T_2 while it cannot be observed at T_1 and T_3. The perception of the time dependent mechanical behaviour of polymer networks is directly related to the experimental timescale. If the relaxation phenomena cannot be observed within the experimental timescale, meaning that the related relaxation times are either too short or too long in comparison with the experimental time scale, the mechanical response of the polymer seems to be elastic and thus time independent.
The time-delayed mechanical response is a characteristic feature of viscoelastic behaviour of polymers. Thus, even if the *external* deformation applied by the testing machine is removed at $t = t_e$, a period of time is necessary until the load-free initial state of the sample is restored. During this time, a strain in the polymer network subsists and a stress with inverted sign appears due to the forced condition of the sample clamping (see green curve for $t > t_e$ in Figure 2-1).

Figure 2-2 represents the shear stress $T_{12}(t)$ as a function of the shear strain $\gamma(t)$ for the experiments described in Figure 2-1 for $0 \le t \le t_e$. Again, the time dependence of the viscoelastic response at temperature T_2 is visible while it is not perceptible for temperatures T_1 and T_3. Note here the behaviour of the polymer for $0 \le t \le t_0$ which is subjected to constant shear rate, $\dot{\gamma} = \frac{d\gamma}{dt}$: the non-linear evolution of $T_{12}(\gamma)$ for T_2 (in green) is characteristic of a viscoelastic response and results from occurring relaxation processes. This feature is discussed in more detail below – Figure 2-4. At T_1 and T_3 the polymer network behaves according to the Hooke's law, i. e. $T_{12}(\gamma)$ is linear.

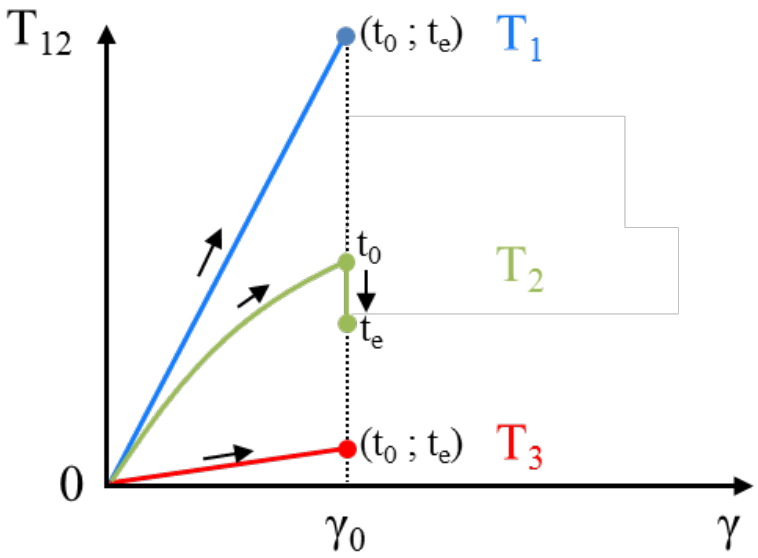

Figure 2-2: Shear stress $T_{12}(t)$ as a function of the shear strain $\gamma(t)$ for shear stress relaxation experiments performed at different temperatures: $T_1 < T_2 < T_3$ as described in Figure 2-1

For any temperature T, the shear stress relaxation modulus $G(t)$ with $t_0 \le t \le t_e$ is defined as

$$G(t,T) = \left.\frac{T_{12}(t)}{\gamma_0}\right|_{T=const} \qquad (2.2)$$

Figure 2-3 depicts the evolution of shear stress relaxation modulus $G(t)$ for the three experiments described in Figure 2-1 at the three different temperatures $T_1 < T_2 < T_3$. As expected for elastic responses, $G(t)$ remains constant at T_1 and T_3 whereas $G(t)$ decreases over time at T_2 showing a stress relaxation in the polymer network.

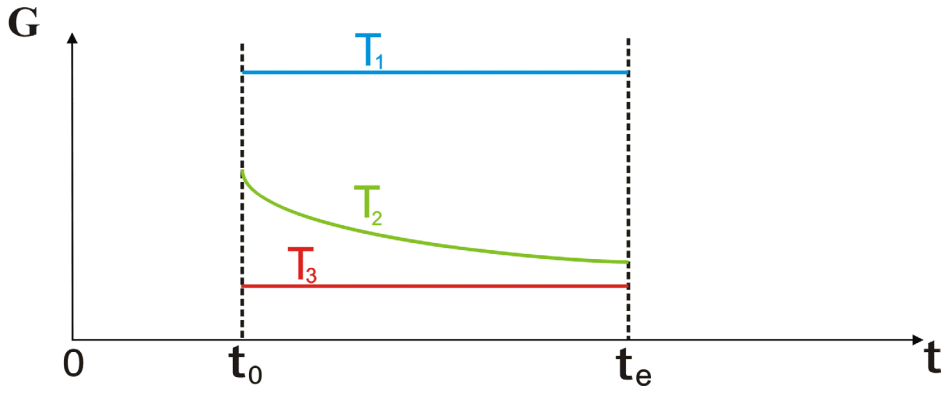

Figure 2-3: Shear stress relaxation modulus *G(t)* for shear stress relaxation experiments performed at different temperatures: $T_1 < T_2 < T_3$

Through the examples discussed above, three states of the polymer network can be identified. Each exhibits a different mechanical response, depending on the measuring temperature T:

- Energy-"elastic" response also called "glassy state" (T_1 – Figure 2-1): the shear relaxation modulus seems to remain constant in the measuring time domain $G(t,T)$
- Glass transition region which shows a visible viscoelastic response (T_2 – Figure 2-1): $G(t,T)$ decreases over time. The polymer network exhibits relaxation processes in the experimental time window
- Entropy-"elastic" state also called rubber-like elastic (T_3 – Figure 2-1): $G(t,T)$ appears to not depend on time.

Each polymer exhibits a given spectrum of structural relaxations and every single relaxation process displays, in turn, a characteristic probability and speed. This results in specific spectra of probability and speed for the corresponding structural rearrangements.
Provided that relaxation/retardation processes can occur at the measuring temperature, the involved material rearrangements in a polymer network can be influenced by the rate of the applied external load or deformation for a given experimental timescale.
The applied strain rate $\dot{\gamma}$ determines which part of these rearrangements absorbs mechanical energy and thus significantly builds up the deformation. Assuming that the strains are infinitesimal, the speed spectrum itself remains though unchanged during this process.

To illustrate this effect, isothermal shear tests at five different constant shear rates $\dot{\gamma}_1 > \dot{\gamma}_2 > \dot{\gamma}_3 > \dot{\gamma}_4 > \dot{\gamma}_5$ with $\dot{\gamma} = \left.\frac{d\gamma}{dt}\right|_{T=const}$ are considered. The shear stress T_{12} is represented as a function of the shear strain γ in Figure 2-4 for a given experimental timescale.

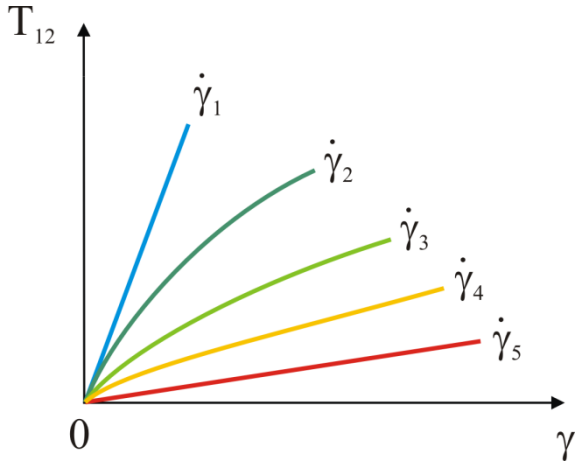

Figure 2-4: Isothermal shear tests at five different constant shear rates: $\dot{\gamma}_1 > \dot{\gamma}_2 > \dot{\gamma}_3 > \dot{\gamma}_4 > \dot{\gamma}_5$.

The dynamic shear modulus $M(t,T,\gamma)$ can be calculated by:

$$M(t,T,\gamma) = \left.\frac{T_{12}(t)}{\gamma(t)}\right|_{T,\dot{\gamma}=const} \tag{2.3}$$

Depending on the measuring strain rate $\dot{\gamma}_1 > \dot{\gamma}_2 > \dot{\gamma}_3 > \dot{\gamma}_4 > \dot{\gamma}_5$, three typical evolutions of $T_{12}(\gamma)$ and thus $M(t,T,\gamma)$ can be observed. These responses correspond respectively to the different mechanical behaviours:

- Energy-"elastic" response ($\dot{\gamma}_1$ – Figure 2-4): the shear modulus appears to be constant in the measuring strain range $M(t,T,\not{\gamma})$. Since the strain rate dependence of the mechanical response is not measurable in the energy-"elastic" region under usual experimental conditions, the shear modulus is often erroneously considered to be independent of strain rate $\dot{\gamma}$ and thus of time. In theory, since a polymer always shows a viscoelastic response, $T_{12}(\gamma)$ cannot be linear and must have a curvature. Experimental conditions determine whether this curvature is detectable or not. These remarks are also valid for the entropy-"elastic" response.
- Glass transition region which shows a visible viscoelastic response ($\dot{\gamma}_2, \dot{\gamma}_3, \dot{\gamma}_4$ – Figure 2-4): the shear modulus depends on the measuring strain $\mu(t,T,\gamma)$
- Entropy-"elastic" response ($\dot{\gamma}_5$ – Figure 2-4): $M(t,T,\not{\gamma})$ seems to remain constant in the measuring strain range.

2.1.1.1. Energy-elastic state

In the extreme case where the deformation rate is faster than any relaxation/retardation processes in the polymer network, the rearrangement of its structural elements appears to be fully blocked and the interatomic bonds are directly strained. In fact, both the extreme fast relaxation times resulting from the shift of atoms or groups of atoms and the extreme slow relaxation times issued from the rearrangement of bigger structural elements cannot be monitored with the experimental time and intensity resolution. No relaxation process can be experimentally observed at T_1 in Figure 2-1, Figure 2-2 and Figure 2-3 and the shear relaxation modulus $G(T)$ seems to remain constant in the measuring time range.

The externally applied shear deformation on this apparently blocked polymer network causes a drastic increase of the stress while the strain remains small as depicted by the result obtained with a strain rate $\dot{\gamma}_1$ in Figure 2-4.

The mechanical response appears to be energy-elastic, i.e. independent of time and thus $\dot{\gamma}$. The shear stress T_{12} is then linear proportional to the shear strain γ and the resulting shear modulus (i.e. the slope in Figure 2-4) is high and seems to remain constant over the measured deformation range.

2.1.1.2. Glass transition region

Provided that structural elements can rearrange within the experimental time scale and that the intensity of the corresponding relaxation phenomena is high enough to be experimentally detected, the viscoelastic response of the polymer network becomes evident – green curves in Figure 2-1, Figure 2-2 and Figure 2-3.

Another example is represented for the strain rates $\dot{\gamma}_2$, $\dot{\gamma}_3$ and $\dot{\gamma}_4$ in Figure 2-4. The evolution of shear stress $T_{12}(\gamma)$ for these strain rates as a function of the shear deformation is obviously no longer linear resulting in a shear strain dependent shear modulus.

At a given strain rate, the rearrangement of each of the structural elements lowers the stress in the polymer network, resulting in a negative curvature of $T_{12} = f(\gamma)\big|_{T=const}$.

With decreasing strain rate $\dot{\gamma} < \dot{\gamma}_1$, more and more structural elements can rearrange according to the externally imposed deformation within the experimental time scale, resulting in a decreasing shear modulus.

2.1.1.3. Entropy-elastic state

When all the rearrangements in the polymer network are at least as fast as the measured strain rate, no relaxation phenomena can be detected anymore. The polymer network behaves apparently elastic and $T_{12} = f(\gamma)\big|_{T=const}$ is linear. Further decrease of the strain rate no longer seems to affect the evolution of $T_{12}(\gamma)$.

2.1.2. **Temperature dependence**

Thermal motions influence the relaxation/retardation phenomena in the macromolecular structure of polymers and thus their mechanical properties. This reveals the interdependence of the influence of time and temperature on the mechanical behaviour of polymers. The relationship between time and temperature is discussed in section 4.3.2.

Repeating the experiment described in Figure 2-1 at different temperatures, the shear stress relaxation modulus $G(T)$ is measured at an arbitrarily constant time t with $t_0 \le t \le t_e$. Figure 2-5 depicts the temperature dependence of the shear stress relaxation modulus $G(T)\big|_{t=const.}$ for a typical crosslinked amorphous polymer. Note that similar curves are obtained considering other types of deformation. In this plot, the three apparent regions of the viscoelastic behaviour described above can be identified.

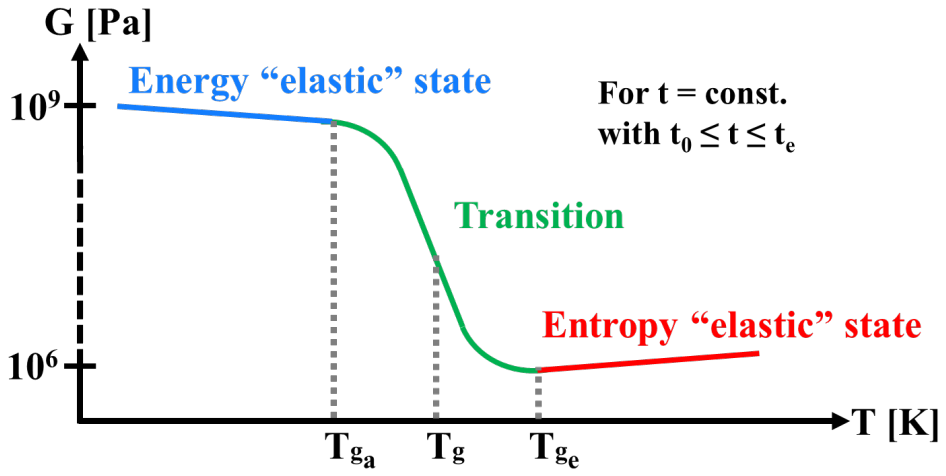

Figure 2-5: Shear stress relaxation modulus-temperature curve after a constant relaxation time t with $t_0 \le t \le t_e$ showing the different regions of the viscoelastic behaviour (according to [75])

2.1.2.1. Energy-elastic state

The measuring temperature T_1 is lower than the beginning of the mechanical glass transition $(T_1 < T_{g_a})$ - Figure 2-5. Cooperative mobility of the statistical polymer segments within the polymer network remains possible whatever the temperature ($T > 0$ K). Nevertheless its probability of occurrence is directly related to the temperature T as:

$$p_{1\to 2} \propto \exp\left(-\frac{\Delta\bar{G}_{1\to 2}}{R\cdot T}\right) \tag{2.4}$$

with $p_{1\to 2}$ the transition probability of the considered type of cooperative segmental mobility from a state 1 to a state 2.

$\Delta\bar{G}_{1\to 2}$ is the difference in molar free enthalpy due to the transition from state 1 to state 2 for a given type of motion and R is the gas constant and is defined as

$$\Delta\bar{G}_{1\to 2} = \Delta\bar{H}_{1\to 2} - T\cdot\Delta\bar{S}_{1\to 2} \tag{2.5}$$

where $\Delta\bar{H}_{1\to 2}$ and $\Delta\bar{S}_{1\to 2}$ are respectively the molar enthalpy and the molar entropy due to the transition from state 1 to state 2.

It implies that the transition probability per unit of time $r_{1\to 2}$ depends also on the temperature as:

$$r_{1\to 2} \propto \exp\left(-\frac{\Delta\bar{G}_{1\to 2}}{R\cdot T}\right) \tag{2.6}$$

With decreasing temperature, the polymer network needs longer to reach equilibrium because the transition probability per unit of time decreases as well.
Note that $\Delta\bar{G}_{1\to 2} = \Delta\bar{H}_{1\to 2} - T\cdot\Delta\bar{S}_{1\to 2}$ depends slightly on the temperature too because the mass density and thus the interaction energy increases. However, the decisive factor in equation (2.6) is the term T in the denominator of the exponent.

In the considered temperature region $(T_1 < T_{g_a})$, the rearrangement of the structural elements appears then to be "blocked" and the corresponding relaxation phenomena seem to be inexistent. This gives the impression that no phenomenon of relaxation takes place and is often interpreted as an elastic response, since the corresponding times of relaxation are extreme long compared to the experimental timescale. The relaxation of the polymer network to reach equilibrium is though never "blocked" since $r_{1\to 2} > 0$.

However, the relaxation processes of the polymer network cannot come to their equilibrium on the experimental timescale and the polymer network in this glassy state behaves almost like a material usually referred as "elastic solid"[2]. As a result, the shear stress $T_{12}(t)$ in Figure 2-1 is proportional to the applied shear strain γ_0 during the whole test. Such materials are termed Cauchy elastic. The Cauchy stress $T_{12}(t)$ does not depend on the strain path via the current

[2] However, such an "elastic solid" is a purely theoretical consideration since there is no matter with a non-zero mass which can move instantaneously and without loss of energy. Thus, with this consideration, all real materials show relaxation phenomena, even if these cannot be observed within the experimental timescale. Therefore, in the strict meaning of the term, all real materials behave viscoelastic, regardless of the measuring temperature and timescale.

strain level is attained, but the work done by the stress, also called strain energy which can depend on the deformation path.

Under external stress, the strong covalent intramolecular bonds of the glassy network are strained, resulting in a mechanical elastic modulus in the range of 1-10 GPa – Figure 2-5. As this apparent "elasticity" involves essentially internal energy changes[3] in the polymer due to the displacement of atoms or molecular groups in potential energy wells, the macroscopic mechanical response of this region is named energy elasticity. With increasing temperature, anharmonic effects increase the distance between the structural elements of the polymeric chains. Therefore, the bond strengths and the elastic moduli slightly decrease with increasing temperature [76].

In the energy-"elastic" state, the polymer network is in a non-equilibrium state which tends towards equilibrium through very slow relaxation processes at temperatures far below the glass transition temperature, T_g. These processes are sometimes denominated as "physical ageing" [77].

2.1.2.2. Glass transition region

With increasing temperature $T_{g_a} < T_2 < T_{g_e}$ motions of the polymer segments begin to be experimentally detectable in the glassy polymer. Brought out of equilibrium by the action of external stresses or deformations, the polymer network undergoes processes to re-establish its equilibrium. It results in a decrease of $T_{12}(t)$ with increasing measuring time as shown in Figure 2-1. In this temperature region, the higher is the measuring temperature, the faster are the relaxation processes and the faster is the equilibrium reached.

The rearrangements in the polymer network are then varied and different numbers of segments under different conditions of interaction are involved. Responsible forces for the rearrangement are driven by both enthalpic and entropic effects. With increasing temperature, the role of the entropic contribution increases (see section 2.1.3). The corresponding relaxation processes and associated relaxation times are responsible for the time-delayed mechanical response in the experimental timescale. In this glass transition range, the mechanical properties of the polymer are considerably sensitive to any temperature change. As indicated in Figure 2-5, the relaxation modulus decreases of several decades during this transition.

[3] As the polymer chains cannot be significantly stretched along the deformation axis, the entropic contribution of the elasticity of the system can be here neglected in comparison to the energetic/enthalpic one (see section 2.1.3).

2.1.2.3. Entropy-elastic state

As the temperature is further increased ($T_3 > T_{g_e}$), the rearrangement of the structural elements occurs so rapidly that no relaxation phenomena can be observed on the experimental timescale as depicted in Figure 2-1. There is always time for equilibrium to be established. As this elasticity involves essentially changes of entropy in the polymer due to the configurational changes in the deforming polymer network, the macroscopic mechanical response of this region is named entropy elasticity. This elastic behaviour differs sharply from the energy elasticity of the glassy polymer in the low values of the moduli of elasticity, in the huge invertible deformation and in the opposite temperature dependence of the elastic moduli as shown in Figure 2-5. Based on these experimental observations, a theory of the entropy elasticity has been developed. A detailed overview of the different thermodynamic and statistical approaches are discussed in [78, 79]. The thermodynamic description of entropy elasticity considers only the macroscopic behaviour (see section 2.1.3) of the polymer network whereas the statistical treatment focuses on the (statistical) molecular structure of the polymer network.

In the statistical consideration, it is assumed that the network is a one in that all polymer chains contribute to the elastic stress and that the elastic force of the polymer network is entirely attributed to the conformational entropy of the deformation. Any other kind of interatomic interaction is not considered here. As previously mentioned, the entropy elasticity of the investigated polyurethane elastomer confirms this assumption. The mechanical behaviour of the polymer can be then determined by calculating the entropy S of the system using the Boltzmann's relation:

$$S = k \cdot \ln(\Omega) \tag{2.7}$$

k is the Boltzmann's constant and Ω the total number of conformations available to the system. Statistical mechanics considers the structure of polymer chains and the many different conformations that they can assume to determine the entropy of the system. However, the presence of various kinds of interactions in polymers makes this statistical calculation very complex. To simplify the statistical consideration of the polymer network, idealised models are used to derive the average properties and the following assumptions are made [75]:

- All conformations are isoenergetic. Hence, the internal energy of the system is independent of the conformations of the individual chains.
- Each network chain is freely joined, volumeless and continually undergoing conformational rearrangements due to thermal motion. The number of conformations available to each individual chain is given by the Gaussian distribution function.
- The total number of conformations of an isotropic network of such Gaussian chains is the product of the number of conformations of the individual network chains.
- Crosslink nodes are fixed at their mean positions in the network and deform affinely. The microscopic strain of the chains is then directly proportional to the macroscopic strain of the elastomer.
- Upon deformation, the volume of the elastomer sample remains constant.

Naturally these considerations differ from the behaviour of a real elastomer network and different approaches are discussed [70, 78-83]. If an elastomer is incompressible and has a perfect three-dimensional network with tetrafunctional crosslink points, it can be shown that

$$\mu = \kappa \cdot R \cdot T \tag{2.8}$$

where μ is the relaxed shear modulus of the polymer network, κ is a parameter representing the average crosslink density in the polymer network, R is the gas constant and T is the absolute temperature. Note that, according to equation (2.8), the cross-link density is also 0 at a theoretical temperature of 0 K as this theory considers only the entropic contribution to the internal energy of the sample. This is obviously not the case in reality and this shows one of the limitations of this theory.

Simulations have shown that models based on a Gaussian network describe insufficiently the experimental results for finite deformation while a model considering Langevin chains obtains in general better results, including at large strain [84]. In that case, the expression of κ in equation (2.8) is then modified but the linear relation between μ and T remains unchanged.

The experimental results presented later in this work show a linear increase of the relaxed shear modulus with increasing temperature and confirm in this way the validity of the equation (2.8) for the investigated polyurethane adhesive.

2.1.3. **Thermodynamic description**

The thermodynamic considerations provide information about the relative significance of the energy and the entropy contributions in the apparent elasticity of the polymer network. Since these considerations use the equilibrium thermodynamics, only the equilibrium moduli are here concerned.
Let consider a relaxed polymer network (system) with a volume, V, having the internal energy, U, and the entropy, S, be deformed by an amount, dl, in tension. The deforming force, f, exerted by the sample in equilibrium is measured as a function of temperature, T. This closed system, i.e. the polymer sample, is able to exchange work and heat with its surroundings: dW is the increment of work performed on the system by its surroundings and dQ the increment of heat transferred to the system. The first law of thermodynamics gives[4]:

$$dU = dQ + dW \tag{2.9}$$

[4] Sign convention: all energy transfers to the system are considered as positive and all energy transfers from the system as negative.

The initial state (undeformed) and the deformed state of the sample are both in thermodynamic equilibrium:

$$dU = dU_{deform} - dU_{undeform} \tag{2.10}$$

For T and p constant and for a change from one equilibrium state to another, the heat quantity

$$dQ = TdS \tag{2.11}$$

must have been exchanged with the environment, even if the deformation process is naturally not reversible.

The increment of mechanical work, dW , includes the contributions of the mechanical work, fdl due to the deformation and of the volume work, $-pdV$, caused by external hydrostatic pressure, *p*, on :

$$dW = -pdV + fdl \tag{2.12}$$

p is the atmospheric pressure and dV the volume change of the elastomer due to the elongation. The sign of the term fdl is the opposite of pdV because f is the force applied to the system by the environment. In this example, only the one-dimensional elongation dl of the elastomer sample in the longitudinal direction and the corresponding mechanical work dW are considered.
Equation (2.9) can also be written, after substituting the values of dQ and dW as:

$$dU = TdS - pdV + fdl \tag{2.13}$$

Since the experiments are performed at constant (atmospheric) pressure, the state of the system can be described using the enthalpy H as thermodynamic potential:

$$H = U + pV \tag{2.14}$$

The corresponding differential equation at constant pressure is:

$$dH = dU + pdV \tag{2.15}$$

The expression of dU from equation (2.13) is replaced in (2.15):

$$dH = TdS + fdl \tag{2.16}$$

Hence the deforming force f , applied to the system by the environment at constant temperature and pressure, can be expressed as:

$$f = \left(\frac{dH}{dl}\right)_{T,p} - T\left(\frac{dS}{dl}\right)_{T,p} \tag{2.17}$$

In equation (2.17), the elastic force f results from enthalpic and entropic effects. To discuss the influence of these contributions, the temperature dependence of the force is considered. According to one of the Maxwell's relations:

$$\left(\frac{dS}{dl}\right)_{T,p} = -\left(\frac{df}{dT}\right)_{l,p} \tag{2.18}$$

It should be noted that equation (2.18) is of interest because it links a tangible experimental result to an entropy change of the system. If during a tensile test at a higher temperature, a greater force *f* is required to deform the sample by the same *dl* than before (i.e. $\left(\frac{df}{dT}\right)_{l,p} > 0$) also this means that $\left(\frac{dS}{dl}\right)_{T,p} < 0$: the entropy of the system therefore decreases due to the deformation.

In the opposite case where $\left(\frac{df}{dT}\right)_{l,p} < 0$ is observed, the entropy of the system is increased due to the deformation.

Thus the equation (2.17) becomes

$$f = \left(\frac{dH}{dl}\right)_{T,p} + T\left(\frac{df}{dT}\right)_{l,p}, \tag{2.19}$$

which can be re-expressed as:

$$\left(\frac{df}{dT}\right)_{l,p} = \frac{f - \left(\frac{dH}{dl}\right)_{T,p}}{T} = -\left(\frac{dS}{dl}\right)_{T,p} \tag{2.20}$$

The equation (2.20) shows that:

- $\left(\frac{df}{dT}\right)_{l,p} < 0$ when $\left(\frac{dH}{dl}\right)_{T,p} > f$
- $\left(\frac{df}{dT}\right)_{l,p} > 0$ when $\left(\frac{dH}{dl}\right)_{T,p} < f$

As described above, the deforming force is directly related to the equilibrium stress of the relaxed polymer network. The experimental results in the entropy-elastic temperature region of the polymer network, presented later in the section 4.1.2 (see Figure 4-6, for example), indicate that the equilibrium stress, i.e. the force f increases with increasing temperature and thus $\left(\frac{dH}{dl}\right)_{T,p} < f$.

If the enthalpic term can be neglected in comparison with f, equation (2.17) gives the borlerline case for the entropy-elastic temperature region:

$$f \approx -T\left(\frac{dS}{dl}\right)_{T,p} \tag{2.21}$$

In this case, the elastic response of the relaxed polymer network originates solely from the entropic effect. For this reason, the rubber elasticity is also called entropy elasticity.
As the external force *f* is balanced by the restoring force in the deformed material in equilibrium, we can write

$$f = \left| f_{restoring} \right| = M \cdot dl \tag{2.22}$$

with *M* the equilibrium mechanical modulus for uniaxial stretch

With equation (2.21), we get

$$M = \frac{f}{dl} \approx -T\left(\frac{dS}{dl}\right)_{T,p} \tag{2.23}$$

for the entropy-elastic temperature region of the polymer network.

The restoring force – i.e. the mechanical moduli – of the relaxed polymer network is then directly proportional to the absolute temperature.
Hence, $\left(\frac{dS}{dl}\right)_{T,p} < 0$ since $M > 0$ is found in the mechanical experiments.

The linear temperature dependence of the (relaxed) elastic response of the polymer network presented in the section 4.1.2 confirms that the elastic behaviour of the elastomer is governed by the entropic contribution under the chosen experimental conditions. At very high deformation, the crosslinks limit the motion of the polymer chains and the enthalpic effects cannot be neglected anymore because of the finite extensibility of the network chains. It may be noted in passing that the experimental results indicate that the investigated elastomer behaves quasi incompressible as the volume work can be neglected.

In the above development, the considered properties are only defined when the polymer network is in a state of thermodynamic equilibrium. This means that all relaxation/retardation processes take place on a timescale that is long in comparison to any relaxation time relevant to the phenomena that are occurring. Nonetheless the application of these considerations to "frozen" inequilibrium, in which relaxation times are infinitely long such as in the energy elastic state of the polymer network, is experimentally successful [85].
In the energy-elastic temperature region of the polymer network, entropy changes can be neglected as the cooperative mobility in the polymer network is no longer relevant: $p_{1\to 2}$ in equation (2.4) and $r_{1\to 2}$ in equation (2.6) are small enough to be neglected.

This gives the borderline case for the energy-elastic temperature region of the polymer network in which $\left(\frac{dH}{dl}\right)_{T,p} >> T\left(\frac{dS}{dl}\right)_{T,p}$

Equation (2.17) becomes

$$f \approx \left(\frac{dH}{dl}\right)_{T,p} = \left(\frac{dU}{dl}\right)_{T,p} + p\left(\frac{dV}{dl}\right)_{T,p} \tag{2.24}$$

With eq. (2.23) in eq. (2.24), we get

$$M = \frac{f}{dl} \approx \frac{1}{dl}\left(\frac{dH}{dl}\right)_{T,p} \approx \frac{1}{dl}\left(\frac{dU}{dl}\right)_{T,p} + \frac{p}{dl}\left(\frac{dV}{dl}\right)_{T,p} \tag{2.25}$$

This equation confirms that M is not only correlated with U but also with V when the considered material is compressible.

In the glass transition temperature region of the polymer network, the equilibrium mechanical properties change from one borderline case to the other (E-elastic to S-Elastic or vice versa).

2.1.4. **Mechanical models for linear viscoelasticity**

Independently of the phenomenological description developed above, models are often considered to represent linear viscoelastic behaviour of polymers in order to better visualise the relaxation/retardation processes. One of the main groups of models is based on mechanical elements. These models usually consist of combinations of elastic elements (springs) and damping elements (dashpots).

The elastic element is a Hookean spring which describes purely elastic behaviour, without any inertial effect. Subjected to a sudden external load, such a spring responds instantaneously and any deformation is completely reversible as shown in Figure 2-6. The relation between the applied shear stress T_{12} and resulting shear strain γ can be described using Hooke's law and the shear modulus G [Pa]:

$$\gamma^{spring} = \frac{T_{12}^{spring}}{G} \tag{2.26}$$

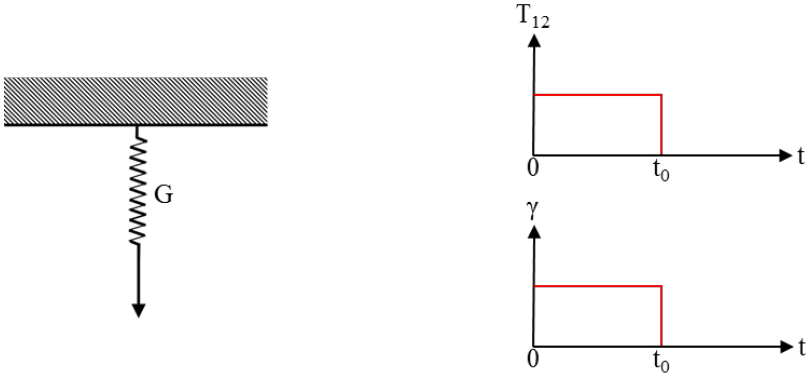

Figure 2-6: Elastic element (left) obeying Hooke's law and its mechanical response when subjected to a sudden shear load applied between $0 \leq t \leq t_0$ (right).

The damping element is a Newtonian dashpot that describes the dissipation of mechanical work during deformation. When the load is applied, there is no instantaneous strain and after its removing, there is no elastic recovery but a permanent strain. Newton's law gives:

$$\frac{d\gamma^{dashpot}}{dt} = \dot{\gamma}^{dashpot} = \frac{T_{12}^{dashpot}}{\eta} \tag{2.27}$$

where $\dot{\gamma}$ [s^{-1}] is the shear rate and η [Pa·s] the characteristic viscosity of the damping element.

The resulting shear strain $\gamma^{dashpot}$ does not only depend on the applied shear stress $T_{12}^{dashpot}$ but also on the time as illustrated in Figure 2-7 (right).

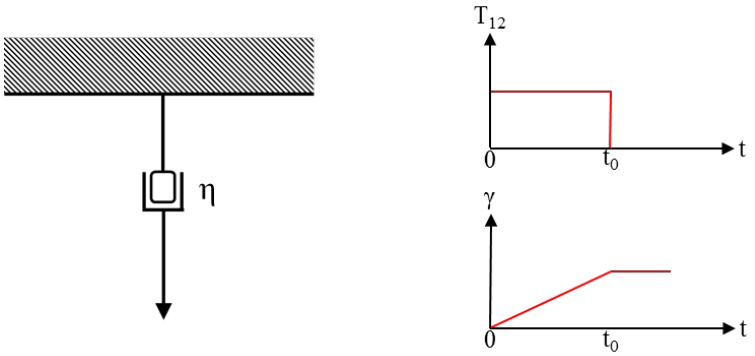

Figure 2-7: Damping element (left) consisting of a piston moving in a viscous liquid obeying Newton's viscosity law and its mechanical response when subjected to a sudden shear load applied between $0 \leq t \leq t_0$ (right).

Linear viscoelastic behaviour of polymers cannot be modelled by these simple elements, but combinations of these elements can do the job. The simplest conceivable combinations of spring and damper are the Maxwell model (Figure 2-8) and the Kelvin-Voigt model (Figure 2-9).

Maxwell model

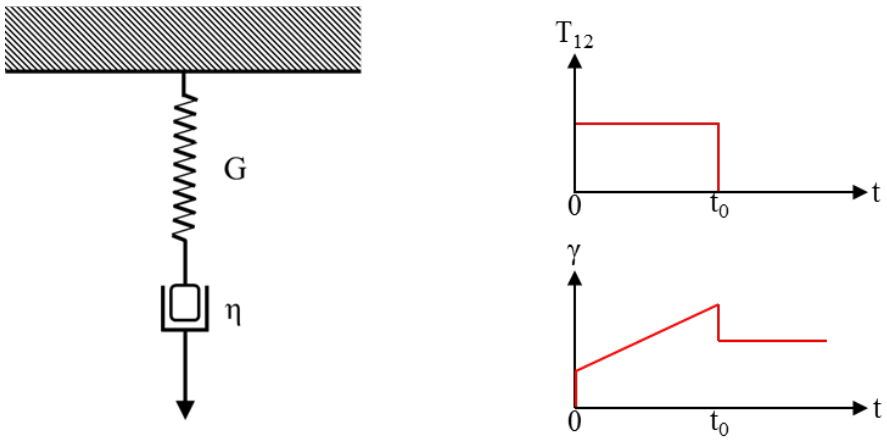

Figure 2-8: Maxwell model (left) and its mechanical response to a sudden constant shear load $T_{12}^{ext}(t)$ applied between $0 \leq t \leq t_0$ (right)

The Maxwell model consists of an elastic element and a damping element in series. Subjected to an external shear load, the resulting stress is the same in both elements whereas the resulting strain is the sum of the strains of each element:

$$T_{12}^{ext}(t) = T_{12}^{Maxwell}(t) = T_{12}^{spring}(t) = T_{12}^{dashpot}(t) \tag{2.28}$$

$$\gamma^{Maxwell}(t) = \gamma^{spring}(t) + \gamma^{dashpot}(t) \tag{2.29}$$

Differentiating (2.29) gives:

$$\dot{\gamma}^{Maxwell}(t) = \dot{\gamma}^{spring}(t) + \dot{\gamma}^{dashpot}(t) \tag{2.30}$$

Putting the first derivative of (2.26) and (2.27) into (2.30) gives the constitutive relation for the Maxwell model:

$$\dot{\gamma}^{Maxwell}(t) = \frac{\dot{T}_{12}^{Maxwell}(t)}{G} + \frac{T_{12}^{Maxwell}(t)}{\eta} \tag{2.31}$$

Considering a sudden and constant load $T_{12}^{ext}(t) = T_{12}^{0}$ for $t \geq 0$, the response of a Maxwell model is:

$$\gamma^{Maxwell}(t) = \frac{T_{12}^{0}}{G}\left(1 + \frac{t}{\tau}\right) \tag{2.32}$$

where the relaxation time τ [s] is defined as follows:

$$\tau = \frac{\eta}{G} \tag{2.33}$$

Polymer networks are not able to macroscopically flow such as thermoplastics. Therefore, the viscosity parameter η in the mechanical models is a macroscopic model parameter that depicts mechanical energy dissipation due to molecular friction. η never appears separately but only as numerator in the retardation and respectively relaxation times τ_i which are considered in this work.

As illustrated in Figure 2-8, when the load is applied, an instantaneous strain is observed and then the strain increases linearly with a slope of $\frac{T_{12}^{0}}{G} \cdot \frac{1}{\tau}$. After removing this load, there is an elastic recovery as well as a permanent strain remaining due to the dashpot. A single Maxwell model is not able to describe the mechanical behaviour of a polymer network.

If the Maxwell model is suddenly deformed and held to a constant shear strain γ_0 for $t \geq 0$, the solution of equation (2.31) is

$$T_{12}'(t) = \gamma_0 \cdot G \cdot e^{-t/\tau} \tag{2.34}$$

The stress decays within a period of time which equals $\tau = \frac{\eta}{G}$.

Kelvin-Voigt model

The Kelvin-Voigt model consists of an elastic element and a damping element in parallel – Figure 2-9 (left).

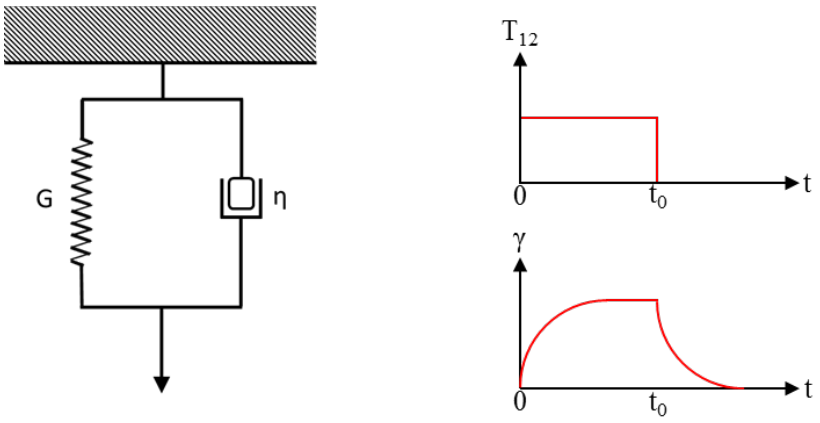

Figure 2-9: Kelvin-Voigt model (left) and its mechanical response to a sudden constant shear load $T_{12}^{ext}(t)$ applied between $0 \le t \le t_0$ (right)

In this parallel arrangement, the resulting stress is the sum of the stress in each element whereas the strains in both elements are identical:

$$T_{12}^{ext}(t) = T_{12}^{Kelvin-Voigt}(t) = T_{12}^{spring}(t) + T_{12}^{dashpot}(t) \tag{2.35}$$

$$\gamma^{Kelvin-Voigt}(t) = \gamma^{spring}(t) = \gamma^{dashpot}(t) \tag{2.36}$$

Using (2.26) and (2.27) in (2.35) the constitutive law for the Kelvin-Voigt model is obtained:

$$T_{12}^{Kelvin-Voigt}(t) = G \cdot \gamma^{Kelvin-Voigt}(t) + \eta \cdot \dot{\gamma}^{Kelvin-Voigt}(t) \tag{2.37}$$

If a constant load $T_{12}^{ext}(t) = T_{12}^{0}$ is suddenly applied to this model for $t \ge 0$, the elastic element does not stretch immediately because of the delayed response of the damping element – Figure 2-9 (right). Thus, there is no instantaneous strain and the whole stress is borne by the damping element. If the differential equation (2.37) is integrated considering the initial condition $\gamma^{Kelvin-Voigt}(0) = 0$, the response of the Kelvin-Voigt model is:

$$\gamma^{Kelvin-Voigt}(t) = \frac{T_{12}^{0}}{G}\left(1 - e^{-t/\tau}\right) \tag{2.38}$$

When the strain starts to take place, the stress is transferred over time from the damping element to the elastic one. After infinite time, all the stress will be borne by the elastic element and the maximal strain $\gamma_{\max}^{Kelvin-Voigt}(t \to \infty) = \frac{T_{12}^{0}}{G}$ is reached.

After removing the load at t_0, the damping element retards the response of the elastic element. For $t = t_0$, equation (2.38) gives

$$\gamma^{Kelvin-Voigt}(t_0) = \frac{T_{12}^{0}}{G}\left(1 - e^{-t_0/\tau}\right) \tag{2.39}$$

Using equation (2.39) as initial condition in (2.37) one finds

$$\gamma^{Kelvin-Voigt}\left(t \geq t_0\right) = \frac{T_{12}^0}{G}\left(e^{(t_0-t)/\tau} - e^{-t/\tau}\right) \text{ for } t \geq t_0 \tag{2.40}$$

The Kelvin-Voigt model is still too simple to describe appropriately the mechanical behaviour of polymer networks because it offers only one relaxation time. Therefore, more sophisticated combinations of mechanical elements are necessary to give a more realistic approximation of the complex mechanical behaviour of polymer networks. Two models are used in this work for this purpose: the generalised Maxwell model and the Zener model. These models contain an arbitrary number of model parameters and exhibit a whole array of relaxation and retardation times.

Generalised Maxwell model

The generalised Maxwell model consists of *n*-Maxwell models and a spring connected in parallel, each unit having different parameter values (see Figure 2-10). The isolated spring in the generalised Maxwell model describes the long-term behaviour of viscoelastic polymer network.

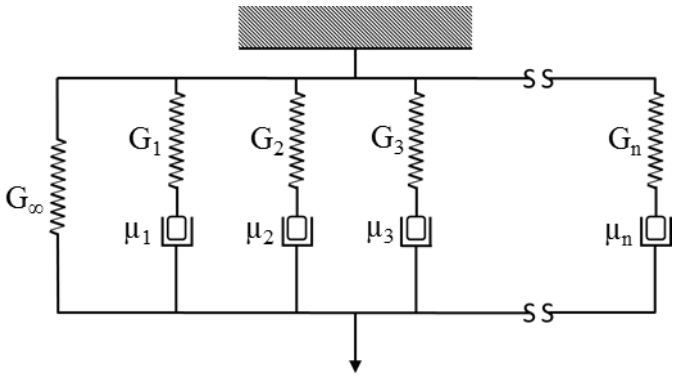

Figure 2-10: Generalised Maxwell model

During stress relaxation tests, the shear strain $\gamma\left(t \geq 0\right) = \gamma_0$ is maintained constant and the (shear) stress $T_{12}\left(t\right)$ is measured as a function of time. Since the sum of the stresses of each branch corresponds to the total stress and each branch experiences the same strain, the generalised Maxwell model is usually chosen to describe such *stress relaxation experiments*. The corresponding analytical solution for such a sudden constant strain γ_0 is then according to (2.26) and (2.34):

$$T_{12}^{gen.Maxwell}\left(t\right) = \gamma_0 \cdot \left(G_\infty + \sum_{i=1}^{n} G_i \cdot e^{-t/\tau_i}\right) \text{ for } t \geq 0 \tag{2.41}$$

The development of the analytical solution for the generalised Maxwell model is presented in section 2.5.

The generalised Maxwell model is also used to describe *shear tests at constant shear rate* since the deformation rate is identical in each branch of the model (see section 2.6).

Zener model

The Zener model consists of *n*-Kelvin-Voigt models and an isolated spring connected in series (see Figure 2-11). The isolated spring in the Zener model provides an instantaneous response under load. Such a response is only a theoretical consideration to describe all retardation or relaxation processes that occur too fast to be detected experimentally.

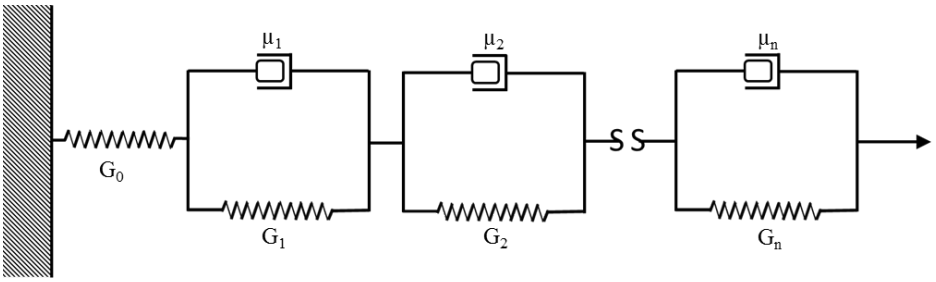

Figure 2-11: Zener model

The sum of each elementary strain (isolated spring and each Kelvin-Voigt model) is equal to the total strain. Each element experiences the same stress. For this reason, this model is preferred for the description of *creep experiments* (see section 2.4). The corresponding analytical solution for such a sudden constant load T_{12}^0 for $t \geq 0$ is then according to (2.26) and (2.38):

$$\gamma^{Zener}(t) = T_{12}^0 \left(\frac{1}{G_0} + \sum_{i=1}^{n} \frac{1}{G_i} \left(1 - e^{-t/\tau_i} \right) \right) \text{ for } t \geq 0 \qquad (2.42)$$

The generalised Maxwell model and the Zener model describe both well the usual features of the viscoelastic behaviour of polymer networks, such as the "instantaneous" deformation, the creep/relaxation plateau and the relaxation/retardation processes.
Provided that the number of elements of the two models are equal and that there are certain relationships between their parameters, the two models are mechanically equivalent [86].

The number *n* of individual elements in both models is not fixed and can be chosen to achieve the highest possible accuracy in modelling the complex mechanical behaviour of polymer networks. The distribution of retardation and relaxation times which is, in reality, continuous is discretised.
In fact, the τ_i provided by the model cannot in principle be attributed to molecular relaxations. Polymer physics proves that behind every individual relaxation element ($\sigma_i; \tau_i$), there is a weighted superposition of all molecular motions. Only in the rare exception would only one of these weighting factors be 1 and all others 0. The rheological models serve the macroscopic phenomenological quantitative description of the mechanical infinitesimal deformation behaviour, but they do not give access to the molecular movements and their time constants.

However, the description of the behaviour of polymer networks by means of such one-dimensional mechanical models is only a simplified approximation; they are an adequate tool to better understand the experimental results of this work.

2.2. Tensile tests

Uniaxial isothermal tensile tests have been used in this work to determine the mechanical properties of the bulk adhesive – i.e. without any influence of metal polymer interphase.

During such tensile tests the applied force, F, the change in length, $\Delta l = l - l_0$, and width, $\Delta w = w - w_0$, of the specimen are measured – see Figure 2-12.

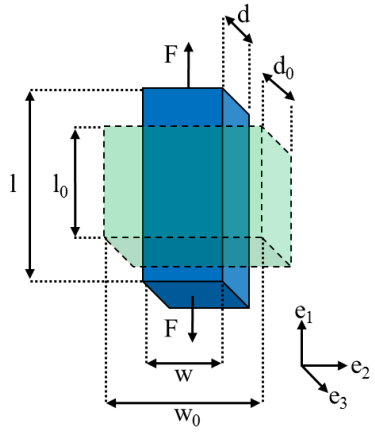

Figure 2-12: Uniform deformation during tensile test

Knowing the initial length l_0, width w_0 and thickness d_0, the longitudinal strain ε_1 and the transverse strain ε_2 can be calculated according to the following equations:

$$\varepsilon_1 = \frac{dl}{l_0}, \varepsilon_2 = \frac{dw}{w_0} \tag{2.43}$$

Usually, strains ε_i are utilised as measures for small deformations only.

The stretches λ_i $(i = 1,2,3)$ of the sample in the three spatial directions (e_1, e_2, e_3) are defined as the ratios of the actual dimension of the sample (l, w, d) and the initial dimension (l_0, w_0, d_0):

$$\lambda_1 = \frac{l}{l_0}, \lambda_2 = \frac{w}{w_0}, \lambda_3 = \frac{d}{d_0} \tag{2.44}$$

The stretches λ_i describe large deformations as well.

Due to the amorphous character of the chosen polyurethane adhesive (see section 3.1.2) it can be assumed that the material behaves isotropic when stretched within reasonable limits[5], i.e. thickness and width change equally:

$$\lambda_2 = \lambda_3 \tag{2.45}$$

[5] Uniaxial stretching will generate anisotropy at some point.

If the polyurethane adhesive can be considered as "incompressible", then the following condition is fulfilled:

$$\lambda_1 \cdot \lambda_2 \cdot \lambda_3 = \lambda_1 \cdot \lambda_2^2 = 1 \tag{2.46}$$

Thus λ_2 can be expressed in function of λ_1 with equation (2.46):

$$\lambda_2 = \frac{1}{\sqrt{\lambda_1}} \tag{2.47}$$

The equation (2.47) is used to experimentally verify whether the investigated polyurethane can be considered as "incompressible": the measured values of λ_2 are compared to the calculated ones using the measured values of λ_1 as illustrated in Figure 2-13. As there is no significant deviation between the measured λ_2 and the calculated values in Figure 2-13 (right), the investigated polyurethane can be considered incompressible within the measured strain range.

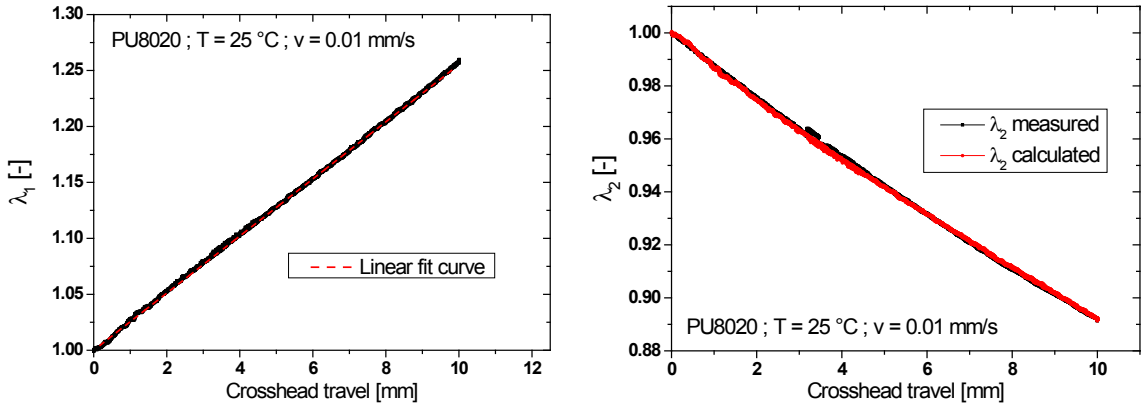

Figure 2-13: Tensile test with the polyurethane adhesive "PU8020" at 25 °C with a crosshead speed of 0.01 mm/s: stretching λ_1 as a function of the crosshead travel (left) and stretching λ_2 as a function of the crosshead travel (right)

The Cauchy stress component, T_{11}, (in the direction of the applied load) provides the reaction force to the external load, $\vec{F}$ in the tensile test, i.e.

$$|T_{11}| = \frac{|\vec{F}|}{A} = \frac{F}{w \cdot d} \tag{2.48}$$

For the rectangular sample with actual cross section area A, as shown in Figure 2-12.

Then, using the equation (2.44) and the fact that the investigated polyurethane is isotropic – eq. (2.45) and incompressible – eq. (2.46), the Cauchy stress component T_{11} can be rewritten as:

$$T_{11} = \frac{F}{w_0 \cdot d_0 \cdot \sqrt{\lambda_1}} \tag{2.49}$$

Since all the values in the equation (2.49) are measured during the tensile test T_{11} can be easily calculated.

Previous works [1, 72] have shown that the Mooney-Rivlin material model [68, 87] can provide a good description of the mechanical behaviour of polyurethane adhesives under larger deformations. As the investigated polyurethane adhesive is very similar to the one used in these works, the analytical solution of the Mooney-Rivlin model has been also used to describe the tensile tests. In this analytical solution, the Cauchy stress tensor $\overline{T}$ is given as a function of the Cauchy-Green deformation tensor $\overline{B}$:

$$\overline{T} = -p\overline{I} + \mu_{Bulk}\left(\frac{1}{2}+\beta\right)\overline{B} - \mu_{Bulk}\left(\frac{1}{2}-\beta\right)\overline{B}^{-1} \tag{2.50}$$

where p is the pressure, $\overline{I}$ the identity tensor, μ_{Bulk} the hyperelastic shear modulus of the bulk adhesive and β is a material parameter which follows the condition $-0.5 \leq \beta \leq 0.5$.

The Cauchy-Green deformation tensor $\overline{B}$ is determined from the deformation gradient. After taking into account the isotropy and incompressibility conditions for the adhesive, $\overline{B}$ and $\overline{B}^{-1}$ can be expressed as:

$$\overline{B} = \begin{bmatrix} \lambda_1^2 & 0 & 0 \\ 0 & 1/\lambda_1 & 0 \\ 0 & 0 & 1/\lambda_1 \end{bmatrix}, \overline{B}^{-1} = \begin{bmatrix} 1/\lambda_1^2 & 0 & 0 \\ 0 & \lambda_1 & 0 \\ 0 & 0 & \lambda_1 \end{bmatrix} \tag{2.51}$$

As uniaxial tensile tests are considered, only the Cauchy stress component in the direction of the applied load T_{11} is not equal to 0:

$$T_{22} = T_{33} = 0 \tag{2.52}$$

Therefore the pressure p can be deduced from eq. (2.50):

$$p = \mu_{Bulk}\left(\frac{1}{2}+\beta\right)\frac{1}{\lambda_1} - \mu_{Bulk}\left(\frac{1}{2}-\beta\right)\lambda_1 \tag{2.53}$$

Introducing eq. (2.53) in eq. (2.50) the normal stress component in axial load direction T_{11} becomes:

$$T_{11} = \mu_{Bulk}\left(\frac{1}{2}+\beta\right)\left(\lambda_1^2 - \frac{1}{\lambda_1}\right) - \mu_{Bulk}\left(\frac{1}{2}-\beta\right)\left(\lambda_1^{-2} - \lambda_1\right) \tag{2.54}$$

Johlitz shows in his work [72] that the material parameter β must be set to 0.5 in order to achieve a physically meaningful fit of the experimental data. So, it turns out that a special case of the Mooney-Rivlin model, the incompressible Neo-Hooke model is obtained:

$$T_{11} = \mu_{Bulk} \cdot \left(\lambda_1^2 - \frac{1}{\lambda_1}\right) \tag{2.55}$$

Thus, the shear modulus of the bulk adhesive can be calculated using uniaxial isothermal tensile tests.

2.3. Shear tests at constant shear rate

Isothermal shear tests at constant shear rate have been performed in this work in order to investigate a potential bond line thickness dependence of the shear modulus in adhesive joints. The corresponding results are presented in chapter 4.

2.3.1. Description of shear tests at constant shear rate

The sample geometry and the experimental set-ups for these experiments have been designed in such a way that the variations in the deformation of the adhesive layer can be neglected (no edge effects) and that the adhesive thickness d_P remains constant during the test (see sections 3.2.2 and 3.3.3).

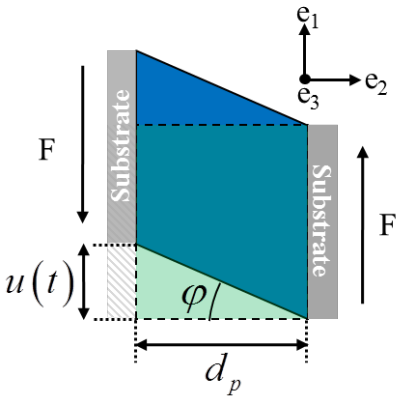

Figure 2-14: Homogeneous deformation during shear test

In such simple shear tests, the substrates move parallel at a constant distance d_P along the direction e_1 – Figure 2-14. The quantity $u(t)$ denotes the applied displacement in the direction e_1 and the angle φ is related to the effective shear strain $\gamma_{eff}(t)$ in the following way:

$$\gamma_{eff}(t) = \tan\varphi(t) = \frac{u(t)}{d_p} \tag{2.56}$$

The resulting Cauchy shear stress $T_{12}(t)$ is calculated as follows:

$$T_{12}(t) = \frac{F(t)}{A} \tag{2.57}$$

where $F(t)$ is the applied force and A the bonded area (2000 mm²).

In equation (2.56) the effective shear strain $\gamma_{eff}(t)$ is introduced because the displacement $u(t)$ is determined macroscopically across d_P and thus refers to the entire adhesive layer. However, as discussed in chapter 1, assuming a mechanical interphase at the interface "substrate-adhesive", the deformation of the adhesive layer cannot be homogeneous and local

gradients in its mechanical properties should exist. This mechanical interphase can be either more or less compliant than the bulk adhesive. In the continuation of this work, all the measured shear strains must be considered as effective values regardless of the type of experiment (creep, stress relaxation or shear tests at constant shear rate).

The Mooney-Rivlin model describes the quasistatic shear tests for finite shear deformation. As for the tensile tests, the Cauchy stress tensor $\overline{T}$ is given as a function of the Cauchy-Green deformation tensor $\overline{B}$:

$$\overline{T} = -p\overline{I} + \mu_{eff}\left(\frac{1}{2}+\beta\right)\overline{B} - \mu_{eff}\left(\frac{1}{2}-\beta\right)\overline{B}^{-1} \tag{2.58}$$

where p is the pressure, $\overline{I}$ the identity tensor, μ_{eff} the effective hyperelastic shear modulus of the adhesive bondline in an adhesive joint and β is a material parameter which follows the condition $-0.5 \leq \beta \leq 0.5$.

After taking into account the isotropy and incompressibility conditions for the adhesive, $\overline{B}$ and $\overline{B}^{-1}$ become:

$$\overline{B} = \begin{bmatrix} 1+\gamma_{eff}^{\ 2} & \gamma_{eff} & 0 \\ \gamma_{eff} & 1 & 0 \\ 0 & 0 & 1 \end{bmatrix}, \overline{B}^{-1} = \begin{bmatrix} 1 & -\gamma_{eff} & 0 \\ -\gamma_{eff} & 1+\gamma_{eff}^{\ 2} & 0 \\ 0 & 0 & 1 \end{bmatrix} \tag{2.59}$$

As shear tests are considered, the Cauchy stress component $T_{33} = 0$. Therefore the pressure p can be deduced from eq. (2.58):

$$p = 2 \cdot \mu_{eff} \cdot \beta \tag{2.60}$$

Introducing eq. (2.60) in eq. (2.58) the other shear stress components of the Cauchy stress tensor $\overline{T}$ become:

$$\begin{aligned} T_{11} &= \mu_{eff} \cdot \gamma_{eff}^{\ 2} \cdot \left(\frac{1}{2}+\beta\right) \\ T_{12} &= \mu_{eff} \cdot \gamma_{eff} \\ T_{22} &= -\mu_{eff} \cdot \gamma_{eff}^{\ 2} \cdot \left(\frac{1}{2}-\beta\right) \end{aligned} \tag{2.61}$$

Considering the neo-Hookean behaviour ($\beta = 0.5$) of the polyurethane adhesive stated in [72], we obtain

$$\begin{aligned} T_{11} &= \mu_{eff} \cdot \gamma_{eff}^{\ 2} \\ T_{12} &= \mu_{eff} \cdot \gamma_{eff} \\ T_{22} &= 0 \\ T_{33} &= 0 \end{aligned} \tag{2.62}$$

Thus, the effective hyperelastic shear modulus of the bondline in adhesive joints is defined as:

$$\mu_{eff} = \frac{T_{12}}{\gamma_{eff}} \tag{2.63}$$

In the entropy elastic range of the adhesive, the stress-strain behaviour results in a straight line whose slope corresponds to the, in this case, constant effective shear modulus μ_{eff} in the measured strain range.

In the viscoelastic range, the plot $T_{12}(t)$ as a function of the effective shear strain $\gamma_{eff}(t)$ does not result in a straight line and the dynamic shear modulus M_{eff} strongly depends on the shear strain and the shear rate $\dot{\gamma}_{eff} = \frac{d\gamma_{eff}(t)}{dt}$.

The shear strength or effective dynamic shear modulus $M_{eff}(\gamma, t, T)$ can be determined by plotting the shear stress $T_{12}(t)$ as a function of the effective shear strain $\gamma_{eff}(t)$:

$$M_{eff}(\gamma, t, T) = \frac{dT_{12}(t)}{d\gamma_{eff}(t)} \tag{2.64}$$

2.3.2. **Analytical solution of the generalised Maxwell model**

The generalised Maxwell model offers a relatively simple analytical solution for shear tests at constant shear rate that can be used to identify material parameters from experimental results.

The generalised Maxwell model consists of *n* Maxwell models and one spring connected in parallel (see Figure 2-10). By first considering a single Maxwell model (see Figure 2-8), we assume that the shear strain rate remains constant during the whole shear test[6]:

$$\dot{\gamma}(t) = \frac{d\gamma(t)}{dt} = const \tag{2.65}$$

Inserting eq. (2.65) in eq. (2.31) yields to the following ordinary differential equation:

$$\dot{\gamma}^{Maxwell} = \frac{\dot{T}_{12}^{Maxwell}(t)}{G_{eff}} + \frac{T_{12}^{Maxwell}(t)}{\eta} \tag{2.66}$$

- Solution of the homogeneous equation $T_{12}^{Maxwell,c}(t)$:

$$\dot{T}_{12}^{Maxwell,c}(t) + \frac{T_{12}^{Maxwell,c}(t)}{\tau} = 0 \tag{2.67}$$

$$T_{12}^{Maxwell,c}(t) = C \cdot e^{-t/\tau} \tag{2.68}$$

where *C* is a constant.

[6] Note that the testing machine needs in practice a short period of time to reach a constant shear strain rate.

- Solution of the inhomogeneous equation $T_{12}^{Maxwell,p}(t)$:

  $C(t)$ is now considered as a time dependent function, thus eq. (2.68) becomes

$$T_{12}^{Maxwell,p}(t) = C(t) \cdot e^{-t/\tau} \tag{2.69}$$

  Eq. (2.69) in eq. (2.66) gives

$$\frac{dC(t)}{dt} = \dot{\gamma} \cdot G \cdot e^{t/\tau} \tag{2.70}$$

  Integrating eq. (2.70) for $t \geq 0$, we obtain

$$C(t) = \dot{\gamma} \cdot G \cdot \tau \cdot \left(e^{t/\tau} - 1\right) + D \tag{2.71}$$

  where D is a constant.

  Eq. (2.71) in eq. (2.69) gives the solution of the inhomogeneous equation:

$$\begin{aligned} T_{12}^{Maxwell,p}(t) &= \left(\dot{\gamma} \cdot G \cdot \tau \cdot \left(e^{t/\tau} - 1\right) + D\right) \cdot e^{-t/\tau} \\ &= \dot{\gamma} \cdot G \cdot \tau \cdot \left(1 - e^{-t/\tau}\right) + D \cdot e^{-t/\tau} \end{aligned} \tag{2.72}$$

  The general solution $T_{12}^{Maxwell}(t)$ of the ordinary differential equation (2.66) is then the addition of the trivial solution $T_{12}^{Maxwell,c}(t)$ and the particular solution $T_{12}^{Maxwell,p}(t)$:

$$\begin{aligned} T_{12}^{Maxwell,I}(t) &= T_{12}^{Maxwell,Ic}(t) + T_{12}^{Maxwell,Ip}(t) \\ &= C \cdot e^{-t/\tau} + \dot{\gamma} \cdot G \cdot \tau \cdot \left(1 - e^{-t/\tau}\right) + D \cdot e^{-t/\tau} \end{aligned} \tag{2.73}$$

  The boundary value at t = 0 is used to determine the constants C and D:

$$T_{12}^{Maxwell}(0) = 0 \tag{2.74}$$

  It follows that:

$$T_{12}^{Maxwell,I}(0) = C + D = 0 \tag{2.75}$$

  The shear stress during a shear test at constant shear strain rate for a Maxwell element is then:

$$T_{12}^{Maxwell}(t) = \dot{\gamma} \cdot G \cdot \tau \cdot \left(1 - e^{-t/\tau}\right) \qquad \forall t \geq 0 \tag{2.76}$$

Let now consider a generalised Maxwell model (see Figure 2-10), consisting of a spring and n Maxwell models connected in parallel. The resulting shear stress in this model is the addition of the shear stress of each element:

$$T_{12}^{gen.Maxwell}(t) = T_{12}^{spring}(t) + \sum_{i=1}^{n} T_{12}^{i-Maxwell}(t) \tag{2.77}$$

Inserting(2.26) and eq. (2.76) in eq. (2.77) yields to:

$$T_{12}^{gen.Maxwell}(t) = G_{\infty} \cdot \dot{\gamma} \cdot t + \sum_{i=1}^{n} \left(\dot{\gamma} \cdot G_i \cdot \tau_i \cdot \left(1 - e^{-t/\tau_i}\right)\right) \tag{2.78}$$

where G_{∞} is the relaxed or equilibrium shear modulus.

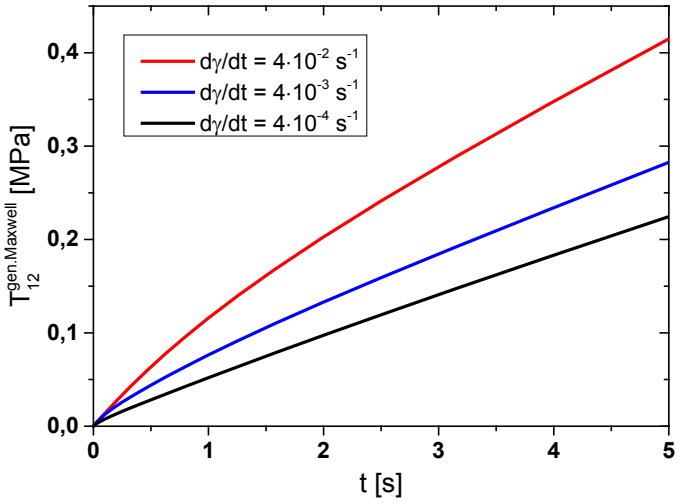

Figure 2-15: Calculated shear stress $T_{12}^{gen.Maxwell}(t)$ as a function of time during shear tests at constant shear rates using 3 Maxwell elements in eq. (2.78). The chosen material parameters (G_∞, G_i, τ_i) are issued from the experimental results obtained for PU-Al joint with $d_P = 736 \pm 9$ µm at 15 °C.

The evolution of $T_{12}^{gen.Maxwell}(t)$ during shear tests at constant shear rate is illustrated in Figure 2-15 for three different shear rates $\dot{\gamma}$: $4 \cdot 10^{-2}$ s^{-1}, $4 \cdot 10^{-3}$ s^{-1} and $4 \cdot 10^{-4}$ s^{-1}. The plots show a curvature ($\ddot{T}_{12}^{gen.Maxwell}(t) < 0$) at small times and run linearly afterwards. The faster the shear rate, the stronger the curvature and the longer it takes. At the slowest shear rate ($\dot{\gamma} = 4 \cdot 10^{-4}$ s^{-1}), this curvature is still present but is sometimes difficult to measure experimentally because disturbances during the loading process of the sample (adjustment of the shear rate) overlay this phenomenon.

According to eq. (2.64) the effective shear modulus $M_{eff}(t)$ is given for a constant shear strain rate $\dot{\gamma}$ by:

$$M_{eff}(t) = \frac{1}{\dot{\gamma}} \cdot \frac{dT_{12}(t)}{dt} = G_\infty + \sum_{i=1}^{n} G_i \cdot e^{-t/\tau_i} \tag{2.79}$$

By convention, τ_i grows with increasing index $i = 1 \ldots n$.

Based on the eq. (2.79), two limiting cases can be discussed:

- $t << \tau_1$ (or $\tau_1 \to +\infty$ or $\dot{\gamma} \to +\infty$) and t the experimental time scale or the duration of the experiment: within the experimental time scale none of the Maxwell elements have enough time to start to relax, the dashpots are "frozen" and the stress is distributed into all the spring elements – see Figure 2-16.

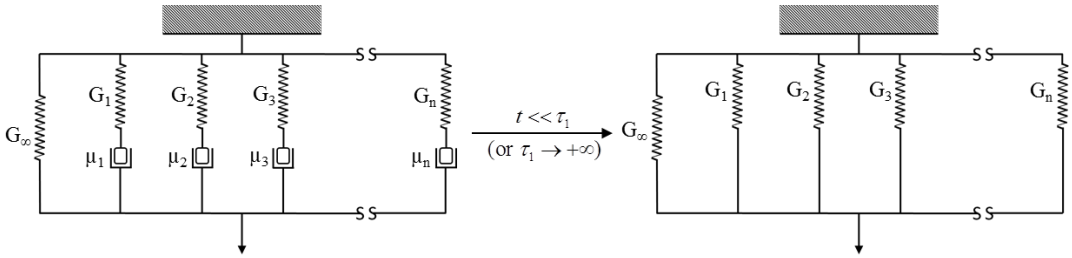

Figure 2-16: Equivalent model (right) of the generalised Maxwell model (left) when $t << \tau_1$ (or $\tau_1 \to +\infty$ or $\dot{\gamma} \to +\infty$).

Under such conditions, the polymer network is in the glassy state and the equation (2.79) becomes:

$$M_{eff}^{E-elast} = G_\infty + \sum_{i=1}^{n} G_i \tag{2.80}$$

The effective shear modulus is constant over time and $T_{12}^{gen.Maxwell}(t)$ would appear linear in Figure 2-15 with an infinite slope (overlap with the ordinate axis).

- $t >> \tau_n$ (or $\tau_n \to 0$ or $\dot{\gamma} \to 0$): all the relaxation times of the Maxwell elements are much shorter than the experimental time scale – i. e. the relaxation processes are faster than the applied strain rate so that the corresponding stress only comes from the shear modulus of the unpaired spring – see Figure 2-17.

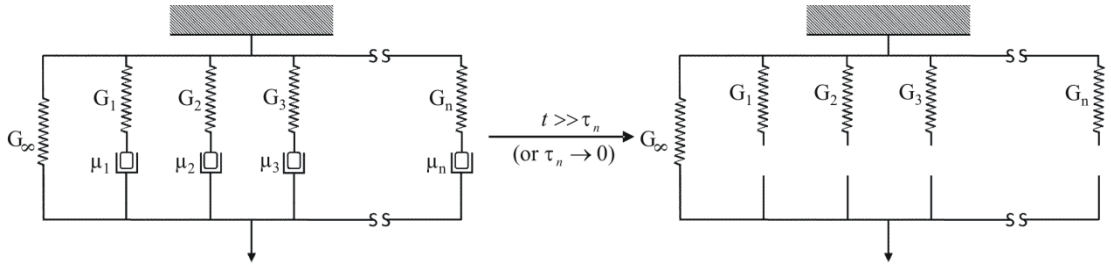

Figure 2-17: Equivalent model (right) of the generalised Maxwell model (left) when $t >> \tau_i$ (or $\tau_i \to 0$ or $\dot{\gamma} \to 0$).

The polymer network is therefore in equilibrium at any time and the equation (2.79) becomes:

$$\mu_{eff} = G_\infty \tag{2.81}$$

Thus, the effective hyperelastic shear modulus is constant over time as well and $T_{12}^{gen.Maxwell}(t)$ would appear linear in Figure 2-15 with a zero slope (overlap with the abscissa axis).

The equation (2.79) can be used to evaluate the experimental shear curves in order to identify the material parameters (G_∞, G_i, τ_i). However, because of the short duration of the tests, a fitting operation such as explained later in the sections 2.4.2 and 2.5.2 delivers only few parameters. Moreover, the identified parameters are prone to be affected with larger error than those obtained with creep or stress relaxation experiments due to the limited experimental data.

2.4. Creep experiments at constant shear stress

Due to the short duration of a shear test, only limited information can be acquired about the relaxation/retardation processes and the associated retardation times which characterise the viscoelastic behaviour of the polymer network. Therefore, creep experiments are carried out in order to have a broader insight into those retardation processes. An appropriate evaluation of the creep results provides quantitative information about retardation times and the associated retardation spectra as well as their dependence on temperature using the Zener model.

2.4.1. Analytical solution of the Zener model for creep experiments

In an idealised creep experiment, a constant shear stress $T_{12}^{\,0}$ is instantaneously applied at a time $t = 0$ and then held constant (Figure 2-18 - red plot). The resulting effective shear deformation $\gamma_{eff}(t)$ is measured as a function of time. In polymer networks, the maximal shear deformation reaches a plateau after a sufficiently long time ($\gamma_{eff} = const.$). Since the resulting effective shear is directly proportional to the applied stress $T_{12}^{\,0}$ according to Boltzmann's superposition principle, the results are plotted using the creep function or compliance, $J(t)$, defined as

$$J(t) = \frac{\gamma_{eff}(t)}{T_{12}^{\,0}} \tag{2.82}$$

Thus, the results of creep experiments using different shear stresses $T_{12}^{\,0}$ can be compared with each other.

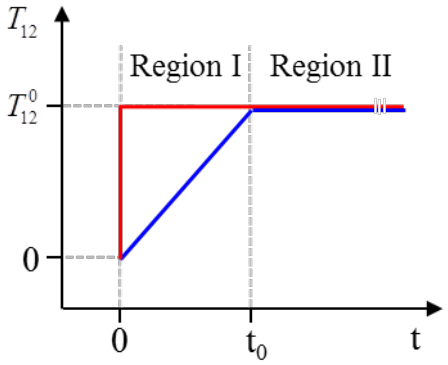

Figure 2-18: Shear stress T_{12} as a function of time during creep experiments (red: instantaneously applied stress load; blue: applied stress load in practice)

In practice, a sample can however not be loaded instantaneously and a time interval [0; t_0] is necessary to reach $T_{12}^{\,0}$. In this work, the time interval *[0; t_0]* is so small (0 s ≤ t_0 ≤ 2 s) that the loading stage of the sample can be considered to be linear (Figure 2-18 - blue plot). Of course, this is only an approximation of reality but, as shown by the following calculations, the decisive factor is the duration of the loading stage and not its evolution. Furthermore, since the

Boltzmann's superposition principle applies, the evolution of the sample load for $t \in [0, t_0]$ does not influence the creep behaviour for $t \geq t_0$. Therefore, the creep experiment can be separated into two stages:

- the loading stage (I): $t \in [0, t_0]$ and $T_{12}(t)$ increases linearly from 0 to ${T_{12}}^0$:

$$T_{12}(t) = \left(\frac{{T_{12}}^0}{t_0} \right) \cdot t \tag{2.83}$$

- and the creep stage (II) for $t \geq t_0$ where $T_{12}(t) = const. = {T_{12}}^0$.

To be able to determine the material parameters, the experimental creep function $J(t)$ is fitted using the analytical solution for the Zener model (see section 2.1.4). Although only the experimental data in the creep stage are evaluated, both stages must be considered in this analytical solution.

The Zener model consists of a spring and *n* Kelvin-Voigt models connected in series. In order to calculate the analytical solution of the Zener model (Figure 2-11) taking into account the two previously described stress stages, a single Kelvin-Voigt model (Figure 2-9) is considered first:

i. "Loading stage" (region I); $t \in [0, t_0]$ and $T_{12}^I(t) = \left(\frac{{T_{12}}^0}{t_0} \right) \cdot t$:

Using eq. (2.83) in eq. (2.37), the following ordinary differential equation is obtained:

$$\frac{1}{\tau} \gamma_{KV}^I(t) + \dot{\gamma}_{KV}^I(t) = \frac{{T_{12}}^0}{t_0 \cdot \eta} \cdot t \tag{2.84}$$

- Solution of the homogeneous equation $\gamma_{KV}^{Ic}(t)$:

$$\frac{1}{\tau} \gamma_{KV}^I(t) + \dot{\gamma}_{KV}^I(t) = 0 \tag{2.85}$$

$$\gamma_{KV}^{Ic}(t) = C \cdot e^{-t/\tau} \tag{2.86}$$

where *C* is a constant.

- Solution of the inhomogeneous equation $\gamma_{KV}^{Ip}(t)$:

$C(t)$ is now a function of time, so (2.86) becomes

$$\gamma_{KV}^{Ip}(t) = C(t) \cdot e^{-t/\tau} \tag{2.87}$$

Eq. (2.87) in eq. (2.84) gives

$$\frac{dC(t)}{dt} = \frac{{T_{12}}^0}{t_0 \cdot \eta} \cdot t \cdot e^{t/\tau} \tag{2.88}$$

Integrating eq. (2.88) for $t \in [0;t_0]$, we obtain

$$C(t) = \frac{T_{12}^{\ 0}}{t_0 \cdot \eta} \cdot \left(t \cdot \tau \cdot e^{t/\tau} - \tau^2 \cdot e^{t/\tau} + \tau^2 + D \right) \tag{2.89}$$

where D is a constant.

Eq. (2.89) in eq. (2.87) gives the solution of the inhomogeneous equation:

$$\begin{aligned} \gamma_{KV}^{Ip}(t) &= \left(\frac{T_{12}^{\ 0}}{t_0 \cdot \eta} \cdot \left(t \cdot \tau \cdot e^{t/\tau} - \tau^2 \cdot e^{t/\tau} + \tau^2 + D \right) \right) \cdot e^{-t/\tau} \\ &= \frac{T_{12}^{\ 0}}{t_0 \cdot \eta} \left(t \cdot \tau - \tau^2 + \tau^2 \cdot e^{-t/\tau} + D \cdot e^{-t/\tau} \right) \end{aligned} \tag{2.90}$$

The general solution $\gamma_{KV}^{I}(t)$ of the ordinary differential equation (2.84) is then the addition of the trivial solution $\gamma_{KV}^{Ic}(t)$ (eq. (2.86)) and the particular solution $\gamma_{KV}^{Ip}(t)$ (eq. (2.90)):

$$\begin{aligned} \gamma_{KV}^{I}(t) &= \gamma_{KV}^{Ic}(t) + \gamma_{KV}^{Ip}(t) \\ &= C \cdot e^{-t/\tau} + \frac{T_{12}^{\ 0}}{t_0 \cdot \eta} \left(t \cdot \tau - \tau^2 + \tau^2 \cdot e^{-t/\tau} + D \cdot e^{-t/\tau} \right) \end{aligned} \tag{2.91}$$

The following boundary values are used to determine the constants C and D:

- at t = 0:

$$\gamma_{KV}^{I}(0) = 0 \tag{2.92}$$

It follows that:

$$C + \frac{T_{12}^{\ 0}}{t_0 \cdot \eta} \cdot D = 0 \tag{2.93}$$

- at $t = t_0$: the shear strain reaches a given value $\gamma_{KV}^{I}(t_0)$

$$\begin{aligned} \gamma_{KV}^{I}(t_0) &= C \cdot e^{-t_0/\tau} + \frac{T_{12}^{\ 0}}{t_0 \cdot \eta} \left(t_0 \cdot \tau - \tau^2 + \tau^2 \cdot e^{-t_0/\tau} + D \cdot e^{-t_0/\tau} \right) \\ &= \underbrace{\left(C + \frac{T_{12}^{\ 0}}{t_0 \cdot \eta} \cdot D \right)}_{=0} \cdot e^{-t_0/\tau} + \frac{T_{12}^{\ 0}}{\eta} \cdot \tau - \frac{T_{12}^{\ 0}}{t_0 \cdot \eta} \cdot \tau^2 + \frac{T_{12}^{\ 0}}{t_0 \cdot \eta} \cdot \tau^2 \cdot e^{-t_0/\tau} \\ &= \frac{T_{12}^{\ 0}}{G} + \frac{T_{12}^{\ 0} \cdot \tau}{t_0 \cdot G} \cdot \left(e^{-t_0/\tau} - 1 \right) \end{aligned} \tag{2.94}$$

The shear deformation in the region I (loading stage; $t \in [0,t_0]$) is then:

$$\gamma_{KV}^{I}(t) = \frac{T_{12}^{\ 0}}{G}(t - \tau) + \frac{T_{12}^{\ 0} \cdot \tau}{t_0 \cdot G} \cdot e^{-t/\tau} \qquad \forall t \in [0,t_0] \tag{2.95}$$

In a Zener model, consisting of a spring and n Kelvin-Voigt models connected in series, the shear deformation for $t \in [0, t_0]$ is

$$\begin{aligned} \gamma^I_{Zener}(t) &= \gamma^I_{spring} + \sum_{i=1}^{n} \gamma^I_{KVi}(t) \\ &= \frac{T_{12}{}^0}{G_0} + \sum_{i=1}^{n} \left[\frac{T_{12}{}^0}{G_i}(t - \tau_i) + \frac{T_{12}{}^0 \cdot \tau_i}{t_0 \cdot G_i} \cdot e^{-t/\tau_i} \right] \quad \forall t \in [0, t_0] \end{aligned} \tag{2.96}$$

ii. "Creep stage" (region II); $t \geq t_0$ and $T_{12}(t) = const. = T_{12}{}^0$

Under these conditions, the differential equation (2.37) becomes:

$$\frac{1}{\tau}\gamma^{II}_{KV}(t) + \dot{\gamma}^{II}_{KV}(t) = \frac{T_{12}{}^0}{\eta} \tag{2.97}$$

- Solution of the homogeneous equation $\gamma^{IIc}_{KV}(t)$:

$$\frac{1}{\tau}\gamma^{II}_{KV}(t) + \dot{\gamma}^{II}_{KV}(t) = 0 \tag{2.98}$$

$$\gamma^{IIc}_{KV}(t) = K \cdot e^{-t/\tau} \tag{2.99}$$

where *K* is a constant.

- Solution of the inhomogeneous equation $\gamma^{IIp}_{KV}(t)$:

Considering $K(t)$, now a function of time, eq. (2.99) becomes

$$\gamma^{IIp}_{KV}(t) = K(t) \cdot e^{-t/\tau} \tag{2.100}$$

Eq. (2.100) in eq. (2.97) gives

$$\frac{dK(t)}{dt} = \frac{T_{12}{}^0}{\eta} \cdot e^{t/\tau} \tag{2.101}$$

The integration of eq. (2.101) for $t \geq t_0$ yields to

$$K(t) = \frac{T_{12}{}^0}{\eta} \cdot \tau \cdot \left(e^{t/\tau} - e^{t_0/\tau} \right) + B \tag{2.102}$$

with *B* the constant of integration.

Inserting eq. (2.102) in eq. (2.100), we obtain the solution of the inhomogeneous equation:

$$\begin{aligned} \gamma^{IIp}_{KV}(t) &= \left(\frac{T_{12}{}^0}{\eta} \cdot \tau \cdot \left(e^{t/\tau} - e^{t_0/\tau} \right) + B \right) \cdot e^{-t/\tau} \\ &= \frac{T_{12}{}^0}{G} \cdot \left(1 - e^{(t_0 - t)/\tau} \right) + B \cdot e^{-t/\tau} \end{aligned} \tag{2.103}$$

The general solution $\gamma^{II}_{KV}(t)$ is then

$$\begin{aligned} \gamma^{II}_{KV}(t) &= K \cdot e^{-t/\tau} + \frac{T_{12}{}^0}{G} \cdot \left(1 - e^{(t_0 - t)/\tau} \right) + B \cdot e^{-t/\tau} \\ &= (K + B) \cdot e^{-t/\tau} + \frac{T_{12}{}^0}{G} \cdot \left(1 - e^{(t_0 - t)/\tau} \right) \end{aligned} \tag{2.104}$$

Let us introduce a new constant defined as following: $A = K + B$ and consider the eq. (2.104) for the boundary condition at $t = t_0$:

$$\gamma_{KV}^{II}\left(t_0\right) = A \cdot e^{-t_0/\tau} \tag{2.105}$$

At $t = t_0$, the shear strain in both regions I and II must be equal:

$$\gamma_{KV}^{I}\left(t_0\right) = \gamma_{KV}^{II}\left(t_0\right) \tag{2.106}$$

$$\frac{T_{12}^{\ 0}}{G} + \frac{T_{12}^{\ 0}}{t_0 \cdot G} \cdot \tau \cdot \left(e^{-t_0/\tau} - 1\right) = A \cdot e^{-t_0/\tau} \tag{2.107}$$

The constant A can be then determined:

$$A = \frac{T_{12}^{\ 0}}{G} \cdot e^{t_0/\tau} + \frac{T_{12}^{\ 0}}{t_0 \cdot G} \cdot \tau \cdot \left(1 - e^{t_0/\tau}\right) \tag{2.108}$$

The shear strain as a function of the time in the creep stage (or region II) for one Kelvin-Voigt element $\gamma_{KV}^{II}\left(t\right)$ is then

$$\begin{aligned} \gamma_{KV}^{II}\left(t\right) &= \left(\frac{T_{12}^{\ 0}}{G} \cdot e^{t_0/\tau} + \frac{T_{12}^{\ 0}}{t_0 \cdot G} \cdot \tau \cdot \left(1 - e^{t_0/\tau}\right)\right) \cdot e^{-t/\tau} + \frac{T_{12}^{\ 0}}{G} \cdot \left(1 - e^{(t_0 - t)/\tau}\right) \\ &= \frac{T_{12}^{\ 0}}{G} + \frac{T_{12}^{\ 0} \cdot \tau}{t_0 \cdot G} \cdot \left(e^{-t/\tau} - e^{(t_0 - t)/\tau}\right) \qquad \forall t \geq t_0 \end{aligned} \tag{2.109}$$

In a Zener model, consisting of a spring and n Kelvin-Voigt models connected in series, the resulting shear strain during the creep stage ($t \geq t_0$) is the addition of the shear strains of each element:

$$\gamma_{Zener}\left(t \geq t_0\right) = \gamma_{spring}\left(t \geq t_0\right) + \sum_{i=1}^{n} \gamma_{KV}^{i}\left(t \geq t_0\right) \tag{2.110}$$

Inserting(2.26) and eq. (2.109) in eq. (2.110) yields to

$$\begin{aligned} \gamma_{Zener}\left(t \geq t_0\right) &= \frac{T_{12}^{\ 0}}{G_0} + \sum_{i=1}^{n}\left(\frac{T_{12}^{\ 0}}{G_i} + \frac{T_{12}^{\ 0} \cdot \tau_i}{t_0 \cdot G_i} \cdot \left(e^{-t/\tau_i} - e^{(t_0 - t)/\tau_i}\right)\right) \\ &= T_{12}^{\ 0} \cdot \left(\frac{1}{G_0} + \sum_{i=1}^{n}\left(\frac{1}{G_i} + \frac{\tau_i}{t_0 \cdot G_i} \cdot \left(e^{-t/\tau_i} - e^{(t_0 - t)/\tau_i}\right)\right)\right) \end{aligned} \tag{2.111}$$

The corresponding effective creep compliance for $t \geq t_0$ can be expressed as

$$\begin{aligned} J_{eff}\left(t \geq t_0\right) &= J_0 + \sum_{i=1}^{n}\left(J_i + \frac{J_i \cdot \tau_i}{t_0} \cdot \left(e^{-t/\tau_i} - e^{(t_0 - t)/\tau_i}\right)\right) \\ &= J_0 + \sum_{i=1}^{n} J_i + \sum_{i=1}^{n}\left(\frac{J_i \cdot \tau_i}{t_0} \cdot \left(e^{-t/\tau_i} - e^{(t_0 - t)/\tau_i}\right)\right) \quad \forall \mathrm{t} \geq \mathrm{t}_0 \end{aligned} \tag{2.112}$$

with $J_0 = \frac{1}{G_0}$ and $J_i = \frac{1}{G_i}$.

The equation (2.111) will be used to evaluate the experimental creep curves in order to identify the pairs of material parameters $\left(J_i, \tau_i\right)$ and J_0.

As previously for the shear test at constant shear rate, two limiting cases of the eq. (2.112) can be discussed:

- $t << \tau_1$ (or $\tau_1 \to +\infty$) with $(i = 1 \ldots n)$: within the experimental time scale t none of the Kelvin-Voigt elements has enough time to start to relax, the dampers are "frozen" and avoid the deformation of their paired spring elements. Thus, the stress and the strain come solely from the unpaired spring element – see Figure 2-19.

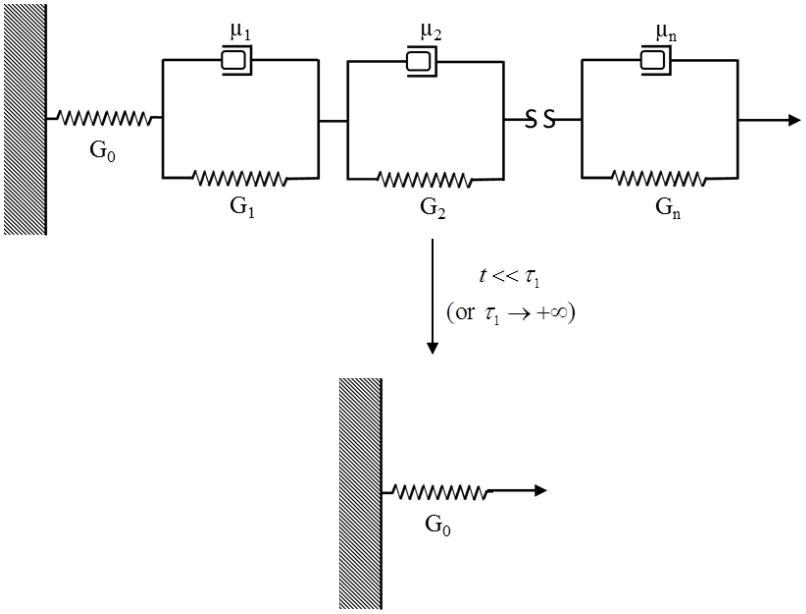

Figure 2-19: Equivalent model (bottom) of the Zener model (top) when $t << \tau_1$ (or $\tau_1 \to +\infty$).

Under such conditions, the polymer network is in the glassy state and equation (2.112) becomes:

$$J_{eff}^{glassy} = J_0 = \frac{1}{G_0} \tag{2.113}$$

The effective creep compliance is constant over time.

- $t >> \tau_n$ (or $\tau_n \to 0$) with $(i = 1 \ldots n)$: all the retardation times of the Kelvin-Voigt elements are much shorter than the experimental time scale – i. e. the retardation processes are faster than the applied strain rate so that the corresponding stress and strain are distributed in all the spring elements – see Figure 2-20.

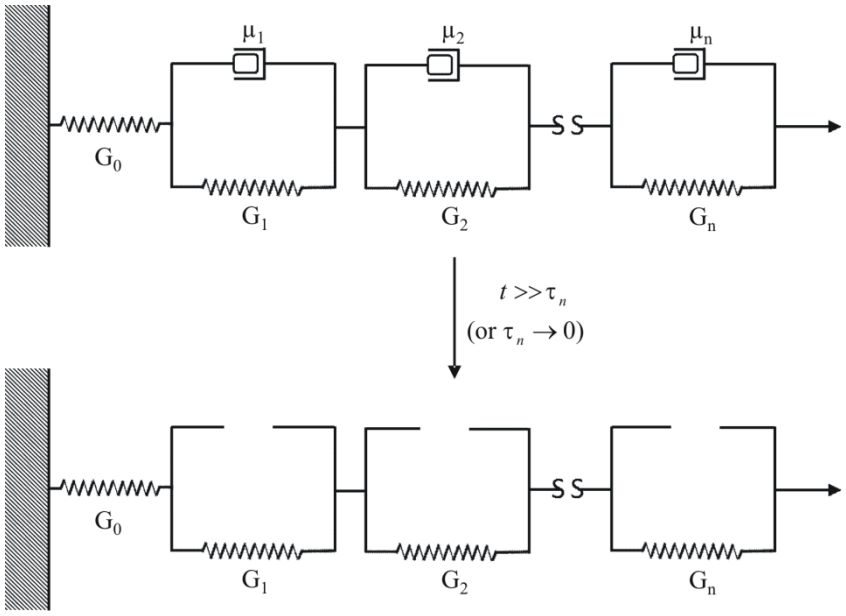

Figure 2-20: Equivalent model (bottom) of the Zener model (top) when $t >> \tau_n$ (or $\tau_n \to 0$).

The polymer network is therefore in an equilibrium state and equation (2.79) becomes:

$$J\left(t \to \infty\right) = J_\infty = \sum_{i=0}^{n} J_i = \sum_{i=0}^{n} \frac{1}{G_i} \tag{2.114}$$

Thus, the effective creep compliance is constant over time as well.

2.4.2. **Calculation of the discrete retardation time spectrum**

As mentioned above, the experimental data for $t \geq t_0$ of creep tests are fitted using the analytical solution of the Zener model in order to determine material parameters. This is done using the Origin® software, into which the equation (2.111) has been implemented as follows:

$$\gamma\left(t\right) = \gamma_0 + \sum_{i=1}^{n} A_i \cdot \left(e^{-t/\tau_i} - e^{(t_0 - t)/\tau_i}\right) \tag{2.115}$$

where the fit parameters by identification with eq. (2.111) are:

$\gamma_0 = T_{12}{}^0 \cdot \left(J_0 + \sum_{i=1}^{n} J_i\right)$ and $A_i = \frac{T_{12}{}^0 \cdot J_i \cdot \tau_i}{t_0}$.

While $T_{12}{}^0$ and t_0 are directly read from the experimental data[7], equation (2.115) provides the values of the fit parameters J_0, A_i and τ_i, with which the material parameters (J_i, τ_i) with $(i = 1 \ldots n)$ can be calculated. The number n of Kelvin-Voigt elements in the chosen Zener model is empirically selected in such a way that the error of the fit parameters is as small as

[7] t_0 is defined as the time when a constant load is reached. The corresponding value of $T_{12}{}^0$ is then determined for t = t_0.

possible. Based on the experience gained from experiments a maximal error of 10 % of the fitting parameters has been chosen as upper limit. Therefore, n corresponds to the number of discrete retardation times that can be determined and depends strongly on the quality of the measurement (measuring duration, noise and stable measuring conditions). The "cleaner" the measurement is, the more pairs of material parameters (J_i, τ_i) can be determined with small errors. Moreover, the number of discrete retardation times is also limited through the calculation method presented here, namely a maximum of one per time decade. The resolution and the sampling frequency of the sensors limit the identification of the retardation processes and therefore the number of discrete retardation times. As the sample becomes more and more elastic with increasing temperature, there comes a point where the viscoelastic properties cannot be spotted anymore at a given temperature and the calculation of the (discrete) retardation spectrum is thereby impossible. This limit is also determined by the quality of the measurement.

An example of the fitting operation of a creep experiment performed at 15 °C with a PU-AlMg3 adhesive joint with an adhesive thickness d_P = 736 ± 9 µm is displayed in Figure 2-21. In this example, the number of Kelvin-Voigt elements is n = 7. The thus obtained parameters are shown in Table 2-1. The low values of the standard deviations of the fit parameters as well as those of the coefficient of determination R^2 and the reduced χ^2 attest the goodness of the fit operation.

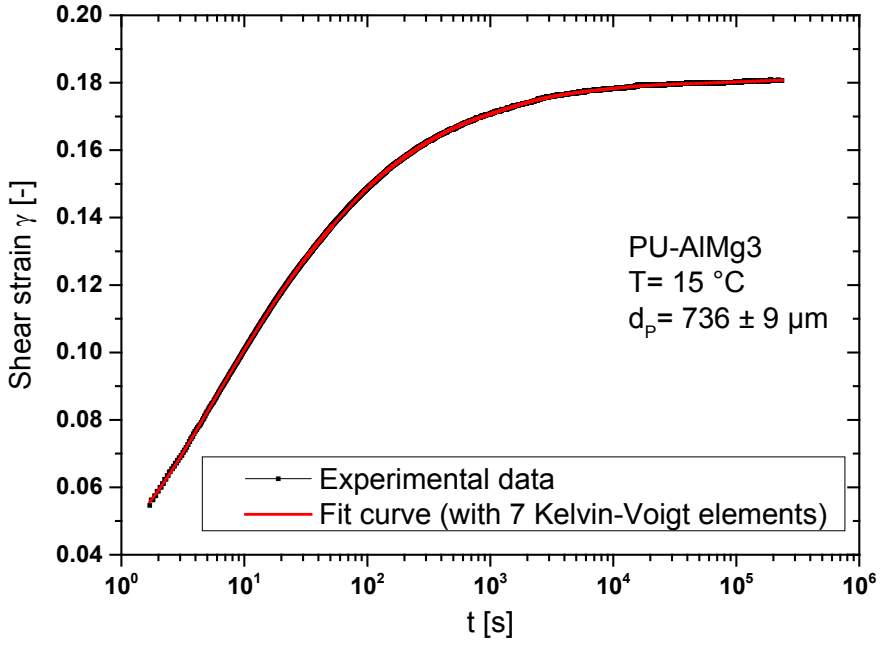

Figure 2-21: Experimental creep test with a PU-AlMg3 adhesive joint with an adhesive thickness d_P = 736 ± 9 µm at 15 °C (in black) and the fit curve using 7 Kelvin-Voigt elements in eq. (2.111) (in red).

Table 2-1: Fit parameters of the creep curve shown in Figure 2-21

Model	ExpDec_Retard_ZN_7 (User)		
Equation	$\gamma = A_1 \cdot(\exp(-t/\tau_1)-\exp((t_0-t)/\tau_1)) + A_2 \cdot(\exp(-t/\tau_2)-\exp((t_0-t)/\tau_2))$ $+ A_3 \cdot(\exp(-t/\tau_3)-\exp((t_0-t)/\tau_3)) + A_4 \cdot(\exp(-t/\tau_4)-\exp((t_0-t)/\tau_4))$ $+ A_5 \cdot(\exp(-t/\tau_5)-\exp((t_0-t)/\tau_5)) + A_6 \cdot(\exp(-t/\tau_6)-\exp((t_0-t)/\tau_6))$ $+ A_7 \cdot(\exp(-t/\tau_7)-\exp((t_0-t)/\tau_7)) + \gamma_0$		
Reduced χ^2	$4.25609 \cdot 10^{-9}$		
Coeff. of determination R^2	0.99964		
	Parameter	Value	Standard deviation [%]
	t_0; set	1.70	0
	γ_0	0.18	$4.6 \cdot 10^{-4}$
	A_1	0.03	1.06
	τ_1	2.38	0.62
	A_2	0.22	0.39
	τ_2	9.41	0.44
	A_3	2.26	0.14
	τ_3	178	0.29
	A_4	17.41	0.06
	τ_4	6818.47	0.12
	A_5	0.81	0.35
	τ_5	42.32	0.39
	A_6	112.1	0.15
	τ_6	107902.05	0.15
	A_7	7.37	0.1
	τ_7	1074.51	0.16

The obtained fit parameters are then used to determine the retardation spectrum of the material at 15 °C. A retardation spectrum describes the distribution of the retardation times by assigning each discrete retardation time τ_i an associated spectral compliance J_i [88]. The Zener model (see Figure 2-11), which describes linear viscoelastic behaviour of polymer networks, represents a discrete retardation time spectrum. Most of the methods exposed in the scientific literature to calculate retardation time spectra are based on creep experiments in which the stress test is suddenly applied, i.e. t_0 is set to zero. In this case, the creep compliance $J(t)$ can be represented as follows [86, 89]:

$$J(t) = J_0 + \sum_{i=1}^{n} J_i \cdot \left(1 - e^{-t/\tau_i}\right) \quad \forall t \geq 0 \tag{2.116}$$

Here again each retardation time τ_i is associated with a spectral compliance J_i. In the Zener model the term J_0 describes the "instantaneous compliance" corresponding to the elastic response of the spring G_0.

The summation notation of eq. (2.116) can be generalised using the following integration notation [86]:

$$J(t) = J_0 + \int_0^{+\infty} \frac{L(\tau)}{\tau} \cdot \left(1 - e^{-t/\tau}\right) d\tau \quad \forall t \geq 0 \tag{2.117}$$

with $L(\tau)$ the continuous retardation time spectrum.

According to Alfrey's approximation, it is assumed that [89-91]:

$$\begin{cases} e^{-t/\tau} \approx 0 \text{ for } \tau \le t \\ e^{-t/\tau} \approx 1 \text{ for } \tau > t \end{cases} \tag{2.118}$$

$$\begin{aligned} \int_0^{+\infty} \frac{L(\tau)}{\tau} \cdot \left(1 - e^{-t/\tau}\right) d\tau &= \int_0^t \frac{L(\tau)}{\tau} \cdot \left(1 - \underbrace{e^{-t/\tau}}_{\approx 0}\right) d\tau + \int_t^{+\infty} \frac{L(\tau)}{\tau} \cdot \left(1 - \underbrace{e^{-t/\tau}}_{\approx 1}\right) d\tau \\ &\approx \int_0^t \frac{L(\tau)}{\tau} \cdot d\tau \end{aligned} \tag{2.119}$$

So, we can write:

$$J(t) \approx J_0 + \int_0^t \frac{L(\tau)}{\tau} \cdot d\tau \tag{2.120}$$

The derivative of eq. (2.120) gives the retardation time spectrum:

$$L(\tau) \approx t \cdot \left. \frac{dJ(t)}{dt} \right|_{t=\tau} \tag{2.121}$$

The continuous retardation time spectrum $L(\tau)$ is a material function for the linear viscoelastic deformation range at constant temperature. It is difficult to determine the continuous retardation time spectrum from the retardation function but the difference between a continuous spectrum and a discrete spectrum is a mathematical formality [92].

Therefore the time derivative of $J(t)$ given in eq. (2.116) is inserted in eq. (2.121) to obtain the discrete retardation time spectrum $L^*(\tau)$:

$$L^*(\tau) \approx t \cdot \left. \sum_{i=1}^{n} \frac{J_i}{\tau_i} \cdot e^{-\frac{t}{\tau_i}} \right|_{t=\tau} \tag{2.122}$$

With the equation (2.122) it is then possible to determine a discrete retardation time spectrum $L^*(\tau)$ from creep compliance $J(t)$. The fit parameters in Table 2-1 are independent of the experimental procedure (e.g. sudden load or linear loading stage) and can therefore be used to calculate the retardation time spectra. The results are presented in Figure 2-22. The Gaussian error propagation is used to calculate the error bars in the retardation time spectrum from the errors of the fit parameters. A close-up view gives an impression of these error bars.

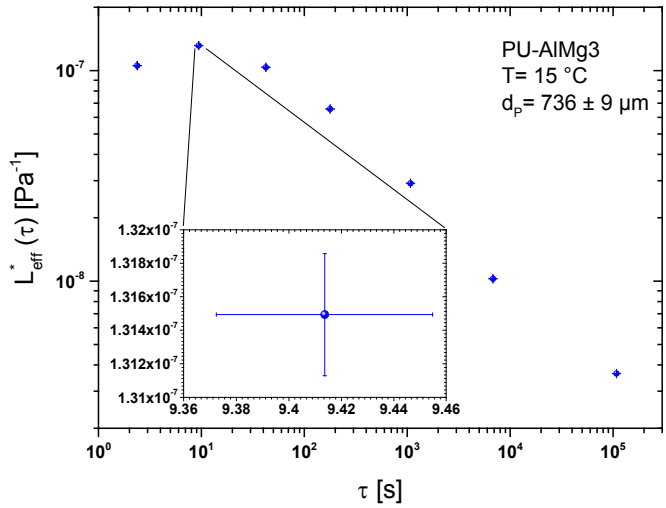

Figure 2-22: Discrete retardation time spectrum for an AlMg3-PU adhesive joint with d_P = 736 ± 9 µm at 15 °C.

2.5. Stress relaxation experiments at constant shear strain

Stress relaxation experiments offer another possibility to gain information about the viscoelastic behaviour of the investigated polyurethane adhesive. Furthermore these results are used to complete and verify the calculations presented in the section 2.6 to model the viscoelastic functions of adhesive joints.

2.5.1. Analytical solution of the generalised Maxwell model

In relaxation experiments, an effective shear strain γ_0 is imposed to the sample at $t = 0$. The shear strain is then maintained constant and the resulting shear stress $T_{12}(t)$ is measured as a function of time. In the case of cross-linked polymers, the stress rises abruptly as the strain is applied and then falls steadily until it reaches a plateau value after a sufficiently long time. Analogous to the creep function $J_{eff}(t)$, the measured stress curve is also normalised to the applied shear strain γ_0 during relaxation tests in order to compare the results of different measurements. The relaxation function $G_{eff}(t)$, also referred to as relaxation modulus, is thus defined as:

$$G_{eff}(t) = \frac{T_{12}(t)}{\gamma_0} \tag{2.123}$$

Similar to the creep test, the shear strain cannot be imposed instantaneously in an experiment but within a brief period $[0,t_0]$. Therefore, two regions have to be distinguished (see Figure 2-23):

- Region 1, "loading stage": $t \in [0,t_0]$ the shear strain is applied by a constant shear strain rate $\dot{\gamma} = \frac{\gamma_0}{t_0}$; $\gamma(t) = \frac{\gamma_0}{t_0} \cdot t$
- Region 2, "relaxation stage": $t \geq t_0$ the constant shear strain γ_0 is reached and kept constant.

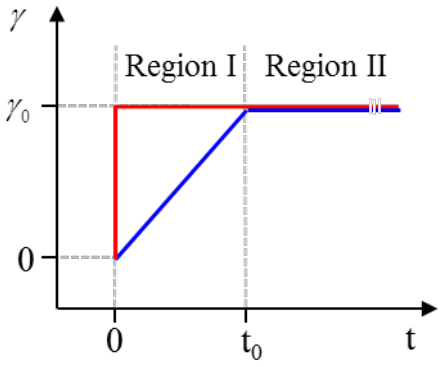

Figure 2-23: Shear strain γ as a function of time during stress relaxation experiments (red: instantaneously applied strain; blue: applied strain in practice)

In order to determine the relaxation times analogous to the retardation times, the experimental data of $G(t)$ are fitted with the analytical solution of the generalised Maxwell model. Like the creep experiments, both shear strain regions must be considered, although only the data at constant shear strain (region 2) are evaluated.

The generalised Maxwell model consists of *n* Maxwell models and one spring connected in parallel (see Figure 2-10). In order to calculate the solution for the generalised Maxwell model, taking into account the shear strain regions described above, a single Maxwell model is first considered (see Figure 2-8).

i. "Loading stage" (region I); $t \in [0,t_0]$:

$$\gamma(t) = \frac{\gamma_0}{t_0} \cdot t \; ; \; \dot{\gamma}(t) = \frac{\gamma_0}{t_0} \tag{2.124}$$

Inserting eq. (2.124) in eq. (2.31) yields to the following ordinary differential equation:

$$\dot{\gamma}^{Maxwell,I} = \frac{\gamma_0}{t_0} = \frac{\dot{T}_{12}^{Maxwell,I}(t)}{G} + \frac{T_{12}^{Maxwell,I}(t)}{\eta} \tag{2.125}$$

- Solution of the homogeneous equation $T_{12}^{Maxwell,Ic}(t)$:

$$\dot{T}_{12}^{Maxwell,I}(t) + \frac{T_{12}^{Maxwell,I}(t)}{\tau} = 0 \tag{2.126}$$

$$T_{12}^{Maxwell,Ic}(t) = C \cdot e^{-t/\tau} \tag{2.127}$$

where C is a constant.

- Solution of the inhomogeneous equation $T_{12}^{Maxwell,Ip}(t)$:

  Introducing $C(t)$, now a time dependent function, eq. (2.127) becomes

$$T_{12}^{Maxwell,Ip}(t) = C(t) \cdot e^{-t/\tau} \tag{2.128}$$

  Eq. (2.128) in eq. (2.125) gives

$$\frac{dC(t)}{dt} = \frac{\gamma_0 \cdot G}{t_0} \cdot e^{t/\tau} \tag{2.129}$$

  Integrating eq. (2.129) for $t \in [0; t_0]$, we obtain

$$C(t) = \frac{\gamma_0 \cdot G \cdot \tau}{t_0} \cdot \left(e^{t/\tau} - 1\right) + D \tag{2.130}$$

  where D is a constant.

  Eq. (2.130) in eq. (2.128) gives the solution of the inhomogeneous equation:

$$\begin{aligned} T_{12}^{Maxwell,Ip}(t) &= \left(\frac{\gamma_0 \cdot G \cdot \tau}{t_0} \cdot \left(e^{t/\tau} - 1\right) + D \right) \cdot e^{-t/\tau} \\ &= \frac{\gamma_0 \cdot G \cdot \tau}{t_0} \cdot \left(1 - e^{-t/\tau}\right) + D \cdot e^{-t/\tau} \end{aligned} \tag{2.131}$$

  The general solution $T_{12}^{Maxwell,I}(t)$ of the ordinary differential equation (2.125) is then the addition of the trivial solution $T_{12}^{Maxwell,Ic}(t)$ (eq. (2.127)) and the particular solution $T_{12}^{Maxwell,Ip}(t)$ (eq. (2.131)):

$$\begin{aligned} T_{12}^{Maxwell,I}(t) &= T_{12}^{Maxwell,Ic}(t) + T_{12}^{Maxwell,Ip}(t) \\ &= C \cdot e^{-t/\tau} + \frac{\gamma_0 \cdot G \cdot \tau}{t_0} \cdot \left(1 - e^{-t/\tau}\right) + D \cdot e^{-t/\tau} \end{aligned} \tag{2.132}$$

  The following boundary values are used to determine the constants C and D:

  - at t = 0:

$$T_{12}^{Maxwell,I}(0) = 0 \tag{2.133}$$

    It follows that:

$$T_{12}^{Maxwell,I}(0) = C + D = 0 \tag{2.134}$$

  - at t = t_0: the shear stress reaches a given value $T_{12}^{Maxwell,I}(t_0)$

$$\begin{aligned} T_{12}^{Maxwell,I}(t_0) &= \frac{\gamma_0 \cdot G \cdot \tau}{t_0} \cdot \left(1 - e^{-t_0/\tau}\right) + \underbrace{(C + D)}_{=0} \cdot e^{-t_0/\tau} \\ &= \frac{\gamma_0 \cdot G \cdot \tau}{t_0} \cdot \left(1 - e^{-t_0/\tau}\right) \end{aligned} \tag{2.135}$$

The shear stress in the region I (loading stage; $t \in [0, t_0]$) is then:

$$T_{12}^{Maxwell,I}(t) = \frac{\gamma_0 \cdot G \cdot \tau}{t_0} \cdot \left(1 - e^{-t/\tau}\right) \quad \forall t \in [0, t_0] \tag{2.136}$$

In a generalised Maxwell model (see Figure 2-10), consisting of a spring and *n* Maxwell models connected in parallel, the resulting shear stress during the loading stage ($t \in [0, t_0]$) is the addition of the shear stress of each element:

$$\begin{aligned} T_{12}^{gen.Maxwell,I}(t) &= T_{12}^{0} + \sum_{i=1}^{n} T_{12}^{i-Maxwell,I}(t) \\ &= \frac{\gamma_0 \cdot G_\infty}{t_0} \cdot t + \sum_{i=1}^{n} \frac{\gamma_0 \cdot G_i \cdot \tau_i}{t_0} \cdot \left(1 - e^{-t/\tau_i}\right) \quad \forall t \in [0, t_0] \end{aligned} \tag{2.137}$$

At $t = t_0$, eq. (2.137) gives

$$T_{12}^{gen.Maxwell,I}(t_0) = \gamma_0 \cdot G_\infty + \sum_{i=1}^{n} \frac{\gamma_0 \cdot G_i \cdot \tau_i}{t_0} \cdot \left(1 - e^{-t_0/\tau_i}\right) \tag{2.138}$$

ii. "Relaxation stage" (region II); $t \geq t_0$ and $\gamma^{Maxwell,II}(t) = const. = \gamma_0$

The shear strain is kept constant, so the differential equation (2.125) becomes:

$$\frac{\dot{T}_{12}^{Maxwell,II}(t)}{G} + \frac{T_{12}^{Maxwell,II}(t)}{\eta} = 0 \tag{2.139}$$

Thus, only this homogeneous differential equation must be solved $T_{12}^{Maxwell,IIc}(t)$:

$$T_{12}^{Maxwell,II}(t) = K \cdot e^{-t/\tau_i} \tag{2.140}$$

where K is a constant.

At $t = t_0$, the shear stress in both regions I and II must be equal:

$$T_{12}^{Maxwell,I}(t_0) = T_{12}^{Maxwell,II}(t_0) \tag{2.141}$$

$$\frac{\gamma_0 \cdot G \cdot \tau}{t_0} \cdot \left(1 - e^{-t_0/\tau}\right) = K \cdot e^{-t_0/\tau} \tag{2.142}$$

The constant K can be then determined:

$$K = \frac{\gamma_0 \cdot G \cdot \tau}{t_0} \cdot \left(e^{t_0/\tau} - 1\right) \tag{2.143}$$

Inserting eq. (2.143) in eq. (2.140), we obtain the shear stress as a function of the time in the relaxation stage (or region II) for one Maxwell element $T_{12}^{Maxwell,II}(t)$:

$$T_{12}^{Maxwell,II}(t) = \frac{\gamma_0 \cdot G \cdot \tau}{t_0} \cdot \left(e^{(t_0 - t)/\tau} - e^{-t/\tau}\right) \quad \forall t \geq t_0 \tag{2.144}$$

In a generalised Maxwell model (see Figure 2-10), consisting of a spring and *n* Maxwell models connected in parallel, the resulting shear stress during the relaxation stage ($t \geq t_0$) is the addition of the shear stress of each element:

$$T_{12}^{gen.Maxwell}\left(t \geq t_0\right) = T_{12}^{spring}\left(t \geq t_0\right) + \sum_{i=1}^{n} T_{12}^{i-Maxwell,II}\left(t \geq t_0\right) \tag{2.145}$$

Inserting(2.26) and eq. (2.144) in eq. (2.145) yields to:

$$T_{12}^{gen.Maxwell}\left(t \geq t_0\right) = G_\infty \cdot \gamma_0 + \sum_{i=1}^{n}\left(\frac{\gamma_0 \cdot G_i \cdot \tau_i}{t_0} \cdot \left(e^{(t_0 - t)/\tau_i} - e^{-t/\tau_i}\right)\right) \tag{2.146}$$

where $G_\infty = \dfrac{T_{12}\left(t \to \infty\right)}{\gamma_0}$ is the relaxed shear modulus.

The equation (2.146) will be used to evaluate the experimental stress relaxation curves in order to identify the pairs of fit parameters $\left(G_i, \tau_i\right)$ and G_∞.

The corresponding stress relaxation function or relaxation modulus for $t \geq t_0$ is then:

$$G_{eff}^{gen.Maxwell}\left(t \geq t_0\right) = G_\infty + \sum_{i=1}^{n}\left(\frac{G_i \cdot \tau_i}{t_0} \cdot \left(e^{(t_0 - t)/\tau_i} - e^{-t/\tau_i}\right)\right) \quad \forall t \geq t_0 \tag{2.147}$$

As shown in Figure 2-24, $G_{eff}^{gen.Maxwell}$ decreases over time to reach asymptotically the value of G_∞.

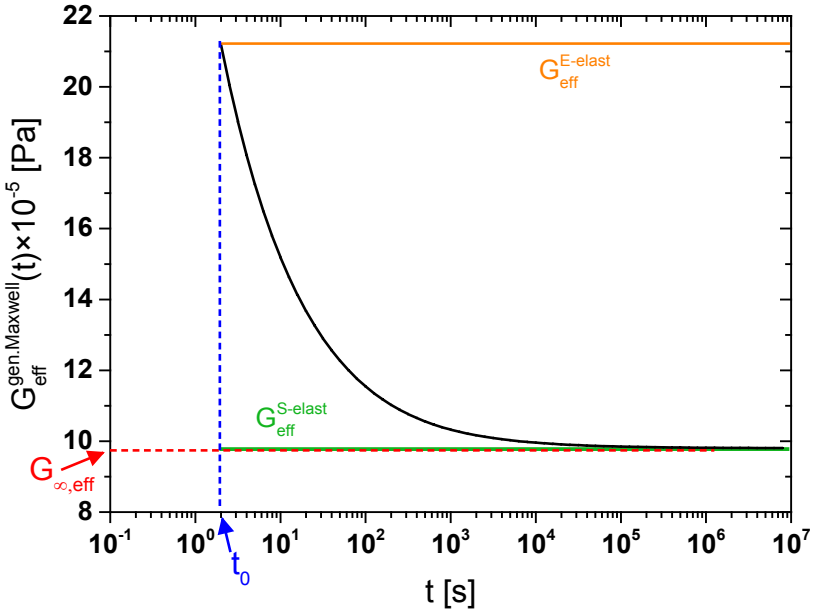

Figure 2-24: Calculated shear stress relaxation modulus $G_{eff}^{gen.Maxwell}\left(t \geq t_0\right)$ (in black) as a function of time during stress relaxation test at constant shear strain using 3 maxwell elements in eq. (2.147). The orange and green plots represent the limiting cases of (2.147). The chosen parameters $\left(G_\infty, G_i, \tau_i\right)$ are issued from the experimental results obtained for PU-Al joint with d_P = 736 ± 9 µm at 15 °C.

Two limiting cases of the eq. (2.147) can be discussed:

- $t << \tau_1$ (or $\tau_1 \to +\infty$) with $(i = 1 \ldots n)$: within the experimental time scale t none of the Maxwell elements has enough time to start to relax, the dampers are "frozen" and the stress and strain are distributed into all spring elements – see Figure 2-25.

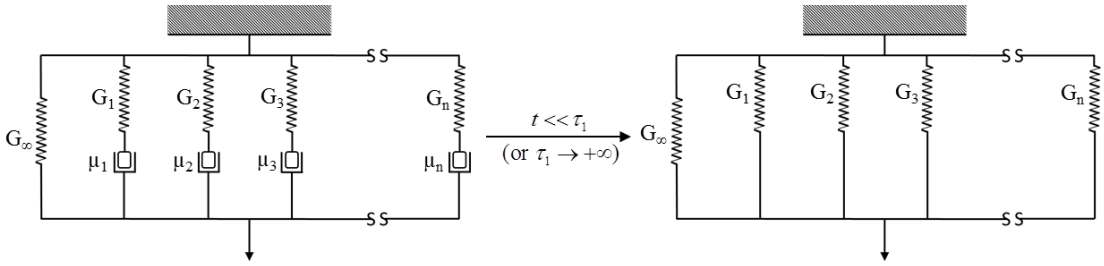

Figure 2-25: Equivalent model (right) of the generalised Maxwell model (left) when $t << \tau_i$ (or $\tau_i \to +\infty$).

Under such conditions, the polymer network is in the glassy state (non-equilibrium) and equation (2.147) becomes:

$$G_{eff}^{E-elast} = G_\infty + \sum_{i=1}^{n} G_i \tag{2.148}$$

The effective shear relaxation modulus in the glassy state is constant over time – see orange plot in Figure 2-24.

- $t >> \tau_n$ (or $\tau_n \to 0$) with $(i = 1 \ldots n)$: all relaxation times of the Maxwell elements are much shorter than the experimental time scale – i. e. the relaxation processes are faster than the applied strain rate so that the stress and the strain come solely from the unpaired spring element – see Figure 2-26.

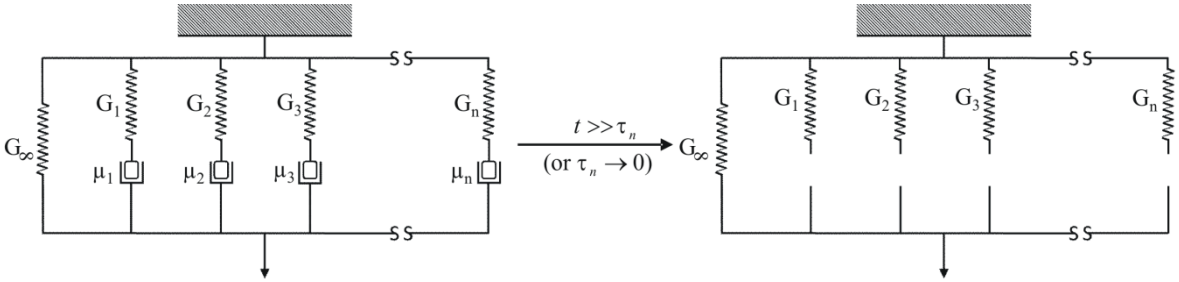

Figure 2-26: Equivalent model (right) of the generalised Maxwell model (left) when $t >> \tau_n$ (or $\tau_n \to 0$).

The polymer network is therefore in an equilibrium state and equation (2.147) becomes:

$$G_{eff}^{S-elast} = \mu_{eff} = G_\infty \tag{2.149}$$

Thus, the effective relaxation modulus at the equilibrium is constant over time – see green plot in Figure 2-24.

It may be noted that these borderline cases are the same as for the shear tests at constant shear rate since the rheological model used is identical.

2.5.2. **Calculation of the discrete relaxation time spectrum**

Like the method described above for the evaluation of the creep curves, the experimental data obtained for the relaxation modulus are fitted using the analytical solution of the generalised Maxwell model in order to determine material parameters. This is done using Origin® software, into which the equation (2.146) has been implemented as follows:

$$y(x) = y_0 + \sum_{i=1}^{n} A_i \cdot \left(e^{(t_0 - t)/\tau_i} - e^{-t/\tau_i} \right) \tag{2.150}$$

with $y_0 = G_\infty \cdot \gamma_0$ and $A_i = \dfrac{G_i \cdot \tau_i \cdot \gamma_0}{t_0}$.

The fitting provides the fit parameters A_i, τ_i and y_0, while t_0 is known from the experiment. Using these values, the material parameters $G_\infty, (G_i, \tau_i)$ with (i = 1...n) can be calculated. The number n of Maxwell elements is adjusted so that the errors of the fit parameters are minimal. As for the creep experiments, the number n of determinable discrete relaxation times depends strongly on the quality of the measured curve and is also limited to one relaxation time per decade.

An example of the fitting operation of a stress relaxation experiment performed at 15 °C with a PU-AlMg3 adhesive joint (with an adhesive thickness d_P = 736 ± 9 µm) is displayed in Figure 2-27. In this example, the number of Maxwell elements is n = 3. The obtained parameters are shown in Table 2-2.

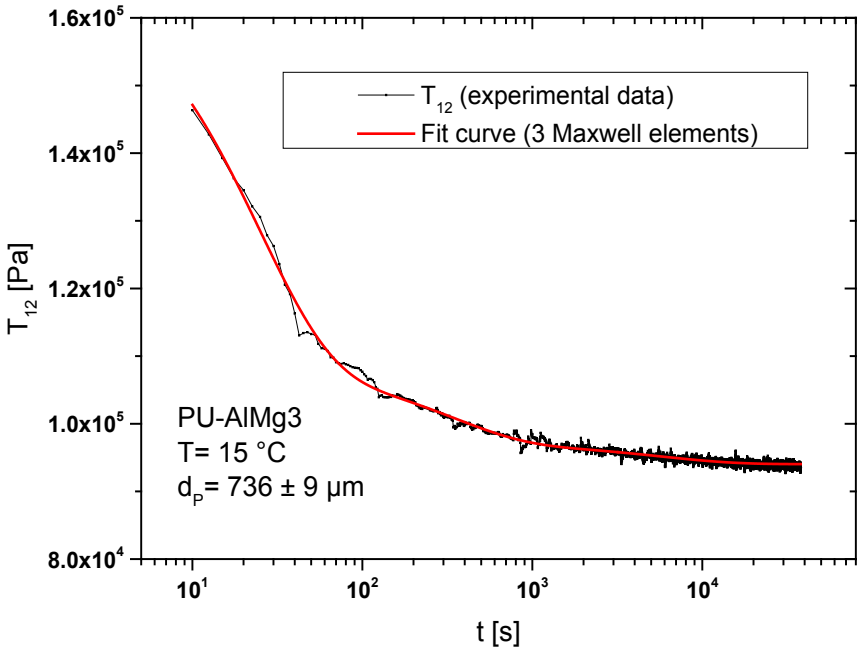

Figure 2-27: Experimental stress relaxation test with a PU-AlMg3 adhesive joint with an adhesive thickness d_P = 736 ± 9 µm at 15 °C (in black) and the fit curve using 3 Maxwell elements in eq. (2.150) (in red).

Table 2-2: Fit parameters of the relaxation modulus shown in Figure 2-27

Model	ExpDec_Relax_Mx_3 (User)		
Equation	$y = A_1 \cdot (\exp((t_0-t)/\tau_1)-\exp(-t/\tau_1)) + A_2 \cdot (\exp((t_0-t)/\tau_2)-\exp(-t/\tau_2)) + A_3 \cdot (\exp((t_0-t)/\tau_3)-\exp(-t/\tau_3)) + y_0$		
Reduced χ^2	132750.25		
Coeff. of determination R^2	0.95269		
	Parameter	Value	Standard deviation [%]
	t_0 – set	10.01	0
	y_0	94033.49	0.01
	A_1	117008.77	0.91
	τ_1	24.37	1.09
	A_2	362865.01	0.98
	τ_2	337.62	1.45
	A_3	1.76387E6	0.79
	τ_3	5735.72	1.21

The resulting material parameters provide the possibility to determine a discrete relaxation time spectrum. A relaxation time spectrum describes the distribution of relaxation times by assigning a relaxation modulus G_i to each relaxation time τ_i. The generalised Maxwell model displays a discrete relaxation time spectrum. Assuming an instantaneously applied shear strain to the sample (red curve in Figure 2-23), the relaxation function can then be expressed as follows [86]:

$$G_{eff}(t) = G_\infty + \sum_{i=1}^{n}\left(G_i \cdot e^{-t/\tau_i}\right) \tag{2.151}$$

The summation notation of eq. (2.151) can be generalized using the following integration notation [86]:

$$G_{eff}(t) = G_\infty + \int_0^\infty \frac{H(\tau)}{\tau} \cdot e^{-t/\tau} \cdot d\tau \tag{2.152}$$

$H(\tau)$ is the continuous relaxation time spectrum.

According to Alfrey's approximation, we assume once again that [89-91]:

$$\begin{cases} e^{-t/\tau} \approx 0 \text{ for } \tau \le t \\ e^{-t/\tau} \approx 1 \text{ for } \tau > t \end{cases} \tag{2.153}$$

$$\begin{aligned} \int_0^{+\infty} \frac{H(\tau)}{\tau} \cdot e^{-t/\tau} d\tau &= \int_0^t \frac{H(\tau)}{\tau} \cdot \left(\underbrace{e^{-t/\tau}}_{\approx 0}\right) d\tau + \int_t^{+\infty} \frac{H(\tau)}{\tau} \cdot \left(\underbrace{e^{-t/\tau}}_{\approx 1}\right) d\tau \\ &\approx \int_t^\infty \frac{H(\tau)}{\tau} \cdot d\tau \end{aligned} \tag{2.154}$$

So, we can write:

$$\mathrm{G}_{eff}(t) \approx G_\infty + \int_t^\infty \frac{H(\tau)}{\tau} \cdot d\tau \tag{2.155}$$

After derivating the eq. (2.155) the continuous relaxation time spectrum can be computed as follows:

$$H(\tau) \approx -t \cdot \left. \frac{dG_{eff}(t)}{dt} \right|_{t=\tau} \tag{2.156}$$

The continuous relaxation time spectrum $H(\tau)$ is a material function for the linear viscoelastic deformation range at constant temperature. As for the retardation time spectrum, it is difficult to determine the continuous relaxation time spectrum from the relaxation function but the difference between a continuous spectrum and a discrete spectrum is a mathematical formality [92].

Therefore the time derivative of $G_{eff}(t)$ given in eq. (2.151) is inserted in eq. (2.156) to obtain the discrete relaxation time spectrum $H^*(\tau)$:

$$H^*(\tau) \approx -t \cdot \left. \sum_{i=1}^{n} \frac{G_i}{\tau_i} \cdot e^{-\frac{t}{\tau_i}} \right|_{t=\tau} \tag{2.157}$$

With equation (2.157) it is then possible to determine a discrete relaxation time spectrum $H^*(\tau)$ from the relaxation function or shear modulus $G_{eff}(t)$. The material parameters determined in Table 2-2 are independent of the experimental procedure (e.g. instantaneous load or linear loading stage) and can therefore be used to calculate the discrete relaxation time spectra. The results, calculated from the above presented fit operation, are displayed in Figure 2-28. The Gaussian error propagation is used to calculate the error bars in the relaxation time spectrum from the errors of the fit parameters.

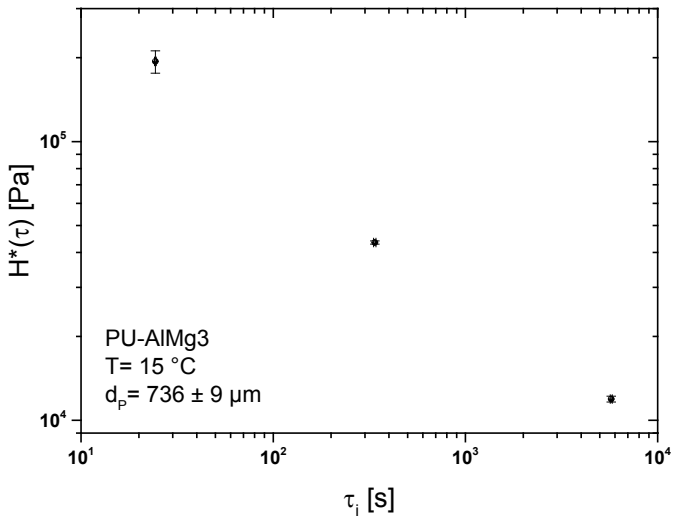

Figure 2-28: Discrete relaxation time spectrum $H^*(\tau)$ for an AlMg3-PU adhesive joint with d_P = 736 ± 9 µm at 15 °C.

2.6. Interrelations among the viscoelastic functions

According to Boltzmann's superposition principle, the applied shear strain is directly related to the resulting shear stress in the linear-viscoelastic range and vice versa – see section 3.4.2.5. Accordingly, the creep function $J_{eff}(t)$ and the relaxation function $G_{eff}(t)$ cannot be independent of each other in the linear-viscoelastic range. Rather, the linear-viscoelastic theory provides equations that describe the relationships between the individual viscoelastic functions. The interrelations between the retardation and relaxation spectra are of particular interest because these spectra describe entirely the viscoelastic properties of the polymer network. In the following section, the approach to calculate the different viscoelastic functions is explained and the corresponding equations are presented. All the numerical implementations (program code and preliminary tests) can be found in [93].

The experiments carried out in this work showed that creep tests provided more information than other types of experiments. For this reason, the results from such experiments are used as starting point for the calculation of other viscoelastic functions. Nevertheless, it is necessary to consider both types of spectra to ensure the accuracy of the calculations. While the relaxation time spectrum weights contributions to modulus, the retardation time spectrum weights contributions to compliance. In most of the references about this topic, interrelations between the spectra are given for the continuous ones. Therefore, the calculation of the continuous spectra from the discrete ones is needed to calculate the other viscoelastic functions.

Continuous retardation time spectra from discrete retardation time spectra:

After the fitting operation of the creep curves described in the section 2.4.2, the discrete retardation time spectrum is obtained for a limited time range (see Figure 2-22). The only further information known at first glance about the continuous retardation time spectrum is:

$$\begin{cases} L(\tau \to 0) = 0 \\ L(\tau \to \infty) = 0 \end{cases} \tag{2.158}$$

From a material physics point of view, there is in every material a fastest process with $\tau^{lower} > 0$, where $L(\tau^{lower}) = 0$ and a slowest process with $\tau^{upper} < \infty$, where $L(\tau^{upper}) = 0$. Thus eq. (2.158) becomes:

$$\begin{cases} L(\tau^{lower}) = 0 \\ L(\tau^{upper}) = 0 \end{cases} \tag{2.159}$$

These limiting conditions imply that:

- $L(\tau)$ must have at least one maximum
- if a minimum in $L(\tau)$ exists (besides those for τ^{lower} and τ^{upper}), this minimum has to be framed between two maxima.

Based on these conditions and on the limited information obtained from the discrete spectra, three functions have been considered to fit the discrete retardation spectra: a Gaussian function, a truncated and inversed "Lennard-Jones potential" function and a cubic polynomial function. The first trials have shown that the fit operation with the cubic polynomial function provides the best result and computing time for the further calculations [93]. For this reason, only the method using the following polynomial function is presented in the rest of this work:

$$L(\tau) = a_0 + a_1 \cdot \tau + a_2 \cdot \tau^2 + a_3 \cdot \tau^3 \tag{2.160}$$

It is obvious that this polynomial function does not satisfy the above conditions since:

$$\begin{cases} \lim\limits_{\tau \to \infty} \left(a_0 + a_1 \cdot \tau + a_2 \cdot \tau^2 + a_3 \cdot \tau^3 \right) = \begin{cases} +\infty \\ -\infty \end{cases} \text{; depending on the sign of } a_3 \\ \lim\limits_{\tau \to 0} L(\tau) = a_0 \end{cases} \tag{2.161}$$

However considering the limited information gained from the discrete retardation time spectra, the results obtained using the cubic polynomial fit reach a sufficient accuracy and reliability as proved by the results shown in section 4.3.1. Nevertheless, it is necessary to define some restrictions for the use of the cubic polynomial fit to describe the continuous retardation time spectra. For example, Figure 2-29 shows that the cubic polynomial function is only reasonable in the time range $[\tau_a, \tau_e]$ to calculate the viscoelastic functions[8]. Further details about these restrictions and their numerical implementation can be found in [93].

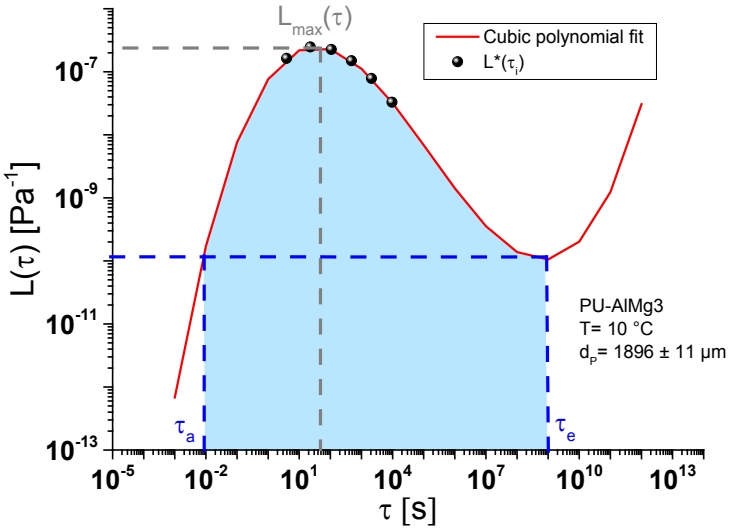

Figure 2-29: Fitting operation of a discrete retardation time spectrum (in black) with a cubic polynomial function (in red) for an AlMg3-PU adhesive joint with d_P = (1896 ± 11) µm at 10 °C. The surface in blue is used for the further calculations.

[8] In order to avoid the limitation of the calculation due to the local minimum of the polynomial function, a further optimisation has also been tested: the continuous spectrum is extended to longer retardation time by a linear slope. The value of this slope corresponds to that calculated at the inflexion point before the local minimum in the cubic polynomial function. However, this consideration has not shown any significant improvement in the further calculations.

The goodness of this fitting operation can be easily assessed by calculating the creep curve using the continuous retardation time spectrum with the eq. (2.120). It is here reasonable to use the same approximation (see eq. (2.118)) for the back calculation as for the approximation of $L^*(\tau)$. If this recalculated creep function matches the measured curve, the approximation for $L(\tau)$ can be regarded as accurate enough to pursue the further calculations.

Continuous relaxation time spectra from continuous retardation time spectra:

With the following approximate equations it is possible to calculate numerically a continuous spectrum if the other is known [89, 94]:

$$L(\tau) = \frac{H(\tau)}{\left[G_\infty - \int_{-\infty}^{+\infty} \frac{H(\varepsilon)}{\tau/\varepsilon - 1} d\ln\varepsilon\right]^2 + \pi^2 \cdot \left(H(\tau)\right)^2} \tag{2.162}$$

$$H(\tau) = \frac{L(\tau)}{\left[J_0 - \int_{-\infty}^{+\infty} \frac{L(\varepsilon)}{1 - \varepsilon/\tau} d\ln\varepsilon\right]^2 + \pi^2 \cdot \left(L(\tau)\right)^2} \tag{2.163}$$

The previously determined $L(\tau)$ is then inserted in the equation (2.163) to obtain an approximation of $H(\tau)$ in the same time range $[\tau_a, \tau_e]$. A series of numerical integrations with the increment $d\ln\varepsilon$ are required to convert $L(\tau)$ into $H(\tau)$ and vice versa.

Stress relaxation modulus from continuous relaxation time spectra:

To evaluate the stress relaxation modulus $G_{eff}(t)$ from the calculated continuous relaxation time spectrum $H(\tau)$, equation (2.155) can be used. The calculations hitherto have been made considering the Alfrey's approximation – see (2.153). That is why equation (2.155) is preferred to eq. (2.152) for the calculation of $G_{eff}(t)$:

$$\mathrm{G}_{eff}(t) - G_\infty \approx \int_{\tau_a}^{\tau_e} \frac{H(\tau)}{\tau} \cdot d\tau \tag{2.164}$$

G_∞ can be obtained from eq. (2.150). If $H(\tau)$ and $L(\tau)$ are known, G_∞ can also be determined from the creep compliance $J_{eff}(t)$ [95]:

$$\int_0^t G_{eff}(t-\varepsilon) J_{eff}(\varepsilon) d\varepsilon = \int_0^t J_{eff}(t-\varepsilon) G_{eff}(\varepsilon) d\varepsilon = t \tag{2.165}$$

This relation has been used in this work to cross-check the consistency of the results obtained from the creep tests with the ones from the stress relaxation tests and vice-versa.
Previously, it has been shown that:

$$\begin{cases} G_{eff}(t) \approx G_{\infty} + \int_0^{+\infty} \frac{H(\tau)}{\tau} \cdot d\tau \\ J_{eff}(t) \approx J_0 + \int_0^{+\infty} \frac{L(\tau)}{\tau} \cdot d\tau \end{cases} \tag{2.166}$$

For the sake of clarity, the following substitution in eq. (2.166) is made:

$$\begin{cases} G_{eff}(t) \approx G_{\infty} + A(t) \\ J_{eff}(t) \approx J_0 + B(t) \end{cases} \tag{2.167}$$

where $A(t) = \int_0^{+\infty} \frac{H(\tau)}{\tau} \cdot d\tau$ and $B(t) = \int_0^{+\infty} \frac{L(\tau)}{\tau} \cdot d\tau$.

Replacing $G_{eff}(t)$ and $J_{eff}(t)$ in eq. (2.165) with their expression from eq. (2.167):

$$\begin{aligned} \int_0^t G_{eff}(t-\varepsilon) J_{eff}(\varepsilon) d\varepsilon &= \int_0^t G_{\infty} \cdot J_0 \cdot d\varepsilon + \int_0^t G_{\infty} \cdot B(\varepsilon) \cdot d\varepsilon \\ &+ \int_0^t [A(t-\varepsilon) \cdot J_0 + A(t-\varepsilon) \cdot B(\varepsilon)] \cdot d\varepsilon \\ &= G_{\infty} \cdot J_0 \cdot t + G_{\infty} \int_0^t B(\varepsilon) \cdot d\varepsilon + \int_0^t [A(t-\varepsilon) \cdot J_0 + A(t-\varepsilon) \cdot B(\varepsilon)] \cdot d\varepsilon \end{aligned} \tag{2.168}$$

According eq. (2.165), we obtain from eq. (2.168):

$$t = G_{\infty} \cdot J_0 \cdot t + G_{\infty} \int_0^t B(\varepsilon) \cdot d\varepsilon + \int_0^t [A(t-\varepsilon) \cdot J_0 + A(t-\varepsilon) \cdot B(\varepsilon)] \cdot d\varepsilon \tag{2.169}$$

It is now possible to deduce G_{∞} from the equation (2.169):

$$G_{\infty} = \frac{t - \int_0^t [A(t-\varepsilon) \cdot J_0 + A(t-\varepsilon) \cdot B(\varepsilon)] \cdot d\varepsilon}{J_0 \cdot t + \int_0^t B(\varepsilon) \cdot d\varepsilon} \tag{2.170}$$

Note that the obtained value for G_{∞} should be constant regardless of the chosen time t.

The value found for G_{∞} can also be compared with those obtained from stress relaxation tests and be placed, for example, in eq. (2.78) to model shear tests at constant shear rate.

The interrelations between viscoelastic functions thus offers the possibility to calculate the results of a relaxation test and shear tests at different shear rates from the experimental results of a creep test – Figure 2-30. Finally, calculated and measured curves can be compared and thus the consistency of the results and the validity of the underlying calculations/equations can be verified – see section 4.3.1. Once this validity is ensured, the mechanical behaviour of the investigated adhesive joints can be calculated using the presented method.

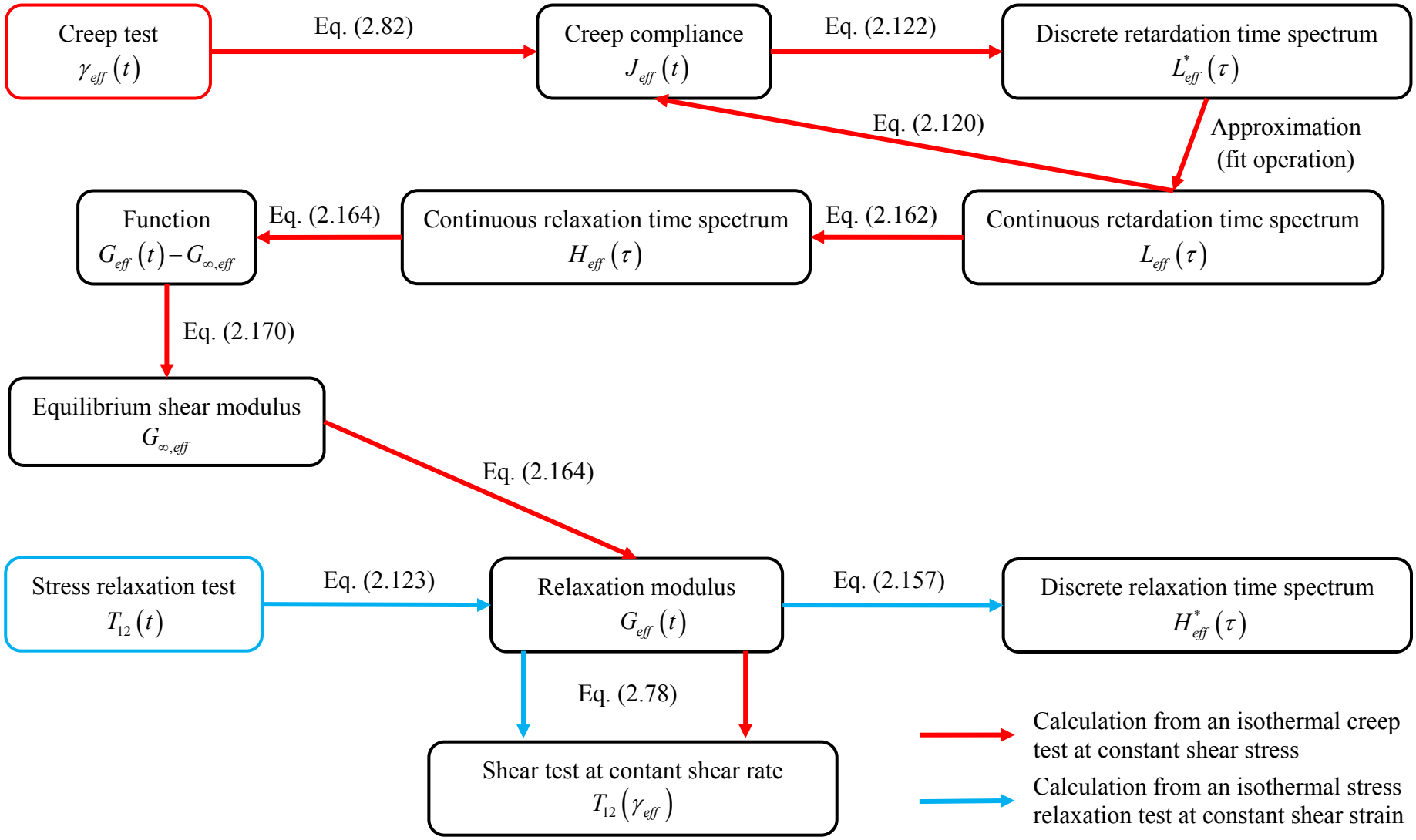

Figure 2-30: Strategy for the calculation of viscoelastic functions from an experimental isothermal creep test (in red) and from an experimental isothermal stress relaxation test (in blue)

3. Experimental approach

3.1. Materials

3.1.1. Polyurethane adhesive

Over the last decades, polyurethanes (PU) are widely used as adhesives because of their reliability and high performance in many applications including, construction, automotive industry, packaging applications and furniture assembly. Depending on the chemical structure of the components used for polyurethane synthesis, the properties of the resulting polymer can be tailored to meet the user's needs [96]. In contrast to most commercial polyurethane adhesive formulations, the reactive PU adhesive utilised for this work contains, for the sake of clarity, no additives. The technical monomers used for the fabrication of all the samples are presented in section 3.1.1.1. The chemical reactions between those components lead to the formation of a crosslinked amorphous polyurethane as described in section 3.1.1.2.
Besides the chemical nature of the components, the properties of the polyurethanes are influenced by stoichiometric ratio of reactive groups, curing conditions and crosslinking density [97-99]. For these reasons, a careful preparation of the adhesive is essential to succeed in detecting interphases in adhesive joints. All the preparation steps as well as the determination of the curing regime of the PU are detailed in section 3.1.3.

3.1.1.1. Polyurethane components

Isocyanate hardener

The commercial monomer Desmodur® VP.PU 1806 (Bayer MaterialScience AG, Leverkusen, Germany) is used as isocyanate hardener in the investigated polyurethane adhesive. It consists of three methylene diphenyl diisocyanate isomers (MDI) - Figure 3-1. At room temperature, this isomer mixture is a yellowish liquid [100]. Due to its structure containing phenylene groups and its relatively low molecular weight (cf. Table 3-1), MDI molecules provide hardness and stiffness to the resulting polymer structures.

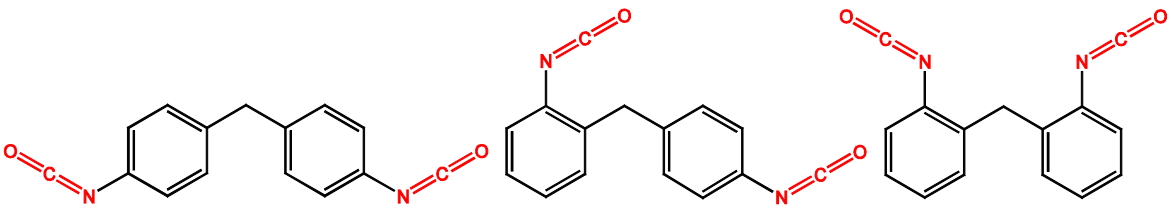

Figure 3-1: Desmodur® VP.PU 1806: mixture of the three methylene diphenyl diisocyanate isomers (MDI), M ≈ 250.26 g/mol, (Bayer MaterialScience AG, Leverkusen, Germany)

Table 3-1: Technical data of Desmodur® VP.PU 1806 [100].

Average molar mass [g·mol^{-1}]	250.26
NCO-content [%]	33.4 – 33.6
Functionality [-]	2
Monomeric diisocyanate content [%]	100
Viscosity at 25 °C [mPa·s]	10 - 14
Density at 25 °C [g·cm^{-3}]	approx. 1.21
Vapour pressure at 20 °C [mbar]	< 1·10^{-5}
Equivalent weight [g·mol^{-1}]	approx. 125

In 2014, MDI was the largest volume industrial isocyanate produced. MDI is an aromatic diisocyanate, wherein the reactivity of each isocyanate functionality [-N=C=O] is governed both by the electrophilic character of the carbon atom, which can react with nucleophilic compounds, and by the nucleophilic character of oxygen and nitrogen atoms, which can react with electrophilic reagents.
In the case of aromatic isocyanates, like MDI, unshared electrons of the nitrogen are delocalised into the aromatic ring, thus increasing the reactivity of the isocyanate group in comparison with aliphatic isocyanates [101].

The isomer structure also influences the physical properties and the reactivity. For example, the 4,4′ isomer is more reactive compared to the sterically hindered 2,4’ and 2,2’ isomers, but it has a limited shelf life. The pure 4,4′ monomer is a solid at room temperature with a melting point of 38 °C [102]. Even in the solid state, the 4,4′ monomer undergoes a facile dimerisation reaction to form uretdione (Figure 3-2) [103]. In the presence of the others isomers, the dimerisation of the 4,4′ monomer in Desmodur® VP.PU 1806 is significantly slowed down due to the steric hindrance [104]. Although the dimer converts back to the monomers on heating (T > 160 °C), MDI must be used in a relatively short time after production and stored at low temperatures [101, 105]. The formation of another class of isocyanate dimer, such as carbodiimides, is also possible through selective catalysis [103] (or long-time storage at high temperature). As no catalyst is used in this work, these structures are not discussed.

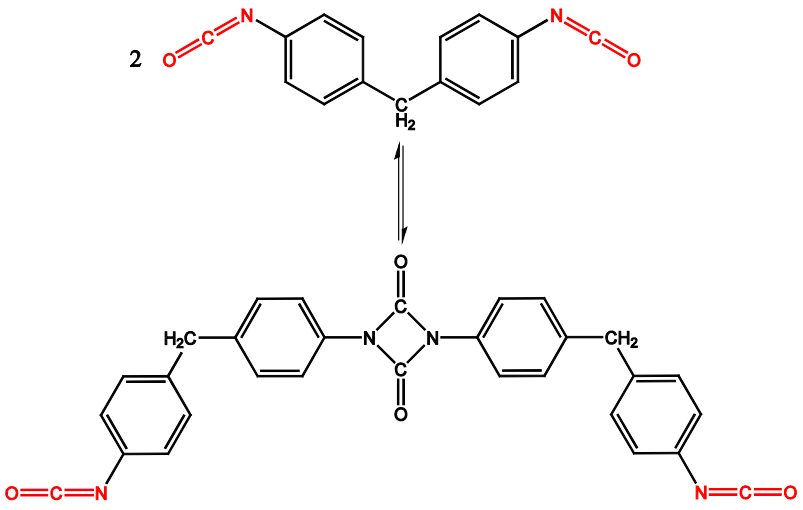

Figure 3-2: Dimerisation reaction of MDI [106]

Upon heating (T > 160 °C) or in the presence of catalysts (as well as some acids, amines and carboxylates), the trimerisation of MDI can also occur to form a thermally stable isocyanurate group (Figure 3-3) [103]. Therefore, the temperature of the monomers during the storage and the fabrication process is still less than 160 °C to limit or even to avoid the formation of such trimers.

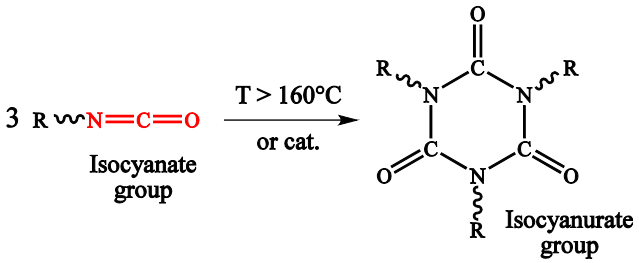

Figure 3-3: Formation of isocyanurates: trimerisation of isocyanates

Polyol resin mixture

A mix of polyol resins, consisting of a linear oligopropylene ether diol (Desmophen® 3600Z, $\overline{M} \approx 2000\ g \cdot mol^{-1}$, Bayer MaterialScience AG, Leverkusen, Germany) and a branched oligopropylene ether triol (Baygal® K55, $\overline{M} \approx 440\ g \cdot mol^{-1}$, Bayer MaterialScience AG, Leverkusen, Germany), is used as comonomers for the diisocyanate hardener - Figure 3-4. Hereinafter these monomers are referred to as diol and triol respectively. At room temperature, both monomers are colourless to yellow-coloured, low viscous liquids (Table 3-2) [107, 108].

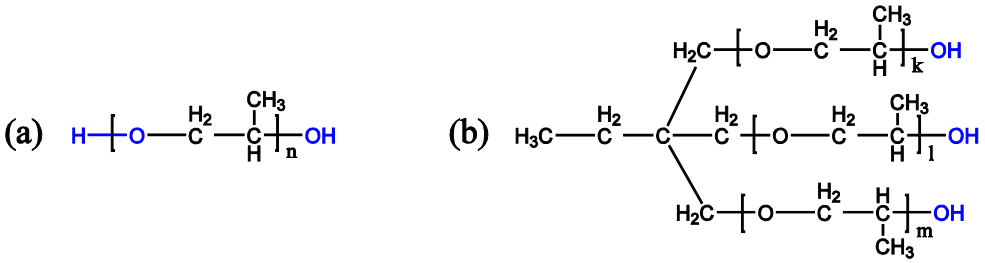

Figure 3-4: Chemical structures of the polyols (a) Linear polypropylene ether diol, $\overline{n} \approx 34.2$, $\overline{M} \approx 2000\ g \cdot mol^{-1}$ (b) Branched polypropylene ether triol, $\overline{k+l+m} \approx 5.3$, $\overline{M} \approx 440\ g \cdot mol^{-1}$

Table 3-2: Technical data of Desmophen® 3600Z and Baygal® K55 [107, 108]

	Desmophen® 3600Z	Baygal® K55
Average molar mass [g·mol^{-1}]	2000	440
Functionality [-]	2 (diol)	3 (triol)
Hydroxyl number [mg (KOH)·g^{-1}]	56 ± 2	385 ± 15
Viscosity at 25 °C [mPa·s]	310 ± 25	600 ± 50
Density [g·cm^{-3}]	approx. 1 (at 20 °C)	approx. 1.03 (at 25 °C)

The polyether polyols are hydroxyl-terminated [-OH] oligomolecules made from the reaction between an initiating alcohol and a cyclic ether (oxirane)

Compared to the MDI monomers, the polyols tend to provide softness and flexibility to the resulting polymer structures due to their flexible etheric backbone and their high-molecular-weight [102]. By choosing different mixing ratios of the two polypropylene polyols (diol and triol), different polyurethane adhesives can be obtained with respect to their molecular mobility/glass transition temperature. Thus, it is possible to design the properties of the resulting polymer to meet the need for this work, without adding any additive.

3.1.1.2. Chemical reactions

The chemistry of polyurethanes is based on the high reactivity of isocyanates towards proton-bearing nucleophiles (cf. section 3.1.1.1). For the purpose of this work, only the reactions, which can occur with the monomers presented in section 3.1.1.1, are considered in this section. The resulting polyurethane structure will be discussed in section 3.1.2.

The major reaction in polyurethanes is the reaction of isocyanates with hydroxyl components, such as alcohols. This addition polymerisation of diisocyanates with macroglycols, or so-called polyols, to produce urethane polymers was pioneered in 1937 at IG Farbenindustrie (Leverkusen, Germany) by O. Bayer [109]. This nucleophilic addition which occurs at room temperature (20 °C) without catalyst, produces urethane groups, also known as carbamate groups (Figure 3-5) [101]. Different mechanisms are proposed for this reaction but they all lead to the same ultimate molecular structure [110, 111].

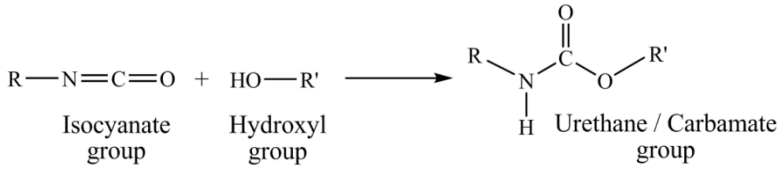

Figure 3-5: Formation of urethane / carbamate groups

Thus, the polyaddition reaction of diisocyanates with polyols forms polyurethane: reaction between bifunctional educts (MDI with diol, for example) results in thermoplastic polyurethanes (i.e. with linear chains) whereas reaction of diisocyanates with triols results in thermoset polyurethanes (i.e. with a three-dimensional cross-linked network).

Besides the relatively straightforward addition reaction, side reactions can occur having profound effects on polyurethane properties. For instance, water, which can come from air moisture or be adsorbed onto the substrate surface, can also react with isocyanate. This reaction is somewhat complex because an unstable carbamic acid is first formed. This intermediate decomposes into an amine and gaseous carbon dioxide. Although this production of CO_2 is a most important reaction in the polyurethane foam industry, the same cannot be said for the

purpose of this work since the presence of CO_2 gas bubbles in the adhesive decreases in a nonhomogeneous way (but significantly) its mechanical properties.
The strong nucleophilic nature of the primary amine, formed by the decomposition of the unstable carbamic acid, allows it to react immediately with an additional isocyanate to give a urea or carbamide, as shown in Figure 3-6. These urea compounds can increase the reaction kinetics of the polyurethane formation [112].

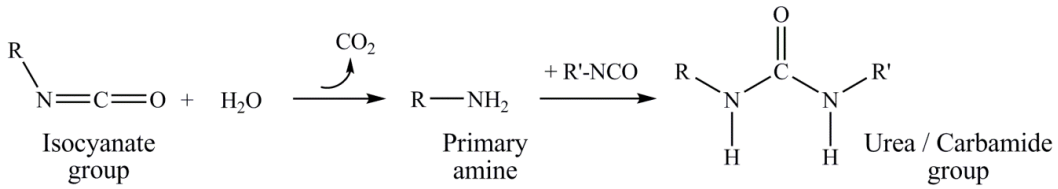

Figure 3-6: Reaction of water with isocyanate

The presence of water in the reaction mixture impacts the final structure and properties of the polyurethane adhesive. Therefore the preparation of the adhesive is carried out in a dried atmosphere (absolute humidity between 0.01 and 0.03 g/m^3) to limit as much as possible the presence of water and so, the formation of urea species (cf. section 3.1.3).

Both urethane and urea group contain acid hydrogen atoms which can react with a further isocyanate group. While these reactions can be neglected at room temperature, they can occur without catalyst at temperatures above 100 °C (generally at 150 °C) [101, 113]. The addition of a urethane to an isocyanate results in the formation of an allophanate (cf. Figure 3-7) whereas the reaction between a urea and an isocyanate forms a biuret (cf. Figure 3-8).

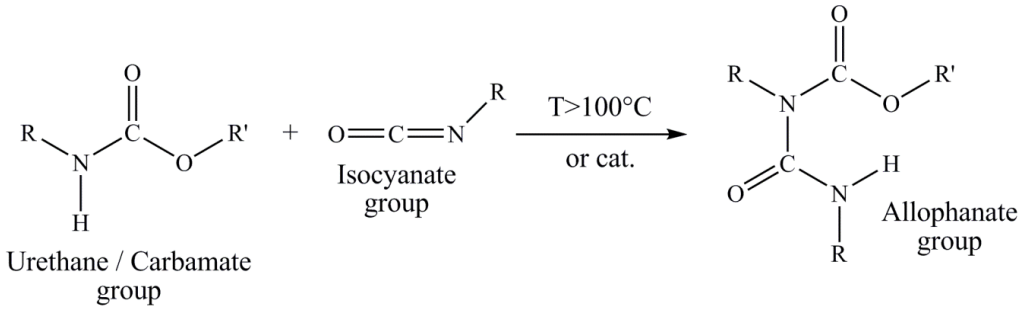

Figure 3-7: Formation of allophanate

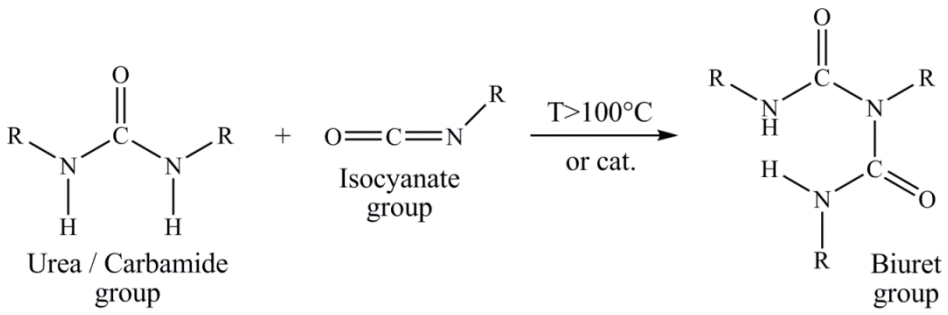

Figure 3-8: Formation of biuret

If the R group in Figure 3-7 or Figure 3-8 contains an additional isocyanate moiety, the formation of an allophanate or, respectively, a biuret results in crosslinking [114, 115]. These new linkages do in turn influence the properties of the resulting polymer [116, 117].

3.1.2. **Structure and homogeneity of the polyurethane adhesive in bulk**

While the primary structure of the two-part polyurethane is largely determined by the addition reaction of isocyanates with alcohols, inter- and intramolecular interactions, such as hydrogen bonds [118, 119], also influence the morphology of the polymer [11, 113]. Nevertheless, the nature of the resulting polyurethane can be discussed considering the structure of the three monomers presented in section 3.1.1.1.

First, the miscibility of components and emerging oligomers as well as kinetic effects are key factors for the formation of a macroscopically homogeneous bulk phase. Mixing of monomers is also an important operation in the adhesive preparation to ensure the reproducibility of the results (cf. section 3.1.3).

Unlike many technical adhesives, no additives are contained in the polyurethane used in this work. The presence of triol in the reaction mixture leads to the formation of polyurethane with a three-dimensional crosslinked network. By choosing different mixing ratios of the two polypropylene polyols, different crosslinked polyurethane adhesives can be obtained with respect to their molecular mobility/glass transition temperature (ranging from duromers to elastomers at room temperature). Thus, the greater the concentration of diol in the reaction mixture, the bigger the mesh size in the resulting polyurethane network and hence, the lower the glass transition temperature of the polymer.

Across the glass transition, the structure and dynamics of polymer systems undergo a major change which results in a drastic modification of its physical properties. That is why the study of the mechanical glass transition of the polyurethane system presented in section 3.1.1 also attracted a particular interest in this work.
Therefore, a polyurethane adhesive having a mechanical glass transition region near room temperature has been chosen to ease the experimental investigations. This means that a temperature variation of only a few Kelvin is necessary to cause a big change in the mechanical properties of the polyurethane.

In the polyurethane adhesive used in this work, the polyols are mixed at a hydroxyl group ratio of $OH_{triol} : OH_{diol} = 80 : 20$. That amount of triol in the reaction mixture results in a considerable crosslink density. As a result, this chemical crosslinking avoids the formation of hard and soft segments [120] which are common in thermoplastic polyurethanes [121-126]. Without such phase separation, a relatively homogeneous polyurethane network can be expected, assuming that all monomers are thoroughly mixed during the preparation, as discussed in the next section.

3.1.3. **Preparation and curing regime of the PU adhesive**

Besides the chemical nature of the monomers, the preparation of the reaction mixture and the curing regime determine the structure and the properties of the resulting polymer. To describe the influence of interphases in adhesive joints, the adhesive bulk must have clearly defined, reproducible and constant properties over time.

The polyols are mixed at a hydroxyl group ratio of OH_{triol} : OH_{diol} = 80 : 20 at room temperature with a magnet stirrer for 15 minutes. The whole preparation of the adhesive and any types of samples is performed in a glove box, purged with dry air (dew point between -55 °C and -60 °C) to minimise any disturbing reaction described in Figure 3-6. Considering a room temperature of 23 °C and a pressure of 1013.25 hPa, the absolute humidity in the glove box lies between 0.01 and 0.03 g/m^3. Therefore, the influence of atmospheric water on crosslinking reactions can be neglected.
The diisocyanate hardener is then added as fast as possible to the polyols and the reactive mixture is stirred for additional 15 minutes at room temperature. Finally, the mixture is gently degassed in vacuum to remove all the air bubbles due to the mixing / stirring operation.

The reactive adhesive is prepared as a mixture of the resin and the hardener with a stoichiometric ratio of hydroxyl and isocyanate groups. Maximal curing to PU is obtained in dried atmosphere by 72 h at room temperature followed by 4 h post-curing at 403 K in dried atmosphere as well. Infrared spectroscopy by attenuated total reflection has been used to monitor the conversion of isocyanate groups over time during the post curing. Figure 3-9 depicts the obtained spectra (left) and the close-up view on the asymmetrical stretch vibrations of the isocyanate groups $\upsilon_a\left(NCO\right)$ (right) after different post-curing conditions. It is only after 4 hours post curing at 130 °C (approx. 403 K) that no remaining isocyanate group could be detected.

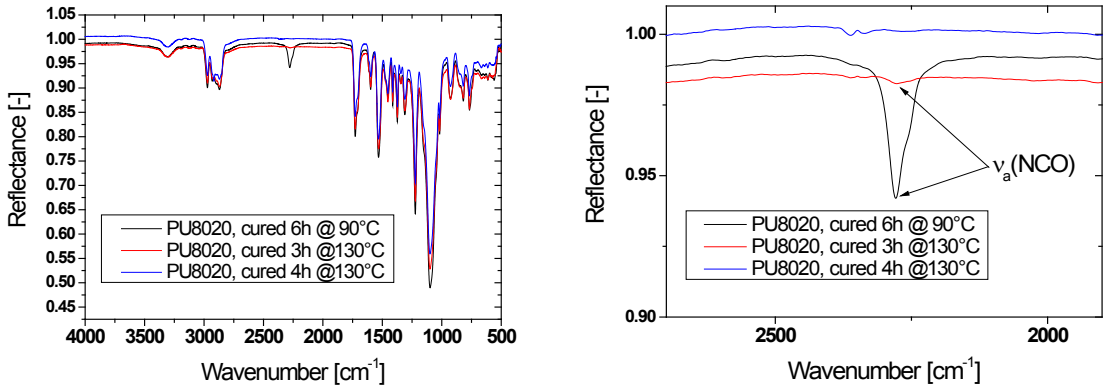

Figure 3-9: Attenuated total reflexion infrared reflectance (IR-ATR) spectra of PU8020 after different post-curing conditions. Complete spectrum (left) and close-up view on the asymmetrical stretch vibrations of the isocyanate groups $\upsilon_a\left(NCO\right)$ (right).

The caloric glass transition of the resulting PU bulk ranges from 213 K to 303 K (measured by DSC at 10 K/min, Figure 3-10). The glass transition temperature is $T_g^{DSC,bulk} = 266 \pm 1$ K.

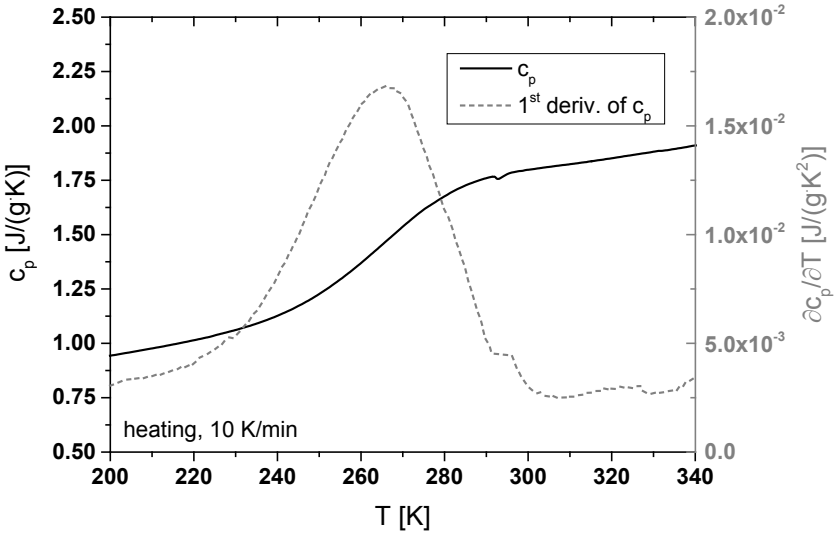

Figure 3-10: Specific heat capacity $c_p(T)$ measured with differential scanning calorimetry (DSC) during heating with 10 K/min for a cured PU-bulk sample and its first derivative for proper identification of the caloric glass transition range and T_g.

Such an adhesive system offers the following advantages for the experimental investigations:

- The temperature region of interest is easy to reach without heavy cooling or heating of the sample. This is especially important for the design of the experimental set-ups (see chapter 3.3)
- Even a slight change in measuring temperature influences significantly the physical properties of the adhesive (see Figure 3-10 and section 4.1)
- At room temperature the PU network is right in the upper part of the glass transition region, but full mobility is achieved by rising the temperature to some 310 K. Therefore the mechanical properties of the adhesive (joints) can be easily characterised in both viscoelastic and entropy elastic states (see section 4.1).

Samples for DSC investigations have been cut from PU 80:20 bulk material, casted in PTFE mold. The clean and smooth surface, which is in direct contact with the dry air atmosphere, is placed on the surface of the DSC pans to ensure the best possible thermal contact between the sample and the DSC pan. Despite thorough adhesive and sample preparation, experimental discrepancies between different batches cannot be completely eliminated, leading to a variation of the adhesive properties. Figure 3-11 illustrates this effect, using the caloric glass transition as an example. Although the presented plots are “normalised” by dividing the heat flow signal by the corresponding sample mass, the absolute value of the specific heat flow, the step height and the peak area are different for each measurement. This can be explained by the difference of heat transfer between the different samples: all samples cannot be identical and the contact surface between the polymer sample and the DSC pan may vary from measurement to measurement, especially for solid samples. Apart from these effects, the glass transition region

also slightly varies between the different batches. This could thus affect the comparability of the results from different batches.

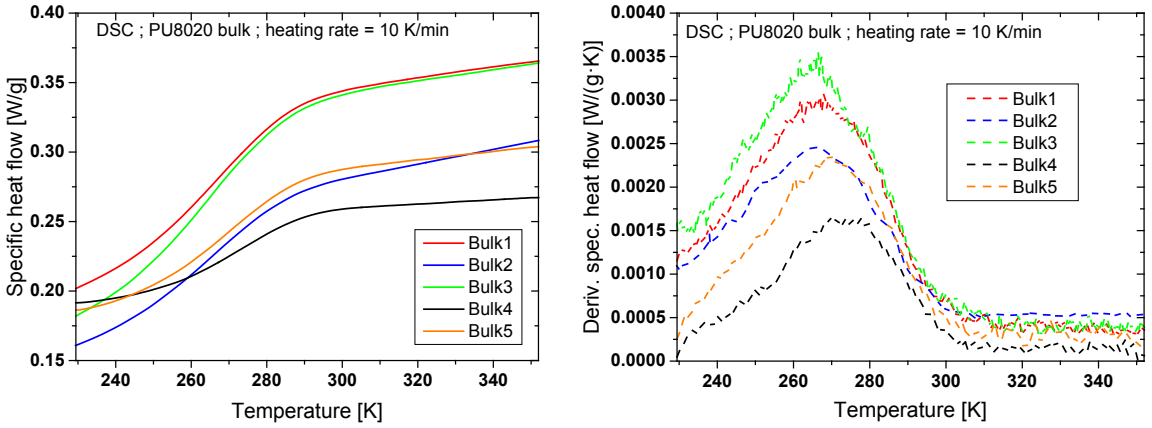

Figure 3-11: Specific heat flow curves measured with DSC during heating with 10 K/min for different cured PU-bulk batches (left) and their first derivative for proper identification of the glass transition range and T_g (right).

Considering these disturbing effects, only the samples prepared from the same adhesive batch can be quantitatively compared. Thus, all the samples for a given test series must be prepared in one shot. Within the same adhesive batch, optical observation (e.g. bubble in the sample), tensile tests, DSC and IR-ATR measurements do not reveal any phase separation or variation in the physical and chemical properties of the polyurethane. A homogeneous polymer network is also expected.
The usual quantity for the preparation of an adhesive batch is 500 g. The reactive adhesive is used within 60 minutes after the last mixing operation. In this time period, the spectroscopic isocyanate conversion of the bulk adhesive is ≤ 8 % [11], the reactive adhesive is still liquid and can be easily cast for the preparation of the sample.

3.2. Sample preparation

3.2.1. Bulk samples for tensile tests

In order to determine the mechanical bulk properties, tensile tests are performed (see section 3.4). For the preparation of the required specimens, the polyurethane adhesive is prepared as described in section 3.1.3 and casted on a PTFE surface to obtain a film of about 2 mm thickness. Specimens for the tension tests according to ISO 527-2:1996 Type 5A (Figure 3-12) are then die cut from the film and marked with a black serigraph colour[9] using a mask, cf. Figure 3-13. With a backlighting system, this dark pattern gives a good contrast for optical deformation measurements – Figure 3-14.

[9] "schwarze Kodierfarbe" supplied by Fiedler Optoelektronik GmbH.

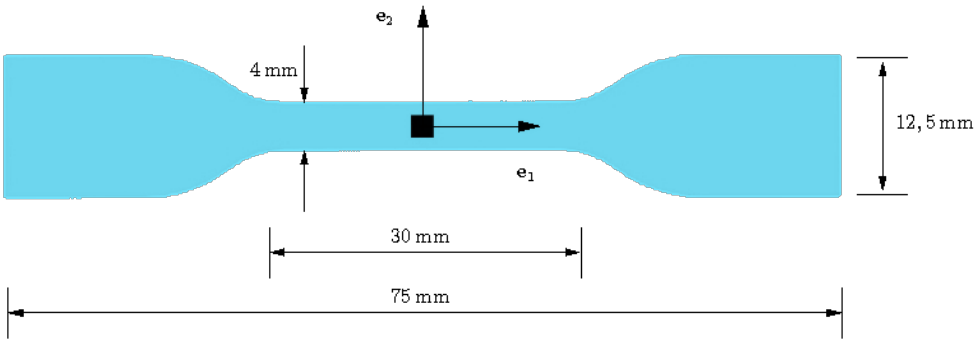

Figure 3-12: Tensile test specimen (according to standard ISO 527-2:1996 Type 5A), marked with a dark pattern [72]

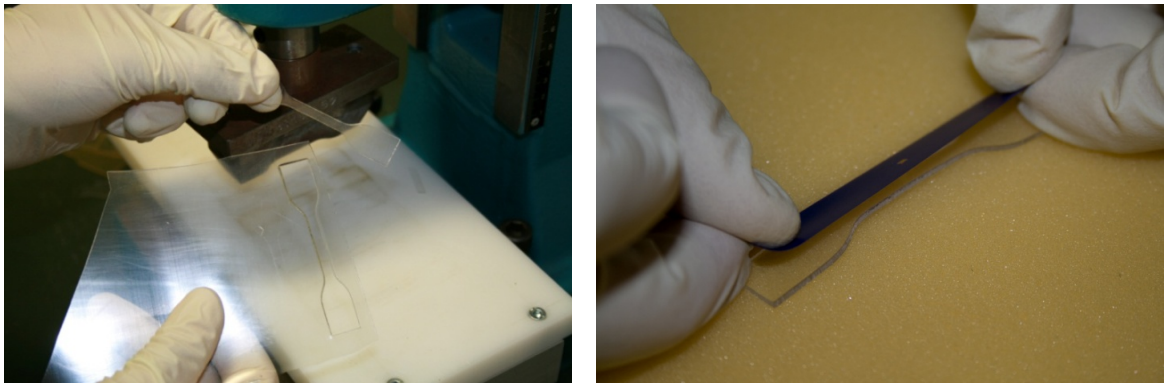

Figure 3-13: Preparation of the tensile test specimens: dye cutting (left) and marking with a template (right)

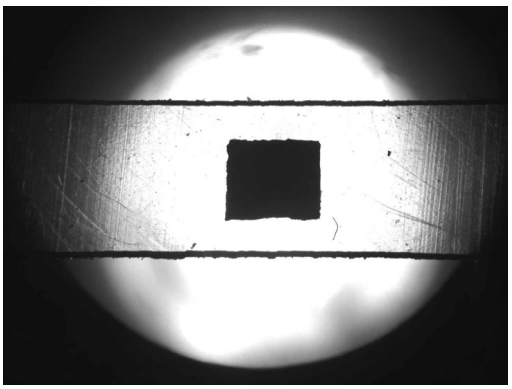

Figure 3-14: Dark pattern captured by the CCD camera

3.2.2. **Polyurethane-metal adhesive joints**

Shear experiments have been chosen to investigate the effective mechanical properties of adhesive joints. In this work, two types of adhesive joints have been investigated to detect the influence of interphases:

- Aluminium-magnesium alloy (AlMg3) substrates bonded with PU8020
- Stainless steel (1.4301) plates bonded with PU8020.

Both substrates are relevant for many technical applications and possess different features which will be described below.

3.2.2.1. PU-AlMg3 adhesive joints

AlMg3 is used as adherend for the preparation of adhesive joints. This alloy is typically used in treadplate, shipbuilding, vehicle bodies, rivets, fishing industry equipment, food processing, welded chemical and nuclear structures. AlMg3 features a modulus of elasticity of about 70.5 GPa and its chemical composition is given in Table 3-3.

Table 3-3: Chemical composition of AlMg3 according to the standard DIN EN 573-3 [127]

Chemical element	Si	Fe	Cu	Mn	Mg	Cr	Zn	Ti	Mn + Cr	Residuals		Al
										each	total	
Min. [wt.%]					2.6				0.1			Rest
Max. [wt.%]	0.4	0.4	0.1	0.5	3.6	0.3	0.2	0.15	0.6	0.05	0.15	

Geometry of the specimens

The sample blanks (20 mm x 190 mm x 100 mm) (Figure 3-15, left) are CNC-machined and provided with the necessary drillings before they are spark eroded into two point-symmetrical halves (Figure 3-15, right). The pairs are numbered with a letter/number punch to prevent mismatching.

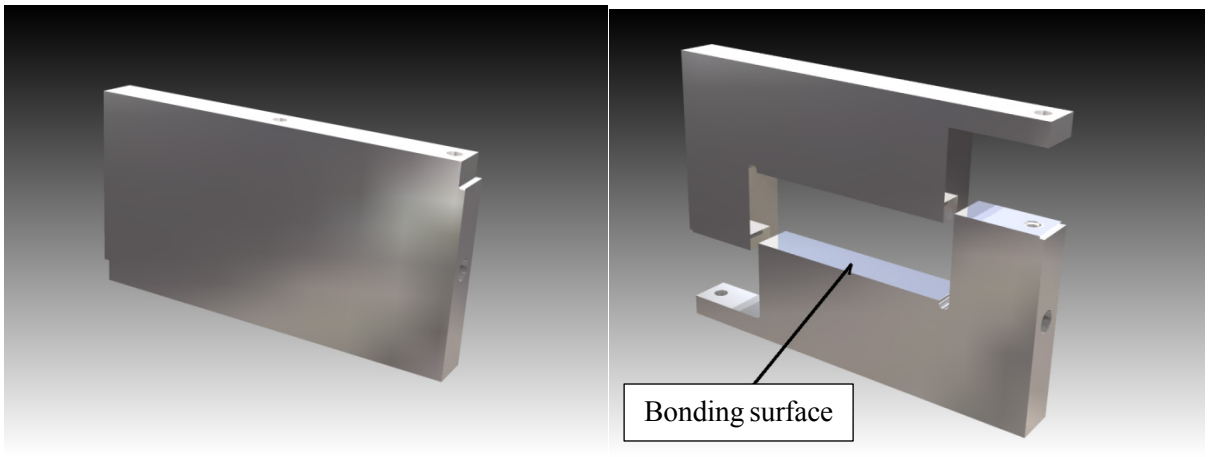

Figure 3-15: AlMg3 sample blank before (left) and after spark erosion machining (right) [1]

The dimensions of the AlMg3 substrates are given in Figure 3-16 and the drillings for the mounting of the displacement transducer, temperature sensors and heating/cooling system are depicted in the technical drawing shown in Figure 3-17.

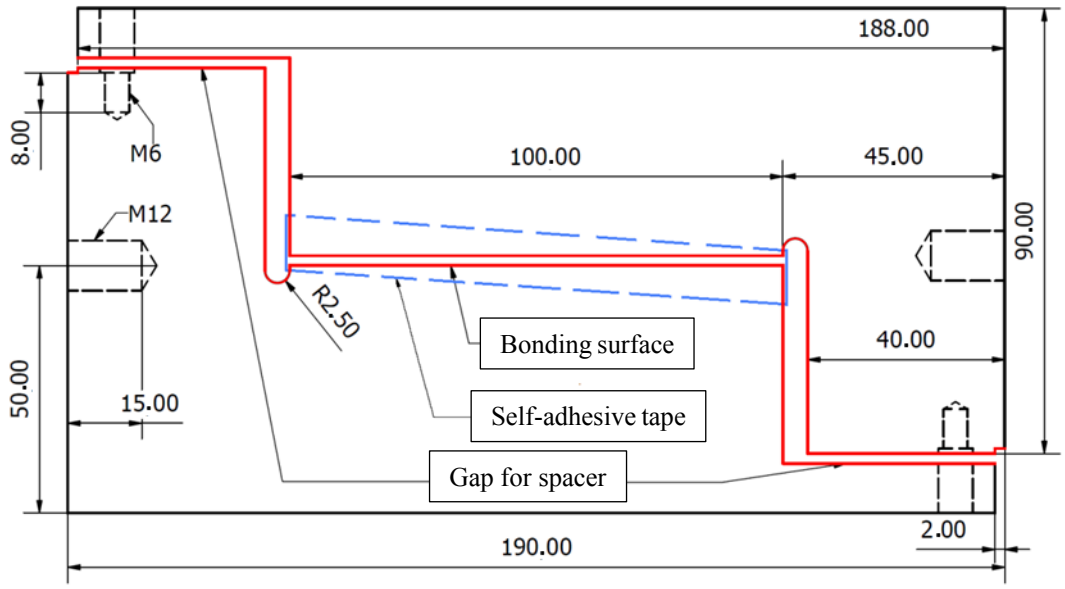

Figure 3-16: Geometry of the PU-AlMg3 shear specimens (dimensions in mm) [1]

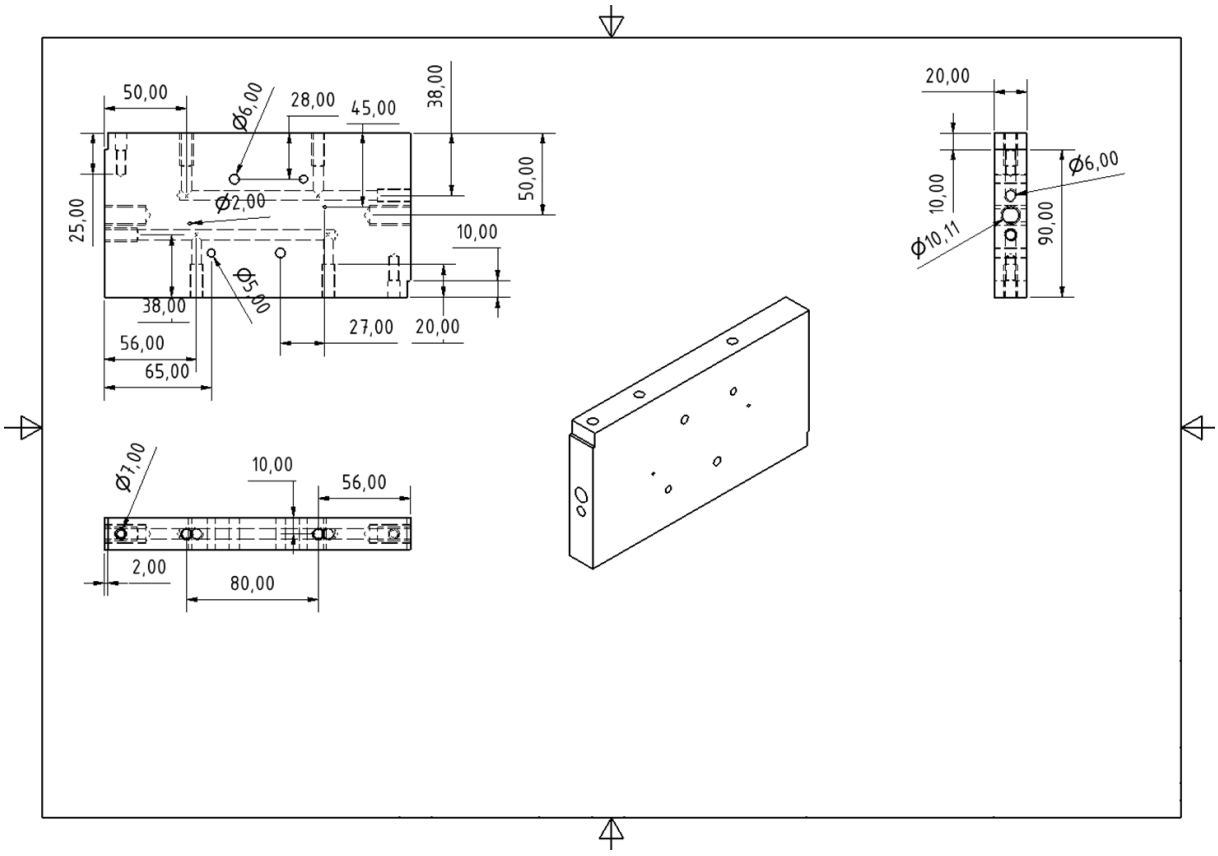

Figure 3-17: Technical drawing of the PU-AlMg3 shear specimens including drillings for sensors and heating/cooling system (dimensions in mm).

Surface treatment

Prior to the bonding operation, the bonding surfaces of the AlMg3 blocks are treated to obtain a defined and reproducible surface quality for all the specimens: During the manufacturing and machining process of the sample blanks, the surface of the alloy comes into contact with various contaminations and the working environment can influence the surface condition as well.

The surfaces are ultrasonically cleaned in acetone for 15 minutes to remove possible organic contamination and etched in 1-molar aqueous NaOH for 15 min. During this step, the aluminium oxide layer naturally formed, and the aluminium metal underneath dissolve:

$$2\,Al_2O_3 + 2\,OH^- + 3\,H_2O \;\leftrightarrows\; 2\,[Al(OH)_4]^-$$

When metallic aluminium is exposed to air or rather to oxygen, a thin amorphous oxide layer (ca. 5 nm) forms instantly on its surface [128]. This natural coating can grow over time, depending on the surrounding conditions (temperature, humidity and pH). Its chemical structure is though irregular, not well-defined [129] and should be removed. Once the Al_2O_3 layer is dissolved, the sodium hydroxide can also react with the subjacent metallic aluminium forming gaseous hydrogen:

$$2\,Al + 2\,OH^- + 6\,H_2O \leftrightarrows 2\,[Al(OH)_4]^- + 3\,H_2$$

It may be thus noted that this treatment must be performed under an extractor hood.

After the etching operation, the sample halves are thoroughly rinsed successively with tap water and distilled water to eliminate all the remains of sodium hydroxide and other residues. As the substrates come into contact with air during this operation, a thin aluminium oxide layer is thus formed again.
The AlMg3 substrates are then pickled in an aqueous nitric acid solution with a concentration of 20 wt.% for 2-3 minutes at room temperature. The diluted nitric acid solution does not etch directly the metallic aluminium but promotes its oxidation, forming a thicker but still amorphous Al_2O_3 coating [130]. The possible chemical reactions which are taking place during etching processes are:

$$2\,Al + 3\,HNO_3 \leftrightarrows Al_2O_3 + 3\,HNO_2$$

$$2\,Al + 6\,HNO_3 \leftrightarrows Al_2O_3 + 6\,NO_2 + 3\,H_2O$$

A slight formation of a brownish gas on the substrate surfaces after the immersion in the acid bath indicates the formation of nitrogen dioxide (NO_2) as described by the last chemical reaction.

Despite the exact progress of the involved chemical reactions during the pickling process is still unclear; a reproducible and chemically defined oxide layer is formed at the surface of the substrates.
Finally, the AlMg3 parts are successively rinsed in distilled water, acetone and dried.

The topography of the bonding surfaces has been analysed with white light interferometry (WLI) provided by Zygo (NewView 200) and mounted with a 3D Imaging Surface Structure Analyser. This technique combines an interferometer and microscope in one instrument. The WLI is a noncontact three-dimensional optical profiler based on the Michelson's interferometer (cf. Figure 3-18).

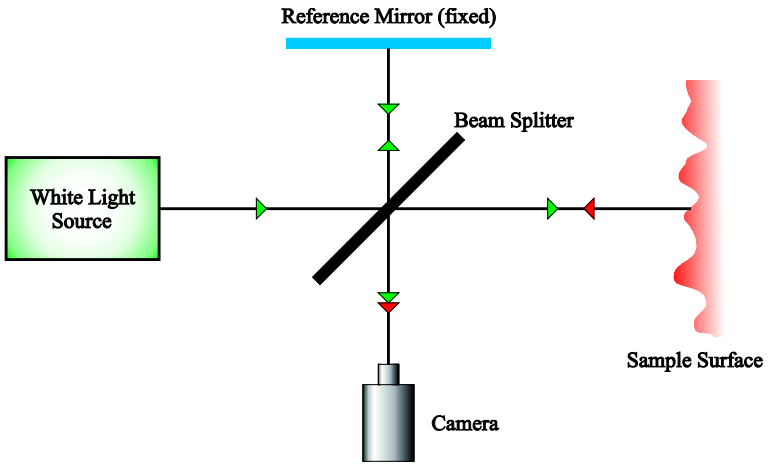

Figure 3-18: Schematic illustration of a Michelson interferometer

Illumination from a white light source with a coherence length in the micron range is spitted into two beams: an object beam and a reference beam. The object beam reflects from the surface being analysed and the reference beam reflects from a reference mirror. The reflected light from each beam is recombined at the beam splitter and captured by a CCD camera. The recombined beams generate an interferogram composed of bright and dark bands called "fringes" [131, 132]. For each point of the surface, the pattern of the fringes is analysed and converted into height information.
If the optical path for a point on the surface in the measurement arm is the same as the optical path in the reference arm, there is constructive interference and the corresponding camera pixel show a high intensity. Otherwise, the pixel has a lower intensity. Consequently, this intensity signal can be processed to determine, which points are at the same height.[133].

Figure 3-19 depicts the obtained bonding surface profile after the surface treatment with WLI.

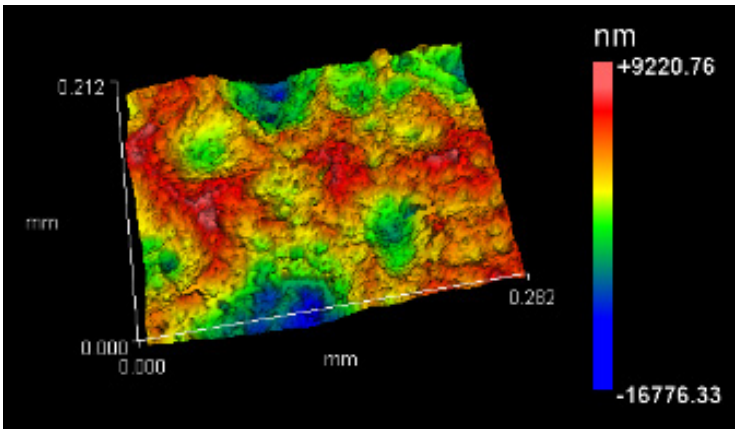

Figure 3-19: Topography of the bonding surface after the surface treatment obtained with WLI (measured surface: 0.283 x 0.212 mm²)

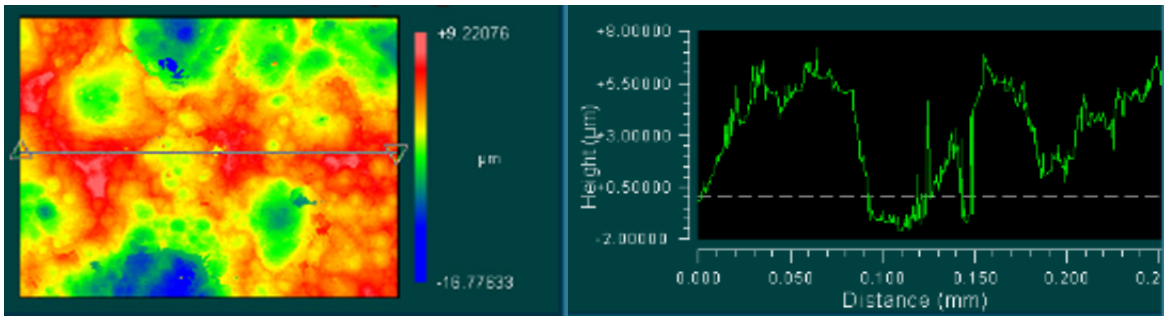

Figure 3-20: Example of a height profile

Thus, the geometrical parameters such as depth and the roughness parameters can be characterised using the WLI. The arithmetic average roughness R_a and the root mean squared roughness R_q are calculated for 5 different height profiles (Figure 3-20). They are defined as following:

$$R_a = \frac{1}{L}\int_0^L \left|z(x)\right| dx \tag{3.1}$$

$$R_q = \sqrt{\frac{1}{L}\int_0^L z^2(x)\, dx} \tag{3.2}$$

where L is the sampling length, z the height at position x along L.
The measured parameters are: $R_a = 2.93 \pm 0.37$ µm and $R_q = 3.67 \pm 0.45$ µm.

Bonding

The sample halves are paired according to their markers and arranged on a clean, flat surface. The clearance between the bonding surfaces is adjusted by inserting spacers with predetermined nominal thickness next to the drill holes. Both halves are screwed together to set their respective position (see Figure 3-21, left). Prior to bonding, the width of the gap between the paired halves is measured at two opposite positions and on both sides with micrometre precision (using a measuring optical microscope with Quadra-Check® system). Poor parallelism can be eventually corrected by slightly tightening/loosening one of the screws or by changing the spacer(s).

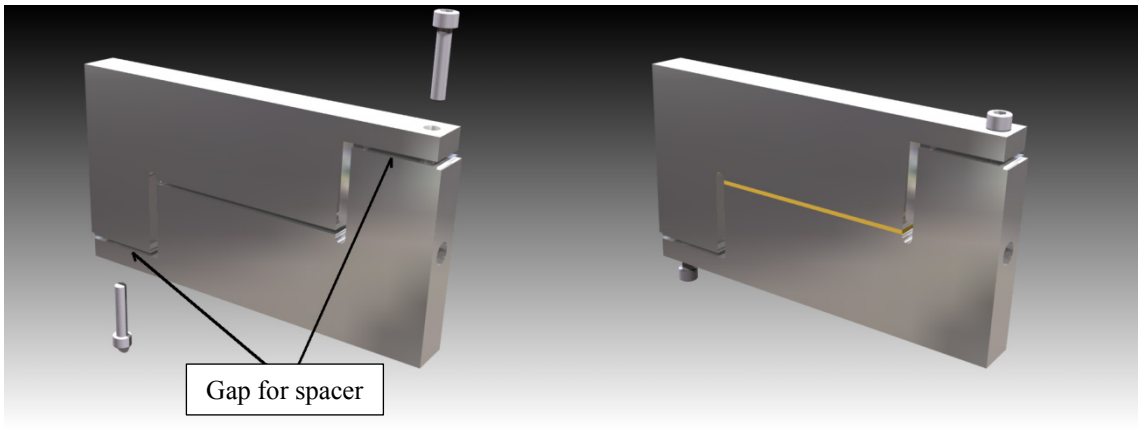

Figure 3-21: Assembling (left) and bonding (right) of the PU-AlMg3 shear specimens [1]

The gap between the bonding surfaces is sealed with adhesive tape at the sides and the bottom, to leave the top side open for later filling with the liquid adhesive. The so prepared AlMg3 substrates are introduced into the glove box through a vacuumable chamber. The samples are evacuated twice inside this chamber down to a pressure of about 5 Torr (≈ 667 Pa) at room temperature. This operation removes most of the water adsorbed on the surfaces of the halves and therefore minimises the unwanted side reaction presented in Figure 3-6. Under these temperature and pressure conditions, non-chemically bound water is in gaseous form and can be evacuated by the vacuum pump [134].
Finally, the gap between the paired halves of the shear samples is carefully filled with the liquid monomer mix (see preparation in chapter 3.1.3) by means of a pipette avoiding the formation of air bubbles. It should be noted that the polyurethane adhesive must be directly used within 60 minutes after the last mixing operation as the polymerisation starts with the addition of MDI in the polyol mixture and thus increases the viscosity of the adhesive.

After the curing (72 hours at room temperature) and the post curing (4 hours at 130 °C) in dry air, the samples are taken out of the glove box and the adhesive tape is removed - Figure 3-21, right. The screws and the spacers are then removed.

During the polymerisation and the cross-linking of the polyurethane adhesive, volume shrinkage occurs which induces internal stresses in the adhesive layer and influences the bond line thickness. After loosening the screws and removing the spacers, it is thus necessary to measure again the thickness of the adhesive layer every 25 mm using the optical microscope for both sides of the joint. The mean value and the standard deviation are calculated from these ten values. In this work, the nominal values of the bond line thickness d_P refer to the thus measured mean values (and standard deviations).

3.2.2.2. PU-stainless steel adhesive joints

The method presented in this work for the identification of mechanical interphases in adhesive joints is implementable to bonding joints with different adhesive-substrate combinations. Therefore, the existence of mechanical interphases in PU-stainless steel adhesive joints has been investigated as well.

Geometry of the specimens

As part of this work, new samples and testing jigs have been designed and manufactured to be able to vary the metal substrates in the adhesive joints. The geometry of the specimens had to be adapted due to the processing and costs.

Chromium-nickel austenitic stainless steel EN 1.4301 is used as substrate. This material is manufactured by ThyssenKrupp AG under the name NIROSTA® 4301 and features an elastic modulus of about 200 GPa. The chemical composition of this classic stainless-steel grade is X5CrNi18-10. The typical applications are automotive industry, building and construction industry, chemical industry, food and beverage industry, decorative items and kitchen utensils, electronic equipment and petrochemical industry.

The surface of a stainless-steel sheet (2 x 1 m) is mirror-like polished and then covered with a protective film. Small plates (130 x 20 x 2 mm) are cut from this metal sheet by laser beam fusion cutting to minimise any mechanical deformation or surface modification during machining or the oxidation of the edges. The longitudinal (length) direction of the plates is the rolling direction of the steel. The flatness of each plate is checked using the nearly perfect flat surface of a silicon wafer to ensure an accurate and homogeneous adhesive thickness after the bonding operation. If there is no visible light gap between the silicon wafer and the steel plate, this latter is used for the fabrication of adhesive joints.

Surface treatment

As for the AlMg3 substrates, the stainless-steel plates must be treated to obtain a defined and reproducible surface quality for all the specimens.
First, the plates are cleaned:

- using lint-free tissues and acetone to remove dirt and residues from the protective film,
- ultrasonically in ethyl acetate for 15 minutes at room temperature,
- ultrasonically in acetone for 15 minutes at room temperature.

After this operation the bonding surfaces are free from organic contaminations. However, the topography and the hydroxide/oxide layer on the surfaces are undefined and may vary from plate to plate. Besides, preliminary tests have shown that adhesion is weak between the polyurethane adhesive and stainless-steel plates without surface treatment.

Therefore, the steel plates are then electropolished to get a defined and reproducible bonding surface state and to achieve a better adhesion between the adhesive and the substrate.

Electropolishing is an anodic treatment removing a thin layer from the metal surface through a series of electrochemical reactions.

The electrodes are immersed in an electrolyte consisting of concentrated acid solutions having a high viscosity. The stainless steel plates to treat serve as the anode: metal on the surface is oxidised and dissolved into the electrolyte while a reduction reaction occurs at the cathode producing hydrogen - Figure 3-22.

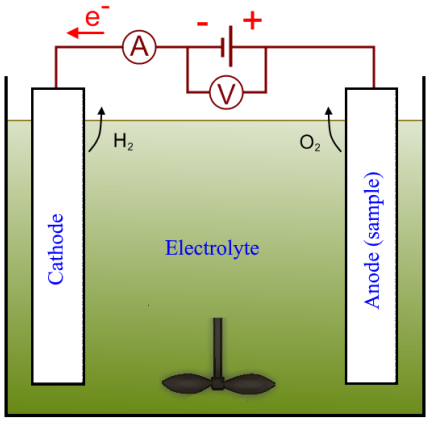

Figure 3-22: Electropolishing principle [135]

Although the exact mechanisms are not fully understood yet, following reactions are described for the two main components of the stainless steel [136, 137]:

Anode surface (sample)	→	Electrolyte	→	Cathode surface
Fe	→	Fe^{3+}	→	Fe^{2+}
Cr	→	Cr^{6+}	→	Cr^{3+}

After electropolishing, the treated parts are thoroughly rinsed with water and passivated with an aqueous nitric acid solution with a concentration of 20 wt.% for 2-3 minutes at room temperature. It results in the formation of a new and thin oxide layer which has an even thickness and rich of chromium oxide [136]. Therefore, electropolished stainless steel parts exhibit a better corrosion resistance [136, 138-141].

The involved mechanisms or reactions as well as the final surface condition after treatment depend on many parameters such as:

- Initial surface condition of the samples
- Type of electrode and electrolyte
- Temperature of the electrolyte
- Stirring conditions during the treatment
- Current density which is inversely proportional to the processing time [142]
- Size of the installation: the distance between the electrodes should be big enough to not obstruct the gassing and the mass transfer [138, 142].

Further information about the influence of these parameters is detailed in [135, 136, 138-140, 142-150].

Based on parameters found in [136], the selected electropolishing parameters for the treatment of the stainless steel plates in this work have been adapted to the experimental set-up presented in Figure 3-23:

- Electrolyte: 50 vol% of 95 wt.% sulphuric acid and 50 vol% of 85 wt.% of orthophosphoric acid
- Cathodes consist of the same stainless-steel grade as the samples
- The electrolyte is tempered between 30 °C and 40 °C and stirred
- Current density: 12.4 $A \cdot dm^{-2}$
- Processing time: 1 hour
- Anode-cathode distance: 2 cm

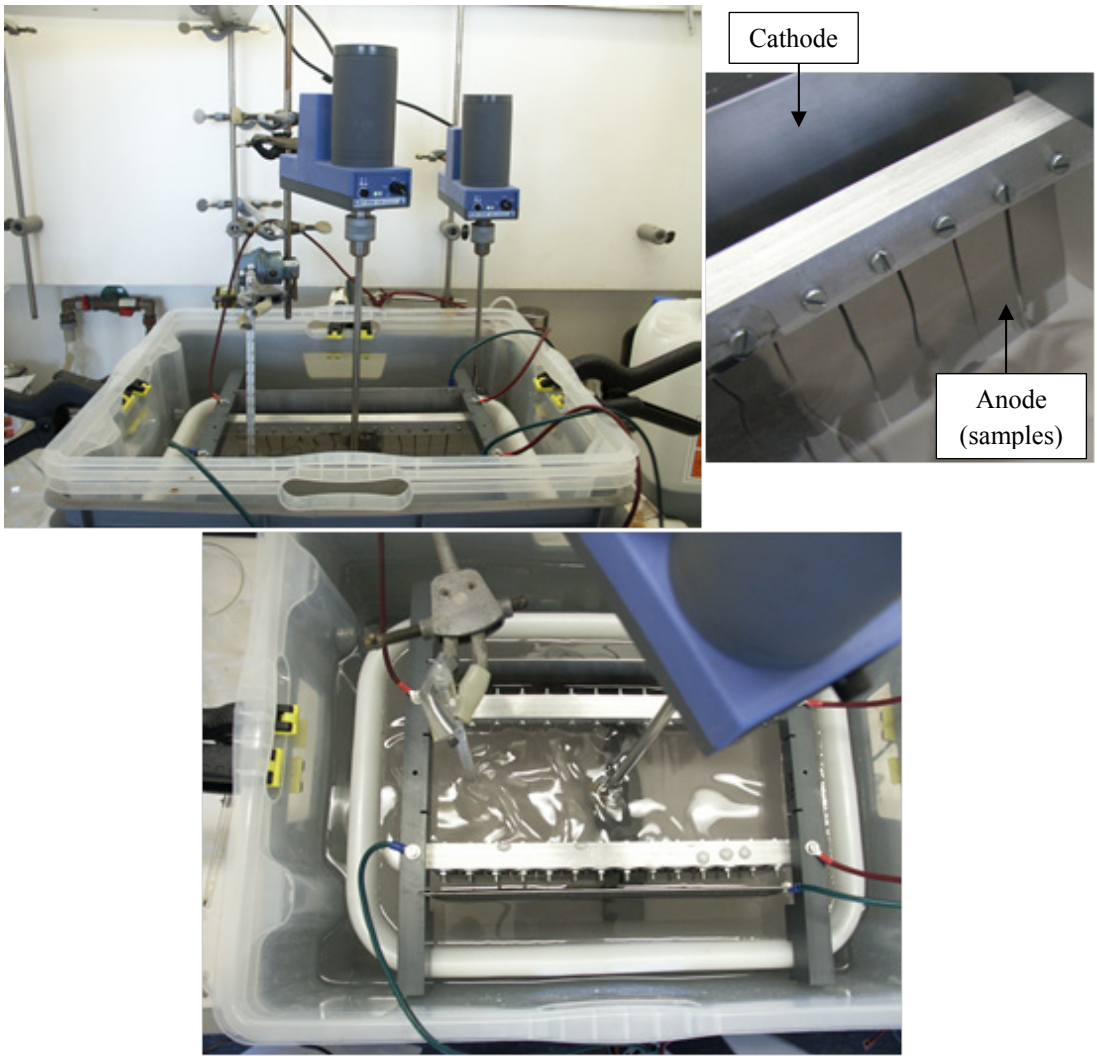

Figure 3-23: Experimental set-up for electropolishing of the stainless steel substrates [135]

After the electropolishing process, the samples are thoroughly washed with distilled water to remove the rests of the acid mixture (electrolyte). Remaining metal salts are eliminated from the surfaces using an aqueous nitric acid solution with a concentration of 20 wt.% for 2-3 minutes at room temperature. With this relatively low concentration, the nitric acid dissolves the metal salts without etching the metal and contributes to the passivation of the stainless steel [143, 145, 148, 150]. Then the samples are rinsed with distilled water once again and dried. The resulting surface condition is designated in the rest of this work as electropolished surface.

Once the treatment is completed, the effect of the treatment is clearly visible as depicted in Figure 3-24: the apparent lines on the right picture indicate hardening from the rolling process during the manufacturing of the stainless steel.

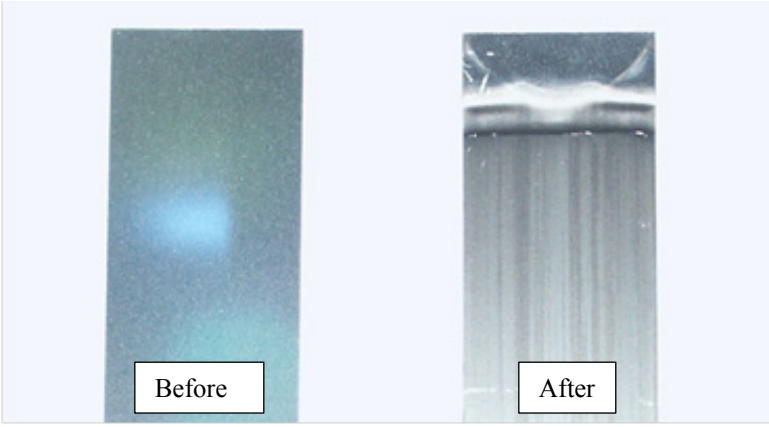

Figure 3-24: Picture of a stainless steel substrate before (left) and after (right) the electropolishing process [135]

White light interferometer (WLI) and scanning electron microscope (SEM) are used to characterise the topography of the bonding surfaces. The effect of the surface treatment is evidenced by comparing surfaces which have been solely treated with solvents (reference) to those after electropolishing.

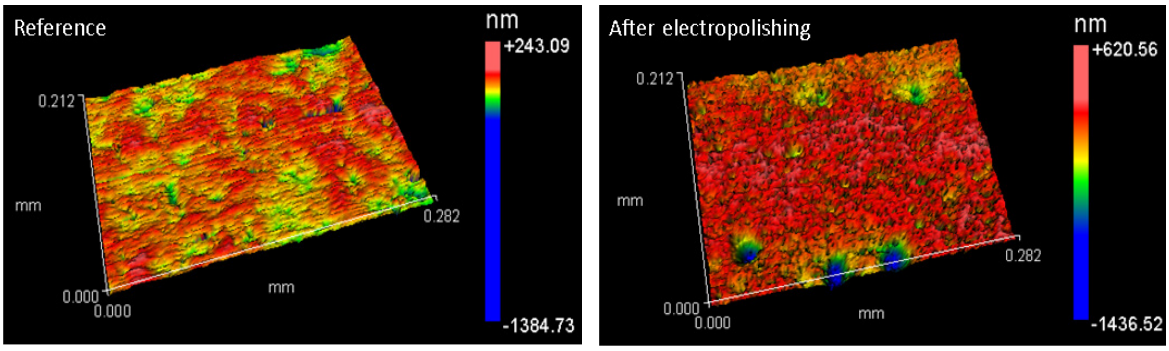

Figure 3-25: Topography of a bonding surface measured by WLI before (left) and after electropolishing (right) [135]

Figure 3-25 shows that the reference surface is smoother than the electropolished one which exhibits small craters (in blue). Cavities and scratches due to the rolling process or the mechanical polishing are microscopically easy to identify on the reference surface (Figure 3-25, left) whereas the surface after electropolishing does seem to have a preferential orientation (Figure 3-25, right). The arithmetic average roughness R_a and the root mean squared roughness R_q are averaged for 5 height profiles. The results in Table 3-4 confirm that the bonding surfaces are rougher after the "electropolishing" operation, contrary to what the name implies.

Table 3-4: Average roughness parameters using WLI (corresponding to **Figure 3-25**) before (reference) and after electropolishing

	Reference	After electropolishing
R_a	0.04 ± 0.01 µm	0.1 ± 0.01 µm
R_q	0.05 ± 0.01 µm	0.13 ± 0.02 µm

The bonding surfaces have been also investigated with scanning electron microscopy (SEM). The secondary electron (SE) imaging provides information on the topography of the sample (Figure 3-26, right). The backscattered electrons (BE) detect contrast between areas with different chemical compositions: elements with a high atomic number backscatter electrons more strongly than lighter elements and thus appear brighter in the image (Figure 3-26, left). BE imaging is also used to determine the grain orientation of the sample.

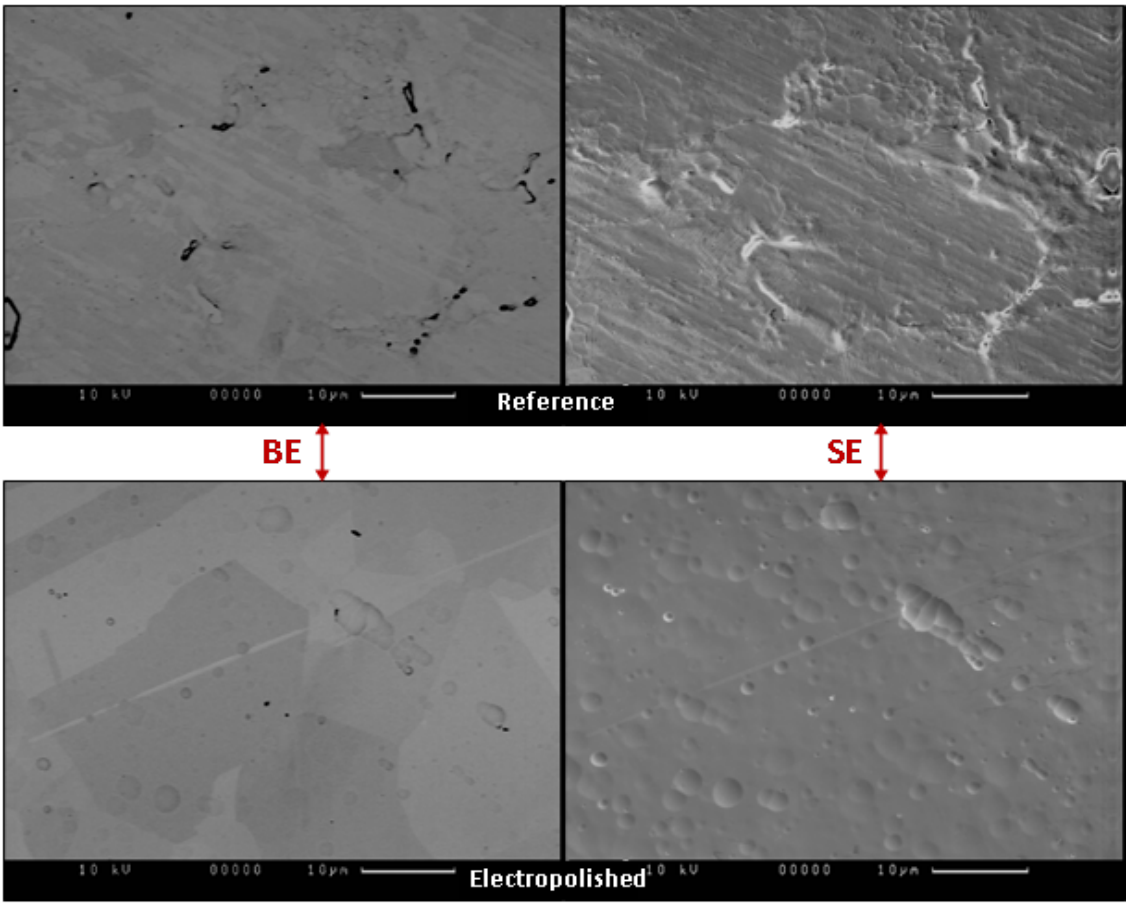

Figure 3-26: Backscattered electron (BE) imaging – grain orientation (left) and secondary electron (SE) imaging – topography (right) of the bonding surface before (top) and after electropolishing (bottom) obtained by SEM (magnification: 2000x) [135]

The reference surface (Figure 3-26, top) exhibits again scratches and cavities probably due to the manufacturing process. The electropolished sample (Figure 3-26, bottom) has a typical pitted surface but no evidence of mechanically-induced surface defects.

A further feature of the SEM used for these investigations is the energy-dispersive X-ray spectroscopy (EDX) to analyse the chemical composition of the sample. However, the depth of information of EDX is much greater than the thickness of the electropolished surface and no significant difference can be identified between the reference and the electropolished sample.

The “electropolished” stainless steel plates are slightly rougher after the treatment and their bonding surfaces are cleaner and well-defined than in their original state. Hence the aim of the surface treatment for this work is achieved and the substrates can be bonded.

Bonding

For the bonding of the stainless-steel substrates, jigs have been designed to hold the stainless-steel plates in place. Between the two substrates, PTFE spacers are used to adjust the bond line thickness and PFTE films are used to prevent the substrate from sticking to the jigs (Figure 3-27).

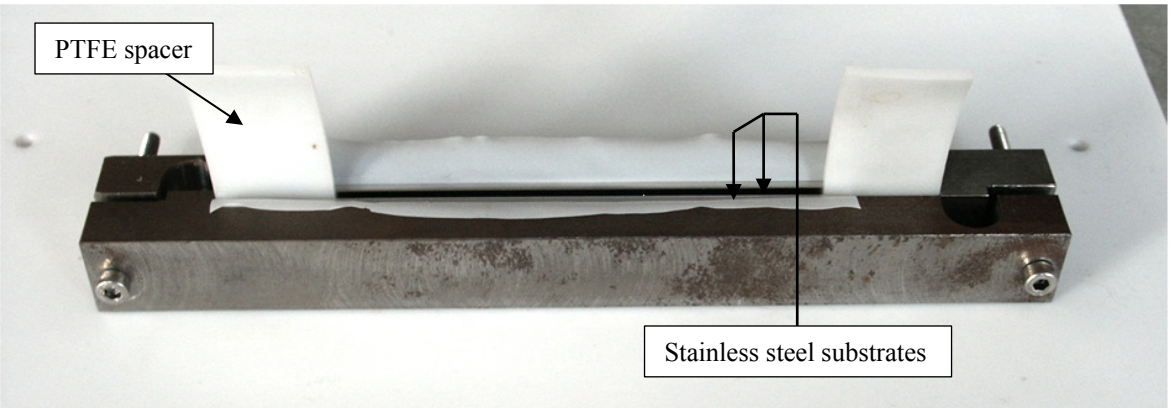

Figure 3-27: Bonding jigs for stainless steel substrates [135]

For these samples, the spacers are also used to seal and to adjust the length of the bonding gap. It is thus necessary to exactly predetermine the size of the spacers to have a bond length of 100 mm. This is achieved by cutting them by means of a hollow punch, designed for this purpose - Figure 3-28.

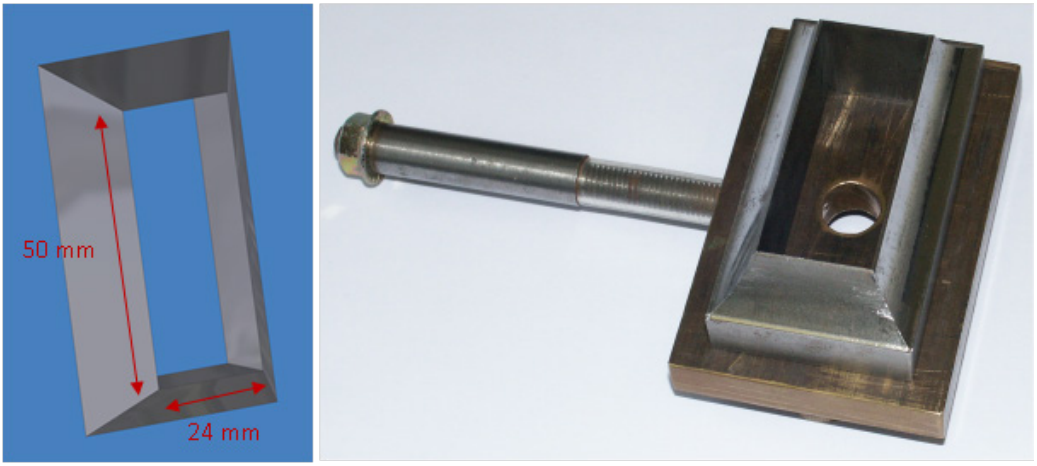

Figure 3-28: Hollow punch for cutting the PTFE spacers [135]

On the bottom side of the assembly, the gap between the bonding surfaces is sealed with adhesive tape. The rest of the bonding process is exactly the same as the one for the PU-AlMg3

samples (see page 77). The resulting samples have an adhesive surface of 100 x 20 mm² as for the PU-AlMg3 samples. As a reminder, the dimensions of the steel plates are: 130 x 20 x 2 mm.

Figure 3-29 depicts a PU-stainless steel specimen ready to be mounted in the testing jig as presented in Figure 3-31.

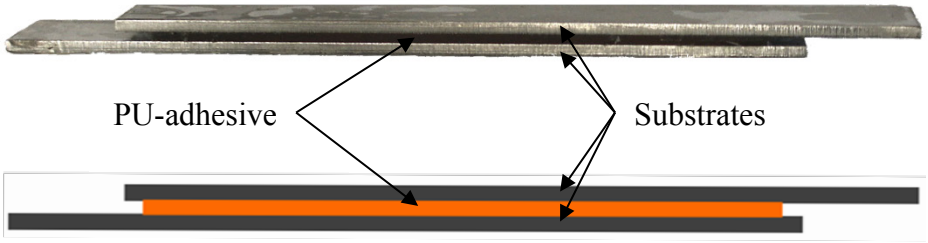

Figure 3-29: PU-stainless steel shear specimen [135]

Mechanical testing

Testing jigs have also been designed and manufactured to be able to test the PU-stainless steel specimens using the same experimental set-ups as for the PU-AlMg3 adhesive joints (Figure 3-30). The stainless-steel plates are mounted in the testing jig only after the bonding operation. The design of the test jig is directly inspired from the specimen geometry of the PU-AlMg3 adhesive joints and can be used in all experimental set-ups described in section 3.3. The adhesive joint is inserted in the slots of the testing jig and is held securely in place by a stop screwed to the rest of the jig as illustrated in Figure 3-31.

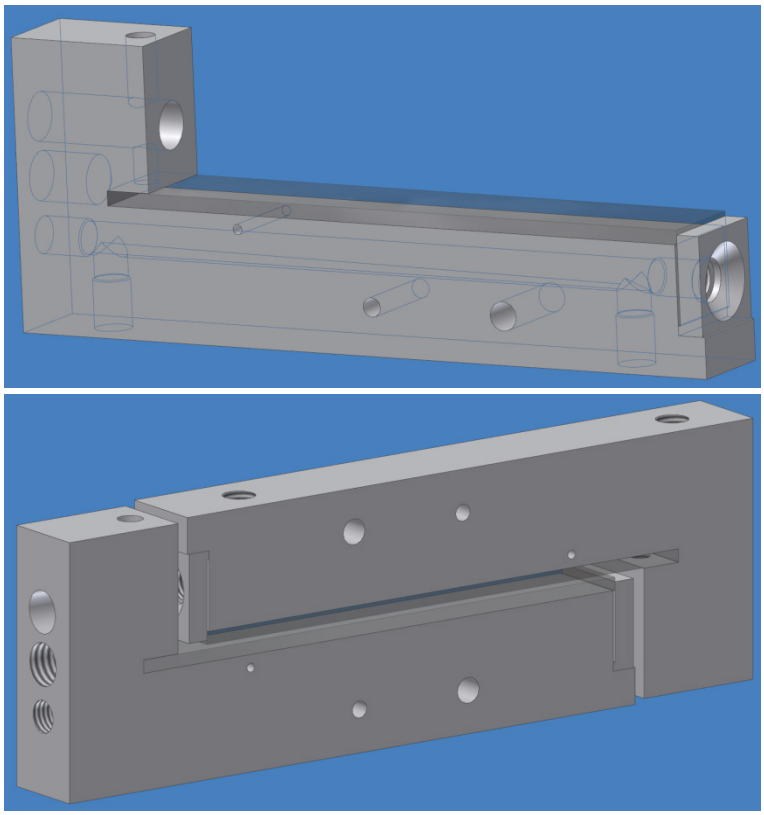

Figure 3-30: Testing jigs for PU-stainless steel adhesive joints

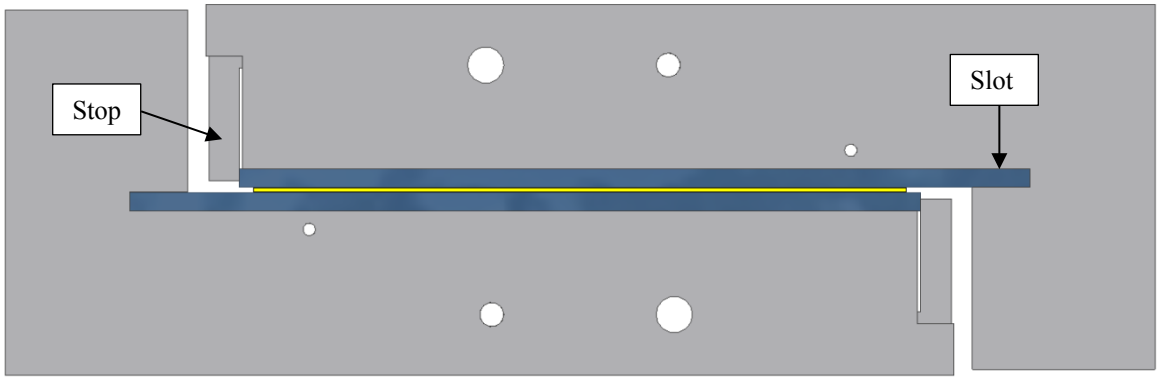

Figure 3-31: Geometry of the PU-stainless steel shear specimen (in dark blue) with the adhesive bond line (in yellow) mounted in a testing jig made of AlMg3 (in grey)

3.2.2.3. Shear stress distribution in polyurethane-metal adhesive joints

In order to minimise the edge effects or any inhomogeneity in the stress and deformation distribution in the adhesive layer during the shear tests, the geometry of the specimens has been designed by means of finite element analysis [1]. These considerations proved that the shear stress along the substrate surface deforms the polymer part without significant deformation of the substrates as well [1, 72]. The selected geometry for the both types of specimen is 100 mm

long and 20 mm wide, resulting in a relatively large bonding surface of 2000 mm² in comparison to the usual standards [151-153].

A crude consideration of the stress distribution in the adhesive layer within the bonded joints is also made using the linear elastic analysis suggested by Volkersen [154]. It is assumed that the adhesive layer deforms only in simple shear while the adherend deforms elastically only in tension. For the case of adherends of equal thickness, the adhesive shear stress distribution $\frac{T_{12}(x)}{T_{12,mean}}$ along the length *l* of the adhesive joint is given by [155]:

$$\frac{T_{12}(x)}{T_{12,mean}} = \frac{\sqrt{2\phi}\cdot\cosh\left(\sqrt{2\phi}\cdot\frac{x}{l}\right)}{2\cdot\sinh\left(\frac{\sqrt{2\phi}}{2}\right)} \tag{3.3}$$

where

$$\phi = \frac{M\cdot l^2}{E\cdot d_s\cdot d_P} \tag{3.4}$$

and M is the adhesive shear modulus, *l* the length of the joint, *E* the substrate Young's modulus, d_s the thickness of the substrate and d_P the adhesive thickness. $T_{12,mean}$ is the averaged applied shear stress to the joint and $T_{12}(x)$ the shear stress at position *x* along the length of the joint ($\frac{-l}{2} \le x \le \frac{l}{2}$).

Figure 3-32 and Figure 3-33 show the calculated shear stress distribution respectively in PU-AlMg3 and PU-stainless steel adhesive joints during a shear test at constant shear rate $d\gamma/dt = 4\cdot10^{-2}\,s^{-1}$ at different temperatures. The x-axis corresponds to the variable position along the length *l* = 100 mm of the adhesive joint. The chosen adhesive thickness, temperatures and shear rate for these calculations correspond to the extreme experimental parameters used in this work. The stiffer the adhesive layer, the worse shear stress distribution in the adhesive joint is expected. That is why the calculations are performed with the fastest shear rate and the lowest temperatures used for the mechanical characterisation of the corresponding adhesive joints in this work. The corresponding experimental values for *M*, obtained by isothermal shear stress at constant shear rate, have been considered.

In all cases, the maximum shear stress occurs at the end of the joints. For a given adhesive thickness, the lower the temperature, the less homogeneous is the shear stress distribution in the adhesive joint. Thin adhesive joints exhibit more heterogeneous shear stress distribution than thicker ones.

For a PU-AlMg3 adhesive joint with d_P = 2000 µm (Figure 3-32, left), the maximal variation in the shear stress distribution is about 0.3 % at 0 °C whereas it reaches about 6 % for a thin adhesive joint at 10 °C (Figure 3-32, right). The Volkersen's analysis shows a quite homogeneous stress distribution in PU-AlMg3 adhesive joints for the experimental parameters.

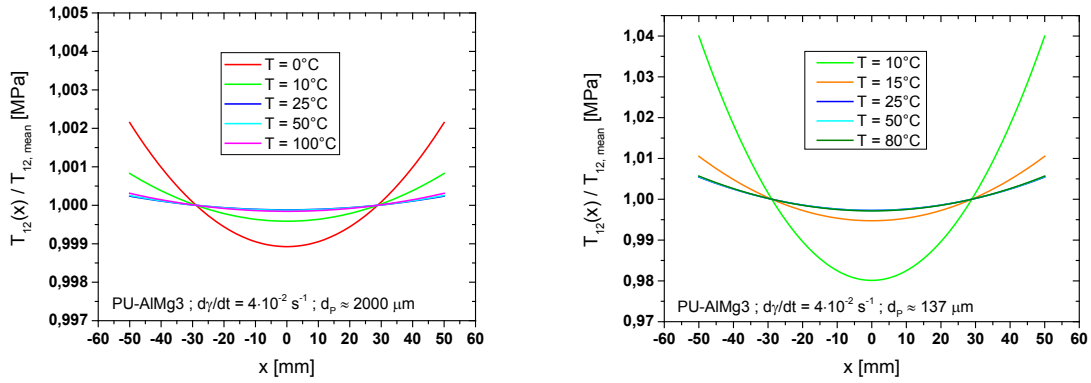

Figure 3-32: Calculation of the shear stress distribution in two different PU-AlMg3 adhesive joints with an adhesive thickness $d_P \approx 2000$ µm (left) and $d_P \approx 137$ µm (right) during a shear test at constant shear rate $d\gamma/dt = 4 \cdot 10^{-2} s^{-1}$ at different temperatures

For comparable values of the adhesive thickness d_P and temperature, PU-stainless steel adhesive joints exhibit a less homogeneous shear stress distribution than PU-AlMg3 joints - Figure 3-33. A maximal shear stress variation of circa 3 % is calculated for a thick PU-stainless steel adhesive joint at 0 °C (Figure 3-33, left). For a thin one, the maximal variation is about 43 % at 10 °C and decreases to circa 12 % at 15 °C. The higher calculated values of the shear stress variation in the PU-stainless steel adhesive joints are due to the smaller thickness of the steel substrates.

To prevent any plastic deformations caused by the inhomogeneity in the stress and deformation distribution in the adhesive joints during their mechanical characterisation, the maximal calculated shear stress magnitude is taken into account to determine the upper limits of shear deformation and stress as discussed in section 3.4.2.5.

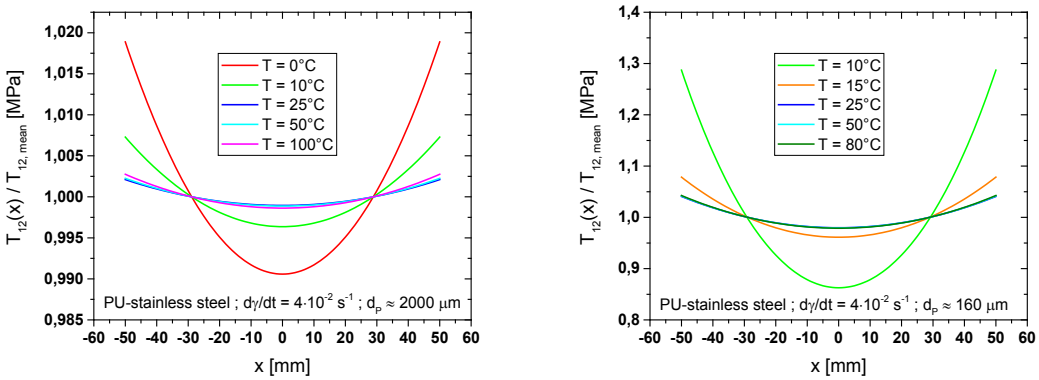

Figure 3-33: Calculation of the shear stress distribution in two different PU-stainless steel adhesive joints with an adhesive thickness $d_P \approx 2000$ µm (left) and $d_P \approx 160$ µm (right) during a shear test at constant shear rate $d\gamma/dt = 4 \cdot 10^{-2} s^{-1}$ at different temperatures.

3.3. Experimental set-ups

The strong influence of temperature on the mechanical behaviour of polymers is mentioned in chapter 2.1. In addition, mechanical testing of polymers, especially in their glass transition region or in their glassy state, requires high sensitivity of force and deformation measurement. These are the requirements for an accurate and reliable characterisation of the mechanical properties of polymers. For these reasons, experimental set-ups have been designed and/or adapted for the investigations presented in this work.

3.3.1. Tensile testing device for bulk samples

The tensile tests presented in this work are performed with a custom-made high precision device consisting in two high-precision linear positioners (x.act LT 150-1 ST, LINOS / Qioptiq), a force sensor (KD24s, ME-Meßsysteme GmbH), a high-resolution CCD camera (XCD-SX910, Sony) and a custom-made temperature control system, positions 1, 2 , 3 and 4 in Figure 3-35, respectively. The sample (see Figure 3-12, page 70) marked with a dark pattern is clamped between the two linear positioners. The central part of the specimen is temperature-controlled in an insulated chamber – Figure 3-36. This chamber is continuously purged with cold nitrogen gas resulting from the evaporation of liquid nitrogen (T = -195.79 °C) while a heating wire heats the chamber atmosphere. The chamber temperature is then controlled by adapting the nitrogen gas flow and the power supply of the heating wire. This system runs automatically using a proportional–integral–derivative controller implemented in LabVIEW® (NI Vision Development Systems®). The temperature sensor measures and controls the temperature of the chamber atmosphere close to the dark pattern on the sample. Isothermal tensile tests with different tempering times show that no difference can be identified in the stress-strain curves (not shown) after 5-7 minutes at the measuring temperature. This result indicates that the thermal equilibrium in the tempered part of the sample is achieved. Considering a safety margin, isothermal tensile tests are performed 15 minutes after reaching the measuring temperature.

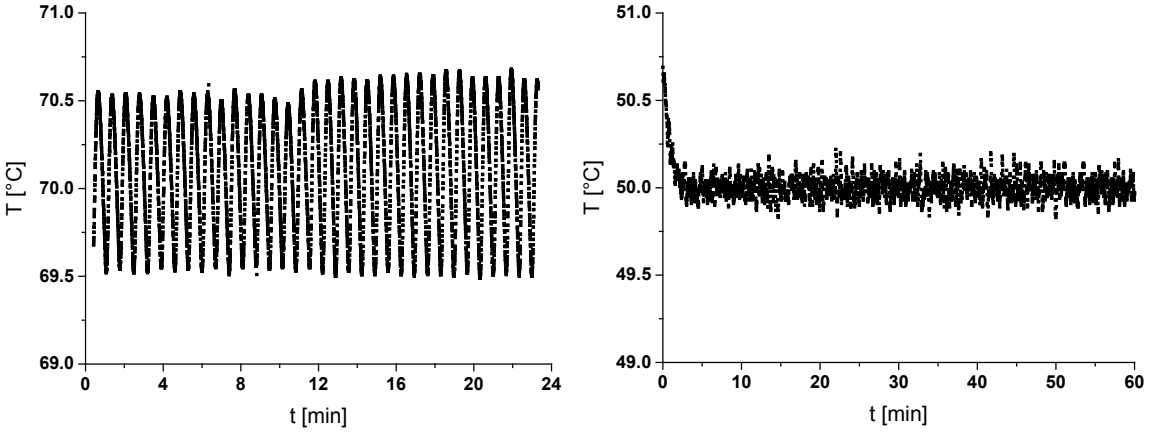

Figure 3-34: Temperature as a function of time in the sample cell of the tensile testing device over time for different set temperatures: 70 °C (left) and 50 °C (right)

The sample cell allows performing isothermal tensile tests in a temperature range from -40 °C to 80 °C with a stability of ± 0.05 K – Figure 3-34.

The CCD camera monitors contact-free and locally the two-dimensional pattern deformation (in e_1 and e_2 directions) in response of the synchronised driving of the two linear positioners – Figure 3-37. During a tensile test, both linear positioners move with the same displacement amplitude and the same constant travel speed. Each positioner has a linear travel range of 150 mm. According to the manufacturer's specifications, the tables have a positioning accuracy of 0.5 µm with a reproducibility of 0.5 µm. The force sensor has a nominal force range of ±20 N with an accuracy < 0.1 %.

The temperature control, the image capture and analysis as well as the control of the linear positioners (position and speed) have been programmed using LabVIEW®. The custom-made temperature control systems used in this work have been designed and built by Mr. Peter Kohl.

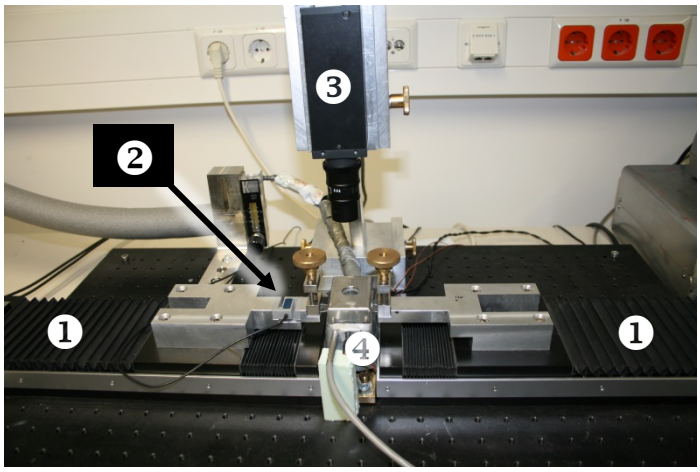

Figure 3-35: Custom-made high precision tensile testing device: ❶ linear table, ❷force sensor, ❸ high-resolution CCD camera and ❹ temperature control system

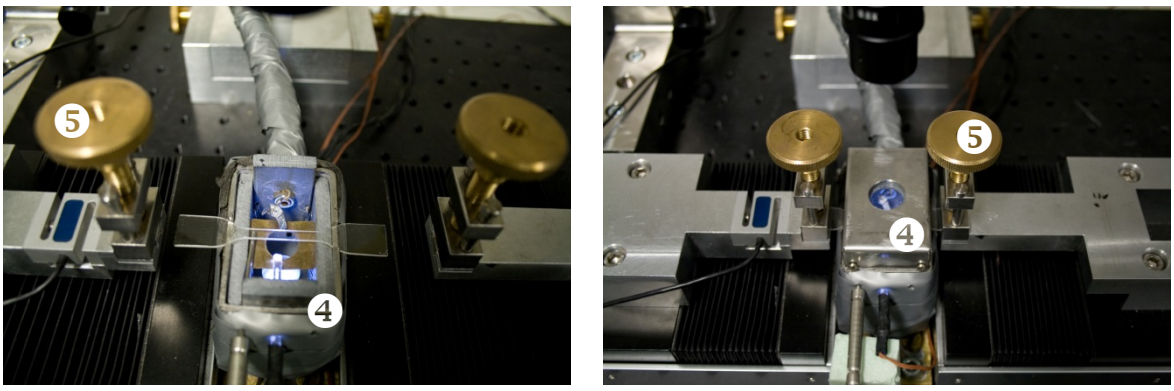

Figure 3-36: Clamping and mounting of a tensile specimen in the testing device: ❹ temperature control system consisting of an insulated chamber with an illumination system of the sample, temperature sensor as well as heating and cooling system; ❺ clamp

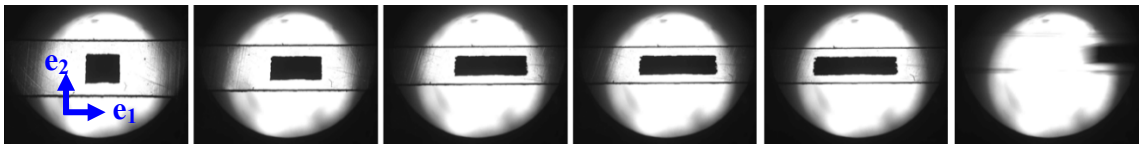

Figure 3-37: Monitoring of the pattern deformation by the CCD camera: from left to right, start of the measurement until fracture of the specimen

3.3.2. **Creep testing machine for adhesive joints**

Isothermal creep tests at constant shear stress have been performed with a custom-made creep testing device consisting of a steel frame, a force sensor (KD9363s ME-Meßsysteme GmbH), an incremental length gauge (MT 1281, HEIDENHAIN GmbH), temperature sensors (Pt 100) and thermostatic devices for heating/cooling of the sample and different sensors – Figure 3-38.

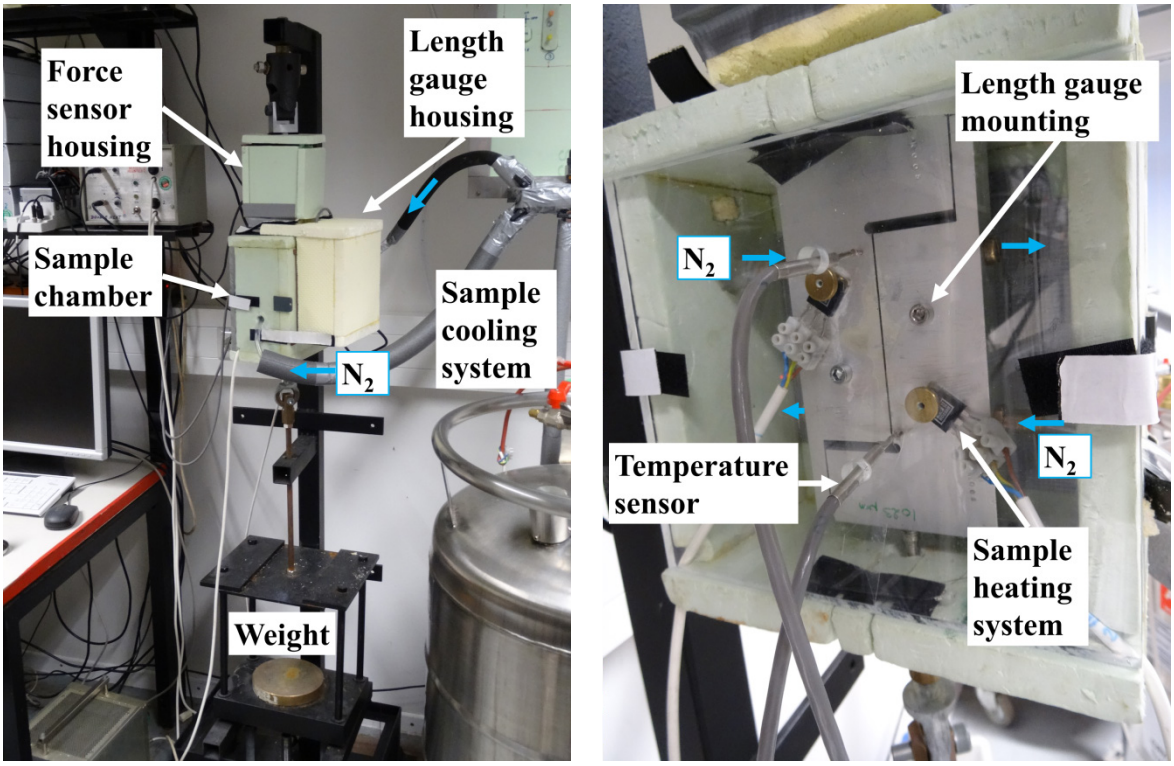

Figure 3-38: Creep testing machine (left) and close up view on the sample chamber (right)

This testing machine has been exclusively designed for creep experiments. Its operating principle is relatively basic: a weight is attached to the sample exerting a constant shear stress (about 178000 Pa; Figure 3-41) due to the gravitational force. A height-adjustable platform is used for the loading and unloading of the sample.

The sample is placed in an insulated chamber and connected to the cooling and heating systems. To control the sample temperature, two thermocouples, placed in each halve near the bonding surface control the heating/cooling system. Cold gaseous nitrogen (evaporated liquid nitrogen) flows continuously with a variable rate (always > 0 l / s) through the cooling channels of the sample while the heating system heats the two halves independently for a better temperature control. Therefore, the measurements are performed in a nitrogen atmosphere. Sample temperatures and thus the heating and cooling powers are permanently controlled by a PID controller implemented in a LabVIEW® program. The heating systems used in this work operate using the heat generated by NPN transistors. The short times of response of the transistors allow controlling the sample temperature accurately. With these self-made devices, the experimental sample temperature range is -100 °C to +100 °C with fluctuations of ± 0.1 K (Figure 3-39 in red and black).

An incremental length gauge is installed on the back of the sample and is thermally isolated from the sample. This sensor measures the displacement between the two substrates and has a measuring range of 12 mm with an accuracy of ± 0.2 µm.

A special feature of creep tests is the long measuring time, especially at low temperatures and high adhesive thickness, d_P – Table 3-5. Therefore, the measuring and control systems must work in a stable way over a long period of time. The values given in Table 3-5 are estimated times on the basis of the experiments and can vary from test to test. A creep test is completed when the shear deformation has reached a plateau.

Table 3-5: Approximate creep test duration at different temperatures for PU-AlMg3 adhesive thickness with $d_P \approx 200$ µm and 2000 µm.

		Measuring temperature [°C]							
		0	5	10	15	20	25	30	35
Creep time (hours)	$d_P \approx 200$ µm	> 97	53	7	4	0.8	0.2	0.1	0.05
	$d_P \approx 2000$ µm	> 525	>280	140	28	6	1.5	0.6	0.1

Observations made during the creep experiments have shown that any temperature variation in the environment of the force and displacement sensors generates signal drifts. An accurate measurement of the shear deformation and force are key factors for the isothermal creep tests performed in this work. Consequently, the length gauge has been housed in an insulated chamber which is equipped with a temperature control device. The temperature of the length gauge is controlled by a PID controller implemented in a LabVIEW® program at 30 °C ± 0.4 K, within its operating temperature range [156]. The electronic interface for the displacement transducer (EIB 741, HEIDENHAIN GmbH) is also influenced by the room temperature variation in the laboratory and has been housed in an insulated chamber as well. Here the heat generated by the electronic components is enough to heat the chamber at 32.5 °C ± 0.5 K without any extra temperature control system. Figure 3-39 illustrates the regulating accuracy and stability of the whole temperature control system for a creep test at 15 °C.

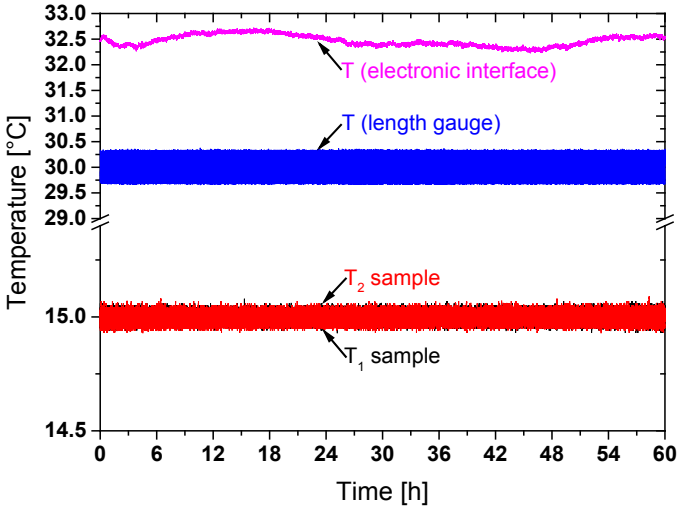

Figure 3-39: Thermal stability of the experimental set-up: sample (red and black), length gauge (blue) and electronic interface (magenta) temperatures as a function of time during a creep test at 15 °C

To reduce the heat transfer between the thermostated specimen and the structure of the machine as well as the length gauge, ceramic insulators are used as depicted in Figure 3-40. These insulators have a high stiffness and therefore do not affect the mechanical characterisation of the adhesive joint.

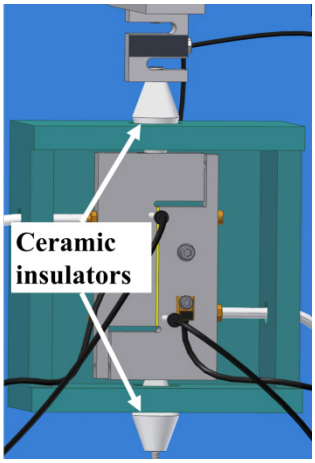

Figure 3-40: Schematic representation of the sample chamber with the ceramic insulators

During creep tests, the force sensor does not play such a significant role as the length gauge because the shear stress results from the gravitational force and thus remains constant. Nevertheless, the force sensor is housed in an insulated box and is used to check in real time the applied load to the sample. Thanks to that, if the weight guiding system gets stuck or something disturbs the load of the sample, it can be directly detected, and a new test can be started. The force sensor has a nominal force range of ±10 kN with an accuracy < 0.1 %.

Before starting a creep experiment, it is necessary to wait until all devices have reached their operating temperatures to ensure accurate measurements: 15 minutes after reaching the set temperatures guarantee thermal equilibrium in the devices and thus the stability of the whole system. Moreover, the sample has to be relaxed before each creep test to release the potential residual stresses in the samples that are arisen from preparation or from previous mechanical tests (cf. section 3.4). In addition, after the installation of the sample in the creep testing machine, it is recommended to load and unload 5 times consecutively at the relaxation temperature to be sure that all devices are firmly in place. Experience shows that more accurate and reproducible results can thereby be obtained [157, 158].

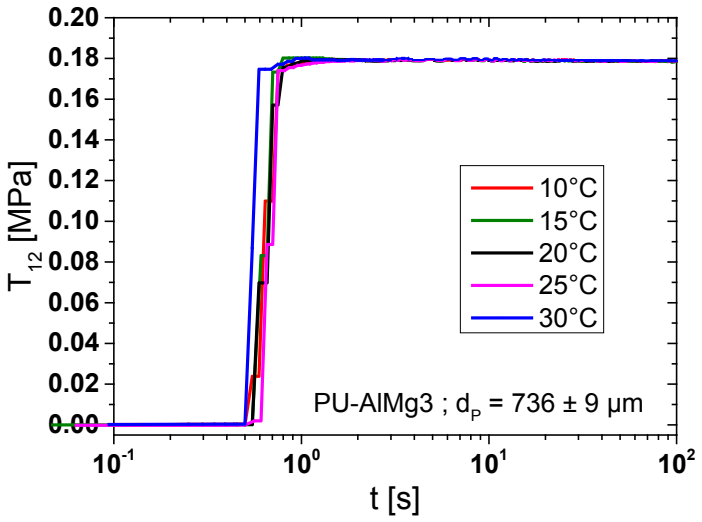

Figure 3-41: Creep tests: loading of a sample at different temperatures; shear stress T_{12} as a function of time

Figure 3-41 shows that the constant shear stress T_{12}, required for a creep test, is not instantly applied to the sample: from few tens of a second to few seconds are necessary to reach the constant stress. This delay has been considered for the subsequent calculations using the results from creep experiments (see section 2.4).
Nevertheless, the loading stage of the sample and the constant stress load are reproducible. The experimental data confirm that the loading stage can be approximated by a linear function.

3.3.3. **Universal testing machine**

A universal testing machine Kappa 20DS [159], manufactured by Messphysik Materials Testing GmbH, is used to perform shear tests, stress relaxation tests and creep tests on polyurethane-metal adhesive joints.
As shown in Figure 3-42, the testing machine is equipped with:

- a load frame with double lead-screw drive and precision guidance provided via 4 steel columns (accuracy of travel measurement is ±7.1 nm and position accuracy < 2 µm) [160]
- a large crosshead travel of about 1000 mm (without sample fixation system)
- constant moving crosshead speed accuracy of ± 0.1 % of specified speed in a measurement range from 1 µm / h to $6 \cdot 10^6$ µm / h
- load cell with a nominal force range of ±20 kN with a maximum display deviation of 1 % of the measured value
- a set of compression plates
- an optical deformation measurement system (video extensometer VideoXtens®): a video camera detects the light-to-dark transitions applied on the specimen surface and tracks these during deformation.

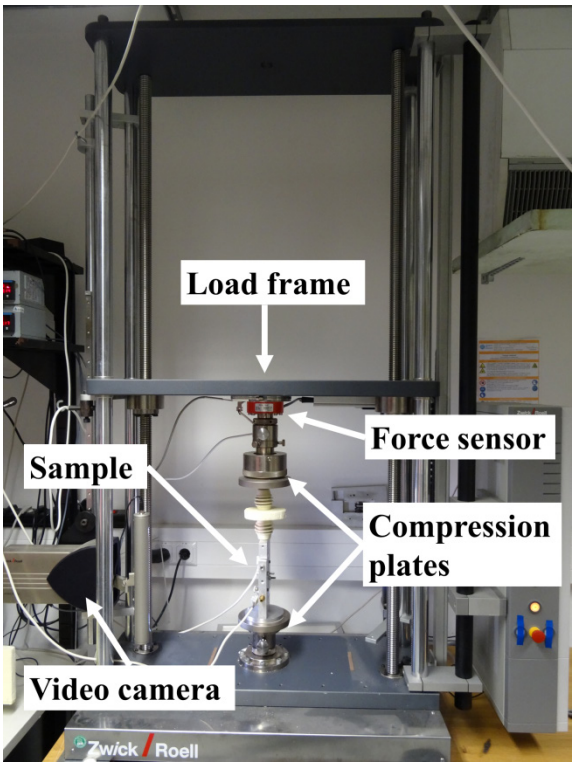

Figure 3-42: Setup of the universal testing machine Kappa 20DS

The machine can operate from 10 °C to 35 °C but temperature variations higher than 1 K should be avoided during the test to exclude the influence of the thermal expansion of the load frame [160]. Therefore, the room in which the testing machines are located has been equipped with an air conditioning and heating system to attenuate variations in the room temperature. Figure 3-43 depicts the evolution of the room temperature over 87 hours with maximal fluctuations smaller than ± 0.5 K.

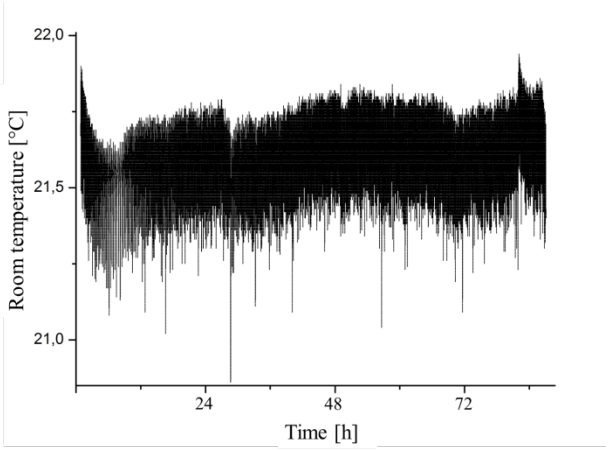

Figure 3-43: Room temperature control over 87 hours

Stress relaxation tests require a good stability of the force signal. For this reason, the load cell has been housed in an insulated box which is actively heated at 30 °C ± 0.4 K – Figure 3-44. The heating system is based on the same principle as for the gauge length temperature control described in section 3.3.2. Since the load cell is directly attached to the load frame, this latter is also heated slightly above room temperature. However, as a result of the relatively high thermal inertia of the system, it takes longer to heat up to the set temperature.

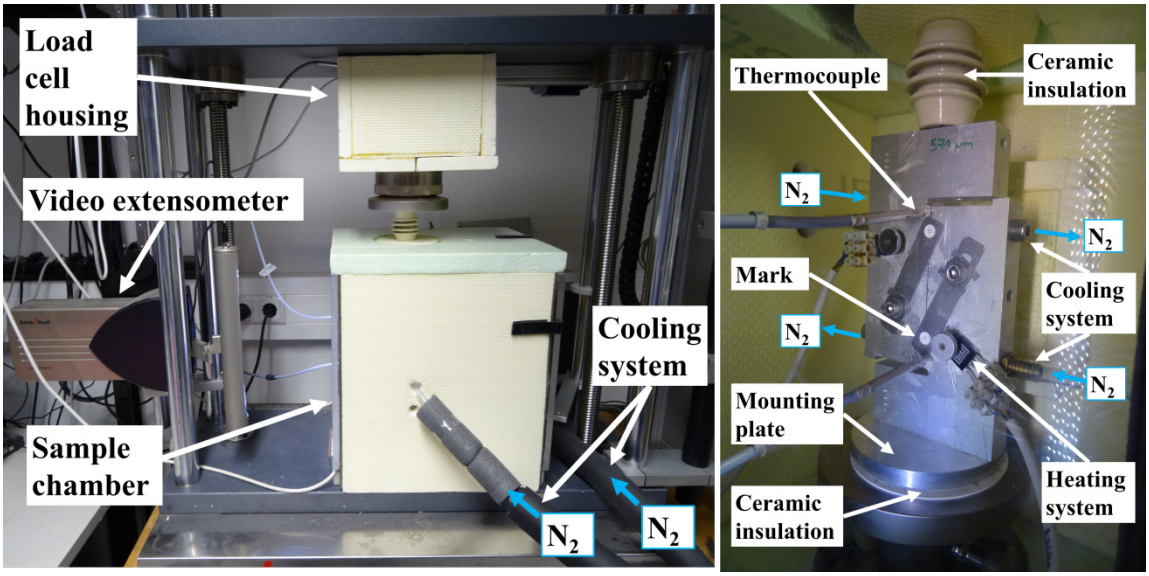

Figure 3-44: Upgrading of the universal testing machine for isothermal mechanical tests

As for the creep testing machine, the sample is housed in a self-made Styrofoam box with a Plexiglas window. The sample box is continuously flowed with gaseous nitrogen issued from the cooling system. A similar temperature control system, implemented in LabVIEW®, is used for the tempering of the specimen. Hence the temperature range and accuracy are comparable to those of the creep testing machine presented in section 3.3.2.

To avoid the heat transfer between the thermostated sample and the structure of the machine, ceramic parts are used. These insulators have a high stiffness and therefore do not influence the mechanical characterisation of the adhesive joint – Figure 3-44, right.

A video camera monitors the displacement of marks applied on the sample: Metal plates marked with a black and white pattern are attached to each substrate in a line so that the displacement of the substrates during the mechanical test corresponds to the one of the marks. The video camera, used as an extensometer, detects the light-to-dark transitions on the marks and tracks these during deformation. For a better measuring accuracy, it is important that the marks are always in the same focal plane which has been used for the calibration of the camera. Therefore, the position of the sample on the lower compression plate is marked during the calibration. The position of the sample on the compression plate is thus determined and always the same for all the tests. The video extensometer provides non-contact, high-resolution measurement of deformations in real time and is also suitable for recording transverse strain. The video camera has a theoretical resolution of 270 nm [161].

Further benefits of the video extensometer in comparison to length gauges are:

- more precise results because they do not influence the test specimen
- more consistent results regardless of operator due to more reproducible positioning of the sample
- wide application range because it can be used with environmental chambers over a broad temperature range without need to temper the extensometer
- large measuring range up to sample failure.

Once all the devices and the sample are mounted, tempered and calibrated, the universal testing machine can be used to perform:

- shear test at constant shear rate
- stress relaxation experiment at constant shear deformation
- creep experiment at constant shear stress (in this work, only to verify and validate the data obtained with the creep testing machine presented in the section 3.3.2).

Shear test at constant shear rate

A constant effective shear rate $\dot{\gamma}_{eff}$ is achieved by controlling the velocity of displacement of the substrates $\dot{u}$, given by the marks, with the video extensometer. The relation between those rates is given by:

$$\dot{u} = \dot{\gamma}_{eff} \cdot d_P \tag{3.5}$$

where d_P is the adhesive thickness.

After each measurement, the effective shear rate is verified as illustrated in Figure 3-45. At the beginning of the test, the video extensometer needs a few seconds to control the deformation rate. Hence the effective shear rate is not constant in this short period of time. Only the data measured with a constant shear rate are analysed.

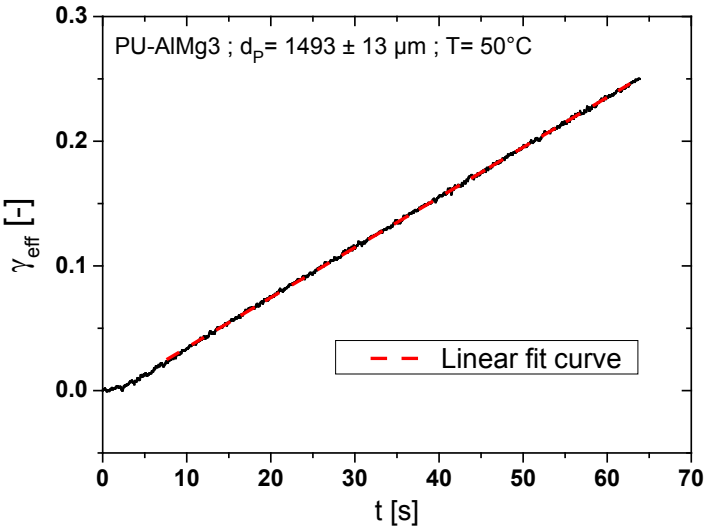

Figure 3-45: Verification of the effective shear rate $\dot{\gamma}_{eff}$

In this example, there is a satisfactory discrepancy of less than 1 % between the nominal effective shear rate ($4 \cdot 10^{-3}$ s^{-1}) and the measured one ($4.01 \cdot 10^{-3}$ s^{-1}). If the experimental effective shear rate deviates from the nominal one by a few per cent, the experiment must be repeated.

Stress relaxation test at constant shear deformation

As for a shear test at constant shear rate, the video extensometer controls the constant sample strain u during the stress relaxation test. The sample displacement in the strained state $u(t)$, measured through the displacement of the marks on the specimen, is proportional to the effective shear strain $\gamma_{eff}(t)$ of the adhesive layer:

$$\gamma_{eff}(t) = \frac{u(t)}{d_P} \tag{3.6}$$

At the beginning of the test, the sample is deformed until reaching a constant effective shear deformation of about 0.1 which is small enough to avoid any plastic strain of the sample (and to stay in the linear viscoelastic region of the adhesive – see chapter 3.4).

Figure 3-46 depicts the evolution of the effective shear deformation during a stress relaxation test at 15 °C. In this temperature region, the adhesive is strongly viscoelastic, and any variation of the deformation affects significantly the resulting stress response. Hence a maximal force of 1300 N is chosen as abort criterion for the relaxation tests to avoid any damage of the sample.

The response time of the strain control system results in overshooting the set value for the effective shear strain as shown in Figure 3-46. This additional loading and unloading phase of the sample influences directly the adhesive dynamics and so, they must be considered for the evaluation of the results. Shear strain stays constant after $t_0 \approx 30$ s in this test.

If the threshold of 1300 N is reached during the loading of the sample or if the overshoot of the strain plateau is too high, the experiment must be repeated with a reduced strain rate to reach the deformation plateau. However, this leads to a significant increase in the duration of the loading stage, t_0, resulting in a loss of information for the calculation of relaxation time spectra for instance. Therefore, a compromise between the amount of data (ideally, t_0 tends to 0) and their accuracy (ideally, without overshooting in γ_{eff}) must be found, limiting the information of stress relaxation tests.

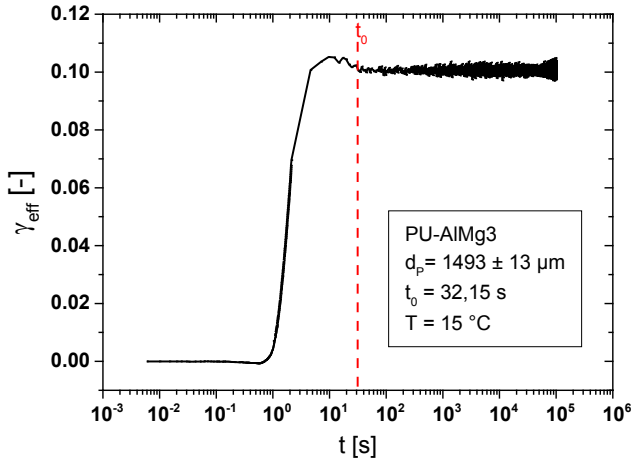

Figure 3-46: Stress relaxation test at constant shear deformation – evolution of the effective shear deformation

Creep test at constant shear stress

For the creep tests, the force sensor controls the positioning of the load frame, i. e. the strain of the sample, to have a constant effective shear stress in the adhesive joint. The set value for the constant shear force is 350 N corresponding to a shear stress of 0.175 MPa, which is comparable to those used in the creep testing machine described in the section 3.3.2.

Similarly to stress relaxation tests, a compromise between a short loading stage and a minimal force overshooting has to be made.

Figure 3-47 illustrates the evolution of the shear stress T_{12} during the loading stage of the sample. The time to reach the plateau, $t_0 \approx 3$ s, is shorter than for the relaxation tests (Figure 3-46) but longer than with the creep testing machine (Figure 3-41). An overshooting of the plateau value during the loading stage cannot be avoided completely and should therefore be considered for the analysis of the results.

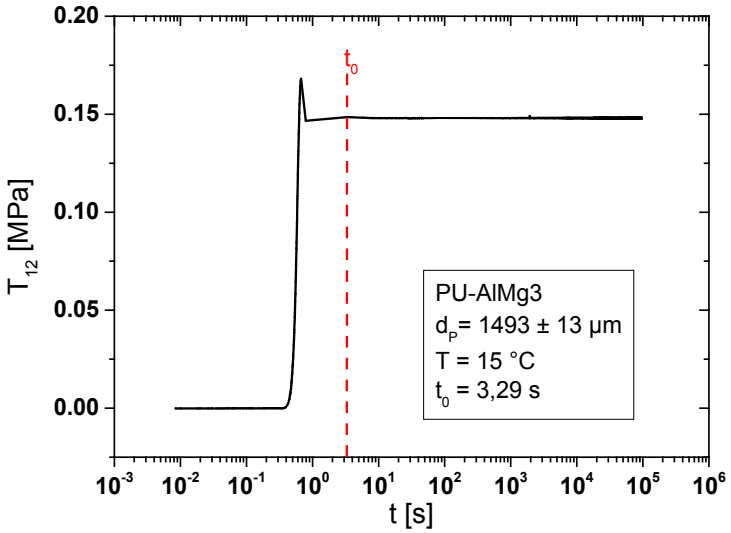

Figure 3-47: Creep test at constant shear stress – evolution of the shear stress T_{12}

In view of the limitations encountered by performing stress relaxation and creep tests, the results, obtained with the universal testing machine, were almost only used for the determination of the relaxed properties ($G_{eff,\infty}$ and $J_{eff,\infty}$). The latter do actually not dependent on the load conditions in contrast to the evolution of T_{12} and γ_{eff} as well as the corresponding relaxation/retardation time spectra.

3.4. Preliminary tests

To characterise the properties of adhesive joints, experiments require well-defined, accurate and reproducible conditions. Tests are performed to detect the possible effects which could disturb or corrupt the analysis of the results.

3.4.1. **Stability of the polyurethane adhesive**

3.4.1.1. Thermal stability of the polyurethane adhesive

The characterisation of the thermomechanical behaviour of the adhesive requires measurements at different temperatures. It is thus necessary to determine the thermal stability of the polyurethane. For this purpose, thermogravimetric analysis (TGA) is performed. TGA or thermogravimetry (TG) is the technique of thermal analysis which monitors continuously the mass[10] of a substance as a function of temperature (or time) as the substance is exposed to a controlled temperature program in a specified atmosphere [163]. Not all thermal events cause a change in the mass of the sample (for example melting, crystallisation or glass transition), but there are some very important physical and chemical phenomena which include desorption, absorption, sublimation, vaporisation, oxidation, reduction and decomposition.

The basic instrumental requirements for thermogravimetric analysis are a precision balance and a furnace which is programmed for a controlled evolution of the temperature with time.

Since the TG investigations are carried out under a gas atmosphere, the sample mass measured by the precision balance, $m_{balance}$, is also subject to buoyancy, i.e.

$$\begin{aligned} m_{balance} \cdot g &= m_{sample} \cdot g - \rho_{gas} \cdot V_{sample} \cdot g \\ m_{balance} &= m_{sample} - \rho_{gas} \cdot V_{sample} \end{aligned} \tag{3.7}$$

Provided that the thermobalance is sensitive enough, the TG measurement $m_{balance}$ thus reacts not only to the change of m_{sample} (due to the above mentioned effects) but also to the change of the sample volume V_{sample} due to thermal expansion and all changes of state where ρ_{sample} changes, such as melting, crystallisation and glass transition.

In this work, TGA is used to evaluate the thermo-oxidative stability of the cured bulk adhesive. The measurements are carried out with the TGA Q5000 IR from TA Instruments (New Castle, DE, USA) in a temperature range of 35–200 °C at a heating rate of 10 K/min under dried air. The result is shown in Figure 3-48. The polyurethane bulk adhesive exhibits a ther-

[10] The International Union of Pure and Applied Chemistry (IUPAC) and the International Confederation of Thermal Analysis and Calorimetry (ICTAC) have determined that the property measured by TGA should be referred to as “mass” and not as “weight.” [162]

mal stability up to about 225 °C (ca. 500 K). In this temperature region, $m_{balance}$ does not remain constant, but small mass changes occurs because $V_{sample}(T)$ grows and, in the opposite direction, $\rho_{gas}(t)$ decreases. Whether, $\rho_{gas} \cdot V_{sample}$ grows or decreases with T depends of course on which factor dominates.

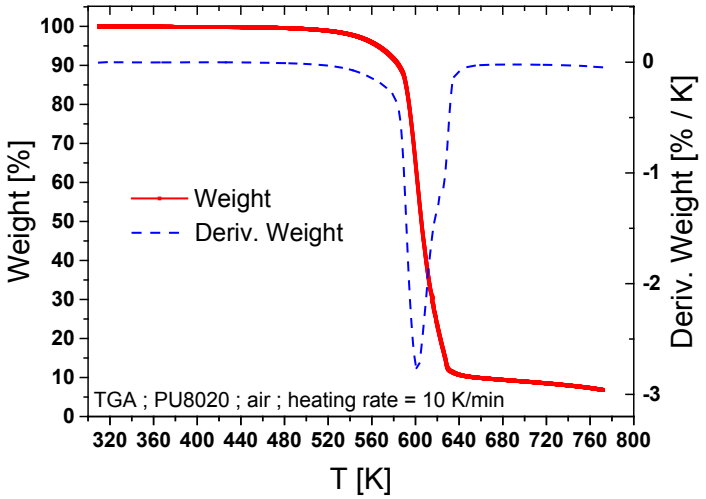

Figure 3-48: Thermo-oxidative stability of PU8020 measured with thermogravimetric analysis (TGA) during heating with 10 K/min in dried air atmosphere: weight loss (in red) and its first derivative (in blue).

3.4.1.2. Stability of the polyurethane bulk properties over time

To determine the adhesive properties, it is essential that they do not change during or between the experiments, as some mechanical tests take several days to be performed. Physical properties of polyurethane can be affected by moisture absorption [164]. To avoid it, all measurements presented in this work are performed in a nitrogen atmosphere. In addition, when the samples are not being tested, they are stored in a glove box, purged with dried air.

Differential scanning calorimetry measurements are performed to ensure the stability of the caloric properties of the adhesive over the time. The basic principles of this investigation method can be found in chapter 5.3. Figure 3-49 shows that the glass transition temperature T_g and the upper half width of the glass transition ($\Delta T = T_{g,e} - T_g$) remain unchanged within the experimental deviation (± 1 K) over 138 days. Data derived from DSC 1st heating runs of 3 samples with T_{start} = -50 °C, $\dot{T}$ = +10 K/min, T_{start} = 120 °C; same samples at each storage time.

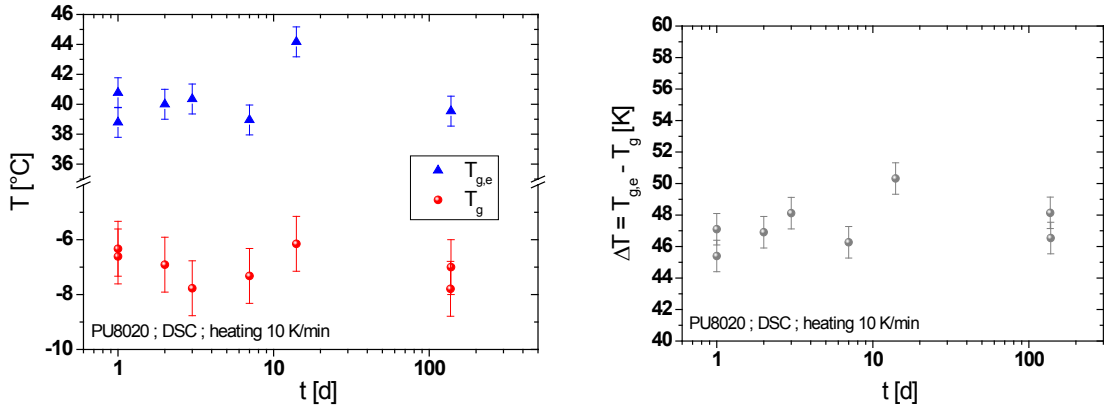

Figure 3-49: Stability of the caloric glass transition of the polyurethane bulk adhesive over storage time: T_g glass transition temperature (left, in red) and $T_{g,e}$ temperature of the end of the glass transition (left, in blue) and the upper half width of the glass transition ΔT (right, in grey).

In the same way, the stability of the mechanical properties of the bulk adhesive is checked by isothermal tensile tests. No modification of the shear modulus of the polyurethane adhesive μ_{bulk} could be identified within 492 days after its preparation – see Figure 3-50.

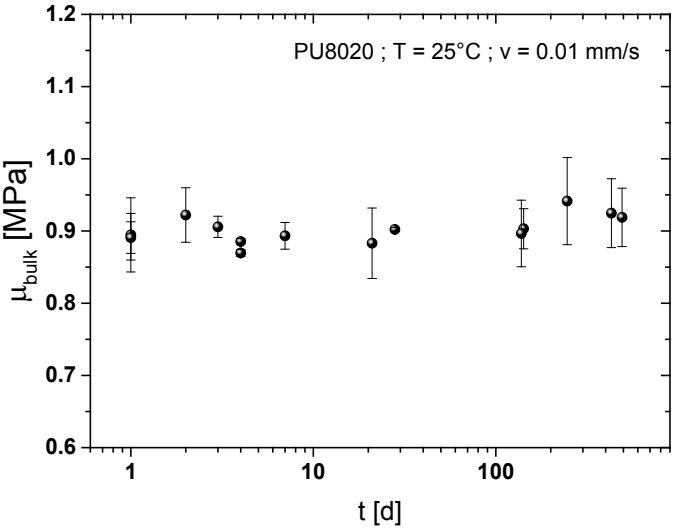

Figure 3-50: Stability over 492 days of the shear modulus of the polyurethane adhesive μ_{bulk} measured by tensile tests at 25 °C with a crosshead speed of 0.01 mm/s.

Under the experimental conditions used in this work, no modification of the physical properties of the bulk adhesive was detected during the whole testing period. Consequently, variations in the mechanical properties of the adhesive joints do not result from ageing effects of the adhesive bulk but reveal a change in the intrinsic properties of the adhesive layer caused by the influence of the substrate.

3.4.2. **Verifications for the mechanical testing**

Prior to detection of possible interphases in adhesive joints, some preliminary tests are necessary to ensure the accuracy and reliability of the mechanical measurements. Adhesive joints are tested several times by means of two different set-ups at different temperatures.

3.4.2.1. Verification of the displacement measuring devices

Preliminary experiments have shown that the signal from the original linear variable displacement transducer (LVDT) was not stable and accurate enough to measure the thermomechanical properties of polymers despite of the controlled measurement conditions discussed in the previous chapter [158, 165]. To ensure the consistency of the results between the set-ups, the performance of the both length gauges, which are used in this work, is checked: the displacement of the two halves of a PU-AlMg3 adhesive joint (d_P = 993 µm) is measured simultaneously with the incremental length gauge of the creep testing machine and the video extensometer of the universal testing machine. The sample is mounted in the universal testing machine and tested with a constant crosshead speed of 40 µm / min at 25 °C. The results are shown in Figure 3-51.

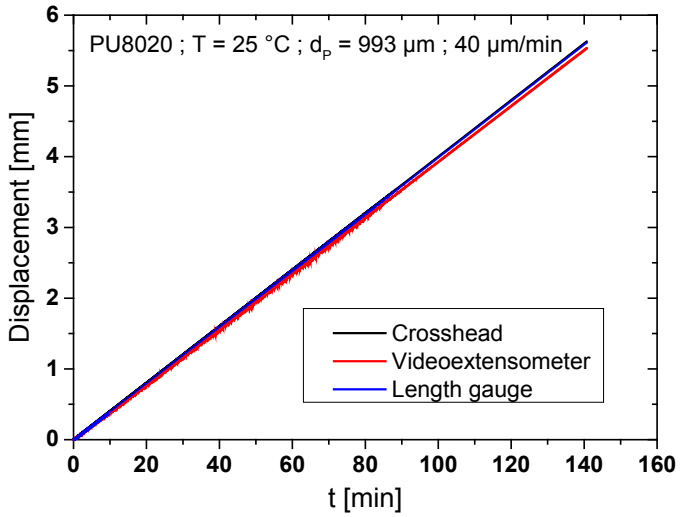

Figure 3-51: Verification of the performance of the different length gauges (blue curve nearly overlaps the blue one)

The video extensometer measures a travel speed of 39.44 µm/min whereas the incremental length gauge 40.03 µm/min. This represents deviations of 1.4 % and 0.76 %, respectively, which are within the experimental tolerance limit.

3.4.2.2. Sample conditioning

In this work, the same adhesive joint must be mechanically characterised many times in different experimental set-ups at different temperatures. Because of the viscoelastic nature of the polyurethane adhesive, mechanical stresses and strains resulting from the mechanical test may take a while to relax, depending on the previous measuring temperature and deformation rate. However, a well-defined initial state of the sample is necessary for comparing the results. To reset the mechanical history of the adhesive joint between two experiments, the samples are heated up to the entropy elastic state where the relaxation processes take place very fast. The conditioning time necessary to reach the initial mechanical state is investigated as shown in Figure 3-52. Shear tests are carried out at a measuring temperature of 15 °C. The sample is then viscoelastic and the induced stresses are not relaxed right after the experiment. Directly after this first test, a further shear test is carried out at 15 °C without any waiting time. The resulting shear modulus seems to be 0.05 MPa higher than the initial one. Of course, this is an artefact caused by the residual stresses from the initial measurement. Subsequently, the sample is heated to 50 °C and after different conditioning times (0; 5; 10; 15 or 20 min), the sample is cooled down to 15 °C with $\dot{T} \approx -0.5\ \mathrm{K \cdot min^{-1}}$ and shear tests are carried out again.

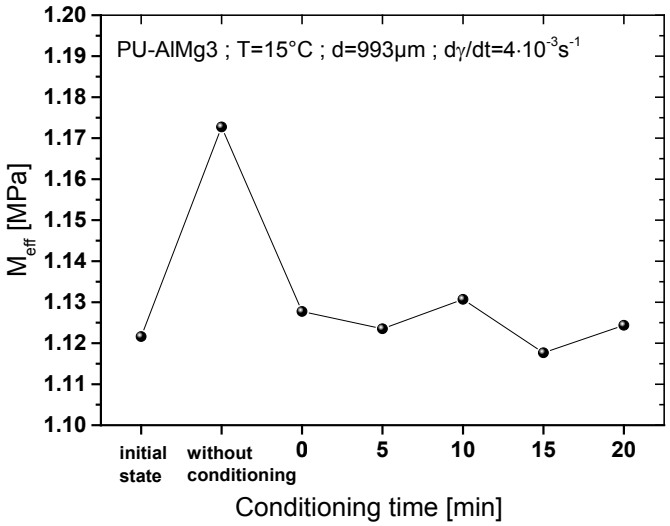

Figure 3-52: Influence of the conditioning time after the 1st test on the effective dynamic shear modulus M_{eff} for a PU-AlMg3 adhesive joint with d_P = 993 µm

Figure 3-52 illustrates that right after reaching 50 °C, the shear modulus is not influenced by the residual stresses in the sample anymore. In this work, samples are heated to 50 °C between each mechanical test (tensile, shear, creep and stress relaxation test) for 15 min in order to ensure that the internal stresses caused by the prior investigation are completely removed. As a consequence of these results, the samples are also conditioned after their preparation to relieve the internal stresses – at least partially – resulting from the adhesive crosslinking.

3.4.2.3. Influence of the mounting of the sample

Considering the relatively complex mounting of the sample in the experimental set-ups, shear tests at constant shear rate are performed with the same sample for repeated mounting. The orientation or arrangement of the different parts could namely influence the measurements. Figure 3-53 illustrates that carefully reproduced sample mounting causes a maximal error of 0.7 % in the determination of the shear modulus.

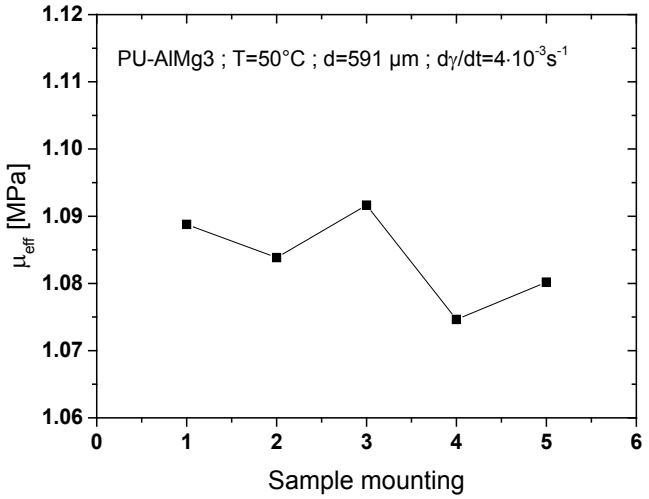

Figure 3-53: Effective hyperelastic **s**hear modulus μ_{eff} of a PU-ALMg3 adhesive joint with d_P = 591 µm at 50 °C and a shear rate of $4 \cdot 10^{-3}$ s^{-1} for five sample mountings

For a given mounting of the sample, the reproducibility of the shear modulus has also a deviation of about 0.7 % as shown in Figure 3-54. Therefore, the mounting of the sample in the experimental set-ups does not influence the measurement and a good reproducibility of the results is provided.

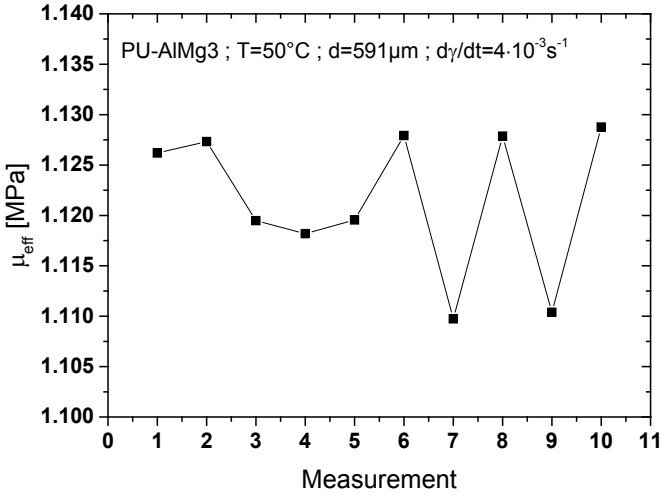

Figure 3-54: Reproducibility of the effective shear modulus measurements for a given sample mounting

3.4.2.4. Influence of the tempering rate during mechanical tests

By cooling the sample to perform measurements at low temperature, relaxation processes slow down. As a result, non-equilibrium molecular dynamics in the adhesive are created and can corrupt the characterisation of the mechanical behaviour of the bonded joint.

To determine the influence of the cooling rate on the mechanical tests, shear tests are performed after treating the sample with different cooling rates. The cooling rate range of the experimental set-ups is relatively narrow because of the considerable dimensions of the specimens. Moreover, the temperature control system is designed to keep the sample temperature constant over a long period of time. The slowest cooling rate is about 0.4 K/min whereas the fastest is about 0.8 K/min. Figure 3-55 proves that the cooling rate in this range does not influence the mechanical response of the sample.

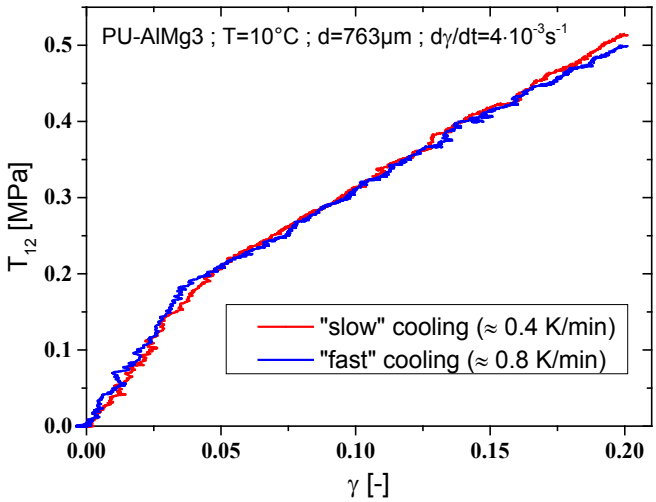

Figure 3-55: Shear tests for a PU-AlMg3 adhesive joint with d_P = 763 µm at 10 °C with a shear rate of $4 \cdot 10^{-3}$ s^{-1} after cooling the sample with different rates from 50 °C.

3.4.2.5. Boltzmann superposition principle – Verification

Most of the equations given in chapter 2, including the constitutive laws generated by the mechanical models, are only applicable for the linear viscoelastic region of the adhesive. That is why it is essential to verify experimentally if the adhesive behaves linear viscoelastic in the measuring ranges of strain, stress and temperature.

Figure 3-56 depicts the tests performed to verify the applicability of the Boltzmann superposition principle. For a given temperature, a constant load $T_{12}^{\,1}$ is applied to the adhesive joint and the resulting shear strain $\gamma_1(t)$ is measured. This experiment is repeated after the conditioning of the sample with a different shear stress $T_{12}^{\,2} = 2 \cdot T_{12}^{\,1}$ which is twice as high as $T_{12}^{\,1}$. According to the equation (2.1), the resulting relaxed shear strain should be equal to $\gamma_2(t) = 2 \cdot \gamma_1(t)$.

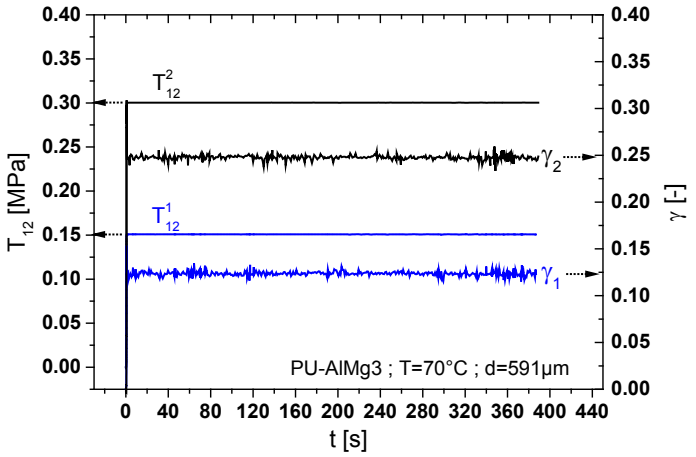

Figure 3-56: Verification of the Boltzmann superposition principle with stress relaxation experiments at 70 °C for a PU-AlMg3 adhesive joint with d_P = 591 µm

Figure 3-56 shows the results obtained for a PU-AlMg3 adhesive joint with d_P = 591 µm at 70 °C. The shear stress is set at T_{12}^{1} = 0.15 MPa. The resulting shear strain at equilibrium is γ_1 = 0.1237. After doubling the shear stress to T_{12}^{2} = 0.3 MPa, the measured shear strain is γ_2 = 0.2471. This corresponds to a deviation of 0.13 % with the theoretically expected result. As this deviation could be an indication that $T_{12}^{2}(\gamma_2)$ is already slightly above the limit of the linear response, the maximal value for the shear stress has been therefore chosen considering the maximal load of the sample during the creep experiments ($T_{12} \approx 0.175$ MPa).

The mechanical behaviour of the polyurethane adhesive strongly depends on the temperature and it is also necessary to verify that the Boltzmann superposition principle applies for the whole measuring temperature range. The same experiments as above are performed at different temperatures. The results are presented in Table 3-6.

Table 3-6: Verification of the Boltzmann superposition principle at different temperatures

Temperature [°C]	T_{12}^{1} [MPa]	T_{12}^{2} [MPa]	γ_1 [-]	γ_2 [-]	Deviation [%]
10	0.149	0.301	0.153	0.316	+ 1.78
30	0.15	0.3	0.151	0.298	- 1.5
50	0.15	0.3	0.131	0.268	+ 2.37
70	0.15	0.3	0.123	0.247	+ 0.13

Considering the small deviation of the experimental values, the results in Table 3-6 indicate that the Boltzmann superposition principle applies to all temperatures for shear strain $\gamma < 0.3$. With the chosen parameters, the polyurethane adhesive behaves linear viscoelastic and the relations presented in chapter 2 can be used. Furthermore, the results show that the shear strain increases with decreasing temperature for a given constant shear stress. This effect is discussed in more detail in the next chapters.

3.4.3. **Mechanical characterisation of the PU bulk adhesive**

The mechanical properties of the thick polyurethane bulk samples are not expected to be influenced by a (mechanical) interphase. Hence, the mechanical behaviour of the adhesive bulk can serve as a reference for the identification of the interphase in adhesive joints and provides data for prospective numerical simulations [47, 72]. Moreover, because of the quite complex preparation of the adhesive joints, bulk samples have been used to determine the appropriate polyol mixture ratio. In this work, the mechanical behaviour of the adhesive bulk is characterised by tensile tests with constant extension rate using the experimental set-up described in section 3.3.1. As the apparatus could only measure with constant travel speed, v [mm / s], the strain rate, $d\varepsilon/dt$ [s^{-1}], can vary from test to test and, of course, with the temperature. However, the corresponding deformation rate is subsequently calculated and only the measurements performed with a constant extension rate are considered.

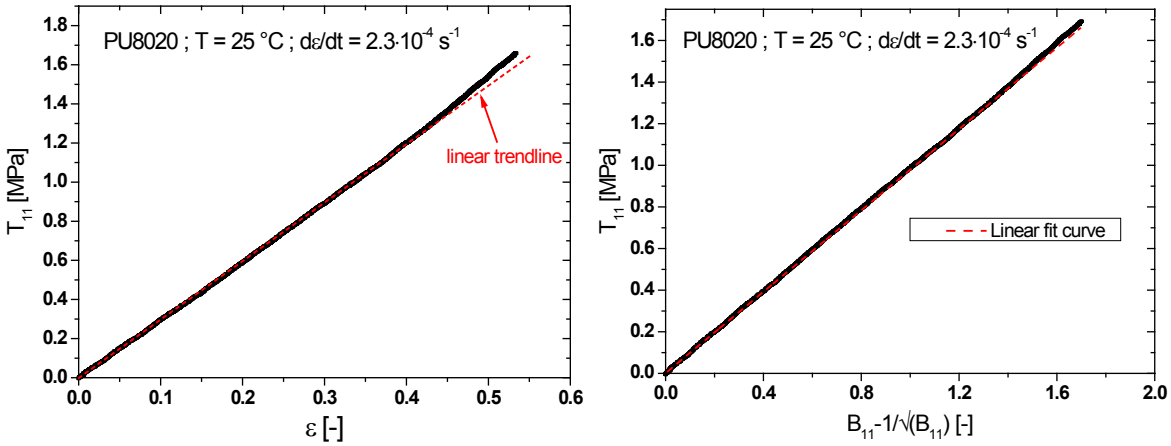

Figure 3-57: Tensile test of PU8020 bulk sample at 25 °C (left) and corresponding determination of the bulk shear modulus μ_{bulk} according to the equation (2.55) (right) (B_{11} is the first component in the left Cauchy-Green strain tensor)

Figure 3-57 (left) illustrates a stress-strain curve for a tensile test performed at 25 °C with an extension rate of about $d\varepsilon/dt = 2.3 \cdot 10^{-4}$ s^{-1} until the rupture of the specimen. For these measuring conditions, $T_{11}(\varepsilon)$ seems to be linear but the comparison with a linear trend curve (in red) reveals a non-linear evolution of $T_{11}(\varepsilon)$ with a positive curvature. This feature is characteristic for hyperelastic behaviour. The modulus of elasticity is thus not constant over the strain range. Using the Neo-Hooke model for an incompressible material (see section 2.2), the bulk shear modulus $\mu_{bulk} = 0.98 \pm 4 \cdot 10^{-5}$ MPa is determined as the slope in the plot shown in Figure 3-57 (right). In the entropy elastic state of the polyurethane, all the relaxation (and retardation) processes are too fast to be detected and thus, μ_{bulk} seems to not significantly depend on time or deformation rate.

Although at first glance the response of the PU8020 bulk at 25°C, as shown in Figure 3-57 (right), appears to be hyperelastic, Figure 3-58 (left) shows that the viscoelasticity of PU8020 bulk is still detectable as μ_{bulk} still depends on the strain rate. In the viscoelastic state, the relaxation processes strongly influence the mechanical response of the adhesive and the shear modulus depends on the strain rate. At 25 °C, the strain rate dependence of the shear modulus

can be identified by the increase of slope with increasing $\dot{\varepsilon}$ and indicates also that the relaxation processes are still "active". Imagine that $\dot{\varepsilon}$ would be increased further and further, one would get negatively bended tensile curve at 25 °C in the same way as observed at 0 °C – Figure 3-58 (right). That is the dynamic nature of the viscoelastic state. At 0 °C, the polymer mobility is slow enough in the PU bulk and hence the $\dot{\varepsilon}$-dependence is seen as negatively bended tensile curve[11]. The viscoelastic response is fully developed.

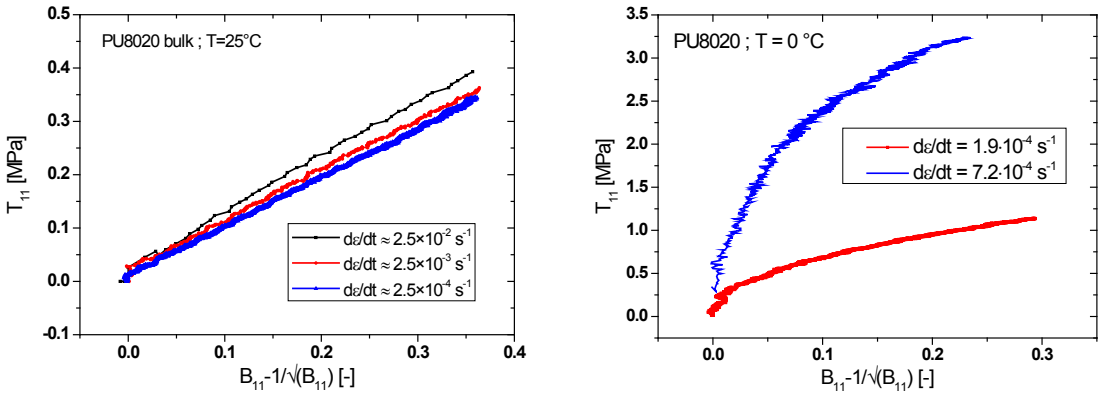

Figure 3-58: Tensile tests of the polyurethane adhesive at 25 °C (left) and 0 °C (right) with different extension rates

Since the desired $\dot{\varepsilon}$ is only met randomly with the set-up, the measurement effort for systematic investigations of the viscoelastic state of the bulk would be incalculably high. Consequently, a quantitative comparison of the results in the viscoelastic range is not possible. That is why the evaluation of the bulk tensile test results is focussed on the entropy elastic range, where the mechanical properties of the adhesive do not significantly depend on the extension rate. An additional reason is that the deformation of the outer (non-thermostated) stiff regions has only a minor influence on the deformation of the pattern when this thermostated region of the sample is in the entropy elastic state. At room temperature, the viscoelastic relaxation processes still exist as shown in Figure 3-58 . Hence the strain of the outer regions of the sample is delayed whereas the strain of the pattern follows instantaneously the applied deformation. Therefore, the travel speed is proportional to the extension rate in the entropy elastic range as follows: $v = 0.01$ mm/s, $v = 0.1$ mm/s and $v = 1$ mm/s correspond to the extension rates $d\varepsilon/dt \approx 2.5 \cdot 10^{-4}$ s^{-1}, $d\varepsilon/dt \approx 2.5 \cdot 10^{-3}$ s^{-1} and $d\varepsilon/dt \approx 2.5 \cdot 10^{-2}$ s^{-1} respectively.

The entropy elastic range begins as soon as the shear modulus shows no systematic dependence on the measured strain rate. For the given measurements and sample sets, this occurs at a temperature of 30 °C as depicted in Figure 3-59.

[11] Note that entropy-elastic tensile curves show positive curvature as indicated in Figure 3-57 (left).

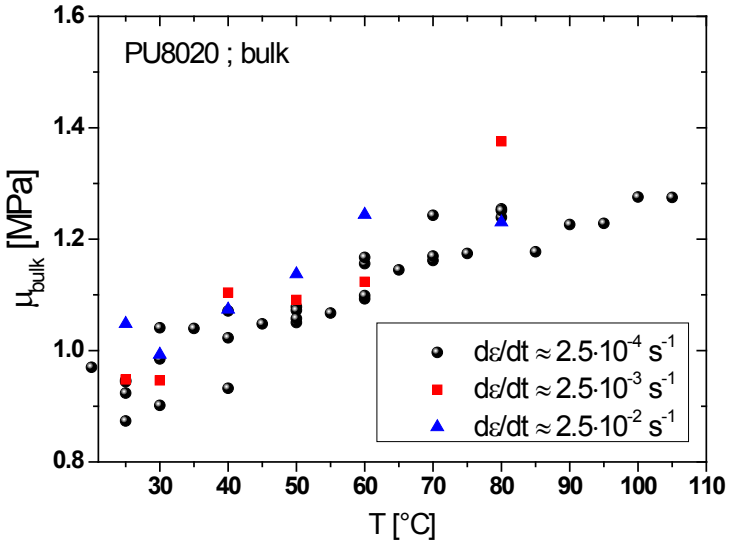

Figure 3-59: Shear modulus of the polyurethane adhesive μ_{bulk} measured at different extension rates and temperatures. These results are from three different polyurethane adhesive batches.

As expected by equation (2.8), the shear modulus increases linearly with increasing temperature in the entropy elastic range. Using this equation, it is possible to calculate the average crosslink density of the polyurethane bulk, κ_{bulk}. The experimental data are fitted with a linear function with a fixed point of intersection with the y-axis at 0 (μ_{bulk} (0 K) = 0), as shown in Figure 3-60 for $d\varepsilon/dt \approx 2.5 \cdot 10^{-4}$ s^{-1}. The slope of the function is proportional to the average crosslink density of the polyurethane adhesive and gives:

$\kappa_{Bulk}(d\varepsilon / dt \approx 2.5 \cdot 10^{-4} s^{-1}) \approx 404 \pm 3$ mol·m^{-3}.

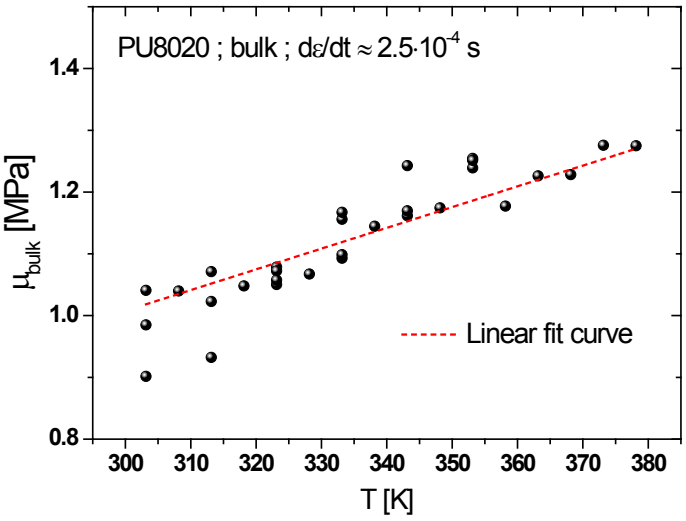

Figure 3-60: Temperature dependence of the shear modulus of the polyurethane adhesive μ_{bulk} measured by tensile tests with $d\varepsilon/dt \approx 2.5 \cdot 10^{-4}$ s^{-1}

Although no systematic dependence of μ_{bulk} as a function of the strain rate, $d\varepsilon/dt$, can be identified in Figure 3-59, the calculated values of the average crosslink density show a tendency to increase with increasing strain rate – see Figure 3-61. This shows that the dynamic nature of the viscoelasticity is still detectable. These dynamic effects are superimposed on the entropic contribution in the stiffness of the polymer network and the measured shear modulus is higher than in a pure entropy elastic state. Thus, the μ_{bulk} values obtained for the slowest strain rate, $d\varepsilon/dt \approx 2.5 \cdot 10^{-4}\ s^{-1}$, give a better approximation of κ_{bulk} since the theory from which equation (2.8) is derived is only valid for a polymer in the entropy elastic state.

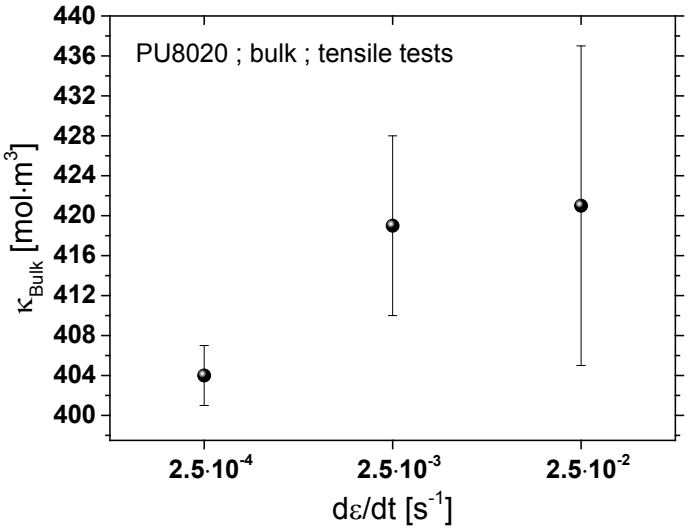

Figure 3-61: Average crosslink density of the polyurethane bulk, κ_{bulk} measured by tensile tests with three different strain rates.

Provided the bondline of the adhesive joint is thick enough, the behaviour of the "bulk-like" adhesive is expected to predominate because a mechanical interphase would not noticeably influence their properties anymore. Therefore, in the entropy elastic state, the values for the shear moduli from tensile tests should be comparable to those from the shear tests. The comparison of these values is illustrated in Figure 3-62.

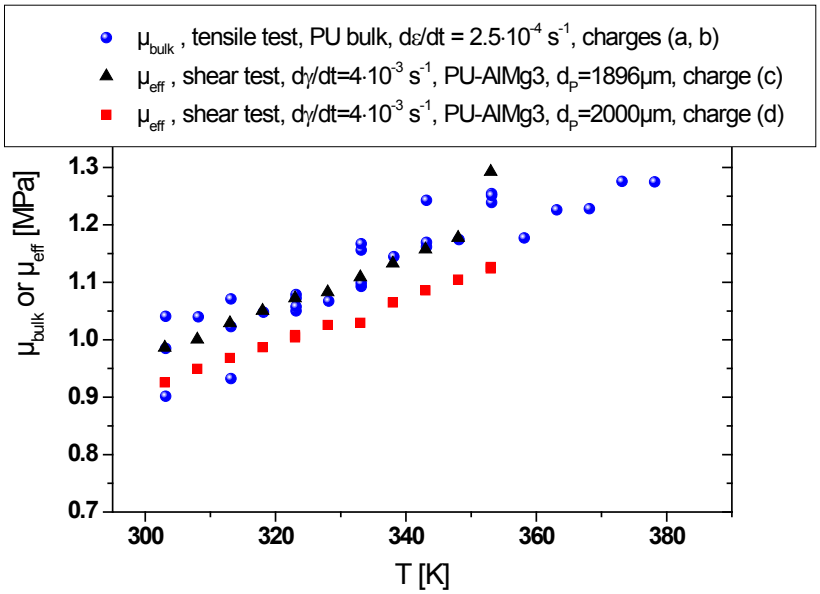

Figure 3-62: Comparison between the shear moduli obtained with tensile tests, μ_{bulk}, and those obtained with shear test at constant shear rate, μ_{eff} in the entropy elastic range of the polyurethane adhesive

The data in Figure 3-62 allow determining the effective cross-linking in the adhesive joints in the same manner as before:

$$\kappa_{1896\mu m(AlMg3)} = 404 \pm 4 \; mol/m^3$$

$$\kappa_{2000\mu m(AlMg3)} = 376 \pm 2 \; mol/m^3$$

These values of κ are also comparable to that from the tensile tests.

Figure 3-62 shows that systematically $\mu_{1896\mu m(AlMg3)} > \mu_{2000\mu m(AlMg3)}$. Even if the μ values for the two bonded joints are in the same range of variation as the bulk, these results show that, on the one hand, only the results from the same adhesive batch can be compared quantitatively.

On the other hand, if mechanical interphases exist in the investigated adhesive joints, they seem to not influence the mechanical behaviour of adhesive joints with $d_P \approx$ 1900 - 2000 µm. Hence, the maximal extent of these interphases is also expected to be a lot smaller than 2000 µm.

4. Mechanical interphase in PU-metal adhesive joints

Once all environmental influences and other disturbing effects have been minimised, the experimental results can be analysed and discussed.

Isothermal shear at constant shear rate, creep and stress relaxation tests were carried out on two types of adhesive joints:

- PU-AlMg3
- PU-stainless steel

These two kinds of adhesive joints were prepared from two different adhesive batches. Despite strict control of the experimental conditions (temperature, atmosphere) and a well-defined experimental protocol during the preparation (see section 3.1.3), small variations in the composition or in the network structure of the bulk material between two batches cannot be completely prevented. These differences could then lead to a wrongly interpreted influence of the substrate. To avoid that, the results for both substrates are not quantitatively compared.
The investigation of PU-stainless steel adhesive joints aims principally to apply and confirm the general method suggested in this work to identify and characterise interphases in adhesive joints.
The mechanical tests (mainly creep experiments), carried out on PU-stainless steel samples, were performed with a displacement sensor having a lower resolution and accuracy, thereby limiting the quantitative evaluation of the results in some cases.

The bond line thickness d_P of the samples varies from about 100 µm to 2000 µm. Experiments were carried out every 5 K in a temperature range from 10 °C to 80 °C.
In this temperature range and for the measured deformation rates, both viscoelastic and relaxed elastic properties of the polyurethane adhesive can be addressed experimentally. The energy-elastic state of the elastomer was not investigated in this work.
As mentioned in chapter 2.1, the definition of the viscoelastic and entropy-elastic state of a polymer is intrinsically tied to the deformation rate or, respectively, the measuring time. Hence, the transition from the entropy-elastic to the viscoelastic response of the adhesive is defined in this work as soon as the viscoelastic properties can be identified with the predetermined experimental conditions.

4.1. Isothermal mechanical properties as a function of temperature

First, the temperature dependence of the isothermal mechanical behaviour of the adhesive joints of varying bondline thickness is discussed. For this purpose, experiments are performed isothermally at different temperatures and the corresponding results are compared.

4.1.1. Isothermal shear tests at constant shear strain rate

Shear tests were carried out for each temperature and sample thickness at three shear rates $\dot{\gamma}$ ($4 \cdot 10^{-2}$ s^{-1}, $4 \cdot 10^{-3}$ s^{-1}, $4 \cdot 10^{-4}$ s^{-1}). Depending on the shear rate, an experiment lasts between 10 minutes for the slowest and 6 seconds for the fastest shear rate. As described in section 2.3, the analysis of the measurements differs for the entropy-elastic and viscoelastic region. The results are therefore presented separately for these two regions.

4.1.1.1. Entropy elastic state

In this hyperelastic region, also called rubber elasticity, a constant effective shear modulus is expected – eq. (2.63). It implies therefore a linear relationship between the effective shear deformation γ and the resulting shear stress T_{12}. Figure 4-1 shows the results of shear tests for three different shear rates at 70 °C on a sample with an average adhesive thickness of 736 µm.

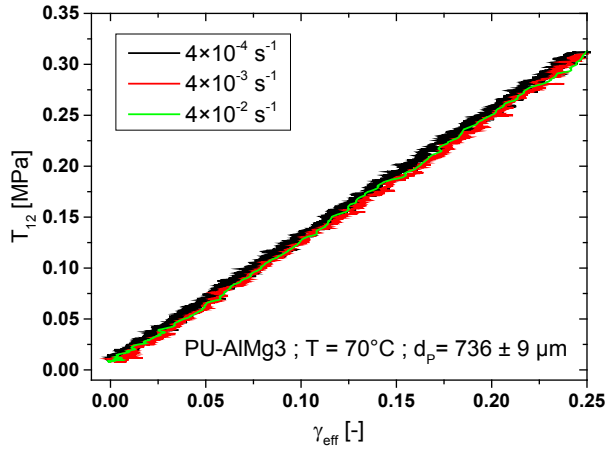

Figure 4-1: Shear tests at different constant shear strain rates at 70 °C for a AlMg3-PU adhesive joint with an adhesive thickness of 736 ± 9 µm

The experimental results confirm the Neo-Hookean linear relation between shear and shear stress – see eq. (2.63). In addition, as expected for the entropy-elastic state, no influence of the shear rate on the results is seen. The cooperative movements of the polyurethane chains are fast enough to follow the shear deformation. This fact also provides a possibility to define the entropy-elastic region for our measurements. As soon as the stress-strain curves depend on the shear rate, the viscoelastic properties of the adhesive can be detected with the measured parameters.

Each stress-strain curve is fitted with a linear function. The slope of the fit curve corresponds to the effective hyperelastic shear modulus μ_{eff} of the adhesive bondline – eq. (2.63). The values of μ_{eff} are determined for each effective shear rate and temperature. Since the effective shear modulus in the entropy-elastic state is independent of the shear rate, μ_{eff} can be averaged over the three values obtained for a given temperature. These average values are then plotted with the corresponding error bars as function of the temperature – Figure 4-2.

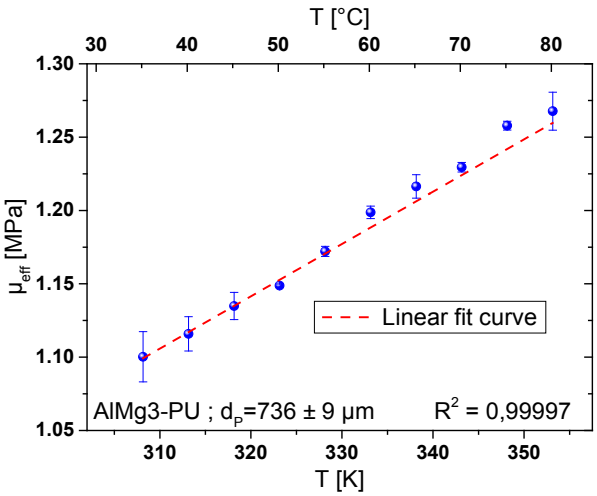

Figure 4-2: Temperature dependence of the effective shear modulus μ_{eff} for a PU-AlMg3 adhesive joint with d_p = 736 µm

As it can be seen in Figure 4-2, the effective shear modulus in the entropy-elastic state depends on the measuring temperature. The restoring force of the polymer network is then mostly governed by entropic effects which increase as the temperature rises. It results thus in an increase of the shear modulus. Despite the influence of the shear rate cannot be directly identified (as $T_{12}(\gamma)$ still seems to be linear), the growing error bar of the results from T ≤ 320 K indicates the "apparition" of the viscoelastic effects. According to eq. (2.8), the temperature dependence of μ_{eff} is fitted with a linear function passing through the origin, with a resulting correlation coefficient $R^2 > 0.99$.

The linear increase of the shear modulus as a function of the temperature expected by the theory of the rubber elasticity is thus confirmed. According to the equation (2.8) the slope of the linear fit curve is proportional to the effective cross-link density κ_{eff} (which is an average value for the whole adhesive thickness). The resulting apparent effective cross-link density is equal to 429.1 ± 0.8 mol·m^{-3} for the given example. The values for different adhesive thicknesses are discussed in section 4.2.1.1.

4.1.1.2. Linear viscoelastic state

Figure 4-3 shows the results of three shear tests with different shear rates on a PU-AlMg3 adhesive joint with a d_P = 736 µm sample at 15 °C. According to eq. (2.78), the shear rate influences the stress-strain curves in the viscoelastic range. As already mentioned in section 2.1.1, the applied strain rate $\dot{\gamma}$ determines which part of the cooperative movements absorbs mechanical energy and thus significantly builds up the deformation.
Provided that relaxation/retardation processes can occur at the measuring temperature, the involved material rearrangements in a polymer network can be influenced by the rate of the applied external load or deformation for a given experimental timescale. With increasing strain rate, fewer and fewer relaxation processes can follow the applied strain leading to an increase of the sample stiffness. The viscoelasticity of the sample can be identified as soon as the applied strain rate is faster than one of the measurable relaxation or retardation processes of the polymer.

The stress-strain curves measured with the shear rates $\dot{\gamma} = 4 \cdot 10^{-2}$ s^{-1} and $4 \cdot 10^{-3}$ s^{-1} no longer show a linear evolution of the shear stress T_{12} as a function of the effective shear strain γ_{eff}. Hence, if $\dot{\gamma} \cdot t = \gamma$ is inserted in eq. (2.78), it is evident that the effective dynamic shear modulus depends on the shear strain in the viscoelastic range. The evolution of the slope of the plots $T_{12}(\gamma)$ is described by the equation (2.79).
At first glance, the measured curve for a shear rate of $\dot{\gamma} = 4 \cdot 10^{-4}$ s^{-1} could be considered as linear by mistake, since the typical curvature at low strain cannot be clearly identified – cf. Figure 2-15 for $\dot{\gamma} = 4 \cdot 10^{-4}$ s^{-1}.

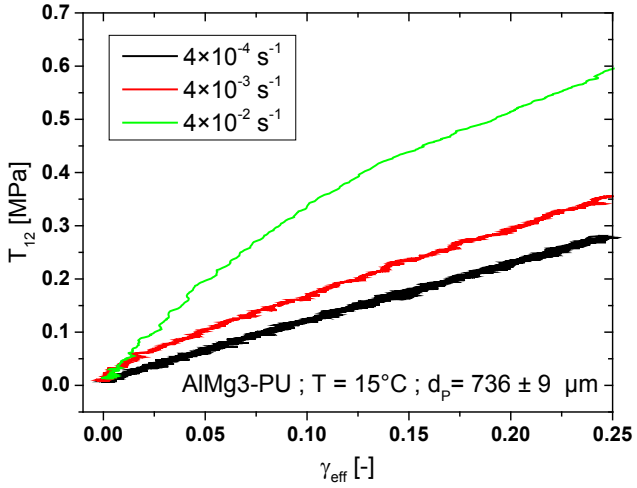

Figure 4-3: Shear tests at different constant shear deformation rates at 15 °C for an AlMg3-PU adhesive joint with an adhesive thickness of 736 ± 9 µm

Since the shear modulus depends on time in the viscoelastic state, the complete evolution must be considered to evaluate the influence of the temperature on the stiffness of the sample. Shear

tests measured with the same constant shear rate and at different temperatures are thus compared in Figure 4-4.

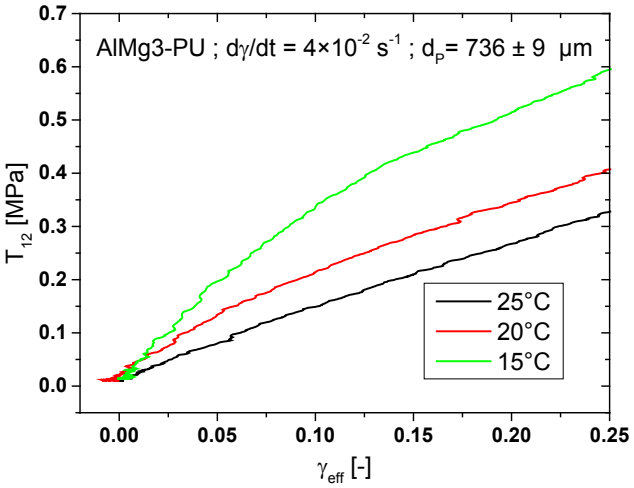

Figure 4-4: Shear tests at a constant shear deformation rate $d\gamma/dt = 4 \cdot 10^{-2}\ s^{-1}$ at different temperatures for an AlMg3-PU adhesive joint with an adhesive thickness of 736 ± 9 µm

Figure 4-4 shows that the dynamic shear modulus M_{eff} of the tested samples – i.e. the slope and the curvature of $T_{12}(\gamma)$ – increases significantly in the viscoelastic range with decreasing measuring temperature. As already mentioned, the lower the temperature, the slower the cooperative movements are and the more the relaxation processes resist against the applied shear deformation. The resulting stresses are then greater than at higher temperature for a given shear rate and the rigidity of the sample is thereby higher.

The evolution of the plots with decreasing temperature reminds those measured at different shear rates presented in Figure 4-3, but the physical origin is quite different: in eq. (2.78), all τ_i become smaller as T increases. Consequently, the curved initial region becomes weaker and "shorter" as T increases.
The question is whether temperature change at $\dot{\gamma} = const$ and variation of $\dot{\gamma}$ at $T = const$ are only phenomenologically similar or if there is a quantitative relation between $\dot{\gamma}$ and T – i.e. a temperature-time equivalence. This will be discussed in section 4.3.2.

Résumé

In the entropy-elastic region, shear tests provide quantitative information about the temperature dependence of the mechanical behaviour of the adhesive joints. At lower temperatures, viscoelastic effects can be observed by detecting the shear rate dependence of the mechanical properties. However, these viscoelastic properties cannot be accurately quantified due to the limited number of measured shear rates and a relatively short measuring time. For this purpose, stress relaxation and creep tests are performed. The corresponding results are presented in the following.

4.1.2. **Stress relaxation tests at constant shear deformation**

In stress relaxation experiments, the relaxation modulus $G_{eff}(t)$ is defined as the strain/stress ratio at constant deformation, as described in section 2.5. To depict the influence of temperature, relaxation moduli are plotted against *t* with logarithmic scale for a given adhesive thickness at different temperatures (Figure 4-5). In presenting the overall aspect of $G_{eff}(t)$, the range of the time scale is so enormous that the only way to give a complete representation in a single graph is to make the time coordinate logarithmic. This procedure is followed in this work for depicting all the viscoelastic functions. The evolution of $G_{eff}(t)$ in the entropy-elastic state (here: 40, 60 and 80 °C) differs from the viscoelastic state (here: 15, 20 °C).

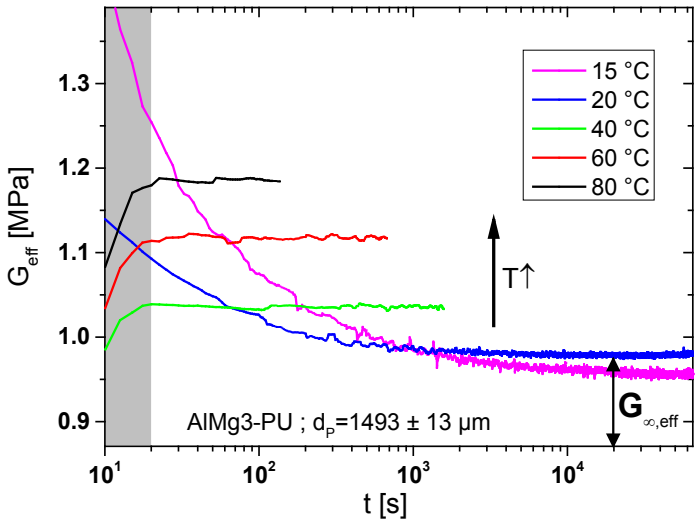

Figure 4-5: Temperature dependence of the shear stress relaxation modulus G_{eff} as a function of time for a AlMg3-PU adhesive joint with an adhesive thickness of 1493 ± 13 µm. The t_0-values of the measurements lie within the grey shaded area.

Above 35 °C, the sample behaves entropy elastic and all the relaxation processes are faster than the loading rate, so that the polymer network is in equilibrium right after loading. The relaxation modulus rises at short times (up to approximately 20 seconds) due to the loading of the sample. Once the constant deformation is reached by the machine, $G_{eff}(t)$ is also constant at a value representing the effective equilibrium shear modulus, $G_{\infty,eff}$.

At lower temperatures (T < 35 °C), stress relaxation processes are active and the stress gradually falls as the deformation of the polymer network adjusts itself through cooperative motions of the segments of the polymer network. Their direction of motions, which is isotropic in a force-free state, becomes anisotropic in the direction of the force due to the applied mechanical force. This preferential direction of the segment motions builds up the deformation, and does so in a delayed manner, because the motions are hindered. Since the loading of the sam-

ple is relatively slow, the stress relaxation of the sample takes already place before reaching the deformation plateau. Therefore, the relaxation processes are influenced by the loading, limiting the analysis of the $G_{eff}(t)$ curves. As the analytical solution of the rheological model only describes the mechanical response of the polymer from t_0 onwards – see equation (2.147), the loss of information is irremediable and the time range of the corresponding relaxation time spectrum is severely affected. That is why the retardation time spectra have been preferred to the relaxation time spectra for the quantitative analysis of the viscoelastic properties of the adhesive.

Nevertheless, the loading stages are throughout the tests almost the same. Hence, the $G_{eff}(t)$ curves can be compared with each other. A comparison of the measured curves at 15 °C and 20 °C shows that the lower the temperature, the slower the relaxation processes. At long times, $G_{eff}(t)$ reaches a constant value corresponding to the relaxed shear modulus, $G_{\infty,eff}$, in a good approximation[12].

In Figure 4-5, it is obvious that the effective relaxed shear modulus $G_{\infty,eff}$ depends on the measuring temperature. The temperature dependence of $G_{\infty,eff}$ is depicted in Figure 4-6.

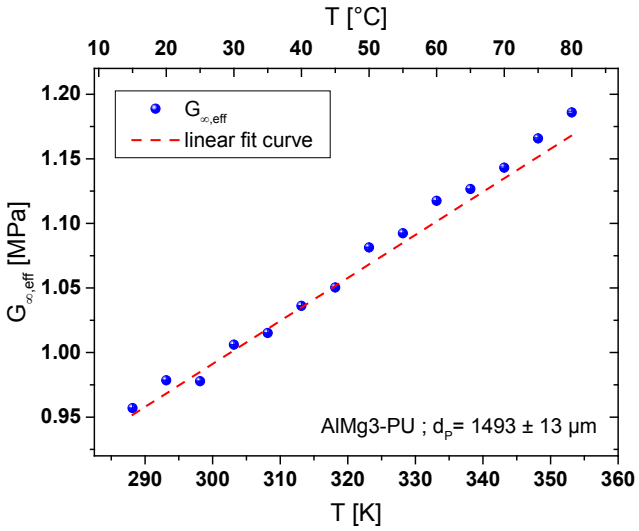

Figure 4-6: Temperature dependence of the equilibrium shear stress relaxation modulus $G_{\infty,eff}$ for a AlMg3-PU adhesive joint with an adhesive thickness of 1493 ± 13 µm. Error bars are smaller than the symbols.

[12] According to eq. (2.147), we have $G_\infty = \lim_{t\to\infty} G(t)$.

Figure 4-6 shows that $G_{\infty,eff}(T)$ is described with a linear function $G_{\infty,eff}^{1493\mu m}(T) = a \cdot T$ with $a = 33 \cdot 10^{-4} \pm 7 \cdot 10^{-6}$ MPa·K^{-1}. It is interesting that both the G_∞ values from the entropy-elastic range (T ≥ 35 °C) and from the viscoelastic range (T < 35 °C) lie on this linear fit curve. It is therefore obvious to compare this result with eq. (2.8), i.e.

$$a = \kappa_{eff}^{1493\mu m} \cdot R \cdot T$$

Thus, we obtain

$$\kappa_{eff}^{1493\mu m} = 397 \pm 0.8 \text{ mol} \cdot \text{m}^{-3}$$

Considering the experimental errors, this value of the effective crosslink density is almost the same as the value obtained from the shear tests at the slow rate ($\dot{\gamma} = 4 \cdot 10^{-4}$ s^{-1}): 400.8 ± 0.3 mol·m^{-3} (see Figure 4-20). Therefore, this shear rate was indeed slow enough to obtain quasi-relaxed deformation.

Thus, it is clear that both $G_{\infty,eff}$ from the stress relaxation experiments and μ_{eff} from the shear tests describe very well the mechanical response of the PU in the entropy-elastic state.
Since the linear evolution of $G_{\infty,eff}(T)$ continues into the viscoelastic state (T < 35 °C, cf. Figure 4-6 and Figure 4-7), it proves that the modulus in the relaxed viscoelastic state is also dominated by the entropic restoring forces.

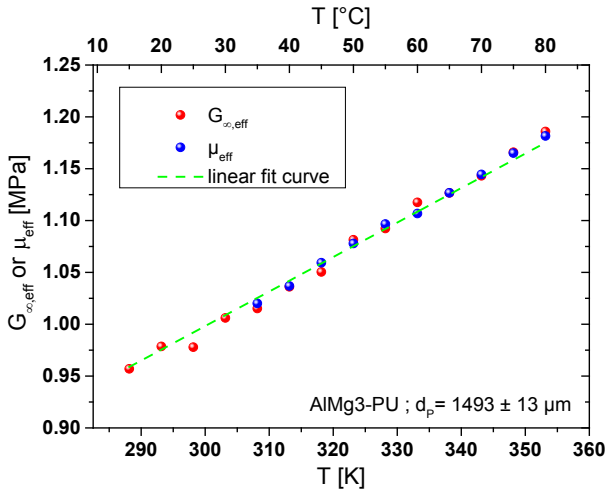

Figure 4-7: Comparison between the equilibrium shear stress relaxation modulus $G_{\infty,eff}$ and the effective hyperelastic shear modulus μ_{eff} with $\dot{\gamma} = 4 \cdot 10^{-4}\ s^{-1}$ for an AlMg3-PU adhesive joint with an adhesive thickness of 1493 ± 13 µm

In addition to the results of the shear tests, the relaxation experiments provide information on the influence of the temperature on the relaxed elastic properties in a broader temperature range. In the viscoelastic region, it is possible to display the relaxation processes and their temperature dependence. However, because of the slowness of the sample loading, relaxation spectra cannot be calculated in a sufficiently large time domain to describe quantitatively the temperature dependence of the viscoelastic properties. For this reason, creep tests at constant shear stress were carried out.

4.1.3. **Creep tests at constant shear stress**

To describe creep experiments, the evolution of the creep compliance $J_{eff}(t)$ is plotted over time. Figure 4-8 shows the creep curves at different temperatures for two adhesive joints: a PU-AlMg3 sample with an average adhesive layer thickness d_P of 736 µm (left) and a PU-stainless steel adhesive joint with d_P = 1853 µm (right). In both cases, the lower the measuring temperature, the longer it takes to reach a given level of deformation or compliance. This implies that the retardation processes slow down with decreasing temperature. At long times, $J_{eff}(t)$ reaches a plateau which corresponds to the effective equilibrium compliance $J_{\infty,eff}$. While it takes some time to reach $J_{\infty,eff}$ in the viscoelastic state, the plateau is reached quickly in the entropy-elastic state directly after applying the load (see orange to brown curves in Figure 4-8, right). Due to the elasticity of the adhesive at high temperatures, the sample oscillates a bit in the testing machine right after the loading, causing small fluctuations in $J_{eff}(t)$.

The corresponding evolution of $T_{12}(t)$ for the same creep tests as in Figure 4-8 are shown in Figure 4-9.

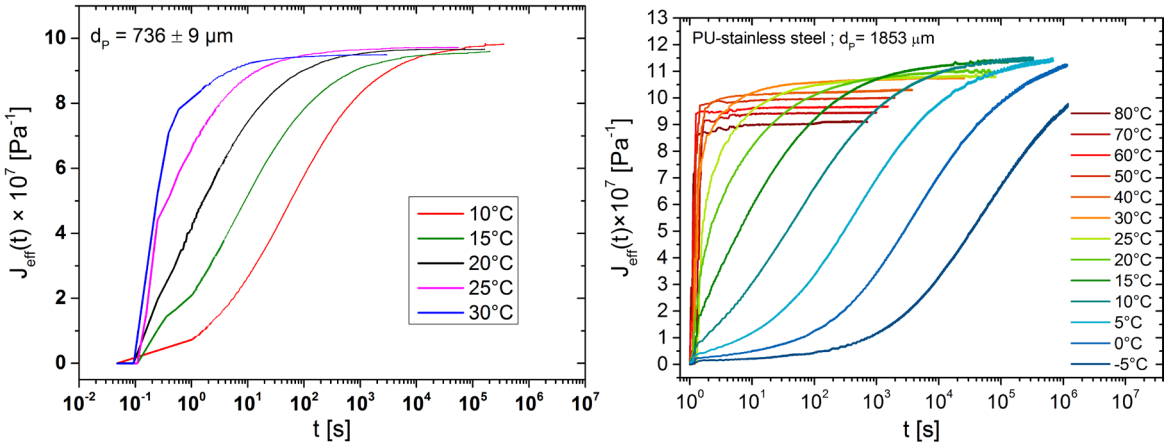

Figure 4-8: Temperature dependence of the effective shear creep compliance $J_{eff}(t)$ as a function of time for a AlMg3-PU adhesive joint with an adhesive thickness of 736 ± 9 µm (left) and a stainless steel-PU with d_P = 1853 µm (right)

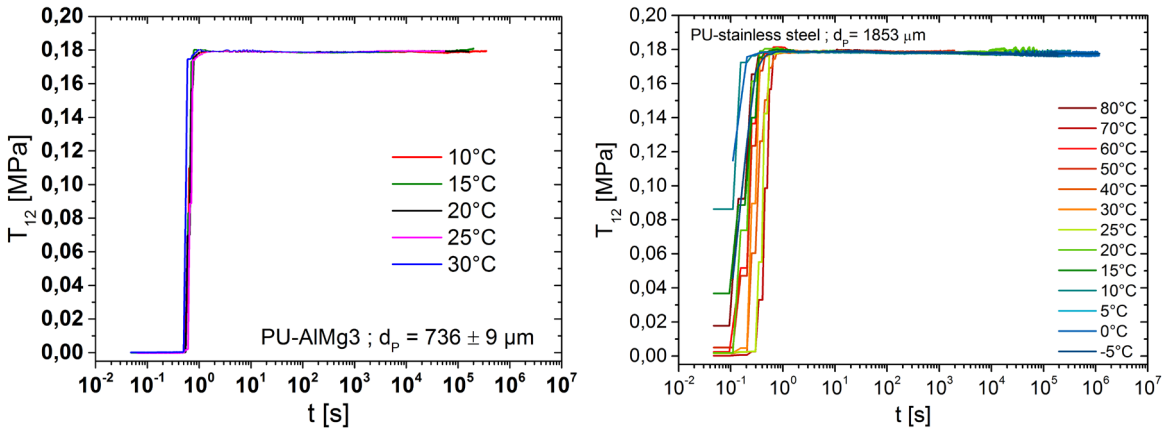

Figure 4-9: Shear stress T_{12} as a function of time for a AlMg3-PU adhesive joint with an adhesive thickness of 736 ± 9 µm (left) and a stainless steel-PU with d_P = 1853 µm (right) during the creep tests shown in Figure 4-8

In Figure 4-8, the temperature dependence of the equilibrium compliance $J_{\infty,eff}$ in adhesive joints can be identified qualitatively. To describe this effect quantitatively, the corresponding values of $J_{\infty,eff}$ are plotted as function of the measuring temperature for both kinds of adhesive joints in Figure 4-10.

The equilibrium creep compliance decreases linearly with increasing temperature: the adhesive becomes also stiffer. This observation confirms the results obtained with shear and relaxation tests for the relaxed elastic properties. At low temperatures, $J_{\infty,eff}$ shows a modification of its temperature dependence in Figure 4-10, left: the equilibrium creep compliance seems to tend to a constant value. This indicates that the equilibrium creep compliance is not yet reached despite a measuring time of about 4 days! These measurements were stopped too early. For thick adhesive joints, the time needed to reach the equilibrium at 5 °C amounts to more than 3 weeks. For measurements at lower temperatures, it will be necessary to improve the stability of the creep testing machine and to increase the measuring time drastically.

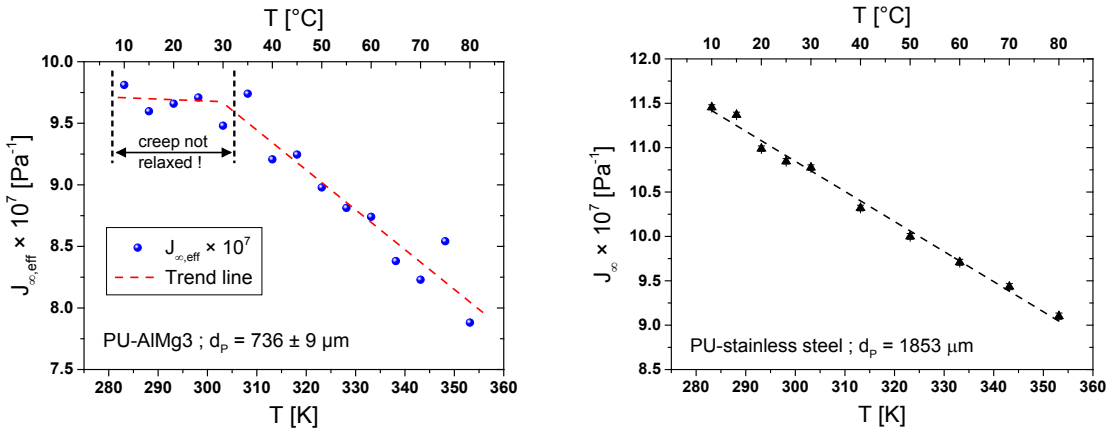

Figure 4-10: Temperature dependence of the effective equilibrium shear compliance $J_{\infty,eff}$ for a AlMg3-PU adhesive joint with an adhesive thickness of 736 ± 9 µm (left) and a PU-stainless steel with a d_P = 1853 µm (right). Error bars are smaller than the symbols.

In contrast to $J_{eff}(t)$ and $G_{eff}(t)$, the effective equilibrium compliance $J_{\infty,eff}$ and the effective equilibrium shear modulus $G_{\infty,eff}$ as well as the effective shear modulus of the adhesive in the entropy-elastic state, μ_{eff}, are *time-independent* material parameters. The following relation should thus be verified [166]:

$$G_{\infty,eff} = \frac{1}{J_{\infty,eff}} = \mu_{eff} \tag{4.1}$$

Only the measured values, obtained at equilibrium deformation, can be considered to test equation (4.1). For example, the equilibrium moduli and compliance for a PU-AlMg3 adhesive joints with a d_P = 1493 µm, represented in Figure 4-11, confirm the relation given by the equation (4.1). Therefore $G_{\infty,eff}$, μ_{eff} and $J^{-1}_{\infty,eff}$ exhibit the same temperature dependence, which is described by the theory of entropy elasticity – see equation (2.8). After linear fitting of the data sets, the values for the average crosslink density $\kappa_{1493\mu m}$ for an AlMg3-PU adhesive joint with an adhesive thickness of 1493 ± 13 µm are calculated:

$$\kappa^{G_{\infty,eff}}_{1493\mu m} = 397 \pm 0.8 \text{ mol} \cdot \text{m}^{-3}$$

$$\kappa^{1/J_{\infty,eff}}_{1493\mu m} = 401.4 \pm 0.5 \text{ mol} \cdot \text{m}^{-3}$$

$$\kappa^{\mu_{eff}}_{1493\mu m} = 400.8 \pm 0.3 \text{ mol} \cdot \text{m}^{-3}$$

It is obvious that $J^{-1}_{\infty,eff}$ from the creep experiments also describes very well the mechanical response of the PU in the entropy-elastic state.

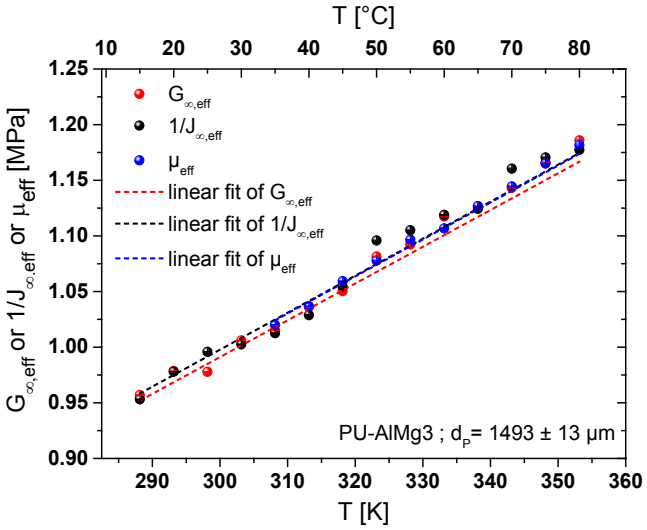

Figure 4-11: Comparison between the effective equilibrium shear stress relaxation modulus $G_{\infty,eff}$, the reciprocal effective equilibrium creep compliance $J^{-1}_{\infty,eff}$ and the effective shear modulus μ_{eff} (in the entropy-elastic temperature range) for a AlMg3-PU adhesive joint with an adhesive thickness of 1493 ± 13 µm. Error bars are smaller than the symbols.

The creep experiments presented in Figure 4-8 were carried out with the creep testing machine featured in section 3.3.2. As already mentioned the loading regime of the sample is approximately the same for all experiments and lasts about one to two seconds only. The consideration of the loading stage in the calculation of the retardation spectra allows an accurate and quantitative evaluation of the viscoelastic properties of the adhesive joints, while limiting the loss of information due to the non-instantaneous response of the sample – see eq. (2.112). The calculation of such retardation time spectra is presented in section 2.4.

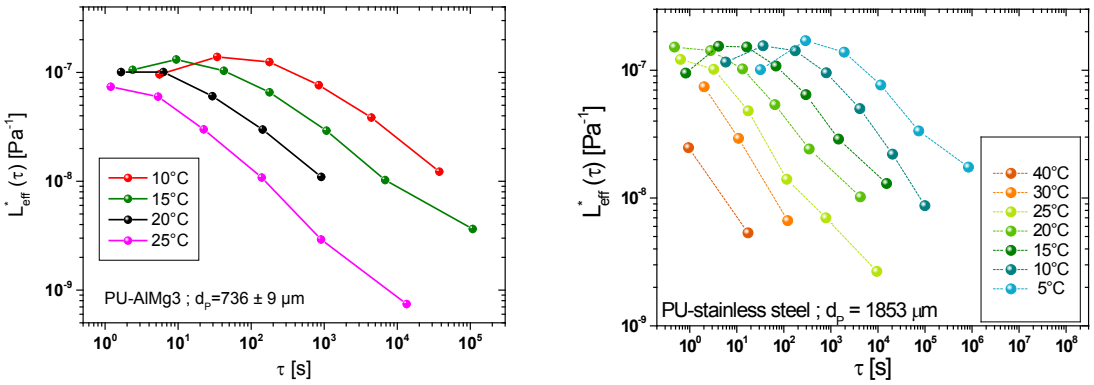

Figure 4-12: Temperature dependence of the discrete effective retardation time spectra for a AlMg3-PU adhesive joint with an adhesive thickness of 736 ± 9 µm and a PU-stainless steel with d_P = 1853 µm plotted on a logarithmic scale.

The calculated discrete effective retardation time spectra[13] for an AlMg3-PU adhesive joint with d_P = 736 ± 9 µm and a PU-stainless steel with d_P = 1853 µm are plotted on a logarithmic scale in Figure 4-12. The error bars; calculated from the error of the fit parameters (see section 2.4), are depicted here, but they are smaller than the symbols. These discrete effective retardation time spectra correspond to the creep curves presented in Figure 4-8.

In the following discussion, the discrete effective retardation time spectra are plotted with logarithmic coordinates on both axes – Figure 4-13. The calculation of the relaxation time spectrum from the retardation time spectrum, presented in the section 2.6, requires indeed this representation for the fitting operation of the discrete effective spectrum with a cubic polynomial function.

[13] The discrete retardation/relaxation time spectra calculated for adhesive joints are *effective* values since the mechanical properties in the bondline are not expected to be homogeneous because of the existence of mechanical interphase. The "true" relaxation/retardation time spectra can only be determined for PU bulk.

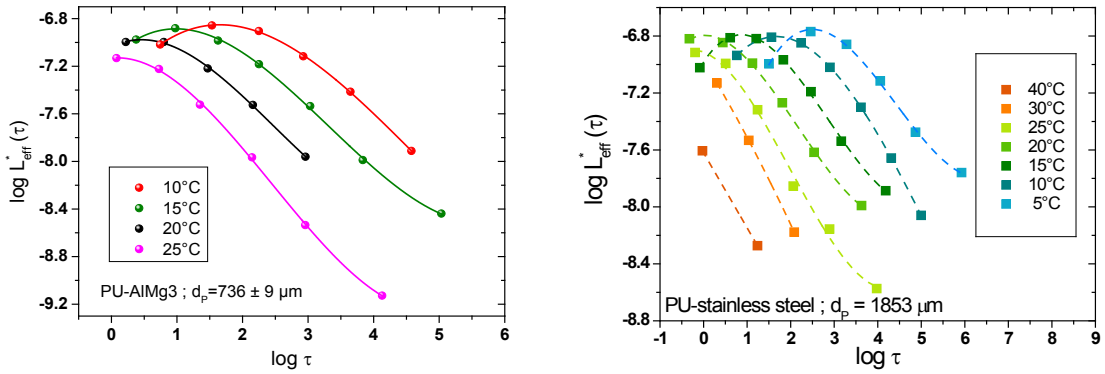

Figure 4-13: Discrete effective retardation time spectra for a AlMg3-PU adhesive joint with an adhesive thickness of 736 ± 9 µm and a PU-stainless steel with d_P = 1853 µm plotted with logarithmic coordinates on both axes. The represented trend lines are the cubic polynomial functions used to calculate the continuous effective retardation time spectra.

In both sample types, the effective retardation time spectra shift to longer retardation times with decreasing temperature. This reflects the fact that the retardation processes are slower. Qualitatively, this is a further indication for the time-temperature equivalence[14].
However, besides the temporal shift of the effective retardation time spectra to longer retardation times, a shift of the spectra to higher compliance with decreasing temperature is identified for PU-AlMg3 adhesive joints (Figure 4-12, left and Figure 4-14) as well as for PU-stainless steel samples (Figure 4-12, right and Figure 4-15).
This issue is discussed further in the section 4.3.2.

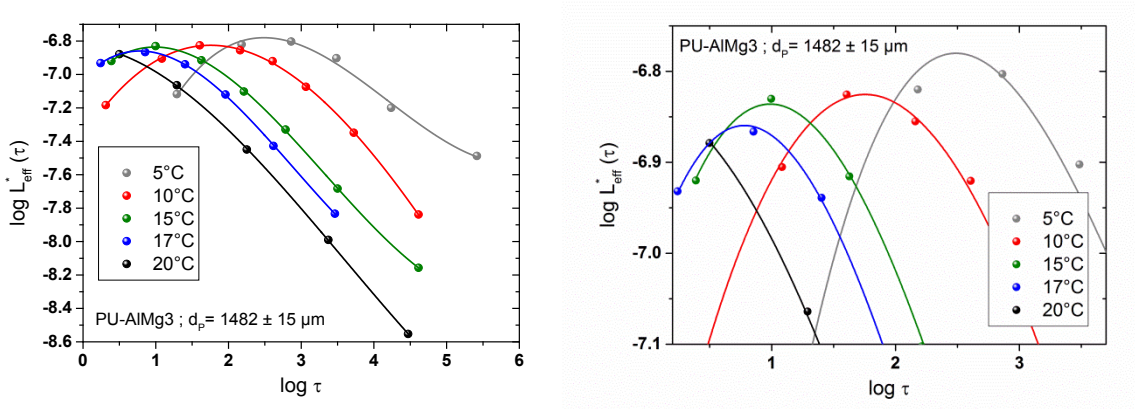

Figure 4-14: Temperature dependence of the discrete effective retardation time spectra for a AlMg3-PU adhesive joint with an adhesive thickness of 1482 ± 15 µm (left) and close-up view on the maxima of the spectra (right). The represented trend lines are the cubic polynomial functions used to calculate the continuous effective retardation time spectra.

[14] A first indication for time-temperature equivalence has already been observed with the results of isothermal shear tests at constant shear strain rate in section 4.1.1.2.

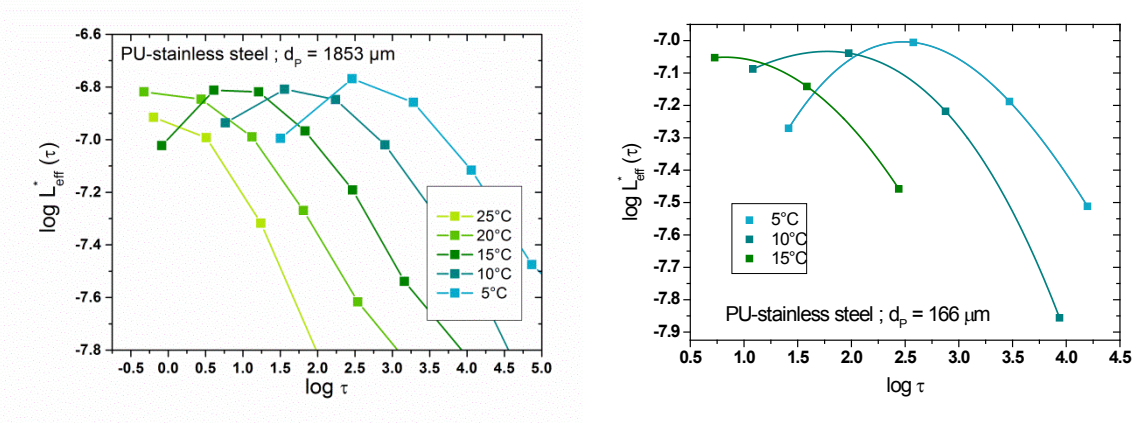

Figure 4-15: Temperature dependence of the discrete effective retardation time spectra for two different PU-stainless steel adhesive joints with d_P = 1853 µm (left) and d_P = 166 µm (right).

In addition to showing the shift of the retardation time spectra to higher value of $L^*_{eff}(\tau)$ with decreasing temperature, Figure 4-14 illustrates once again that even a small temperature difference (only 2 K) has a drastic influence on the viscoelastic properties of the adhesive. By the way, these results demonstrate the high accuracy of measurements and temperature control of the sample.

However, in order to ensure that the observed shifts (to longer retardation time and to higher compliance) do not result from an experimental error, following situations are considered:

a) Between two measurements, the displacement transducer is not reset to zero. This would result in an offset in the measurement of the creep strain for the second test (provided that the position of the length gauge stays in its linear measuring range). Figure 4-16 illustrates a simulation of this effect:

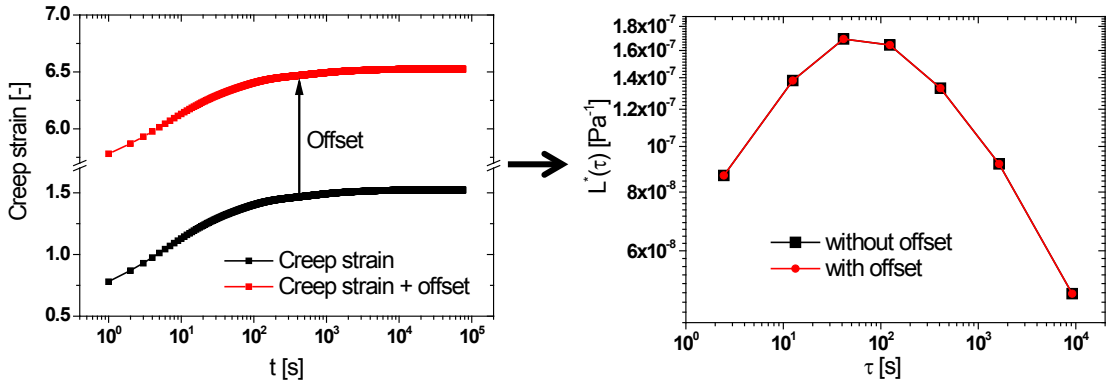

Figure 4-16: Influence of an offset in the creep strain/compliance signal (left) on the retardation time spectrum (right)

An offset in the creep strain or compliance signal has no influence either on the position of the retardation time spectrum or on its shape in the measured time range.

b) The creep equilibrium is not reached at the end of the measurement. As discussed above, the values of $J_{\infty,eff}$ at low temperatures in Figure 4-10 (left) indicates that the creep equilibrium was not completely reached. Therefore, the calculation of the corresponding retardation time spectra is surely affected. However, the issue is to determine how and to what extent this fact will influence the results. Figure 4-17 presents a simulation of this effect. If the creep equilibrium is not reached, the values of the retardation time spectrum are shifted to lower compliances for given retardation times: the longer the retardation time, the bigger is the discrepancy. The shape of the retardation time spectra is thereby impacted, letting this latter appear narrower than it should be. Figure 4-17 depicts a worst case which is experimentally easy to detect. As the consequence, only creep curves that have reached the equilibrium should be used to calculate the retardation time spectra. Nevertheless, at longer measuring times or low measuring temperatures, the attainment of the creep plateau is sometimes hard to identify because the variation of *J(t)* is very small. That is why this effect must be considered in the discussion of the presented results. A method to verify the results is presented and discussed in section 4.3.1.

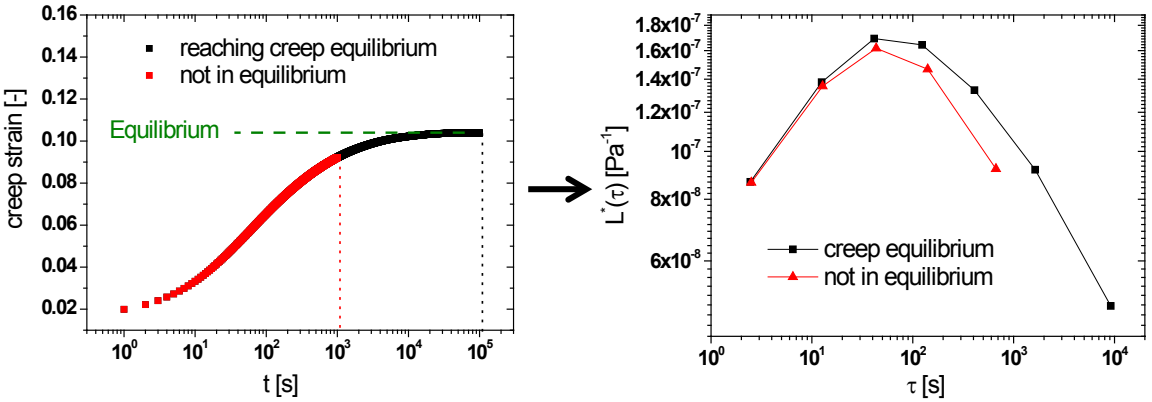

Figure 4-17: Distortion of the retardation time spectrum (right) caused by its calculation using an uncompleted creep test (red curve, left)

Moreover, the experimentally observed shifts to longer retardation time and to higher compliance of the retardation time spectra with decreasing temperature cannot, though, result from the distortion of the spectra illustrated in Figure 4-17:

- The retardation time spectra show namely a constant shift to longer time for all the retardation processes with decreasing temperature, preserving a priori the shape of the spectra (in the measured range).
- The shift of the spectra to higher compliances should be reduced due to the narrowing of the spectra (if it would exist). Even by considering that the creep experiments did not reach the equilibrium, the existence of this upward shift cannot be caused by the distortion of the spectra.

The retardation time spectra describe therefore the effective polymer dynamics of the polyurethane adhesive inside the bonding joint. The evolution of the retardation time spectra with the measuring temperature reveals a complex temperature dependence of the mechanical behaviour of the adhesive joints.

4.2. Bond line thickness dependence of mechanical properties

Now that the temperature dependence of the relaxed effective elastic and viscoelastic properties of the adhesive joints is characterised, the analysis presented so far can also be applied to investigate the influence of the bond line thickness d_P on the mechanical behaviour of adhesive joints. If it turns out that the effective mechanical properties depend on the adhesive thickness, it would prove the existence of mechanical interphases in adhesive joints.

4.2.1. Shear tests at constant shear strain rate

4.2.1.1. Entropy-elastic state

Figure 4-18 shows the evolution of the effective hyperelastic shear modulus μ_{eff} [15] as function of the temperature for samples with different adhesive thickness within the entropy-elastic region of the adhesive. The shear modulus is determined for each temperature and bond line thickness and averaged with the values for the three measured shear rates $\dot{\gamma}$: $4 \cdot 10^{-2}$ s^{-1}, $4 \cdot 10^{-3}$ s^{-1}, $4 \cdot 10^{-4}$ s^{-1} by means of the equation (2.63). For a given shear strain γ, the displacement in the strained state u is smaller for thin adhesive joints than for thick ones. Therefore, the relative measurement error increases with decreasing adhesive thickness.

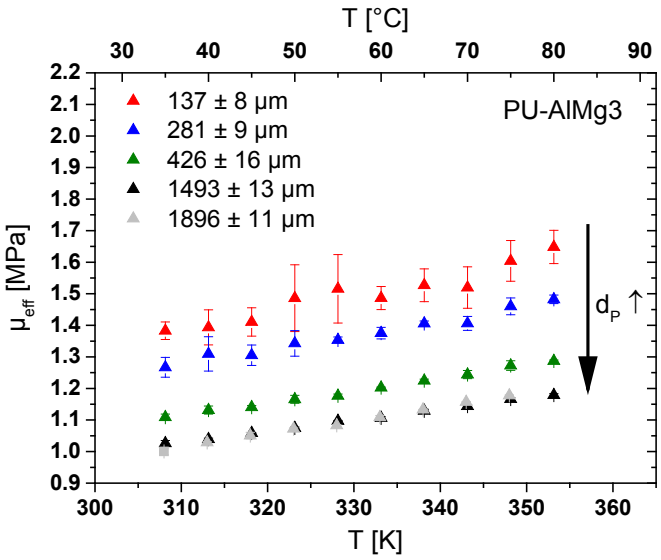

Figure 4-18: Temperature dependence of the effective hyperelastic shear modulus μ_{eff} for PU-AlMg3 adhesive joints with different d_P. To ensure the comparability between the results, all the measurements have been performed with the same maximum shear strain criterion of $\gamma_{eff}^{max} = 0.25$.

[15] cf. eq. (2.63)

For a given temperature, the effective shear modulus rises with decreasing d_P as depicted in Figure 4-18. Thinner adhesive joints behave stiffer than the thicker ones. This bond line thickness dependence of the entropy-elastic μ_{eff} is also represented in Figure 4-19. From $d_P \geq 1493$ µm μ_{eff} lies in the range of the values measured for the PU bulk. This would mean that the influence of the interphase on the mechanical behaviour of those adhesive joints extends up to a range of about 1.5 mm. This result should be confirmed by the stress relaxation and creep experiments.

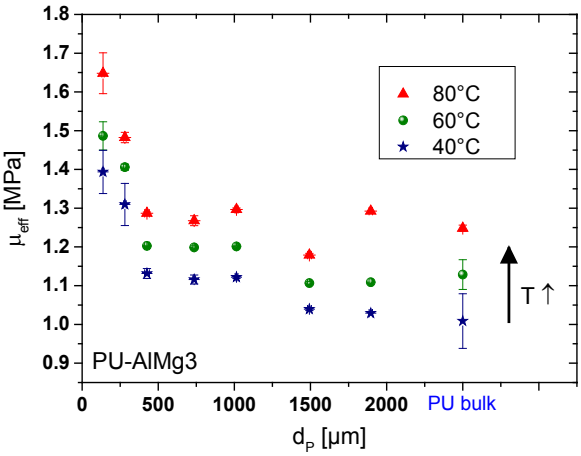

Figure 4-19: Bond line thickness dependence of the effective hyperelastic shear modulus μ_{eff} for PU-AlMg3 adhesive joints and μ_{bulk} at 40 °C, 60 °C and 80 °C

In addition to the variation of μ_{eff} with different d_P, Figure 4-18 depicts the linear evolution of the entropy-elastic μ_{eff} with the measuring temperature, as described in Figure 4-2. This linear dependence applies to all types of samples (data not shown) and across the whole adhesive thickness range as well. The apparent effective crosslink density κ_{eff} can therefore be calculated, as shown in section 4.1.1.1, for different d_P.

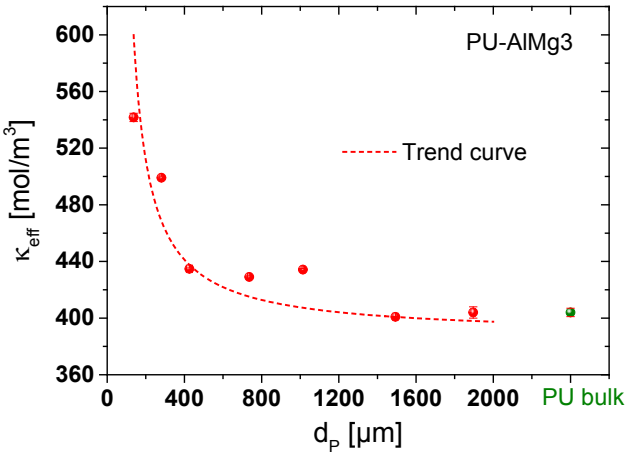

Figure 4-20: Effective crosslink density, κ_{eff} for AlMg3-PU joints as a function of the adhesive thickness, d_P.

The bond line thickness dependence of the apparent κ_{eff} is depicted in Figure 4-20. The horizontal and vertical error bars, resulting respectively from the variations of the adhesive thickness and the error of the fit parameter (slope of the linear regression), are almost completely masked by the symbols. The effective cross-link density κ_{eff} for AlMg3-PU joints increases with decreasing bond line thickness. The calculated values of κ_{eff}, averaging the cross-link density over the whole adhesive thickness, consist in a contribution of the interphases (if existing) and bulk (if still existing) adhesive. As discussed in the introduction of this work, it is obvious that the contribution of the interphases increases with decreasing adhesive thickness. This would mean that the interphase would have an apparently higher cross-link density than the bulk adhesive. However, this assessment must be interpreted with great caution because:

- Besides the simplifications made in the classical theory of the entropy elasticity which considers free crosslinked macromolecules, adhesive molecules in the bonding joint are attached to the surface of the substrates. The adhesion of the molecules on the substrate surfaces results in local immobilisation of the polyurethane network, increasing also its local stiffness without influencing its chemical crosslink density. In other words, the adhesive bonding sites add a new type of immobilisation of the PU network chains but their effect on stiffness cannot be attributed quantitatively.

- The shrinkage during the crosslinking of the polyurethane leads to residual stresses in the adhesive layer. These stresses will grow with decreasing d_P because the adhesion sites provide additional hindrance to their relaxation during and after network formation. Hence a thin adhesive joint could be stiffer than a thick one, even though both samples have the same crosslink density, because residual stresses pretend increased stiffness as demonstrated in section 3.4.2.2 for the PU bulk.

Both the influence of the adhesion mechanism and the residual stresses cannot be separated and can therefore corrupt the calculation of the true crosslink density in adhesive joints.

Despite these limitations, the evolution of the crosslink density, as illustrated by the trend curve in Figure 4-20 matches the results obtained so far, showing that the interphase is stiffer than the bulk adhesive. In addition, the crosslink density approaches a plateau value with increasing sample thickness, which corresponds to the crosslink density of the adhesive bulk. A crude consideration of the polyurethane network architecture provides namely an average crosslink density of about 400 mol·m^{-3} [167].
For thinner adhesive joints than $d_P < 137$ µm, the evolution of the cross-link density remains though undefined since the adhesion mechanism(s) of polyurethane on the metallic substrate are hitherto not well understood. However, recent and future works of the group headed by Professor W. Possart deal with this topic [10, 11, 14, 168-174].

4.2.1.2. Linear viscoelastic state

The linear viscoelastic shear modulus M_{eff} depends on the shear strain γ, the constant shear rate $\dot{\gamma} = \frac{\partial \gamma}{\partial t} = const.$ (proportional to the time) and the measuring temperature: $M_{eff} = M_{eff}(\gamma, t, T)$. To describe the influence of the adhesive thickness on M_{eff}, shear tests measured with given shear rate and at given temperature are compared for different d_P.

Figure 4-21 depicts the results for different PU-AlMg3 joints at 20 °C and different constant shear rates $\dot{\gamma}$. The thinner the adhesive joint, the more sensitive is the measuring curve to the fluctuations in the displacement signal. That is why the red curves exhibit the strongest measurement noise. Nevertheless, the shear stress $T_{12}(\gamma)$ in a thin sample is always higher and more curved than for a thicker one: the effective dynamic shear modulus is higher. Adhesive joints behave thus dynamically stiffer with decreasing d_P in the viscoelastic state. Therefore M_{eff} depends also on the bond line thickness: $M_{eff} = M_{eff}(\gamma, t, T, d_P)$.

In Figure 4-21, the curvature at the beginning of the shear test, which is a defining characteristic of the viscoelastic behaviour, reduces with increasing d_P. This indicates a decreasing hindrance of segment mobility in thicker adhesive bondline.

Since all the PU-AlMg3 joints have been prepared with the same batch of polyurethane and under the same conditions, the bondline thickness dependence of the effective dynamical mechanical properties in adhesive joints is interpreted as an evidence for the existence of mechanical interphase with specific cooperative segment mobility.

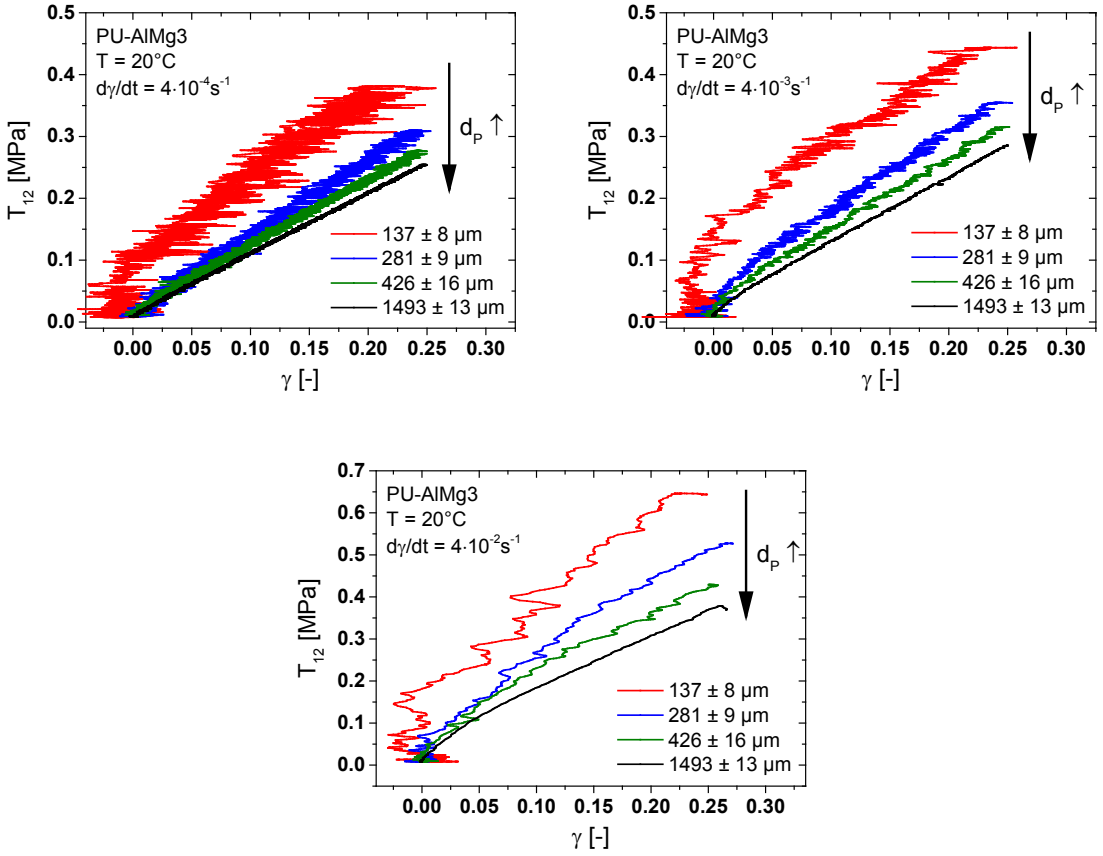

Figure 4-21: Shear tests at different constant shear rates $d\gamma/dt$ at 20 °C for AlMg3-PU adhesive joints with different d_P

4.2.2. **Isothermal stress relaxation tests at constant shear deformation**

In Figure 4-22, the relaxation function $G_{eff}(t)$ is plotted for samples with different adhesive thickness at a constant measuring temperature of 15 °C.
During the variable and relatively long loading of the samples (up to 40 s, see section 3.3.3), the retardation processes of the adhesive cannot be analysed accurately and the evolution of $G_{eff}(t)$ should not be quantitatively considered as displayed in Figure 4-22. The fast relaxation processes are largely relaxed with $\tau_j < 40$ s. Figure 4-22 shows a weak time dependence for $G_{eff}(t)$ for t > 40 s. It follows that the slow relaxations are weak and consequently cannot be quantified due to the limits of measurement accuracy. Therefore, these measurements do not provide enough information to determine the effective relaxation time spectra $H^*_{eff}(\tau)$. That is why the evaluation of the results is focussed on the relaxed elastic properties, at the end of the stress relaxation tests. A qualitative increase of the relaxation modulus with decreasing adhesive thickness is nonetheless observable in Figure 4-22, thus confirming the results obtained hitherto.

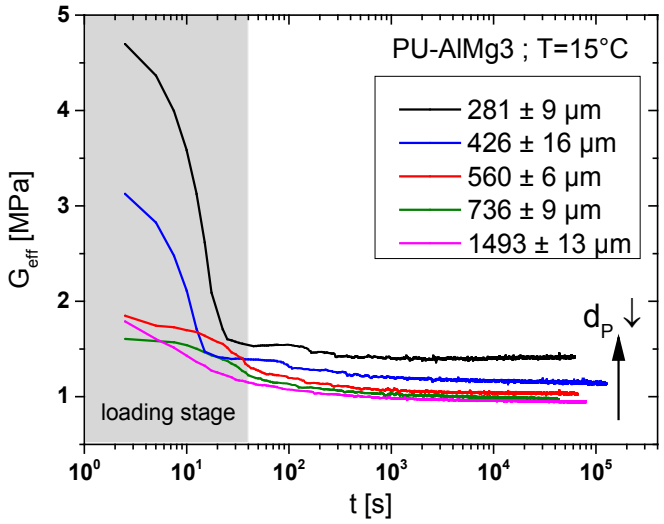

Figure 4-22: Bond line thickness dependence of the effective shear stress relaxation modulus G_{eff} as a function of time at 15 °C for AlMg3-PU adhesive joints

In order to characterise the effect of the bond line thickness more precisely, the equilibrium relaxation modulus $G_{\infty,eff}$ according to eq. (2.147) is plotted as a function of d_P in Figure 4-23. As already mentioned, $G_{\infty,eff}$ is a time-independent material parameter and thereby not affected by the loading of the sample.

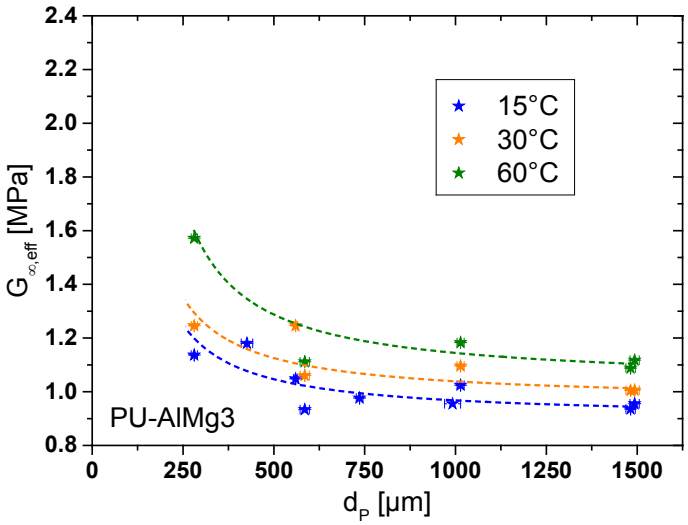

Figure 4-23: Bond line thickness dependence of the equilibrium relaxation modulus $G_{\infty,eff}$ for AlMg3-PU adhesive joints at 15 °C, 30 °C and 60 °C. The dashed lines represent the trend of $G_{\infty,eff}(d_P)$ for each temperature.

The equilibrium relaxation modulus $G_{\infty,eff}$ increases with decreasing adhesive thickness. Hence, this result indicates the existence of stiffer interphases. With increasing adhesive thickness, the equilibrium relaxation modulus tends to reach a plateau. The contribution of the bulk adhesive then predominates in the effective mechanical behaviour of the joints and the contribution of the interphases is minimal. The investigation of adhesive joints with higher d_P is however necessary to assess the extent of the mechanical interphases in these samples.

The evolution of $G_{\infty,eff}$ at lower d_P is also an interesting issue: does $G_{\infty,eff}(d_P)$ continue to increase steadily up to reach a limited value corresponding to the stiffness of the interphase? To answer this question, local investigations of the mechanical properties in the adhesive joints would be necessary in the future.

A comparison of the $G_{\infty,eff}$ values with those of μ_{eff}, presented in Figure 4-18, shows that both $G_{\infty,eff}$ and μ_{eff} lie on the same straight line – cf. Figure 4-24.

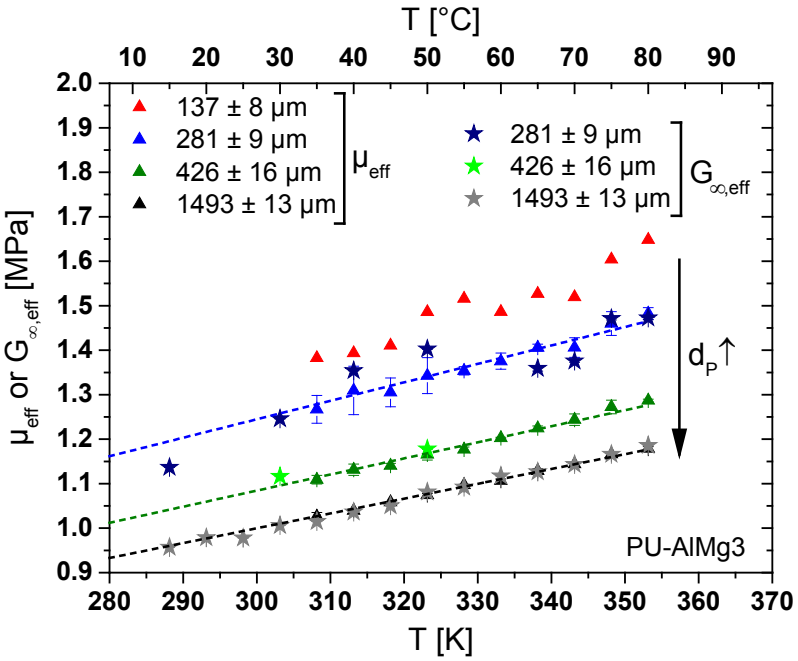

Figure 4-24: Comparison between the equilibrium shear stress relaxation modulus $G_{\infty,eff}$ (symbols "★") and the effective hyperelastic shear modulus μ_{eff} (symbols "▲") for PU-AlMg3 adhesive joints with different d_P.

Since the linear evolution of $G_{\infty,eff}(T)$ and $\mu_{eff}(T)$ continues into the viscoelastic state (T < 35 °C), it proves that the modulus in the relaxed viscoelastic state is also dominated by the entropic restoring forces for the measured d_P. As a consequence, $G_{\infty,eff}(T)$ must satisfy eq. (2.8)[16]. Thus, it is obvious that the evolution of $G_{\infty,eff}(d_P)$ in Figure 4-23 is reminiscent of apparent crosslink density $\kappa_{eff}(d_P)$ presented in Figure 4-20 – see Figure 4-25. Both quantities are directly ($G_{\infty,eff}$) or indirectly (κ_{eff}) related to the stiffness of the sample – see eq. (2.8). The comparison of their evolution with the bond line thickness proves the consistency of the results obtained with the shear tests at constant shear rate (κ_{eff}) and those of stress relaxation tests ($G_{\infty,eff}$). The stiffness and the apparent effective crosslink density of the sample increase with decreasing adhesive thickness. As discussed above, those both effects are surely linked together or even identical. If a link exists, it is though not possible to discern the cause and the effect without investigating the properties of the adhesive locally.

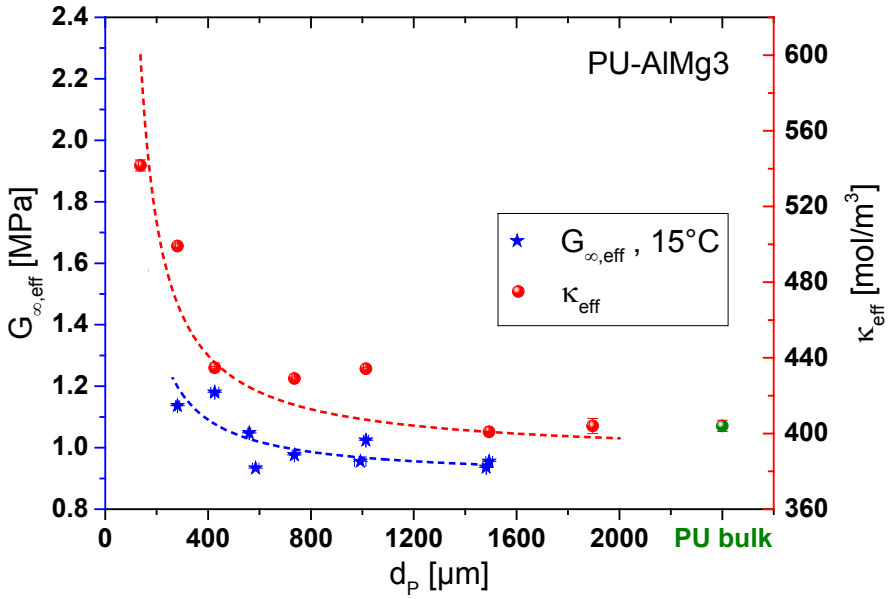

Figure 4-25: Comparison of the evolution of $G_{\infty,eff}(d_P)$ and $\kappa_{eff}(d_P)$ for PU-AlMg3 adhesive joints

To gain quantitative information about the bond line thickness dependence of the viscoelastic properties of the adhesive joints, and hence, to provide the required information for the characterisation of the interphases, creep tests are performed.

[16] Eq. (2.8): $\mu = \kappa \cdot R \cdot T$

4.2.3. **Isothermal creep tests at constant shear stress**

Figure 4-26 shows the creep curves of PU-AlMg3 samples with different d_P for a temperature of 15 °C. The adhesive thickness clearly influences the creep behaviour of the joints. The equilibrium compliance $J_{\infty,eff}$ has a lower value and is reached faster with decreasing d_P. These observations are also valid for the PU-stainless steel adhesive joints, as illustrated in Figure 4-27.

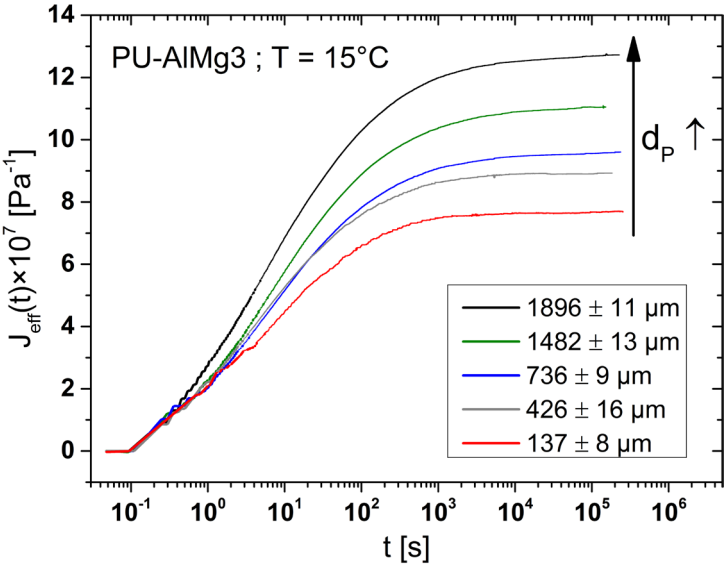

Figure 4-26: Bond line thickness dependence of the shear creep compliance $J_{eff}(t)$ as a function of time for AlMg3-PU adhesive joints at 15 °C.

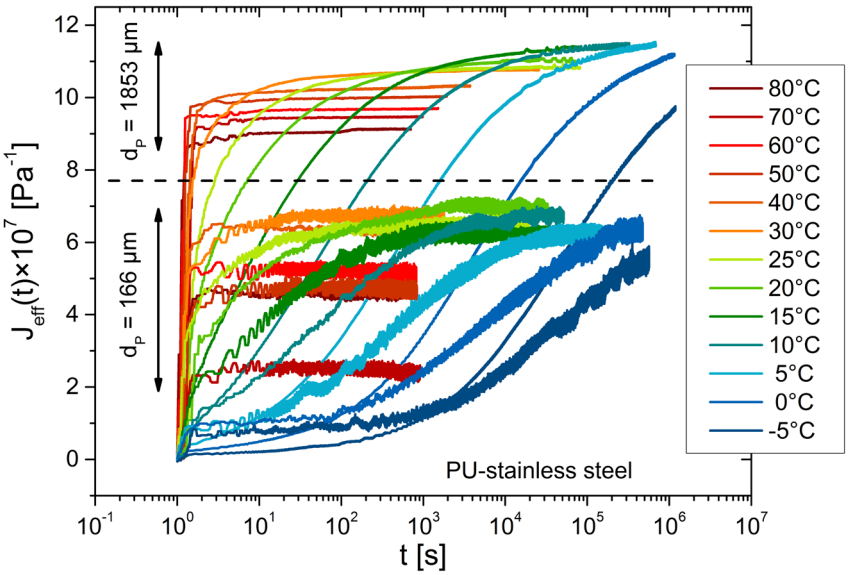

Figure 4-27: Comparison of the creep compliance $J_{eff}(t)$ as a function of time at different temperatures for PU-stainless steel adhesive joints with d_P = 1853 µm and 166 µm

First, the evolution of the reciprocal equilibrium compliance $J_{\infty,eff}^{-1}$ is plotted versus temperature as function of adhesive thickness and for both types of adhesive joint in Figure 4-28. Besides the linear evolution of $J_{\infty,eff}^{-1}$ with the temperature, already discussed in section 4.1.3, its bond line thickness dependence is obvious for both kinds of sample. The values of $J_{\infty,eff}^{-1}$ at high temperatures (T > 313 K) for the thin PU-stainless steel adhesive joint are surprisingly too high and point out a possible measurement error (see Figure 4-28, right). However, this does not affect that the thin and the thick samples have different mechanical properties at equilibrium, which confirms the existence of a mechanical interphase in these adhesive joints.

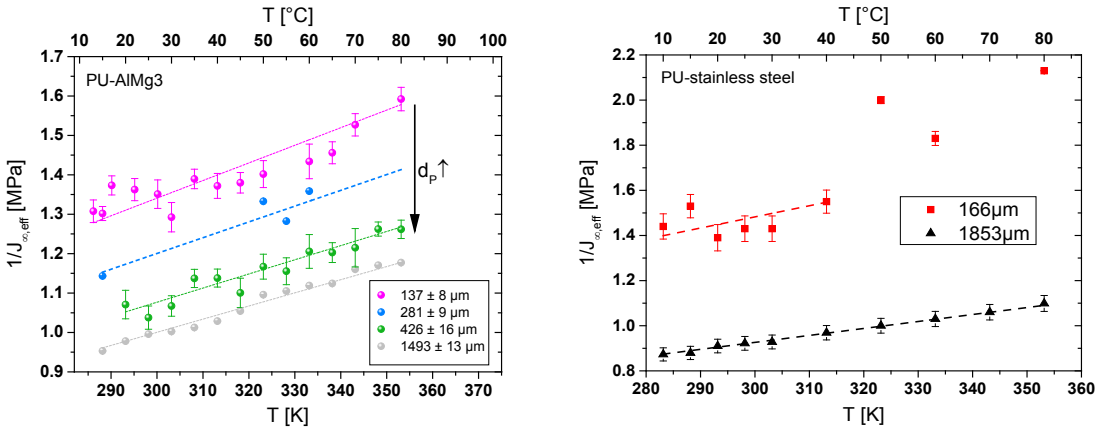

Figure 4-28: Evolution of the reciprocal equilibrium compliance $J_{\infty,eff}^{-1}$ as a function of the temperature for PU-AlMg3 (left) and PU-stainless steel (right) adhesive joints with different d_P. The dashed lines represent the linear fit curves $J_{\infty,eff}^{-1}(T) = a(d_P) \cdot T$ with a the slope of each fit curves.

Figure 4-29 confirms the eq. (4.1) for PU-AlMg3 adhesive joints with different d_P [17]. $J_{\infty,eff}^{-1}$, $G_{\infty,eff}$ and μ_{eff} show the same linear temperature dependence.

[17] No stress relaxation tests were performed on PU- stainless steel joints. Therefore, the following discussion focus only on the results obtained with PU-AlMg3 adhesive joints.

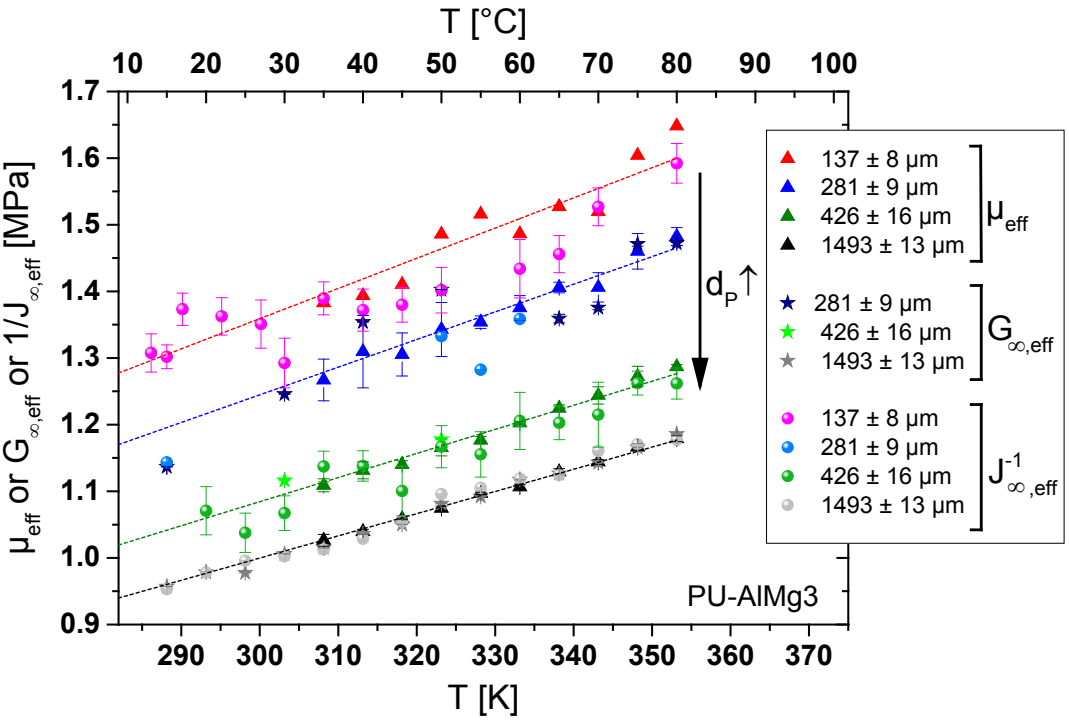

Figure 4-29: Comparison between the reciprocal equilibrium compliance $J_{\infty,eff}^{-1}$ (symbols "●"), the equilibrium shear stress relaxation modulus $G_{\infty,eff}$ (symbols "★") and the effective hyperelastic shear modulus μ_{eff} (symbols "▲") for PU-AlMg3 adhesive joints with different d_P.

Figure 4-30 gives a more precise description of the evolution of the equilibrium compliance $J_{\infty,eff}$ with the adhesive thickness for PU-AlMg3 samples. The measured values depict a nearly linear relation between $J_{\infty,eff}$ and d_P in the measured adhesive thickness range at different temperatures. At high d_P, a plateau value for the bulk adhesive is expected. Further experiments with thicker samples will be necessary to determine the extent of the observed mechanical interphase. At low d_P, $J_{\infty,eff}^{-1}$ is also expected to approach a limit value corresponding to the stiffness of the "pure" interphase according to Figure 1-1. This linear approximation is used to describe quantitatively the influence of d_P on the isothermal equilibrium creep compliance:

$$J_{\infty,eff}(d_P) = \alpha(T) \cdot d_P + \beta(T) \tag{4.2}$$

where $\alpha(T)$ and $\beta(T)$ are fit parameters.

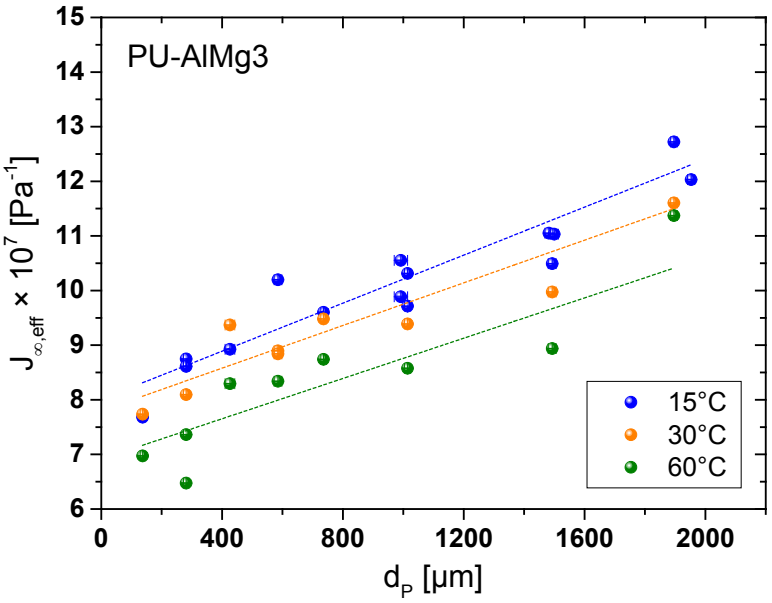

Figure 4-30: Bond line thickness dependence of the equilibrium shear compliance $J_{\infty,eff}$ for AlMg3-PU adhesive joints at 15 °C, 30 °C and 60 °C. The dashed lines represent the linear fit curves $J_{\infty,eff}(d_P) = \alpha(T) \cdot d_P + \beta(T)$ for each temperature.

An increasing creep compliance with increasing adhesive thickness means that thinner samples are stiffer than the thicker ones. The results from shear, stress relaxation and creep tests thus show the same size effect. A comparison between the equilibrium shear stress relaxation modulus $G_{\infty,eff}$ and the reciprocal equilibrium compliance $J^{-1}_{\infty,eff}$ is given in Figure 4-31. According to eq. (4.1) and (4.2), we have

$$G_{\infty,eff}(d_P) = J^{-1}_{\infty,eff}(d_P) = \mu_{eff}(d_P) = \frac{1}{\alpha(T) \cdot d_P + \beta(T)} \tag{4.3}$$

Equation (4.3) is used to quantify the isothermal bondline thickness dependence of $G_{\infty,eff}$ and $J^{-1}_{\infty,eff}$ in PU-AlMg3 adhesive joints – see dashed lines in Figure 4-31. The experimental results show that this rough approximation allows describing the influence of d_P on $G_{\infty,eff}$ and $J^{-1}_{\infty,eff}$ at given temperature. One could note that the plotted values of $J^{-1}_{\infty,eff}$ have been obtained from creep experiments performed with the universal testing machine and the creep testing machine. Since the results are quantitatively similar, the accuracy of the experimental set-ups is thus ensured.

The existence of stiff (or less compliant) interphase in the investigated adhesive joints is thereby proven.

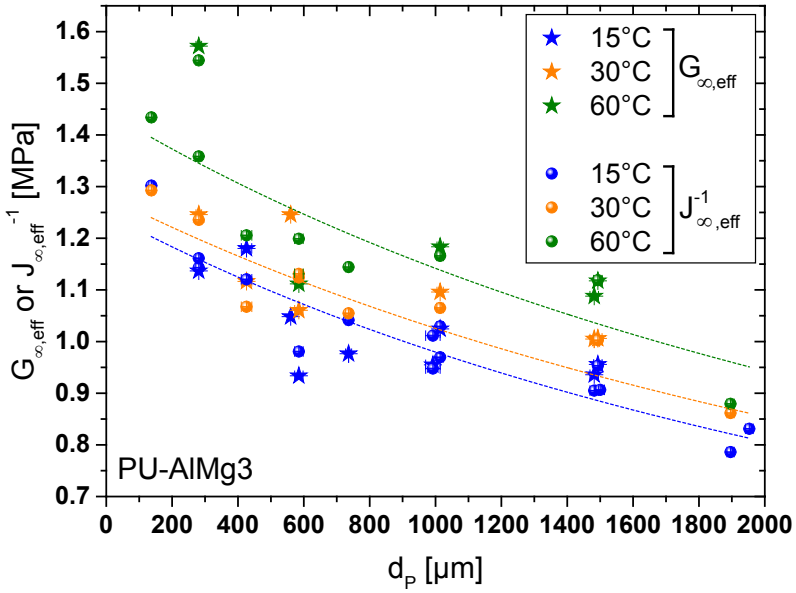

Figure 4-31: Adhesive thickness dependence of the equilibrium shear stress relaxation modulus $G_{\infty,eff}$ and the reciprocal equilibrium compliance $J^{-1}_{\infty,eff}$ for AlMg3-PU joints at 15 °C, 30 °C and 60 °C. Dashed lines represent the isothermal bondline thickness dependence using eq. (4.3).

In order to characterise the viscoelastic properties of that interphase and more generally of the adhesive joints, discrete retardation time spectra are calculated from the creep experiments shown in Figure 4-26. For a better identification of the influence of the bond line thickness, the discrete retardation time spectra, displayed in Figure 4-32, have been fitted with cubic polynomial functions (dashed lines, according to section 2.6).

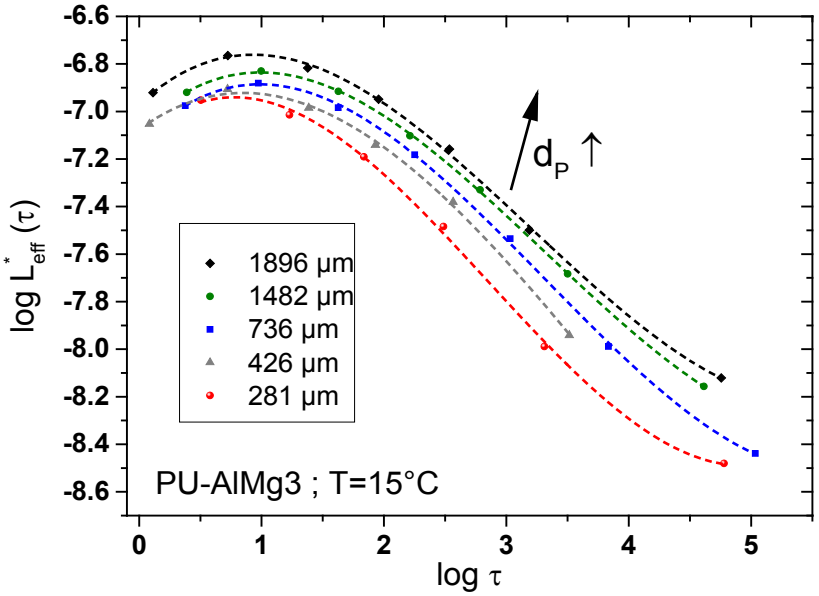

Figure 4-32: Bond line thickness dependence of the discrete retardation time spectra of AlMg3-PU adhesive joints at 15 °C

The retardation time spectra reveal the bond line thickness dependence of the viscoelastic properties in AlMg3-PU adhesive joint. The evolution of the spectra with d_P describes quantitatively the observation made by the eye from the creep curves in Figure 4-26. At a first sight and for a given retardation time τ , the corresponding compliance $L^*_{eff}(\tau)$ is higher for thicker samples.

However, as suggested by the black arrow in Figure 4-32, the influence of the bond line thickness does not only result in a vertical shift of the spectra to higher compliance with increasing d_P, but is also accompanied with a slight temporal shift.

In order to highlight this effect, Figure 4-33 focuses on the maxima of the retardation time spectra for the thinnest and the thickest measured sample. The horizontal shift to longer retardation time is then clearly visible. The spectrum of the thin sample reaches its maximum at shorter retardation times than that of the thick one. This indicates that the retardation processes occur more rapidly in thinner samples, confirming thereby the qualitative observation made from the creep curves in Figure 4-26: The thinner the adhesive joint, the shorter it takes to reach the creep equilibrium.

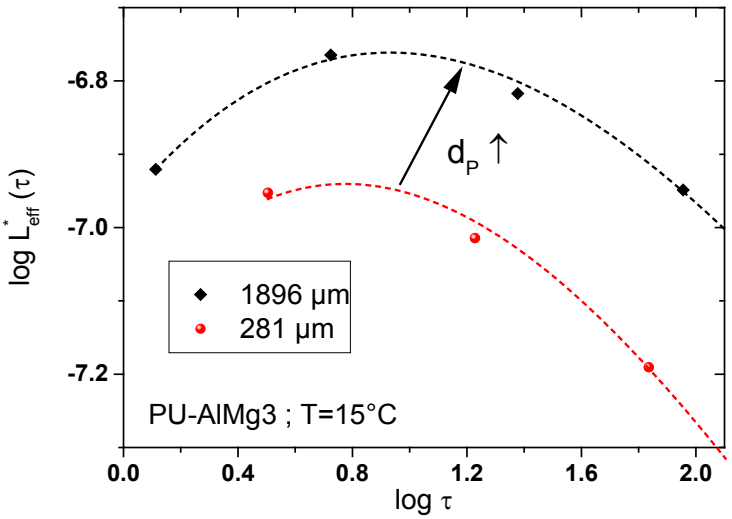

Figure 4-33: Close-up on the bond line thickness dependence of the discrete retardation time spectra of AlMg3-PU adhesive joints at 15 °C

Similar findings concerning the bond line thickness dependence of the retardation time spectra have been noticed for PU-stainless steel adhesive joints, as depicted in Figure 4-34.

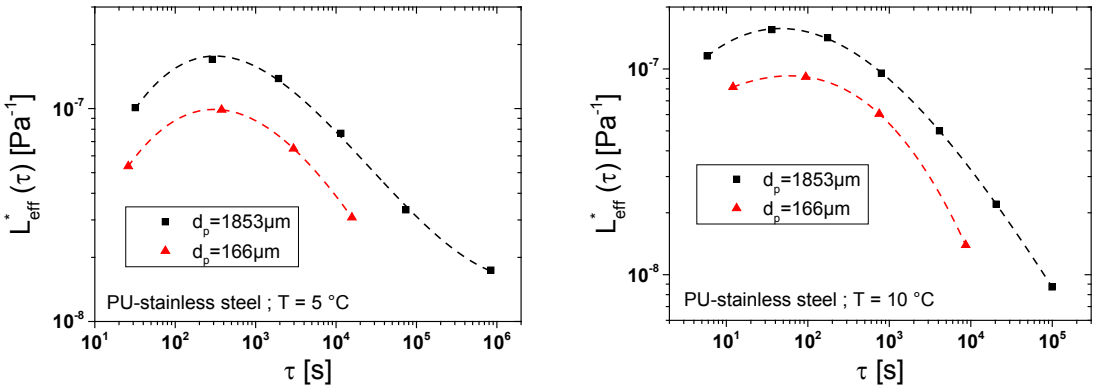

Figure 4-34: Bond line thickness dependence of the discrete retardation time spectra of PU-stainless steel adhesive joints at 5 °C (left) and 10 °C (right)

Résumé

Both elastic and viscoelastic properties of the investigated adhesive joints depend on the bond line thickness. The samples become stiffer with decreasing adhesive thickness. This effect is interpreted as the formation of mechanical interphases in the polyurethane adhesive in contact with the metal substrates. The evaluation of the retardation time spectra reveals complex thermorheological behaviour of the viscoelastic functions in the adhesive joints.
Besides a straight mathematical translation of the retardation spectrum as a function of the temperature and adhesive thickness, a modification of its shape can be envisaged, especially at low temperature and long retardation times. However, the measuring time range and the accuracy of the measurements limit the amount of information in these ranges. A calculation of the viscoelastic function is performed in the next chapter to discuss a further possibility to describe quantatively the influence of interphases on the mechanical behaviour of adhesive joints.

4.3. Calculation of the viscoelastic functions of PU-metal adhesive joints

Now that the adhesive thickness and temperature dependence of the mechanical behaviour of adhesive joints has been independently identified and characterised by means of shear, stress relaxation and creep experiments, the correlation between the measured viscoelastic properties can be assessed. As presented in the previous chapter, the elastic properties of adhesive joints can be directly and completely characterised in the measured range, because they are time-independent material parameters (and thus, not influenced by some measurement conditions such as the strain rate or the measuring time range). This is, by definition, not the case for the viscoelastic properties. Only a part of the adhesive dynamics could be characterised by determining a fraction of the retardation time spectrum. The question is whether this limited amount of information is enough for a good approximation of the mechanical behaviour of the investigated bonded joints and whether this approximation could consider both the temperature and the adhesive thickness dependence.

4.3.1. Interrelation among the viscoelastic functions - Verification

Using the relations given in section 2.6, it is possible to calculate a relaxation time spectrum or any other viscoelastic function or constant from a retardation time spectrum – see red path in Figure 2-30. This interrelation between the viscoelastic functions is of special interest to verify the experimental results. For instance, a relaxation test can be calculated from a creep test and quantitatively compared to an experimental curve. Consequently, this is a way of verifying the accuracy of the measured viscoelastic functions and determining whether the information from the discrete retardation spectrum is enough to describe the viscoelastic properties of the adhesive joints. The results of these calculations are discussed in this section using the measurements obtained for a PU-AlMg3 adhesive joint with a $d_P = 736 \pm 9$ µm.

As already mentioned, all the equations necessary for the calculation of the following results are discussed in chapter 2.6. For the sake of clarity, the calculation steps are here briefly repeated.

In comparison to the other tests performed in this work, creep experiments describe the adhesive dynamics in the broadest time and temperature range, providing more information on the viscoelastic properties of the adhesive joints. Creep compliance $J_{eff}(t)$ is then chosen as starting point for the calculation. The creep curve is fitted with the analytical solution for a creep test in the Zener model, considering the non-sudden load of the sample – see eq. (2.115) [18] and fit parameters in Table 2-1 (page 45). This consideration prevents the influence of the

[18] Eq. (2.115): $\gamma(t) = \gamma_0 + \sum_{i=1}^{n} A_i \cdot \left(e^{-t/\tau_i} - e^{(t_0 - t)/\tau_i} \right)$ with $\gamma_0 = T_{12}^{\,0} \cdot \left(J_0 + \sum_{i=1}^{n} J_i \right)$ and $A_i = \frac{T_{12}^{\,0} \cdot J_i \cdot \tau_i}{t_0}$

sample loading in the calculation of the retardation time spectrum. After the determination of the corresponding discrete retardation time spectrum $L_{eff}^{*}(\tau)$, this latter is fitted with a cubic polynomial function to obtain, by extrapolation, a continuous retardation time spectrum $L_{eff}(\tau)$ (red curve in Figure 4-35) – see eq. (2.160). The cubic polynomial function and the fit parameters used in Figure 4-35 are presented in Table 4-1.

Since $J_{eff}(t)$ is measured for $t \geq t_0$ (see Figure 4-26), the parameters $J_{eff,\infty}$, τ_i and J_i are also determined for $t \geq t_0$. Thus $L_{eff}^{*}(\tau)$ is calculated for the same τ_i interval – Figure 4-32. Through the fit operation with the cubic polynomial function, $L_{eff}^{*}(\tau)$ is converted in $L_{eff}(\tau)$. Therefore, $L_{eff}(\tau)$ is validated by experimental data in the same τ_i interval as $L_{eff}^{*}(\tau)$ - see again Figure 4-32.

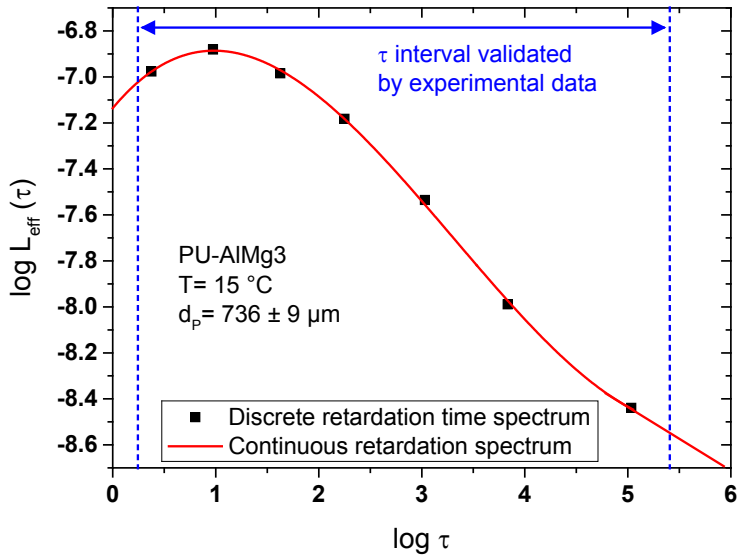

Figure 4-35: Discrete and continuous retardation spectrum for an AlMg3-PU adhesive joint with d_P = 736 ± 9 µm at 15 °C.

Table 4-1: Parameters of the continuous retardation time spectrum shown in Figure 4-35.

Model	Cubic		
Equation	$\text{Log}(L_{eff}(\tau)) = a_0 + a_1 \cdot (\log \tau) + a_2 \cdot (\log \tau)^2 + a_3 \cdot (\log \tau)^3$		
Reduced χ^2	$2.9789 \cdot 10^{-4}$		
Coeff. of determination R^2	0,99915		
	Parameter	Value	Standard deviation [%]
	a_0	-7.136	0.4076
	a_1	0.5396	8.901
	a_2	-0.3221	6.479
	a_3	0.0324	7.84

This simulated continuous retardation spectrum is in turn used for the backward calculation of the creep compliance as a function of time $J_{eff}(t)$. Inserting the cubic polynomial function presented in Table 4-1 in eq. (2.120)[19], it gives

$$\begin{aligned} J_{eff}(t) &\approx J_0 + \int_0^t \frac{L_{eff}(\tau)}{\tau} \cdot d\tau \\ &\approx J_0 + \int_{\tau_a}^{\tau_e} \frac{a_0 + a_1 \cdot \tau + a_2 \cdot \tau^2 + a_3 \cdot \tau^3}{\tau} \cdot d\tau \end{aligned} \tag{4.4}$$

In this way, it is possible to check if the approximations, made hitherto, are acceptable or not by comparing the experimental $J_{eff}(t)$ with the back calculated one, as shown in Figure 4-36.

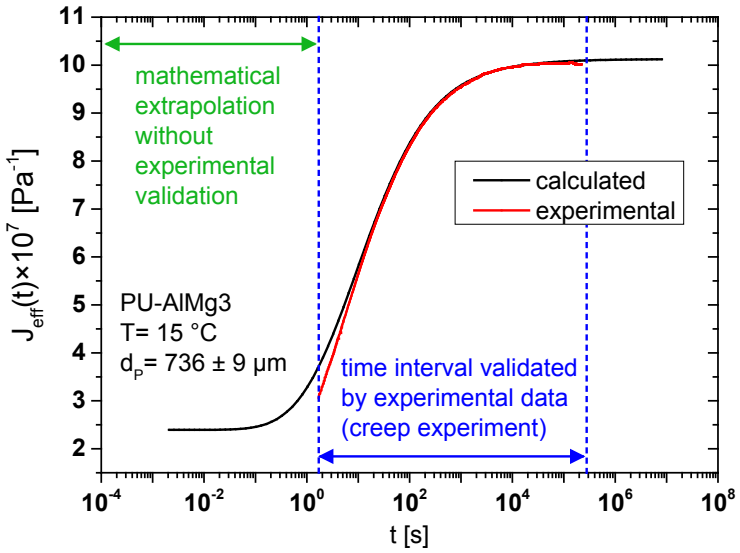

Figure 4-36: Comparison between the experimental and the calculated creep function $J_{eff}(t)$ for an AlMg3-PU adhesive joint with d_P = 736 ± 9 µm at 15 °C

Figure 4-36 shows that the calculated and the experimental creep compliance coincide very well as discussed above. The increasing deviations at short measuring times result from the experimental limitation for measuring times $t \geq 10$ s. Because of the duration of the sample loading, the fast retardation processes, which are already taking place then, cannot be experimentally monitored. In turn, the calculated discrete retardation time spectrum cannot consider these retardation processes. This loss of information affects all further calculations. However, only after about 10 seconds, both curves superimpose. Below this value, the discrepancies between the calculated $J_{eff}(t)$ and the measured one increases as shown in Table 4-2.

[19] Eq. (2.120): $J(t) \approx J_0 + \int_0^t \frac{L(\tau)}{\tau} \cdot d\tau$

Table 4-2: Discrepancy between the calculated and experimental values of $J_{eff}(t)$.

t [s]	$J_{eff}(t)$ experimental [Pa^{-1}]	$J_{eff}(t)$ calculated [Pa^{-1}]	Discrepancy [%]
16.4	$6.3326 \cdot 10^{-7}$	$6.4340 \cdot 10^{-7}$	1.6
10.3	$5.6889 \cdot 10^{-7}$	$5.8414 \cdot 10^{-7}$	2.6
8.2	$5.3361 \cdot 10^{-7}$	$5.6372 \cdot 10^{-7}$	5.4
4.1	$4.3136 \cdot 10^{-7}$	$4.6707 \cdot 10^{-7}$	7.6
2.1	$3.3539 \cdot 10^{-7}$	$3.9025 \cdot 10^{-7}$	14

Hence, the approximations made so far are acceptable and the fitted continuous retardation time spectrum gives a realistic description of the mechanical behaviour of the adhesive joints. In this case, the calculations can be carried on.
If the calculated and measured creep curves would be different, the calculated parameters should not be used for subsequent calculations. Experimental observations have shown that the back calculation of the creep curve succeed when the (main) maximum in the (discrete) retardation time spectrum is clearly displayed. This finding limits the measuring temperature range for these backward calculations. A clear maximum in the retardation spectra can only be observed within the experimental time window if the measuring temperature is in the upper half of the glass transition. If the temperature is too high, most of the retardation processes are too fast to be observed. The maximum occurs then at very short time, which cannot be experimentally measured. At low measuring temperature, the maximum occurs at very long retardation time, drastically increasing the experiment duration.

A successful back calculation of the creep curve also means that the theory underlying the calculations applies and hence that the experiments have been performed in the linear viscoelastic range of the polyurethane adhesive. This confirms the results obtained in the section 3.4.

In the following step, the continuous relaxation time spectrum $H_{eff}(\tau)$ is calculated using eq. (2.163)[20] – see Figure 4-37 in black. Inserting eq. (2.160) in eq. (2.163), we obtain:

$$H_{eff}(\tau) = \frac{a_0 + a_1 \cdot \tau + a_2 \cdot \tau^2 + a_3 \cdot \tau^3}{\left[J_0 - \int_{-\infty}^{+\infty} \frac{a_0 + a_1 \cdot \varepsilon + a_2 \cdot \varepsilon^2 + a_3 \cdot \varepsilon^3}{1 - \varepsilon/\tau} d \ln \varepsilon \right]^2 + \pi^2 \cdot \left(a_0 + a_1 \cdot \tau + a_2 \cdot \tau^2 + a_3 \cdot \tau^3 \right)^2} \quad (4.5)$$

[20] Eq. (2.163): $H(\tau) = \frac{L(\tau)}{\left[J_0 - \int_{-\infty}^{+\infty} \frac{L(\varepsilon)}{1 - \varepsilon/\tau} d \ln \varepsilon \right]^2 + \pi^2 \cdot (L(\tau))^2}$

The numerical values are calculated with the parameters a_i presented in Table 4-1. By calculating $H_{eff}(\tau)$ from $L_{eff}(\tau)$, $H_{eff}(\tau)$ is validated by experimental data in the same τ_i interval as $L(\tau)$. The values of the discrete relaxation time spectrum $H^*_{eff}(\tau)$ (see Figure 4-37 in red) obtained from a stress relaxation experiment (see Figure 2-28) confirm the calculated continuous relaxation time spectrum $H_{eff}(\tau)$.

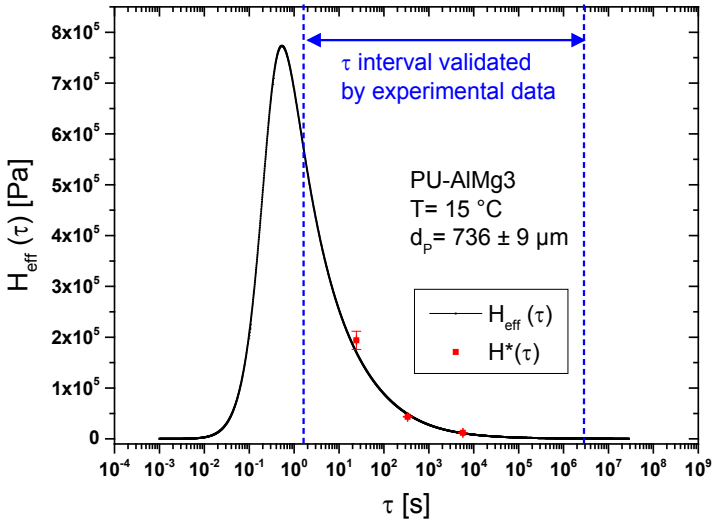

Figure 4-37: Calculated continuous relaxation time spectrum $H_{eff}(\tau)$ from the continuous retardation time spectrum $L_{eff}(\tau)$ and discrete relaxation time spectrum $H^*_{eff}(\tau)$ fitted from the experimental stress relaxation modulus $G_{eff}(t)$ (see Figure 2-28) for an AlMg3-PU adhesive joint with d_P = 736 ± 9 µm at 15 °C

The stress relaxation modulus $G_{eff}(t)$ is determined by means of eq. (2.164)[21]. Again, measured and calculated results are compared - Figure 4-38. The calculated stress relaxation modulus overlaps the experimental one, thereby demonstrating the accuracy of the calculation method. Since the calculated values are based on the results from an experimental creep test, it can be concluded that the measured creep and relaxation tests provide quantitatively comparable results.

Besides the remarkable consistency of the results from creep and stress relaxation tests, Figure 4-38 gives the opportunity to evaluate those relaxation processes, which normally cannot be observed with experimental stress relaxation tests as they occur during the loading of the sample. Figure 4-37 shows that at 15 °C most of the relaxation processes are completed when the

[21] Eq. (2.164): $G_{eff}(t) - G_\infty \approx \int_{\tau_a}^{\tau_e} \frac{H(\tau)}{\tau} \cdot d\tau$

constant strain is reached, after about 40 seconds. Thus, $G_{eff}(t)$ calculated from $H_{eff}(\tau)$ is indirectly validated in a larger time range by the creep test than the stress relaxation test (red curve in Figure 4-38).

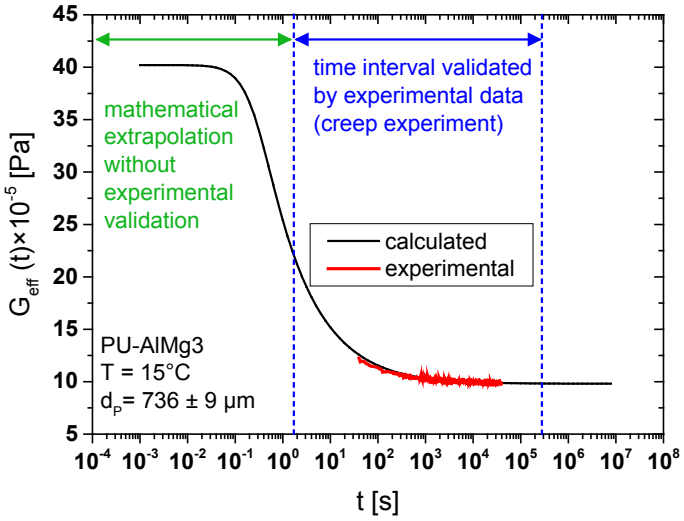

Figure 4-38: Comparison between the experimental and the calculated stress relaxation modulus $G_{eff}(t)$ for an AlMg3-PU adhesive joint with d_P = 736 ± 9 µm at 15 °C

As for the calculated creep function $J_{eff}(t)$ in Figure 4-36, the values of $G_{eff}(t)$ at short relaxation times are only the results of the mathematical extrapolation without any experimental verification. These data cannot be experimentally measured due to the non-sudden loading of the adhesive joint.

One could note that $G_{eff}(t)$ so calculated represents the stress relaxation curve after a sudden strain since the influence of the non-sudden sample loading during the creep experiment have been eliminated. This explains the small discrepancies between the experimental and the calculated values of $G_{eff}(t)$ for t between 40 s and 60 s.

This approach not only shows that the interrelations among the viscoelastic functions for the linear viscoelasticity applies, but also that more information about $H_{eff}(\tau)$ and $G_{eff}(t)$ can be obtained from creep tests than from stress relaxation tests.

Since the calculated stress relaxation modulus $G_{eff}(t)$ reproduces the experimental curves in the experimental time window, the data can be used for the final step of the calculation. The calculated $G_{eff}(t)$ is fitted with the analytical solution of the generalised Maxwell model for a stress relaxation test after sudden strain in order to obtain the discrete material parameter pairs: $(G_i;\tau_i)$. These parameters can be then implemented in the analytical solution of the generalised Maxwell model for shear test at constant shear rate. Figure 4-39 depicts the comparison of calculated and measured shear tests for three different shear rates $\dot{\gamma} = d\gamma/dt$: $4 \cdot 10^{-2}$ s^{-1}, $4 \cdot 10^{-3}$ s^{-1}, $4 \cdot 10^{-4}$ s^{-1}.

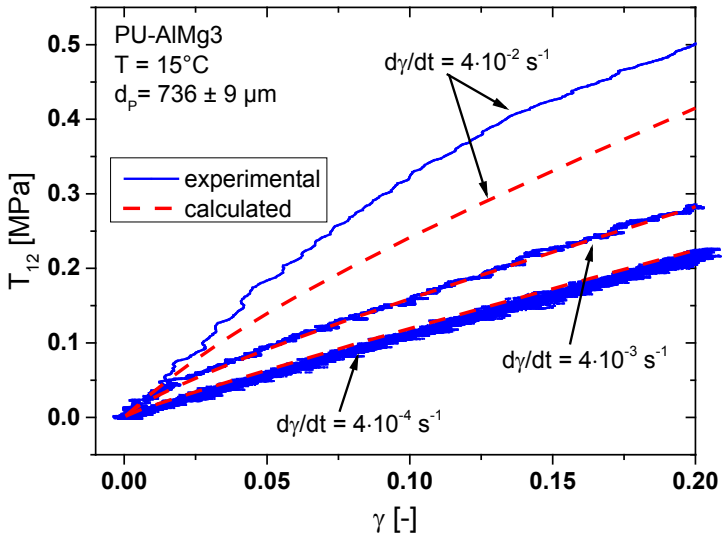

Figure 4-39: Comparison between the experimental and the calculated shear tests at constant shear rate for an AlMg3-PU adhesive joint with d_P = 736 ± 9 µm at 15 °C

The calculated and measured curve coincides very well for the two slower shear rates. However, the calculated shear test for the fastest shear rate shows a big discrepancy with the experimental curve. This statement is observed not only in the example chosen here, but also in all other adhesive joints which have been tested with shear tests. For all samples, the experimental curve with $\dot{\gamma} = 4 \cdot 10^{-2}\, s^{-1}$ shows higher value of the shear modulus $M_{eff}(\gamma, t, d_P)$ than the calculated one. To understand this effect, it is necessary to remember that the original data chosen for performing the calculations are those from the creep tests. As mentioned, many times before, the retardation processes occurring during the sample loading cannot be considered in the subsequent calculations and the corresponding information gets lost. This systematic underestimation of $M_{eff}(t)$, which occurs in the simulated curves, is due to the fact that fast relaxation processes are neither detected in creep experiments ($t_0 \approx$ 2-3 s) nor in stress relaxation experiments ($t_0 \geq$ 30 s). However, these fast processes are obviously already relevant for $T_{12}\left(\gamma, \dot{\gamma} = 4 \cdot 10^{-2}\, s^{-1}\right)$. Shear tests with $\dot{\gamma} = 4 \cdot 10^{-2}\, s^{-1}$ last about five to six seconds. The fast relaxation processes occurring within this period play an important role in the mechanical response of the adhesive joint. Since a significant part of these relaxation processes are not considered by the calculation, the sample appears to be more ductile than it actually is.
The contribution of these fast relaxation processes is not so high for the slower shear rates and thus influences the corresponding calculations to a lesser extent. The mainly relevant contributions of the relaxation processes for the strain rates can be measured in the experimental time window of the creep tests.

With the calculation of shear tests, the calculation is completed. The presented example shows that the calculation of viscoelastic functions allows comparing *quantitatively* the results of the different experiments for a given measuring temperature, time interval or deformation rate and adhesive thickness. The consistency of the results indicates that the experimental procedure is

accurate enough to characterise the mechanical behaviour of adhesive joints. The temperature and thickness dependence of the effective viscoelastic properties, shown in chapter 4 is also verified for different measured temperatures and d_P.

Based on these findings, a way to predict the mechanical behaviour of adhesive joints should be found by implementing both temperature and adhesive thickness dependence into the calculations presented above.

For this purpose, the suitability of the time-temperature equivalence is first considered whether it can describe the temperature dependence of the mechanical properties in adhesive joints discussed in section 4.1.

4.3.2. **Time – temperature equivalence - Discussion**

An indication of the relation between the measuring time and temperature in the mechanical behaviour of the investigated adhesive joints has already been noticed in the results presented in section 4.1.

In practice, the experimental time scale and measuring temperature range are limited. Therefore, not all relaxation phenomena can be observed within one experiment. To overcome this issue, the interdependence of the viscoelastic behaviour on time and temperature has been investigated over the last decades.

As early as in 1941 Leaderman noticed that the shape of the creep curves of some viscoelastic materials at different temperatures does not change much and that the curves shift on time scale [175]. This concept, also known as the time–temperature equivalence, intends to describe the temperature dependence of the mechanical properties in polymers by a simple temporal shift of the viscoelastic functions to longer times with decreasing measuring temperature. It can also be used to build a master curve based on different isothermal creep curves. It implies that the viscoelastic behaviour at one temperature can be related to that at another temperature by only altering the timescale with a shift factor, $a_T(T)$ [176]. The mechanical behaviour of such materials is qualified as “thermo-rheologically simple”.

Based on the fitting of a large number of data for different polymers *in the glass transition region*, Williams, Landel and Ferry suggested the following equation to describe the temperature dependence of the shift factor $a_T(T)$ [177]:

$$\log a_T(T, T_{ref}) = -\frac{C_1 \cdot \left(T - T_{ref}\right)}{C_2 + \left(T - T_{ref}\right)} \tag{4.6}$$

T_{ref} is an arbitrarily chosen reference temperature, C_1 and C_2 are material-specific parameters whose values depend on the chosen reference temperature.

Further models have been established in order to improve the long-term prediction of the creep compliance of polymers because experimental data show that $J(t)$ curves happen to show some vertical shift in addition to the horizontal shift $a_T(T)$. A commonly applied approach is the addition of a vertical shift factor $a_g(T)$ [178]. A time-dependent shift factor can be defined to give a better description of thermo-rheologically complex material behaviour. Although some physical motivations have been put forward, the use of such vertical shift – unlike the horizontal one – does not base on a clear physical foundation [176]. That is why, the simple time-temperature equivalence, i.e. the thermo-rheologically simple shift, is used in this work to give an approximation of the experimentally observed phenomena.

A representative example, illustrating the results obtained for a PU-AlMg3 adhesive joint with d_P = 1482 ± 13 µm, is given in what follows. The temporal shift factor, $a_T(T)$, (or respectively $\log a_T(T)$ in the logarithmic time scale) is determined for the time-temperature equivalence by means of the isothermal creep curves as depicted in Figure 4-40. A reference value of $J_{eff}^{ref}(t)$ is arbitrarily chosen (here: $J_{eff}^{ref}(t) = 6 \cdot 10^{-7}$ Pa^{-1}) and $\log a_T(T)$ is calculated with respect to a reference temperature (here: T_{ref} = 5 °C) for different temperatures:

$$t\left[J_{eff}^{ref}(T)\right] = a_T \cdot t\left[J_{eff}^{ref}(T_{ref})\right] \tag{4.7}$$

Thus

$$\log t\left[J_{eff}^{ref}(T)\right] = \log a_T + \log t\left[J_{eff}^{ref}(T_{ref})\right] \tag{4.8}$$

For a better sensitivity, the chosen value for $J_{eff}^{ref}(t)$ should be in the transition region of the creep curves, i.e. within the range of $J_{eff}(t)$ showing the greatest slope.

At the chosen reference temperature T_{ref} = 5 °C, the retardation processes are slower than at the other measuring temperatures. The time required to reach the specified compliance is then shorter with increasing temperature $t\left[J_{eff}^{ref}(T)\right] < t\left[J_{eff}^{ref}(T_{ref})\right]$. Therefore, $a_T < 1$ and $\log a_T < 0$ hold for all measuring temperatures. These values are then plotted as a function of the temperature difference ($T - T_{ref}$) and fitted with the Williams–Landel–Ferry equation (4.6) in Figure 4-41. The obtained fit curve is supposed to approximate the temperature dependence of the viscoelastic properties of the adhesive joint, at least in the measuring temperature range.

In addition to the time shift of the viscoelastic properties with the measuring temperature, differences in the equilibrium plateau values of the creep curves can also be identified in Figure 4-40. This is the result of the temperature dependence of the equilibrium compliance $J_{\infty,eff}(T)$

which was already discussed in chapter 4.1.3. It is obvious, that this effect cannot be reflected only by a mathematical translation of the creep curve along the time scale with the temperature – see Figure 4-40, right. It is a limitation of the time-temperature equivalence which only describes thermo-rheologically simple behaviour.

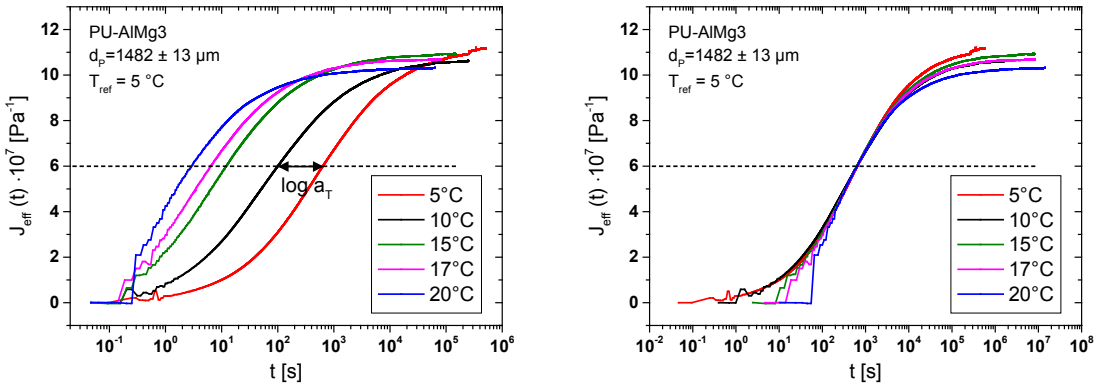

Figure 4-40: Time - temperature equivalence – Determination of the shift factor, $\log a_T$ (left) and shifted creep compliance $J_{eff}(T)$ providing the master curve (right) according to the calculated shift factor for a PU-AlMg3 adhesive joint with d_P = 1482 ± 13 µm.

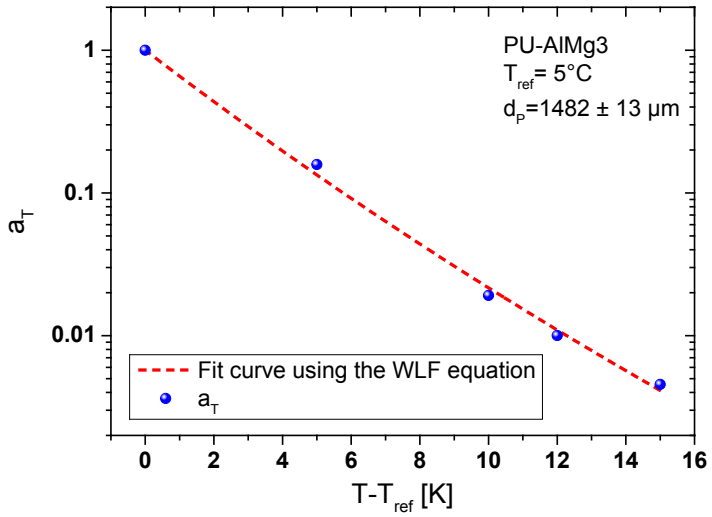

Figure 4-41: Time - temperature equivalence – Approximation of the temperature dependence of the shift factor, a_T, using the Williams–Landel–Ferry equation ; see eq.(4.6), for a PU-AlMg3 adhesive joint with d_P = 1482 ± 13 µm

Table 4-3: Fit parameters of the data shown in Figure 4-41 using the WLF equation.

Model	WLF equation		
Equation	$\log a_T(T,T_{ref}) = -\frac{C_1 \cdot (T - T_{ref})}{C_2 + (T - T_{ref})}$ (4.6)		
Reduced χ^2	0.00382		
Coeff. of determination R^2	0,99583		
	Parameter	Value	Standard deviation [%]
	C_1	95.17133	75
	C_2	17.50789	66

Despite of the limitation of the time-temperature equivalence, this constitutes a relatively easy way to approximate the temperature dependence of the mechanical properties of adhesive joints. Figure 4-40 (right) shows that the so-called master curve for $J(t,T_{ref})$ only works in a certain time range. For smaller and larger times, the creep curves diverge from each other. In order to estimate the relevance of its approximation and its appropriateness for the calculations presented in the previous section, the time-temperature equivalence is applied to the discrete retardation time spectra $L^*_{eff}(\tau,T)$.

At a given retardation time t_1, the corresponding intensity of the discrete retardation time spectrum $\log L^*_{eff}(\tau)$ measured at a temperature T_1 can be calculated with the equation (2.122) expressed in term of logarithms:

$$\begin{aligned} \log L^*_{\mathrm{eff}}(\tau) &\approx \log\left(t_1 \times \sum_{i=1}^{n} \frac{J_i}{\tau_i} \times e^{-\frac{t_1}{\tau_i}}\Big|_{t_1=\tau} \right) \\ &\approx \log\left(t_1\big|_{t_1=\tau} \right) + \log\left(\sum_{i=1}^{n} \frac{J_i}{\tau_i} \times e^{-\frac{t_1}{\tau_i}}\Big|_{t_1=\tau} \right) \end{aligned} \tag{4.9}$$

Figure 4-42 illustrates the mathematical construction of a creep curve at a temperature T_2 (in red) from an experimental creep curve (in black) measured at T_1 ($T_1 > T_2$)[22], as described by the time-temperature equivalence. The relation between the time scales of the creep curves is given by

$$\log t_2 = \log t_1 + \log a_T \tag{4.10}$$

[22] Here is $T_1 > T_2$ considered in contrast to the examples presented in Figure 4-40 and in Figure 4-41.

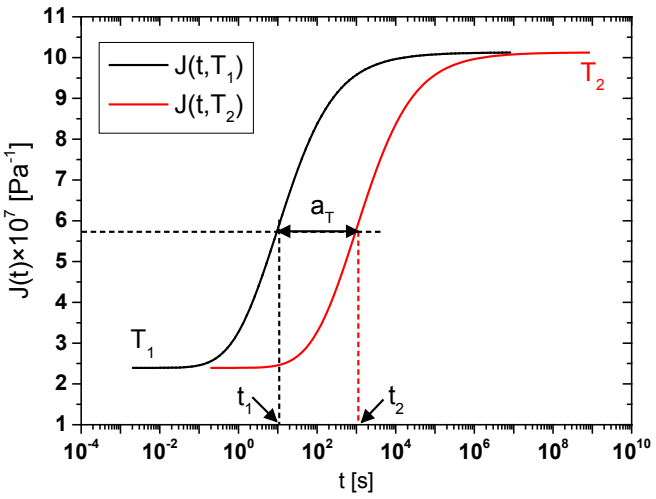

Figure 4-42: Time – temperature equivalence**:** mathematical construction of $J(t,T_2)$ with the experimental creep curve $J(t,T_1)$ with $T_1 > T_2$

This time-temperature equivalence implies that the *shape* of $J_{eff}(t)$ does not depend on T and hence the nature of the relaxation/retardation processes and their activation sequence occur invariant of temperature; only the speed of these processes is changed by the same factor. In this case, all the retardation times are affected by the same shift factor as described by the equation (4.10) for the creep curves:

$$\log \tau_i(T_2) = \log \tau_i(T_1) + \log a_T \qquad \forall \tau_i \tag{4.11}$$

Combining the equations (4.9) and (4.10) the intensity of the shifted discrete retardation time spectrum (obtained using the time-temperature equivalence) is

$$\log L^*_{\text{eff}}[\tau(T_2)] \approx \log\left(t_2\big|_{t_2=\tau(T_2)}\right) + \log\left(\sum_{i=1}^{n} \frac{J_i}{\tau_i(T_2)} \times e^{-\frac{t_2}{\tau_i(T_2)}}\right) \tag{4.12}$$

By considering that $\tau_i(T_2) = 10^{\log \tau_i(T_2)}$ and with equation (4.11), equation (4.12) becomes

$$\begin{aligned} \log L^*_{\text{eff}}[\tau(T_2)] &\approx \log\left[a_T \cdot t_1\big|_{t_1=\tau(T_1)}\right] + \log\left[\sum_{i=1}^{n} \frac{J_i}{a_T \cdot \tau_i(T_1)} \times e^{-\frac{t_1}{\tau_i(T_1)}}\right] \\ &\approx \log a_T + \log t_1\big|_{t_1=\tau(T_1)} - \log a_T + \log\left[\sum_{i=1}^{n} \frac{J_i}{\tau_i(T_1)} \times e^{-\frac{t_1}{\tau_i(T_1)}}\right] \\ &= \log L^*_{\text{eff}}[\tau(T_1)] \end{aligned} \tag{4.13}$$

Eq. (4.13) demonstrates that $L^*_{eff}(\tau)$ shifts only horizontally on τ -axis according to eq. (4.11). Hence, the shape and the intensity of the retardation spectra are thus not modified by applying the time-temperature equivalence in the way defined by eqs. (4.10) and (4.11).

The retardation time spectra, corresponding to the creep curves shown in Figure 4-40, are then shifted using the determined values of $\log a_T$ in Figure 4-41 by means of the WLF equation. The results are shown in Figure 4-43.

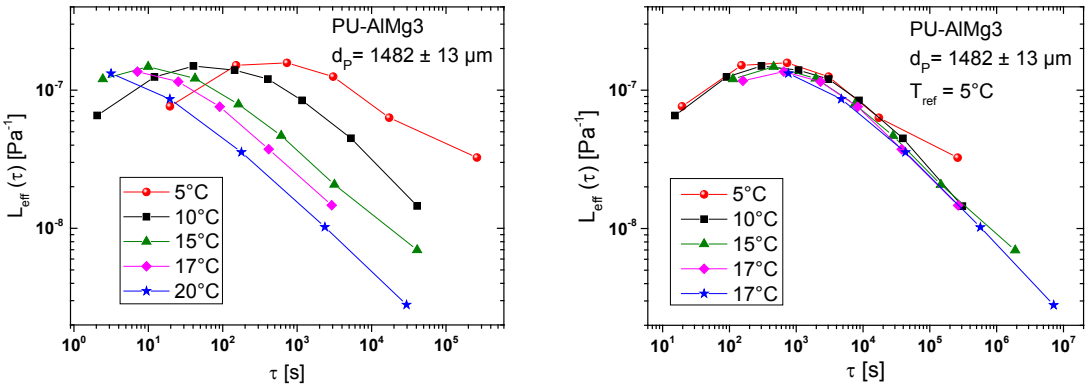

Figure 4-43: Application of the time - temperature equivalence to the retardation spectra of a PU-AlMg3 adhesive joint with d_P = 1482 ± 13 µm: left, measured retardation spectra; right, shifted retardation spectra (T_{ref} = 5 °C) providing the $L_{eff}(\tau)$ master curve.

As expected by the calculations above, the shifted spectra are superimposed at first sight. The deviations occur mainly at large τ:

- The value on the right at 5 °C is too high because $J_{eff}(t)$ did not reach the equilibrium due to the perturbation in $J(t)$ for t = 3-4·10^5 s – see Figure 4-40.
- The value at 15°C is also a little too high, but Figure 4-40 shows that the creep plateau has been reached.
- Figure 4-40 confirms that the creep equilibrium has been reached at 20 °C. Therefore, the value on the right is reliable.

The data in Figure 4-43 are thus consistent, and the temporal shift seems to give a good approximation of the temperature dependence of the retardation time spectra.
A closer examination of Figure 4-43 reveals a slight vertical translation of the shifted spectra, particularly in the region of the maxima. The maximum of the spectrum increases with decreasing temperature, as already discussed in section 4.1.3. This effect cannot be considered by the horizontal shift of the spectra and shows the limitations of the simple time-temperature equivalence.

The consequences of the neglected vertical shift can be checked in the following way. If the time-temperature equivalence gives a good approximation of the temperature dependence of the viscoelastic properties of the adhesive, it is possible to use the superposed spectra in order to have access to more information, namely more values of $L^*_{eff}(\tau)$ in a broader retardation time range, than in a single discrete spectrum. Moreover, the consideration of all the shifted values of $L^*(\tau)$ reduces the effect of measurement errors and averages the vertical shift of the spectra in the measured temperature range. This induces a modification of the spectra intensities in comparison to a pure horizontal shift of the spectra and consists thereby in an alteration

towards the time-temperature equivalence. By combining the data of the shifted discrete spectra, a continuous master retardation time spectrum is constructed in the same way as for the single continuous time spectrum, described in section 2.4 - Figure 4-44 and Table 4-4. The master retardation time spectrum is then not an exact copy of a measured spectrum but an averaged spectrum for all the measuring temperatures and is thus an averaged description of the viscoelastic properties of the adhesive joints in the considered temperature range. Note that the "outlier" in the discrete retardation spectrum at 5 °C (cf. Figure 4-43) has not been considered for the determination of the master retardation time spectrum.

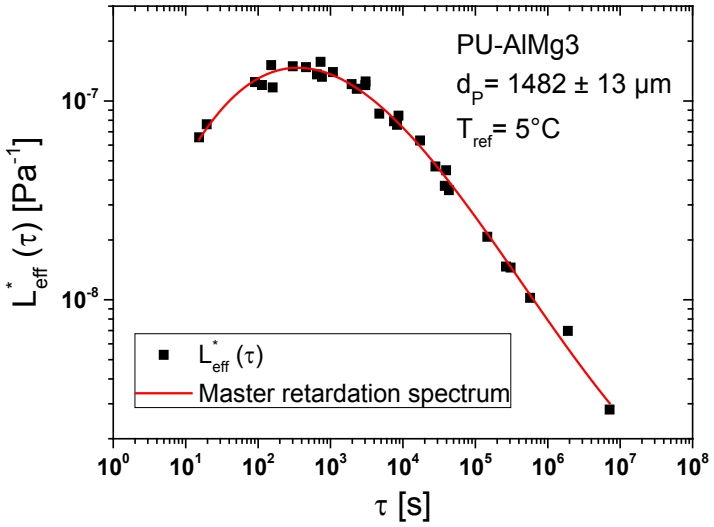

Figure 4-44: Determination of the master retardation time spectrum of a PU-AlMg3 adhesive joint with d_P = 1482 ± 13 µm (T_{ref} = 5 °C)

Table 4-4: Parameters of the master retardation time spectrum shown in Figure 4-44 (in red).

Model	Cubic		
Equation	$\log (L_{eff}(\tau)) = a_0 + a_1 \cdot (\log \tau) + a_2 \cdot (\log \tau)^2 + a_3 \cdot (\log \tau)^3$		
Reduced χ^2	0.0015		
Coeff. of determination R^2	0,9926		
	Parameter	Value	Standard deviation [%]
	a_0	-8.23536	1.11
	a_1	1.21867	6.7
	a_2	-0.30872	7.2
	a_3	0.01822	10.26

The master retardation time spectrum is then shifted back along the time axis into the positions of the original measured retardation spectra, using the values for the shift factor $log\ a_T$ determined using the WLF equation in Figure 4-41. The corresponding creep curves $J_{eff}(t,T)$ are then calculated from the back-shifted master retardation spectrum. Creep curves can obviously be calculated for any temperature within the mechanical glass transition of the adhesive using the WLF equation given in Figure 4-41 but the validity of the time-temperature equivalence should be verified first.

Figure 4-45 illustrates the comparison of the measured creep curves with those calculated from the master retardation spectrum. The calculated curves provide a reasonable approximation of the experimental curves in the transition region (between the glassy and rubber-like plateaux). Due to the averaging of the retardation processes through the determination of the master retardation spectrum, the calculated creep curve at the reference temperature T = 5 °C does not so well fit the measured one as it was the case with the experimental $L_{eff}(\tau)$ spectrum – cf. e.g. Figure 4-36. That is the visualised result of all the simplifications made for the master curve construction.

Deviations between the calculated and the measured curves at short creep time cannot be discussed since the experimental data do not exist because of the non-sudden loading of the sample.

In addition, discrepancies between the experimental and the calculated data in Figure 4-45 can be imputed, at least partially, to the temperature dependence of the equilibrium compliance which is not considered by the simple time-temperature equivalence, cf. Figure 4-42.

Besides the different plateau values for $J_{eff}(t,T)$, it is obvious that the contributions of the long τ_i are not properly included in the master curve. This can be explained as we only have a limited measured time $t_{\exp}$. Consequently, the "plateau" may still be corrupted by much slower processes. These are not explicitly taken into account in $L_{eff}(\tau)$. They merely increase $L_{eff}(\tau_i^{\max})$. But since $\tau_i^{\max} < \tau_{i+...}$ of the slow processes, the calculated $J_{eff}^{calc.}(t,T)$ must decay faster at high measuring time t than the measured $J_{eff}^{\exp.}(t,T)$. This becomes more obvious the lower the measuring temperature $T_{\exp}$ is – see Figure 4-45.

A further assumption for this effect is that the shape and the intensity of the retardation spectrum depend on the measuring temperature but cannot be experimentally identified with the employed experimental set-ups.

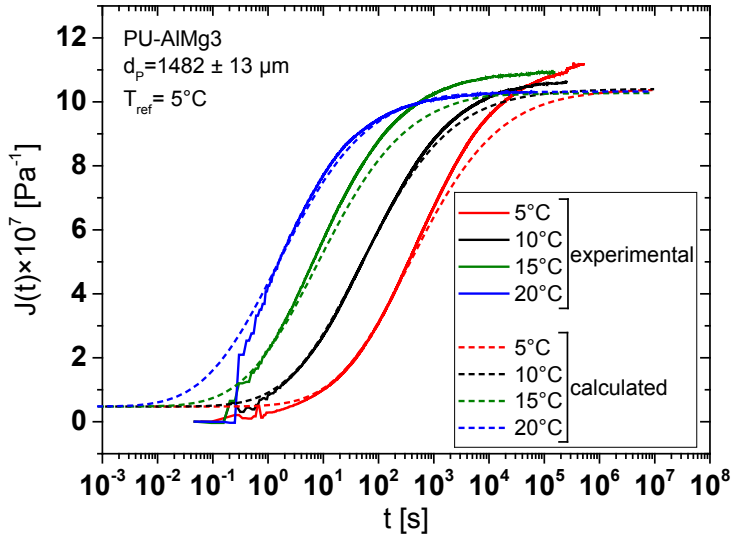

Figure 4-45: Time - temperature equivalence – Comparison between experimental (solid lines) and calculated (dashed lines) creep curves

Despite of its limitations discussed previously, the time-temperature equivalence gives an acceptable approximation of the temperature dependence of the viscoelastic properties of the adhesive joints. This indicates that the shape and the intensity of the retardation spectra do not undergo major changes in the measuring temperature range. Many additional compromises made with the master curve construction for $L_{eff}(\tau)$ result in additional systematic deviations of the calculated from the measured creep curves $J_{eff}(t, T = const.)$.

Since the viscoelastic functions of the adhesive depend on d_P, the WLF parameters C_1 and C_2 are expected to behave in the same way. However, Figure 4-46 shows that the evolution of the shift factor a_T with the temperature seems to not depend on the adhesive thickness in the measuring temperature range. Because of the narrow measuring temperature range and the small number of measured points, the absolute values of the WLF parameters for the different d_P are not discussed. For the given level of accuracy, the dynamics of the interphase and the bulk adhesive in the bonded joints appear to have similar temperature dependence, as evidenced by the apparently adhesive thickness independent shift factor.

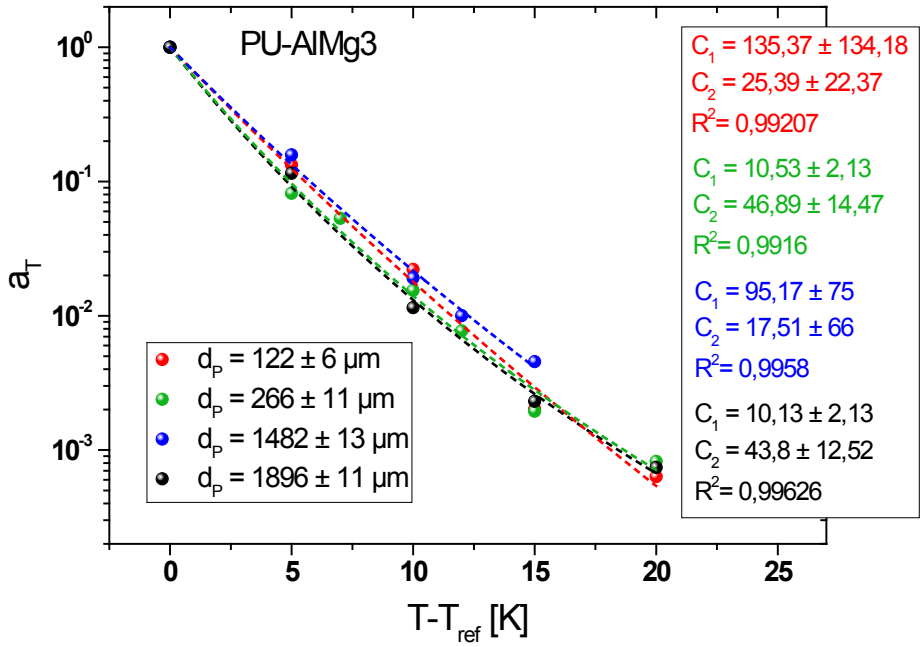

Figure 4-46: Temperature dependence of the shift factor a_T using the Williams–Landel–Ferry equation ; see eq.(4.6), for a PU-AlMg3 adhesive joint with different d_P. The fit parameters show no systematical dependence on d_P.

Nevertheless, the application of the time-temperature equivalence, as it is, gives a first approximation to describe the temperature dependence of the viscoelastic properties of the adhesive joints. Based on this finding, similar considerations as for the time-temperature equivalence are attempted in the following section to describe the bond line thickness dependence of the viscoelastic properties in adhesive joints.

4.3.3. **Bond line thickness - time equivalence – An attempt**

The results discussed in section 4.2 describe the bond line thickness dependence of the viscoelastic behaviour of the investigated adhesive joints. More specifically, the influence of the adhesive thickness on the retardation time spectra is shown in Figure 4-32, Figure 4-33 and Figure 4-34. For the given measuring temperature, the spectra shift to higher $L_{eff}(\tau)$-values and, to a lesser extent, longer retardation times with increasing adhesive thickness d_P. In the same way as for the approximation of the temperature dependence, a shift of the retardation spectra is attempted to depict this bond line thickness dependence.

Unlike the WLF equation for the temporal shift of the linear viscoelastic properties of polymers by varying the measuring temperature, no relation is known so far for the adhesive thickness dependence of the mechanical behaviour in adhesive joints. As a starting point for a first approximation, the combination of a horizontal and vertical shift of the retardation spectrum for a PU-AlMg3 adhesive joint with $d_P = 736 \pm 9$ µm is considered at 15 °C. The spectrum is shifted so that it overlaps the measured retardation spectrum at the same temperature of an adhesive joint with $d_P = 281 \pm 9$ µm as shown in Figure 4-47. In doing so, it is important that the maxima of the spectra are superimposed because they reflect the most important contribution in the adhesive dynamics. Two new shift factors are to be defined for this: b_τ for the horizontal shift and b_L for the vertical shift. Note that the chosen d_P are both influenced by the mechanical interphase, but in different proportions, as the properties of the corresponding adhesive joint depend on d_P, as seen in section 4.2.

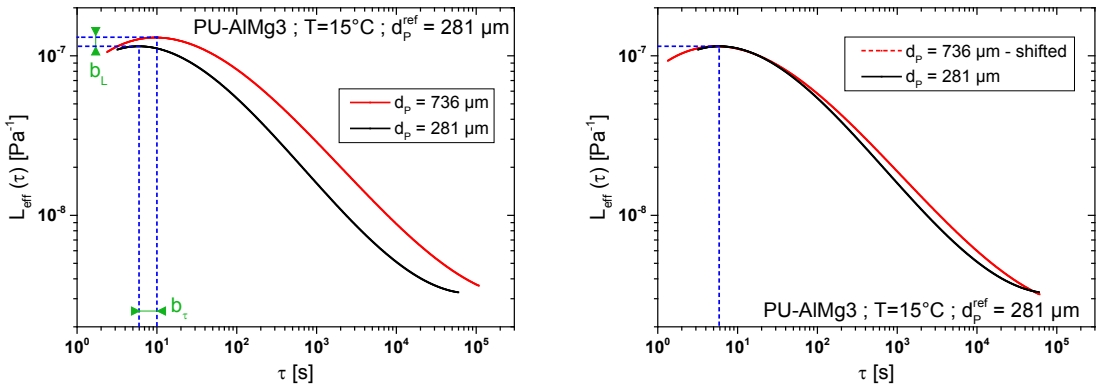

Figure 4-47: Bond line thickness - time equivalence – Shift of the retardation spectrum. Retardation time spectra before (left) and after (right) shift. The blue dashed lines indicate the maxima of the retardation time spectra. Only the measured τ range of the spectra has been considered. The values of the shift factors used here are: $\log b_\tau = 0.25$ and $\log b_L = 0.055$.

Since the two curves have a comparable fit quality with respect to the discrete measured values $L_i^*(\tau_i)$, the deviation shows that the slow processes with $\tau > \tau^{max}$ in the thicker adhesive layer provide a higher contribution to the linear viscoelastic behaviour than in the thinner layer.

After the spectrum measured for $d_P = 736 \pm 9$ µm is shifted to overlap the spectrum measured for $d_P = 281 \pm 9$ µm, as described in Figure 4-47, the back calculation of the corresponding creep curves can be carried out. This approach aims to assess the quality of the approximation obtained with this bond line thickness-temperature equivalence. Figure 4-48 shows the results of these calculations.

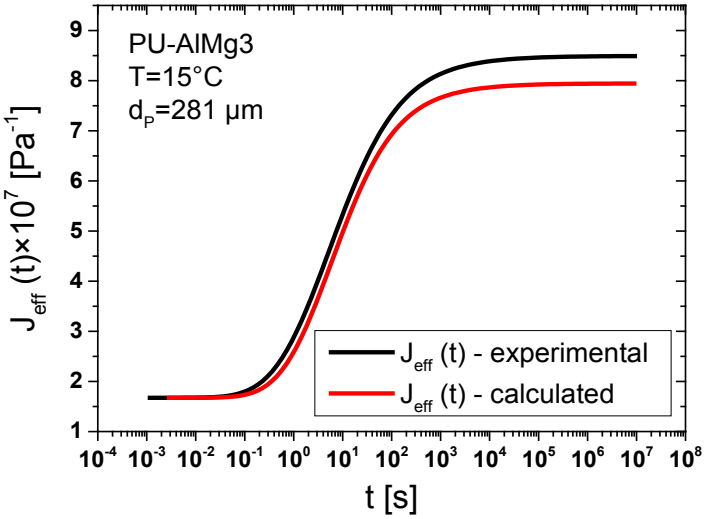

Figure 4-48: Bond line thickness - temperature equivalence – Verification: comparison between experimental and calculated creep curves

The red curve represents the creep function of a PU-AlMg3 adhesive joint with $d_P = 281 \pm 9$ µm, which was calculated based on the shifted spectrum for a PU-AlMg3 adhesive joint with $d_P = 736 \pm 9$ µm. The black creep curve is calculated using the continuous retardation time spectrum obtained from the experimental $L_{eff}^*(\tau)$. At short retardation times, $\tau \to \tau^{lower}$, both curves are identical. This results from the good match of the both spectra in the region of their maxima (3 s $\leq \tau \leq$ 12 s). Thus, the corresponding calculated values of the "instantaneous" compliance $J_{0,eff}$, which are influenced by fast retardation processes, are also identical. The retardation processes are well approximated by the bond line thickness-temperature equivalence in the transition region. By approaching the entropy-elastic plateau, the deviation between the experimental and the calculated curve increases, resulting in a considerable discrepancy between the both plateau values. The influence of d_P on the relaxed elastic properties of the adhesive joint (see chapter 4.2) is not reproduced by the attempted

shift of the retardation time spectrum as described above, even in a relatively narrow range of d_P. The contribution of long retardation processes is underestimated by the calculation whereas the shifted retardation time spectrum is broader that the experimental one in the measured time range – Figure 4-47, right. Figure 4-48 shows that the calculated creep compliance $J_{eff}(t)$ is lower than the measured one at long retardation times. This could indicate that the integral of $L_{eff}(\tau)$ is too small and thus that the calculated spectrum is either too narrow or its maximum too low. In both cases, this proves that there is no simple bond line thickness equivalence for the viscoelastic properties in adhesive joints. The modification of the shape of the retardation spectrum with d_P cannot be neglected to approximate the bond line thickness dependence of the adhesive dynamics. In other words, the mechanical interphases exhibit different properties from those of the adhesive bulk.

A bigger experimental database will be necessary to discuss the quality and the limitations of the bondline thickness - time equivalence. An interesting aspect will be, for instance, the evolution of the shift factors b_τ and b_L as a function of adhesive thickness d_P at different temperatures to determine a WLF-like equation.

4.3.4. **Residual stress as origin of mechanical interphase – short discussion**

The formation of mechanical interphases in adhesive joints causes gradients in the mechanical properties of the adhesive joints. As mentioned in the introduction of this work (cf. chapter 1), several hypotheses are put forward to explain the causes of the formation of mechanical interphases in adhesive joints. One of these suggests that the mechanical interphase originates from residual stresses resulting from the shrinkage of the adhesive during its network formation. Due to the adhesion of the polyurethane molecules in contact with the metallic substrate, these stresses cannot be relaxed and can thereby influence the mechanical properties of the neighbouring adhesive chains and so on. Hence, such internal stresses influence the adhesive dynamics depending on the adhesive thickness. Therefore, the distribution of the retardation and relaxation processes would be also affected by the existence of such internal stresses.

In order to get an impression of the mentioned residual stresses, an adhesive sample with an average thickness of 1896 µm has been delaminated from both substrate surfaces. Figure 4-49 shows a picture of the loosely peeled adhesive layer placed on a substrate half for comparison purpose. The other end of the adhesive layer is made flush with the edge of the bonding surface. As it can be clearly seen, the adhesive layer no longer completely covers the bonding surface. This means that the adhesive layer is considerably shrunk after peeling off the substrates. Once the adhesive forces are no longer present, a significant part of the internal stresses can relax. Figure 4-49 shows the influence of these internal stresses for d_P = 1896 µm. The bulk properties of the adhesive in a bonded joint can also be characterised first when the influence of the internal stresses can be neglected.

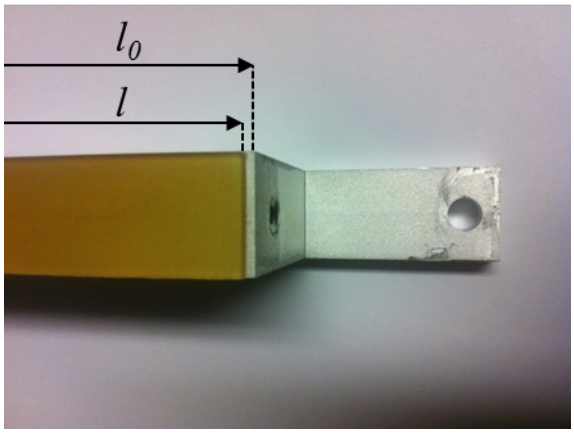

Figure 4-49: Shrinkage of a delaminated adhesive layer at 25 °C [157]

The length of the peeled adhesive layer is determined by means of a measuring microscope: l = 98.47 ± 0.01 mm. The accuracy of the measuring system is not good enough to detect a variation in the width and in the thickness of the adhesive layer after peeling. Considering the original length of the adhesive layer, l_0 = 100 mm, this value is used to estimate the internal stresses in the sample[23].
For this purpose, a specimen is dye cut from the peeled adhesive layer and a tensile test is carried out at a temperature of 50 °C (in entropy-elastic region). A shear modulus μ of 1.15 MPa is determined. As the polyurethane adhesive can be considered as an incompressible material (see section 2.2) the Neo-Hooke material law is used to calculate the normal stress component T_{11} in the longitudinal direction of the sample:

$$T_{11} = \mu \cdot \left(\lambda_1^2 - \frac{1}{\lambda_1} \right) \tag{2.55}$$

where $\lambda_1 = l / l_0$.

The measured data yield to a longitudinal stress of 0.053 MPa. In this case, only the longitudinal stresses are considered because the effects are more pronounced in this direction. The relative error in the measurement of the peeled adhesive layer is therefore the lowest. This result is only an approximation for the internal stresses in the sample. For a more precise description of the residual stresses, the exact three-dimensional deformation state in the adhesive sample should be considered. It is also to be expected that the residual stresses are not homogeneously distributed along the thickness of the sample. As already described, the internal stresses are expected to be substantially higher in the immediate vicinity of the substrate than in the middle layer of the sample.

[23] Δl = (100-98.47) mm = (1.53 ± 0.01) mm and $\frac{\Delta l}{l_0} = \frac{1.52}{100} \cdots \frac{1.54}{100}$ = 1.52…1.54 %

Figure 4-49 proves that residual stresses are present and also gives a clever estimate of these latter. However, residual stress components still exist due to temperature effect. Furthermore, it is not yet clear how the residual stresses influence the modulus, which is then measured in the experiments.

According to the experimental observations made with the tensile tests (cf. Figure 3-58), we have:

- In the entropy-elastic region, T_{11} as a function of $\left(\lambda_1^2 - \frac{1}{\lambda_1}\right)$ is linear with a constant slope, i.e. μ = const. Thus the stress level T_{11} does not affect μ.
- In the viscoelastic region the slope of $T_{11}\left(\lambda_1^2 - \frac{1}{\lambda_1}\right)$ decreases with increasing T_{11} (as a function of λ_1^2). Thus, the local slope $\mu_{eff} = \left.\frac{dT_{11}}{d\left(\lambda_1^2 - \frac{1}{\lambda_1}\right)}\right|_{T_{11}}$ decreases as T_{11} increases.

  It therefore follows that residual stresses should lead to a tendency towards a more compliant response of the polymer network.

With μ-Brillouin spectroscopy [42, 60], the opposite effect has been observed – but with a *static* measurement method. The effect of residual stresses on the viscoelastic modulus is therefore not obvious.

According to these results, it is conceivable that the internal stresses are a possible cause for the existence of the mechanical interphase in adhesive joint. Moreover, the existence of internal stresses can also explain the huge extent of these mechanical interphases, measured in the investigated adhesive joints. The monitoring of the shrinkage during the cure of the polyurethane adhesive is currently studied with a new characterisation method: the temperature modulated optical refractometry (TMOR) [179]. This should contribute to a further improved understanding of the formation of such mechanical interphases in adhesive joints.

5. Further methods to detect interphases in PU-metal adhesive joints

The previous mechanical experiments described the influence of *mechanical* interphases in PU-AlMg3 and PU-stainless steel adhesive joints with a bond line thickness from about 2000 µm to ca. 140 µm. This raises two questions: how is the influence of mechanical interphases in the lower bond line thickness range and does the observed mechanical interphase change other physical properties of the bonded joints?
To investigate these both issues, a new sample geometry with a more accurate bond line thickness is necessary to be able to distinguish the effect of the interphase in thinner adhesive joints ($d_P \leq 100$ µm) by means of dynamic mechanical analysis (DMA), differential scanning calorimetry (DSC) and dielectric spectroscopy (DES).

5.1. Sample preparation

Now, the metal substrate is prepared by physical vapour deposition (PVD) of Au (99.99 %) on clean glass slides in high vacuum. The compact polycrystalline gold layer has a thickness of about 50 - 100 nm[24].

The unreacted adhesive, prepared as described in section 3.1.3, is cast between two gold substrates. PTFE spacers adjust d_P appropriately between 37 and 550 µm. Due to the poor adhesion between gold and glass, the fully cured adhesive joints can be easily pulled off from the glass slide using tweezers. The samples are then used for DMA, DSC and DES measurements (cf. Figure 5-1 for sample geometry).

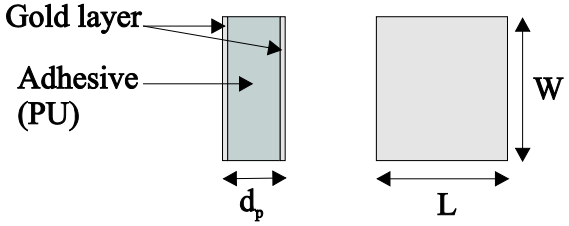

Figure 5-1: Sample geometry (d_P: sample thickness, including the gold layers (50-100 nm); W: width; L: length)

[24] Scanning force microscopy (SFM) has been used in the contact mode to measure the thickness of the gold layer: the glass slide is partially masked before the gold deposition and the so obtained step can be measured with SFM, originally referred also as atomic force microscopy (AFM) [180, 181].

In the same way, copper and aluminium substrates are prepared by vapour deposition, except that a gold layer is first deposited between the glass substrate and the final metal layer to facilitate the separation of the adhesive bond from the glass slides. To avoid the formation of an Au-Cu alloy during the cure of the adhesive [182], an aluminium layer is deposited between the gold and the copper layer.

5.2. Dynamic mechanical analysis

Dynamical Mechanical Analysis (DMA) appears to be a promising tool for the analysis of dynamic stiffness and molecular mobility in adhesive joints, if accuracy and sensitivity are sufficient. For bonded joints of Al foil with a commercial epoxy network, Caussé et al. report a dependence of molecular mobility on d_P within 100 and 600 µm but for only three d_P values [183]. The authors interpret their data as consequence of stiffening that extends from the epoxy-Al contact (interface adhesive-substrate) into the adhesive bond line. However, their body of data is limited and the connection between epoxy immobilisation at the Al surface and the mechanical behaviour remains vague. Moreover, the epoxy composition and the state of curing are not reported in necessary detail. That data encourages extending such measurements. They are needed to model the dynamic mechanical properties of adhesive joints [184]. In this chapter, the suitability of DMA is tested further for gold-polyurethane adhesive joints in an extended thickness range. These results are also presented in [167].

5.2.1. **Experimental**

5.2.1.1. Measuring mode

In material compounds, sample orientation plays an important role for the selection of the optimal measurement mode, for the display of the measured data, and, hence, for the detection of mechanical effects. This is illustrated in Figure 5-2 for coatings or laminates where the compound consists of just two components with different mechanical parameters. Obviously, only shear measurements with shear stress along the substrate surface deform the bi-layer part without significant deformation of the substrates. In the shear mode the stiffness of thin glassy samples is rather high. Moreover, a high-resolution measurement of small deformation is required to make sure that the material properties are determined in the linear range.

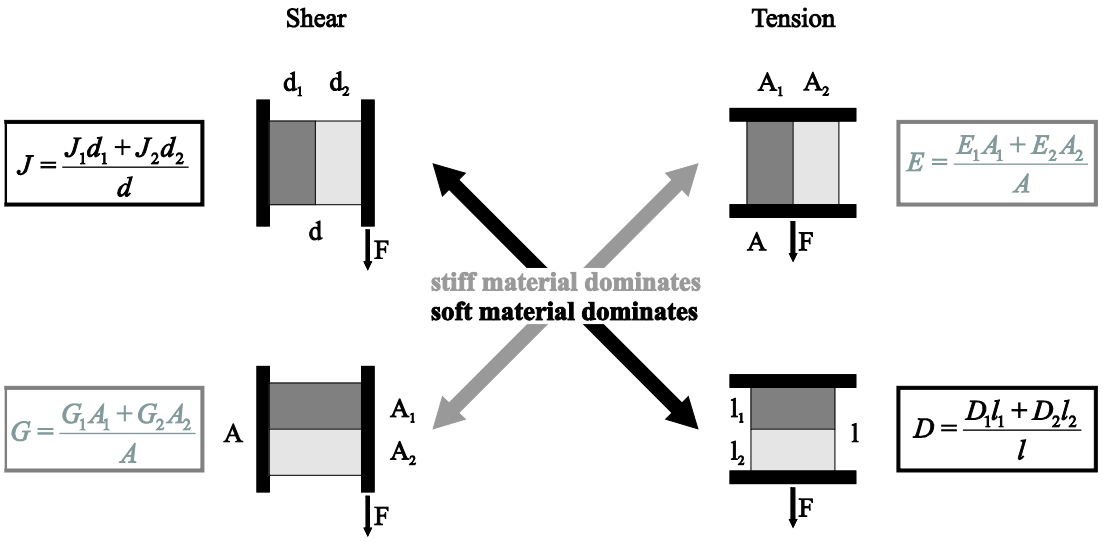

Figure 5-2: Sketch of the influence of the measuring mode on the measured mechanical properties in the case of polymer bi-layered samples consisting of a stiff (dark grey) and a compliant (light grey) layer. A = clamped area, d = sample thickness, l = sample length, J = shear compliance, G = shear modulus, E = tensile modulus, D = tensile compliance of the bi-layer [167]

5.2.1.2. Sample geometry

DMA is performed with a DMA861e from Mettler-Toledo AG. This high-performance instrument combines a stiffness of about $1.4 \cdot 10^8$ N/m with a displacement resolution of about 0.5 nm. The force generator provides 40 N at maximum. The optimum sample size depends on the material properties of the sample. For definition of the sample geometry, an estimation of the mechanical properties is required. The complex shear modulus, $\hat{G} = G' + iG''$, of a material is proportional to the complex sample shear stiffness $\hat{S}$

$$\hat{G} = g \cdot \hat{S} \tag{5.1}$$

with the geometry factor, g, depending on the thickness, d_P, and the clamped area, A, of the sample:

$$g = \frac{d_P}{2A} \tag{5.2}$$

Generally, the sample stiffness must be significantly lower than the stiffness of the instrument, S_i. Otherwise, the measured deformation cannot be attributed to the sample anymore. In the DMA861e the maximum sample stiffness should be at least three times lower than S_i. Insertion of equation (5.2) in (5.1) yields an estimation for the maximum sample area, A_{max}:

$$A_{max} \leq \frac{d \cdot S_i}{6G'_g} \tag{5.3}$$

with G'_g the storage shear modulus to be measured in the stiffest sample state. Assuming $G'_g \approx 1$ GPa as a typical value of for polymers in the glassy region and $d_P = 40$ µm, we get $A_{max} \approx 1$ mm².

For such small samples the external sample preparation is necessary. The samples are first mounted in the shear clamps outside the DMA and then the shear clamps are mounted in the measuring device.

5.2.1.3. Sample mounting

To double the effective sample thickness, sandwiches of two samples with a plane-parallel steel plate in between (see Figure 5-3) are clamped for those adhesive joints having a thickness below 300 µm. The steel plates have a surface area $A \approx 4$ mm² and a thickness $d \approx 350$ µm. The sample area is nearly quadratic in the range of 1 to 3 mm². The larger area is used for the thicker samples to get the optimum for the geometry factor for shear samples to avoid sample bending. Furthermore, the clamps must exert a small but sufficient normal stress on the sample for shear force transfer.

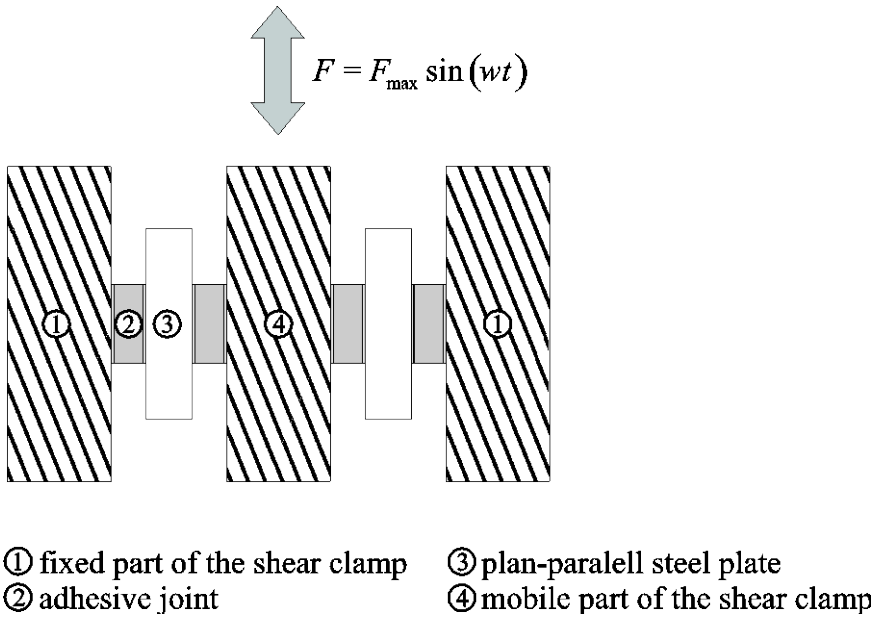

Figure 5-3: Sample mounting in the shear clamps

The shear deformation is given as the deformation amplitude over the effective sample thickness at one side of the shear clamp. Deformation sweep experiments were performed with displacement amplitudes from 1 nm to 500 nm on samples with 50 µm to 200 µm PU thickness at room temperature (T = 22 °C ± 1 K). As the result, a maximum shear strain of 0.3 % was found for linear response. At larger deformations the samples behave non-linear, i.e. the measured modulus declines with increasing deformation amplitude.

In addition, the shear force amplitude must be set small enough to limit the shear stress in the case of a stiff glassy sample - the sample would decouple from the shear clamps at too high shear forces. Thus, DMA force amplitude and clamp force have to be chosen carefully. Otherwise for too large shear and compression stresses, the storage modulus grows with decreasing temperature in the glassy region and/or the loss modulus is too high. Appropriate values were determined in screening experiments in the glassy state.

The sample is pre-clamped at room temperature with a force enough to hold it in place. After reaching the start temperature of about -100 °C, the sample is in glassy state and cannot be easily deformed. The sample is then clamped with the determined force. At this temperature, the samples are in the glassy state and the polymer deformation due to the clamping force can be neglected, therefore.

After mounting shear clamps with the sample, the setup is annealed at 50 °C for 15 minutes in the DMA furnace to eliminate potential internal stresses caused by sample preparation and clamping.

Due to thermal expansion of the samples, the bond line thickness and the sample area vary slightly during the measurement. An estimation of the resulting stress in the sample shows that this effect can be neglected in comparison with the applied small clamping force. The corresponding calculation is discussed in the section 5.2.2.

5.2.1.4. Approach

In the glassy state the measurement is shear stress controlled. During heating, the storage modulus decreases and hence the deformation amplitude grows. To keep the measurement in the linear range the control switches automatically to strain control as the maximum deformation reaches 0.3 %.

The amplitudes of the sinusoidal deformation and force, as well as the related phase shift are measured for temperature sweeps from 210 to 400 K at a heating rate of 4 K/min. A measuring frequency of 10 Hz was chosen in order to determine a sufficient number of data points at this relatively high heating rate.

5.2.2. **Results**

The temperature dependent viscoelastic shear modulus $\hat{G} = G' + iG''$ of a 50 µm gold-polyurethane adhesive joint is shown in Figure 5-4. The curves represent the dynamic glass transition (α-relaxation) of the amorphous PU-network. The storage modulus decreases by about 3 orders of magnitude. The G' inflection point at 279 K correlates with the peak maximum of the loss modulus, G''. The rubbery plateau follows beyond the dynamic glass transition.

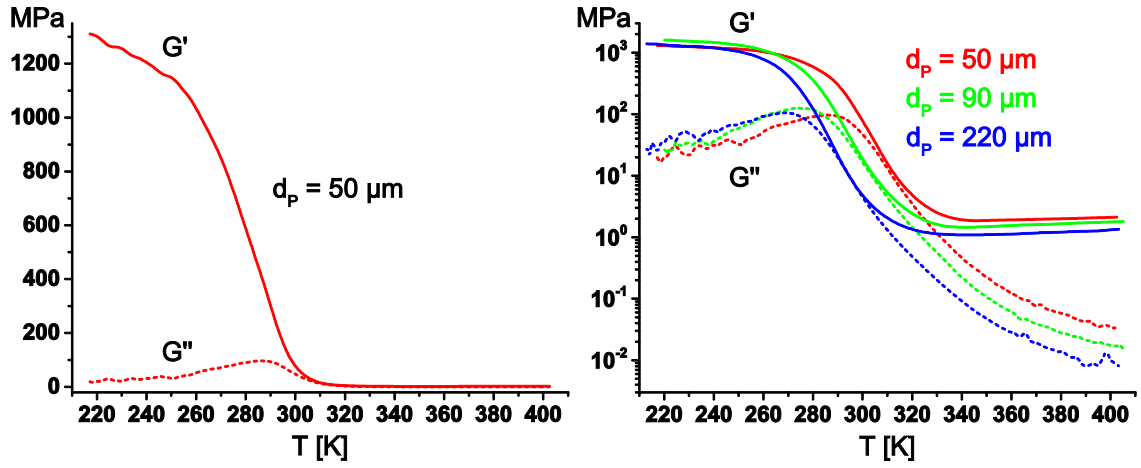

Figure 5-4: Dynamic shear moduli $G'(T)$ and $G''(T)$ at 10 Hz during heating with 4 K/min for gold-PU adhesive joints displayed in the linear (left) and a semi-logarithmic (right) diagram for 50 µm, 90 µm and 220 µm samples as an example

NOTE: As mentioned in section 5.2.1.3, the influence of thermal expansion of the samples on the results has been considered. For a polyurethane adhesive very similar to PU 80:20, the linear thermal expansion coefficient is about $\alpha_{glass} = 47 \cdot 10^{-6}\ K^{-1}$ in the glassy state and $\alpha_{rubber} = 177 \cdot 10^{-6}\ K^{-1}$ in the rubber-like state (personal communication Prof. J.-K. Krüger). With these data, thermal expansion of the free PU (not clamped) is estimated:

- From 173 K to 240 K, the glassy polyurethane adhesive (see Figure 5-4) experiences a thermal expansion of about 0.3 %.
- Across the glass transition (240 - 340 K), $\alpha(T)$ is approximated by a linear curve: $\alpha_{transition} = 1.3 \cdot 10^{-6} \cdot T - 2.65 \cdot 10^{-4}\ K^{-1}$. Correspondingly, the glass transition temperature range provides another contribution of ca. 1.12 % expansion.
- In the rubber-like state, from 340 K to 380 K (the end of the measured T-range), another 0.71 % are added to the thermal expansion of the sample equals.

Thus, the total thermal expansion is ca. 2.1 % for the measured T-range.
If an ideally stiff sample clamping is assumed, the portions of thermal expansion from 173 K to 380 K would give rise to corresponding thermal stress, $\sigma = G \cdot \varepsilon$, where G is the mechanical modulus. For this estimation, the modulus in the glassy state $G'_{glass} = 1.5 \cdot 10^3$ MPa and in the rubber-like state $G'_{rubber} = 20$ MPa from Figure 5-4 are considered. Across the glass transition, $G'(T)$ is again described by a linear approximation $G'_{glass\ transition} = (-14.8 \cdot T + 5052)$ MPa. Then, the total thermal stress is

$$\sigma = \alpha_{glass} \cdot (240 - 173) \cdot 1.5 \cdot 10^3 + \int_{240K}^{340K} \left(1.3 \cdot 10^{-6} \cdot T - 2.65 \cdot 10^{-4}\right)(-14.8 \cdot T + 5052) dT + \alpha_{rubber} \cdot (280 - 240) \cdot 2$$

$$= 11.6 MPa$$

For a sample area of 1 to 3 mm², this stress corresponds to a counterforce of 11.6 to 34.8 N from the stiff clamps, which certainly can be neglected in comparison to usual clamping forces applied in DMA.
Obviously, this calculation is a conservative estimation as real clamps will never be perfectly stiff. The real clamping force would be smaller than the estimated one.
Nevertheless, the effect of clamping, or more generally, external pressure on the viscoelastic properties of adhesive joints is an interesting issue for future work.

According to the interphase and bulk regions in the PU layer, one could expect to see two glass transitions in the modulus curves. This is obviously not the case (Figure 5-4). Consequently, the measured curves represent the effective mechanical response of the adhesive layer. Therefore, the *effective* dynamic glass transition must be analysed in more detail as a function of PU thickness.

The temperature of the *G''*-maximum is taken as the dynamic glass transition temperature, $T_g^{dyn,G''}$ for the given frequency of 10 Hz. The thickness dependence is shown in Figure 5-5.

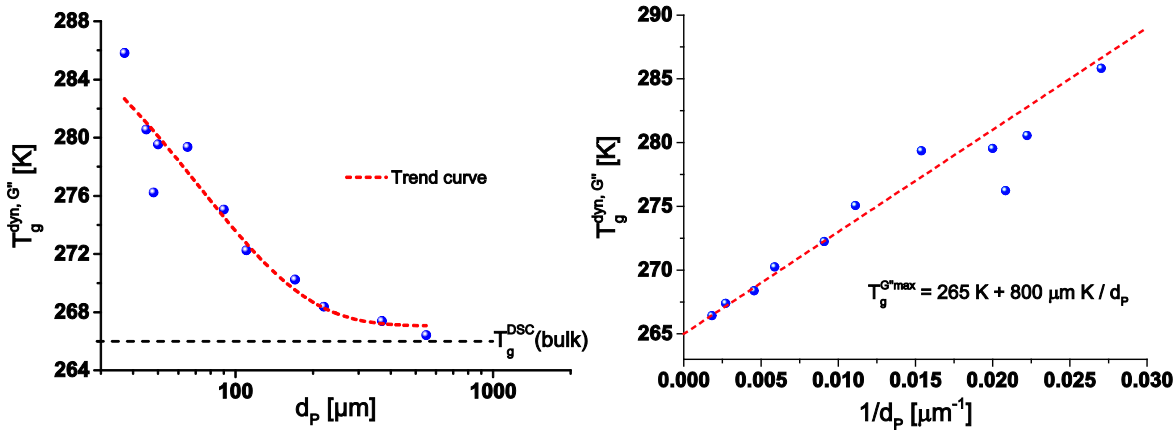

Figure 5-5: Dynamic glass transition temperature, $T_g^{dyn,G''}$ as function of bond line thickness, d_P in Au-PU adhesive joints

According to these data, the function

$$T_g^{dyn,G''}\left(d_P\right) = T_1 + \frac{A}{d_P} \tag{5.4}$$

is chosen for the phenomenological fitting of $T_g^{dyn,G''}\left(d_P\right)$. This provides $T_1 = 265$ K and $A = 800$ µm / K. Interestingly, T_1 is equal to the calorimetric glass transition temperature, measured by DSC at 10 K/min, of a bulk sample ($T_g^{DSC,bulk} = 266 \pm 1$ K.). Thin adhesive joints

tend to possess a higher $T_g^{dyn,G''}$. That dependence indicates the existence of an interphase in terms of cooperative mobility in the polyurethane adhesive at the contact with the gold surface. A higher glass transition temperature in thin joints corresponds to a lower mobility of the polymer network chains. Consequently, one would expect increased mechanical stiffness in a corresponding mechanical interphase.

An equation similar to equation (5.4) results from the assumption of an ideal athermal mixture of bulk and interphase material. This analogy to the well-known DiBenedetto equation [185] is not easy to comprehend for heterogeneous systems as anticipated for the PU adhesive layers. As a first explanation one could assume that the cooperative rearrangement regions average the molecular dynamics.

This view is supported by the thickness dependence of the upper half width of the glass transition, $\left\{T_{end}^{G''}(d_P) - T_g^{dyn,G''}(d_P)\right\}$, from the peak maximum $T_g^{dyn,G''}(d_P)$ to the upper end of the glass transition $T_{end}^{G''}(d_P)$ in G'' (Figure 5-6). The decrease in $\left\{T_{end}^{G''}(d_P) - T_g^{dyn,G''}(d_P)\right\}$ indicates a reduced variation of segmental mobility inside the mechanical interphase.

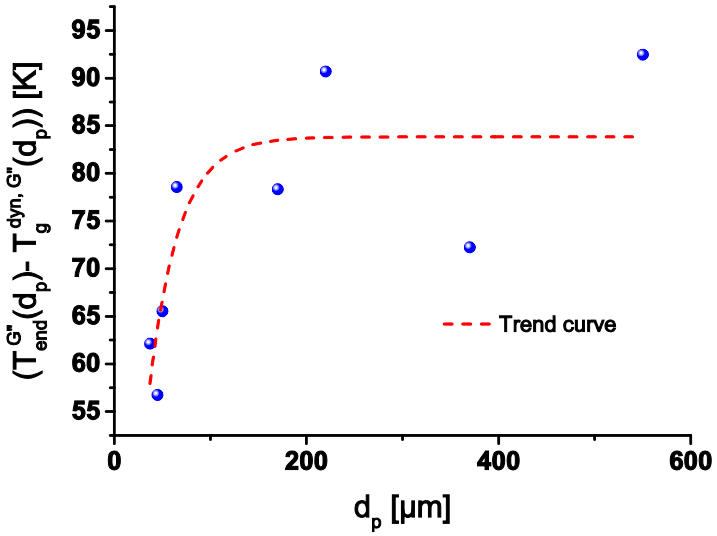

Figure 5-6: Upper half width of the dynamic glass transition in Au-PU adhesive joints

The height of the α-relaxation step in *log G′* from the glassy plateau (T = 233 K) to the rubbery state (T = 353 K) is presented in Figure 5-7. The increase of the logarithmic modulus step height with sample thickness is mainly caused by the modulus change in the rubbery plateau.

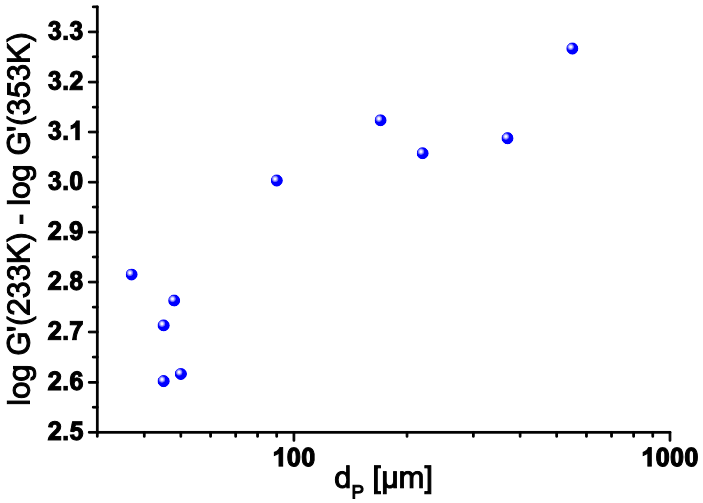

Figure 5-7: Step height $\Delta \log G' = \log G'(233\,K) - \log G'(353\,K)$ as a function of PU thickness, d_P in Au-PU adhesive joints

The height of the *G''*-peak gives a measure of the mechanical energy dissipated at the dynamic glass transition temperature. According to Figure 5-4, no thickness dependence is obtained within experimental uncertainty.

For an ideal entropic network i.e. $T > T_{end}^{G''}(d_P)$, the theory for a Gaussian network with chemical cross-links provides the temperature coefficient for the equilibrium shear modulus G'_{eq} at infinitesimal deformation [79, 86, 89, 186, 187]:

$$\frac{\partial G'_{eq}}{\partial T} = \kappa \cdot R \tag{5.5}$$

where κ is the molar crosslink density of the polymer and R the universal molar gas constant. It is noted in passing that equation (5.5) applies to a 'perfect' network where all network chains contribute to the elastic stress. In particular, the entropy-elastic network has to be homogeneous in the whole sample and, as a consequence, the κ-value obtained from eq. (5.5) must not depend on the size of the sample. In case of a *nonhomogeneous* sample, eq. (5.5) will provide some *effective* value, κ_{eff}, because the straight line measured for $G'_{eq}(T)$ in fact represents G'_{eq}–data averaged over the whole sample volume. Hence, variations of inhomogeneity will result in varying data for κ_{eff}. Actually, the application of eq. (5.5) to $G'_{eq}(T)$ on the rubbery plateau for the various d_P-values of the PU-layer in the Au-joints results in a thickness-dependent apparent effective cross-link density $\kappa_{eff}(d_P)$ - Figure 5-8. The growth of $\kappa_{eff}(d_P)$ with decreasing film thickness indicates a d_P-dependent inhomogeneity in the PU-layers. In accordance with the picture of a mechanical interphase developed above, we conclude that the deduced κ_{eff}–inhomogeneity corresponds to an apparently tighter cross-linking close to the polymer-metal interface. That also explains the higher *G'* in the entropy-elastic state shown in Figure 5-4.

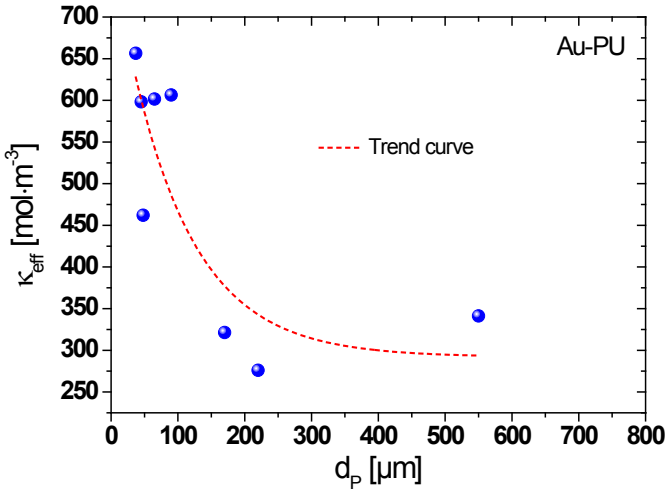

Figure 5-8: Apparent effective cross-link density, κ_{eff} for Au-PU joints of varying polymer thickness, d_P

The comparison of these results with those for AlMg3-PU adhesive joints and PU bulk, presented in Figure 4-20, reveals a discrepancy – Figure 5-9. Several reasons can be at the origin of this difference:

- The samples are made of different adhesive batches.
- Different substrates can cause the formation of different mechanical interphases and thus, influence the apparent κ_{eff}. However, the results obtained with shear test for $d_P \geq 1500$ µm correlate the value obtained for the PU bulk. This confirms the reliability of the results for AlMg3-PU joints. DMA measurements with thicker adhesive joints would help to discuss the difference as well as the evolution of $\kappa_{eff}(d_P)$ in more detail.

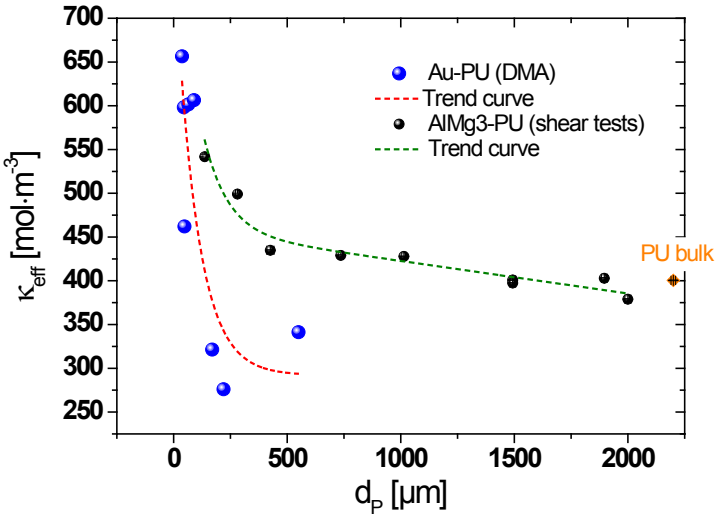

Figure 5-9: Apparent effective cross-link density, κ_{eff} for Au-PU joints measured with DMA (in blue), for AlMg3-PU joints measured with shear tests at constant shear rate (in black), for PU bulk measured with tensile tests (in orange) as a function of polymer thickness, d_P.

The same experiments have been also performed with Al-PU adhesive joints with a d_P down to 5 µm. The thickness dependence of the glass transition temperature in such adhesive joints is shown in Figure 5-10. It is similar to the data for Au-PU joints.

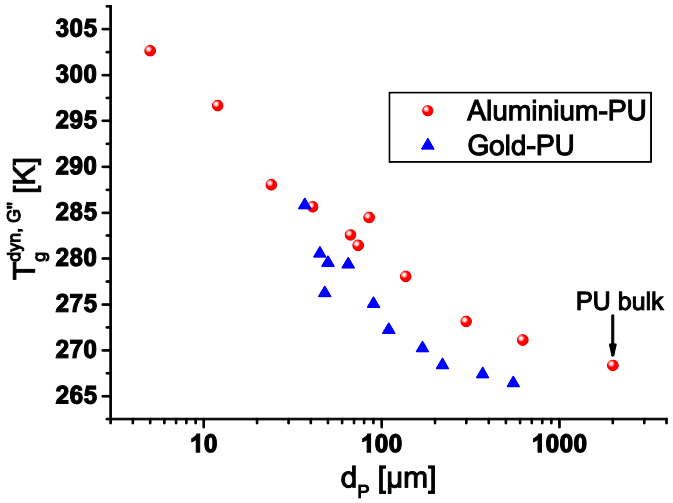

Figure 5-10: Dynamic glass transition temperature, $T_g^{dyn, G''}$ as function of bond line thickness, d_P in Al-PU and Au-PU adhesive joints

The glass transition temperature of the PU bulk (determined with DMA) is also depicted in Figure 5-10. It is important to note that the Al-PU and Au-PU adhesive joints have not been prepared from the same PU preparation batch. That is why the absolute measured values such as the glass transition temperature of the bulk adhesive could differ. For the same reason the influence of the metal substrate on the mechanical properties cannot be discussed here.
Nevertheless, the interphases formed between the aluminium substrates and the polyurethane adhesive influence the dynamic mechanical behaviour of the adhesive joints up to a d_P of about 620 µm.
Unfortunately the measured data do not permit a quantitative evaluation of the rubbery plateau. However, the results indicate qualitatively an increase of the apparent average PU crosslink density with decreasing adhesive thickness.

5.2.3. Conclusions

In the given configuration, high-performance DMA is capable to provide reasonable data for metal-polymer sandwich samples down to some few µm polymer thickness. We mention that DMA is averaging over the whole polymer volume and all deduced parameters are mean values, therefore. For Au-PU samples, the dynamic glass transition parameters as well as the entropy elasticity depend on sample thickness, d_P between ca. 30 and 550 µm. The same observations are made for Al-PU adhesive joints having a d_P between ca. 5 and 620 µm. Assuming ideal entropy elasticity as an approximation for the rubbery plateau, *G'(T)* provides an average PU crosslink density, κ_{eff} as a function of d_P. These findings are interpreted as proof for the

dynamic mechanical properties of an interphase between the polyurethane adhesive and the metal substrate.
As DMA is averaging over the whole polymer volume, all deduced parameters are mean values that cannot be split easily into contributions from the interphase and bulk regions in the polymer layer of given thickness.
In future work it will be possible to consider the effects of the mechanical interphase as a function of the substrate surface state, the adhesive composition and the adhesive joint preparation conditions, etc., provided the sample preparation and thickness are well controlled.

5.3. Differential scanning calorimetry

The classical technique to describe the glass transition and its related effects in polymer bulk materials is differential scanning calorimetry [188-192]. Although the nature of the excitation in DMA and DSC is different, the response of these methods gives in both cases information about the structural relaxation(s) in the sample. For the same reasons, the absolute temperature values characterising the mechanical and the caloric glass transition (obtained respectively with DMA and DSC) cannot be directly compared. However, one can expect that the existence of interphases in metal-polyurethane adhesive joints can be detected with DSC as it has been the case for the mechanical interphases hitherto. Mechanical techniques have indirectly shown the existence of mechanical interphases in adhesive joints, which are stiffer than the bulk adhesive. Therefore, the caloric glass transition in adhesive joint is expected to depend on the adhesive thickness as well. The glass transition of the interphase is supposed to occur at higher temperature than that of the adhesive bulk. Similarly to DMA, DSC is averaging over the whole polymer volume: all deduced parameters are thus mean values.

However, the accuracy of *conventional* DSC measurements is not very high [191], that could preclude the detection of interphases. New differential scanning calorimetry techniques, such as flash differential scanning calorimetry, can reach high sensitivity and reproducibility which are necessary to study such effect.

5.3.1. Conventional differential scanning calorimetry

As for all DSC techniques, heat effects, resulting from chemical reactions and/or physical transitions in the sample are monitored as a function of temperature or time. In a heat flux differential scanning calorimeter such as those used in this work, endothermic and exothermic processes as well as heat capacity changes across the glass transition lead to a temperature difference between the sample and a reference[25]. In steady-state, equal heat flow rates flow from the oven into sample and reference; the differential temperature signal ΔT is thus zero. If a transition or reaction occurs in the sample, a signal ΔT is generated which is proportional

[25] An empty pan has been used as reference in this work.

to the heat flow between the sample and the reference sample Φ_{SR} (this is achieved by a calibration). Since the used differential scanning calorimeter works at constant pressure (atmospheric pressure), the heat flow changes between the sample and the reference for a measurement with a constant cooling/heating rate $\frac{dT}{dt}$ are equivalent to enthalpy changes in the sample (in case that no change occurs in the reference sample):

$$\Phi_{SR} = \left(\frac{dQ}{dt}\right)_p = \left(\frac{dH}{dt}\right)_p = c_p(t) \cdot m \cdot \frac{dT}{dt} + \Phi_r \tag{5.6}$$

where dQ is the change of the amount of heat in the sample, dH the change of the enthalpy in the sample, $c_p(t)$ the specific heat capacity at constant pressure, m the sample mass and Φ_r heat flow contribution resulting from enthalpy changes in the sample due to e.g. chemical reaction(s), mixing and phase transition(s).

For metal-polyurethane adhesive joints similar to those described in section 5.1, conventional DSC has been used to investigate the influence of the substrate on the glass transition temperature as depicted in Figure 5-11. These results have been obtained with a constant heating rate of 10 K / min. The samples exhibit an adhesive thickness of about 40 – 60 µm [1]. Thinner adhesive bondlines did not provide useful signals in the DSC apparatus (DSC TA Q100, TA Instruments) available at that time. These results show a slightly higher glass transition temperature in adhesive joint with gold, aluminium, copper and AlMg3 substrates (neat and anodised: AlOx) than for the adhesive bulk.

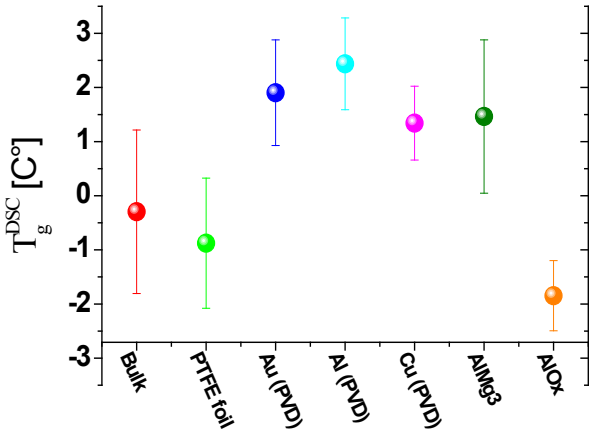

Figure 5-11: Glass transition temperature of a polyurethane adhesive in contact with different substrates (cf. abscissa) compared to the bulk material (in red) [1]

However, due to the relatively high standard deviation of these measurements, these results provide no final proof for the influence of the substrate on the caloric properties of the adhesive joints. Hence additional measurements were conducted in this work with the sample described in 5.1:

- DSC: Pyris-1, Perkin Elmer[26]
- Temperature ramp from 100 °C to -90 °C with a cooling / heating rate of ±10 K / min (2 runs)

As for all others measurement techniques, the samples are annealed at 50 °C for 15 minutes before each first measurement to eliminate potential internal stresses caused by curing and sample preparation.

The caloric glass transition temperature T_g^{cal} is determined as the corresponding maximum of the first derivative of the heat flow. The width of the glass transition is given by the base points of the maximum of that 1st derivative: T_{ga} is the temperature at the beginning of the glass transition and T_{ge} the end. Possible enthalpy retardation during the heating of the sample may have an influence on the analysis of the glass transition temperature. That is why the evaluation of the data has been made by using the cooling runs.

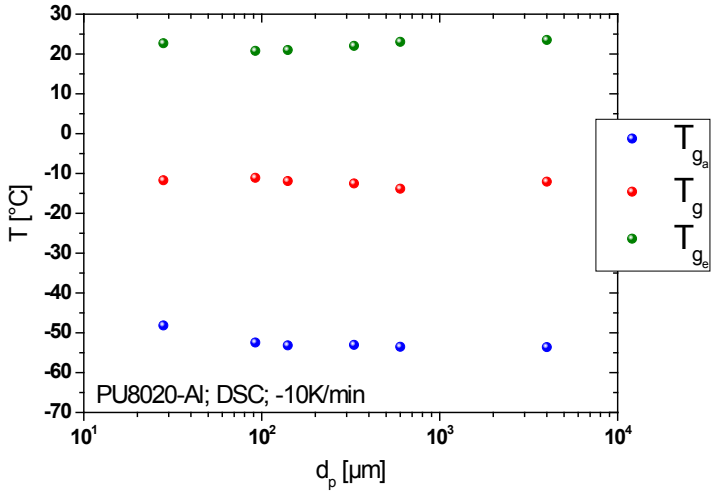

Figure 5-12: Thickness dependence of the caloric glass transition for PU-Al-adhesive joints measured at cooling with -10 K/min (error bars are smaller than the symbols)

No thickness dependence of the caloric glass transition is found for the Al-PU-adhesive joints under the given experimental conditions – Figure 5-12.

The same result holds for the height of the step in the heat capacity – Figure 5-13.

[26] Caloric investigations have been performed at the institute of Physics, university of Rostock. I would like to thank Professor C. Schick and his team for allowing me to carry out the measurements and for their support.

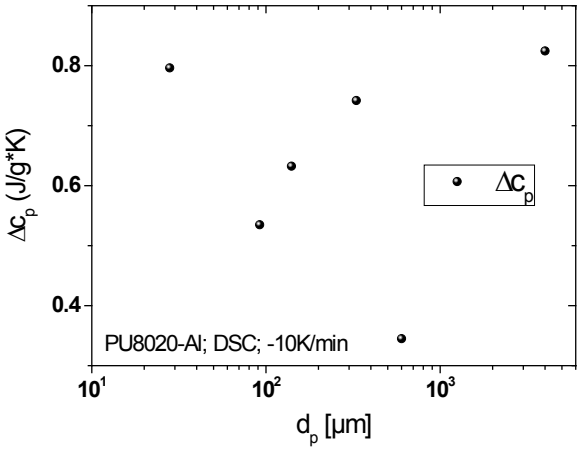

Figure 5-13: Thickness dependence of the height of the step in the heat capacity for PU-Al-adhesive joints measured at cooling with -10 K/min

The same experiments have been performed with PU-Cu adhesive joints and Figure 5-14 shows the corresponding results. Again, there is no thickness dependence of the caloric glass transition.
Moreover, the caloric glass transition is not modified by the other metal substrates – Figure 5-14.

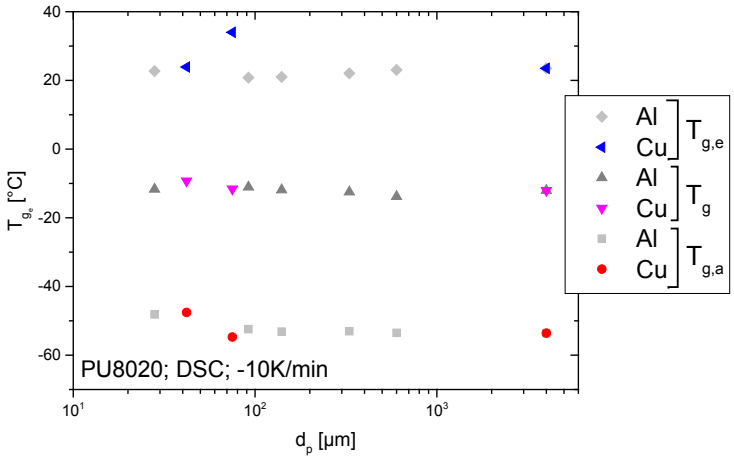

Figure 5-14: Thickness dependence of the caloric glass transition for PU-Al- and PU-Cu-adhesive joints measured at cooling with -10 K/min

5.3.2. **Flash differential scanning calorimetry**

Flash DSC is a calorimetry technique which has a broad range of scanning rates: it allows (quasi) isothermal measurements and scanning rates up to 10000 K/s. As a result, it is possible to generate quantitative information on the temperature dependence of the kinetics of processes which could hardly be obtained with conventional DSC. More detailed discussion on this technique can be found in [147, 193-195]. Such fast scanning calorimetry technique has been successfully used to describe the glass transition under confinement [191].

The presented measurements were performed with the following parameters:

- Apparatus: Flash DSC 1 (*Mettler-Toledo AG, Schwerzenbach, Switzerland*).
- Temperature ramp from 100 °C to -90 °C with -50; -100; -200; -500 and -1000 K / s (2 runs each)

The glass transition temperature and the width of the glass transition are determined by drawing tangents on the heat flow curve at temperatures above and below the glass transition – Figure 5-15. The tangents should be selected carefully because they have a significant effect on the quality and reproducibility of the evaluation. The glass transition temperature has been determined as the temperature at half the step height between the tangents with the measurement curve.

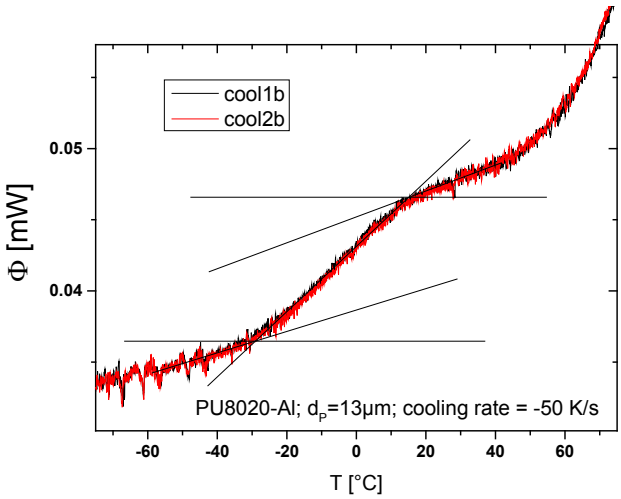

Figure 5-15: Caloric glass transition of a Al-PU adhesive joint with d_P = 13 µm measured by flash-DSC with a cooling rate of -50 K/s

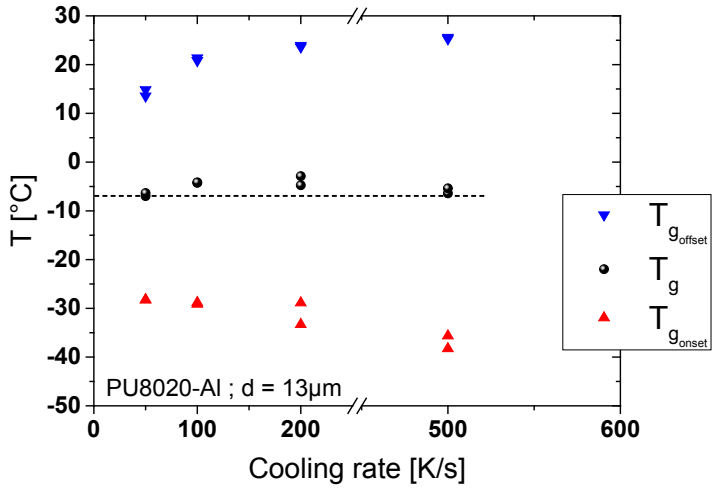

Figure 5-16: Cooling rate dependence of the caloric glass transition for PU-Al-adhesive joints for d_p = 13 µm

Now, a slight increase of the glass transition temperature is noticeable with rising cooling rate – Figure 5-16. In the same way, the width of the glass transition increases. The faster the cooling rate, the bigger is the temperature difference between the set value and the sample and the higher is the thermal inhomogeneity in the sample. The results for a cooling rate of 500 K/s are strongly influenced by the thermal inertia (i.e. thermal inhomogeneity) of the sample and should be considered with prudence.

For the same reason, it is not possible to characterise the thickness dependence of the caloric glass transition with the flash-DSC at a constant cooling rate in a reliable manner for the thicker part of the samples. For the thinner samples, a slight trend to a decreased T_g and width of the glass transition is indicated however for cooling rates of 50 and 100 K/s – Figure 5-17. The influence of thermal inhomogeneity in the samples is also indicated in Figure 5-18 by the non-systematic dependence of the glass transition temperature on the cooling rates for a given d_p. For this reason, only the results for cooling rates of 50 and 100 K/s are reliable for $d_p < 40$ µm. Flash-DSC with constant cooling rates turned out to be not well suited for the detection of caloric effects from the interphases in the PU-metal joints.

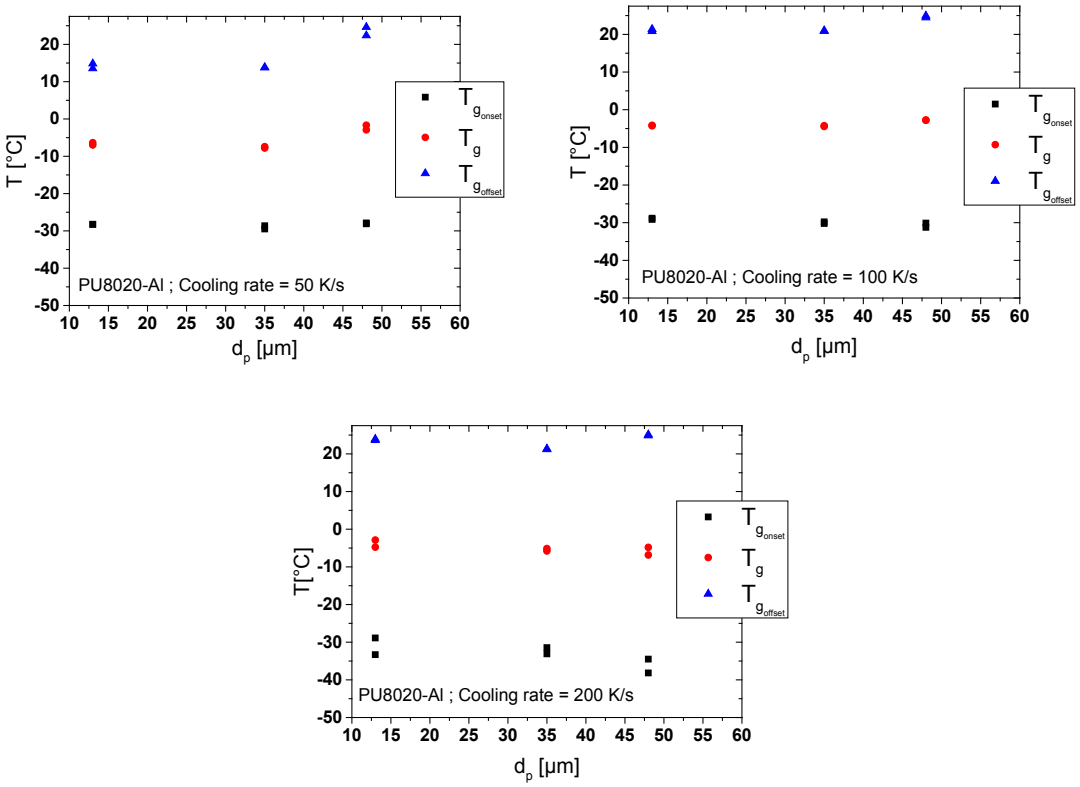

Figure 5-17: Thickness dependence of the caloric glass transition for PU-Al-adhesive joints for different cooling rates: 50, 100 and 200 K/s

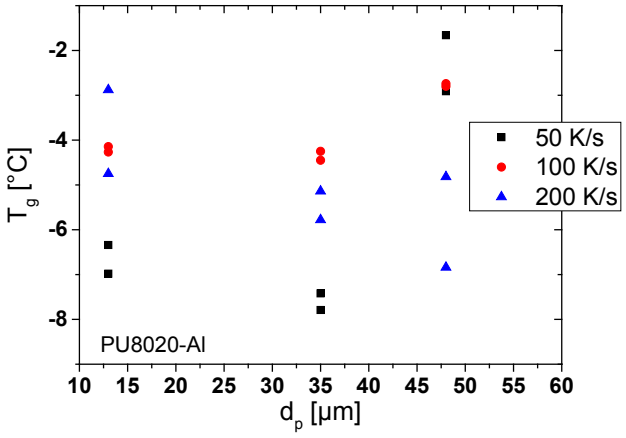

Figure 5-18: Thickness dependence of the caloric glass transition temperature for PU-Al-adhesive joints for different cooling rates: 50, 100 and 200 K/s

5.3.3. **Temperature modulated flash differential scanning calorimetry**

To avoid the influence of thermal inhomogeneity in the sample (see section 5.3.2) temperature modulated DSC has been performed with the flash-DSC as described in Figure 5-19.
A temperature step scan is performed from 100 °C to -90 °C with 1 K step and isotherms for 0.2 s with the flash DSC 1. The measured data are transformed by Fourier transformation from the time domain to the temperature domain.

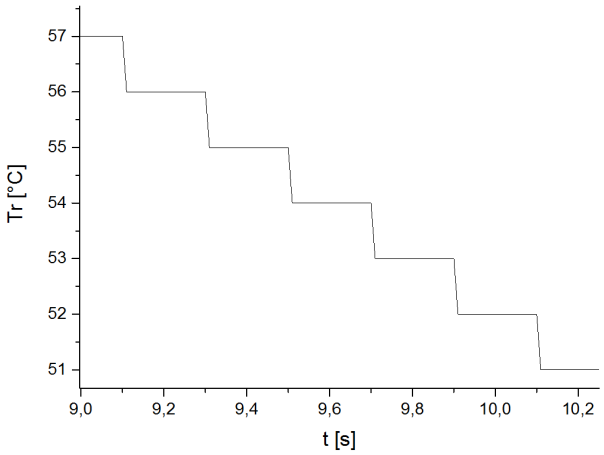

Figure 5-19: Temperature-time profile consisting of repeated isotherm-cooling segments

In Figure 5-20, the resulting convolution curve shows the temperature dependence of the heat capacity for a sample with a bond line thickness of 12 µm. The glass transition is analysed by fitting the first derivative of $C_p(T)$ with a Gaussian function:

$$y = y_0 + b \cdot x + \left(\frac{A}{w \cdot \sqrt{\pi/2}}\right) \cdot e^{\left(-2*((x-x_c)/w)^2\right)} \tag{5.7}$$

The parameter x_c is defined as the glass transition temperature and the width of the glass transition is evaluated with the fit parameter w – Figure 5-21 and Figure 5-22.

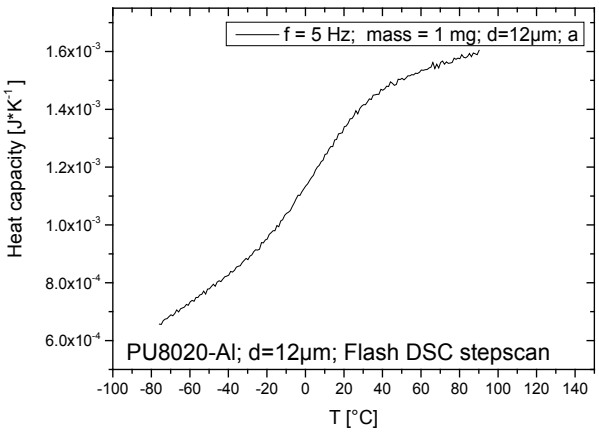

Figure 5-20: Temperature dependence of heat capacity from TM flash-DSC for a PU-Al-adhesive joint with d_p = 12 µm

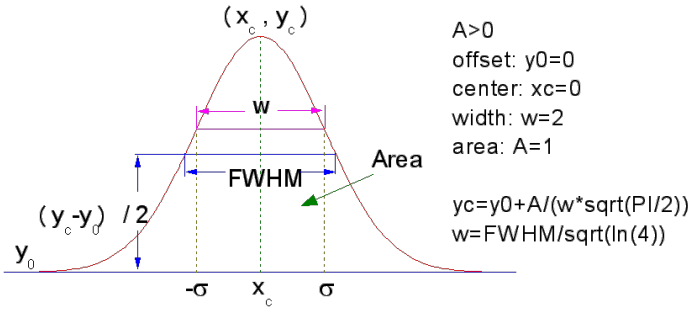

Figure 5-21: Fit parameters of a Gaussian function

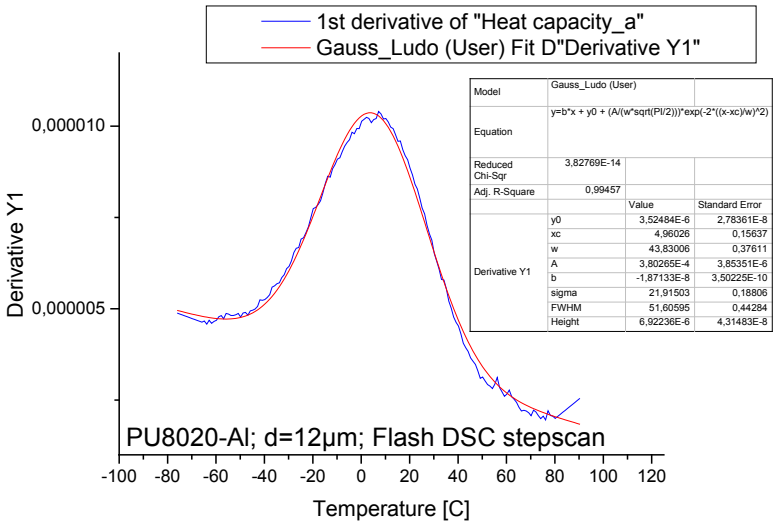

Figure 5-22: Fit of the first derivative of the heat capacity in TM flash-DSC experiments for a PU-Al-adhesive joint with d_p = 12 µm

Figure 5-23 and Figure 5-24 depict the results obtained for different thicknesses. In both plots, the measured points and the error bars results from three successive measurements with the same sample. A thickness dependence of the glass transition temperature (x_c) is noticed for Al-PU-adhesive joints with $0 < d_p < 150$ µm.
Because of the high thermal gradient in samples with $d_p > 150$ µm (cf. contact area 150 x 150 µm²), the corresponding results should not be considered (red points in Figure 5-23).

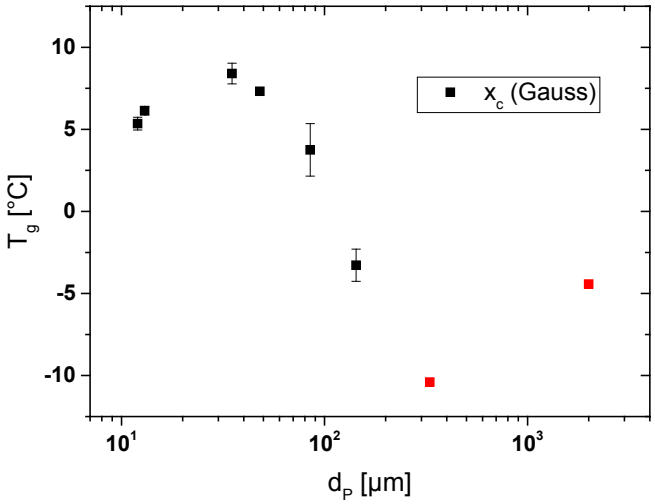

Figure 5-23: Thickness dependence of the caloric glass transition temperature in TM flash-DSC experiments for PU-Al-adhesive joints

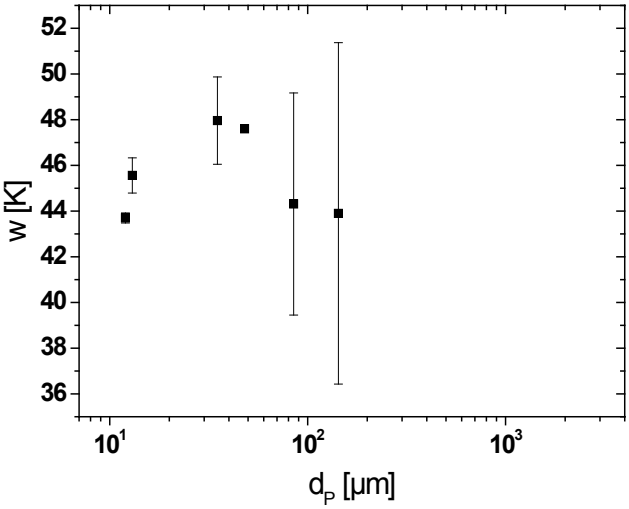

Figure 5-24: Thickness dependence of the width of the caloric glass transition for PU-Al-adhesive joints

The width of the glass transition, w also depends on d_P, cf. Figure 5-24, and it follows the same trend as T_g.

5.3.4. **Conclusions**

Conventional Differential Scanning Calorimetry measurements have shown neither an influence of the adhesive thickness nor of the metallic substrate on the caloric properties of the glass transition in PU-metal-adhesive joints.

Because of experimental problems, the investigations with flash-DSC on these adhesive joints are limited to $d_P < 60$ µm (thicker samples are suspected to develop thermal gradients). The results reveal a trend: T_g for $d_P < 60$ µm lies clearly above T_g of the PU bulk which might result from the very different cooling rates. Also the Flash DSC shows $T_g\left(d_P\right) \approx const$ for thin samples $d_P < 60$ µm. Only the TM-Flash-DSC is sensitive enough to detect $T_g\left(d_P\right)$ for $d_P < 50$ µm.

In conclusion, the caloric results give some possible first hints on the existence of interphases in the adhesive joints, but further investigations are necessary for their characterisation. Nevertheless, the presented results corroborate qualitatively the results obtained so far: the stiffer interphases, as revealed by the mechanical testing, exhibit also higher glass transition temperatures.

5.4. Dielectric spectroscopy

As prominent methods to investigate the glass transition and the related molecular dynamics in polymers, DMA and DSC have already been discussed in the chapter 5.2 and 5.3 respectively. Dielectric spectroscopy is another technique to gain information about structural relaxations in adhesive joints. Polarisation mechanisms and charge carrier transport in the adhesive layer might be affected by the existence of interphases. Both orientation polarisation of permanent dipoles and charge hopping transport in the PU network get support from polymer chain dynamics, namely from the co-operative segment mobility.

DES analyses the frequency and temperature-depending response of the adhesive's structure to an external alternating electric field. Because of the different nature of the excitation, the observed effects cannot be directly correlated with DMA or DSC results.

5.4.1. **Experimental**

The dielectric spectroscopy is based on the temperature- and frequency-dependent interactions of an alternating electric field with the charge carriers and dipoles of the investigated material. The wide frequency range from 10^{-6} to 10^{11} Hz allows characterising the molecular dynamics of the sample in a broad time range at given temperature. However, this wide frequency range can only be covered with the help of different techniques. In this work, the experiments are based on the frequency-response analysis, which enables measurements in the frequency range

from 10^{-6} to 10^{7} Hz. Further information about the physical background and the different techniques of the dielectric spectroscopy can be found in [196, 197].

5.4.1.1. Measuring principle

The principle of the frequency-response analysis is to calculate the complex impedance $Z^*(\omega)$ from the measured harmonic alternating voltage $U^*(\omega)$ (generator voltage) and the resulting sample current $I^*(\omega)$:

$$Z^*(\omega) = \frac{U^*(\omega)}{I^*(\omega)} = \frac{1}{\mathrm{i}\cdot\omega\cdot C^*(\omega)} \tag{5.8}$$

where $C^*(\omega)$ is the complex capacity of a plate capacitor (sample), i, the imaginary unit and $\omega = 2\cdot\pi\cdot f$, the angular frequency

The sample is placed in the experimental setup (cf. Figure 5-25) as a dielectric and is exposed to the alternating electrical field of a plate capacitor at a variable temperature T or frequency f.

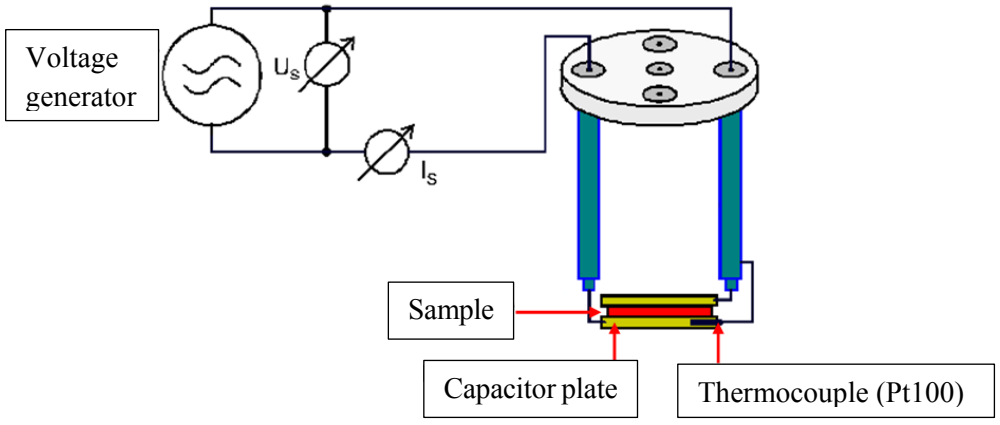

Figure 5-25: Experimental setup of the dielectric spectroscopy [198]

Under the influence of the alternating electric field, hopping of charge carriers and orientation permanent dipoles take place on a molecular level. Thereby, the time dependence of these motions is causes a phase shift between the electric field and the dielectric displacement. This physical process can be described by the dielectric displacement $\vec{D}$ and depends on the magnitude of the electric field $\vec{E}$. Provided that $|\vec{E}|$ obeys the condition of linear response, we have

$$\vec{D} = \varepsilon^*(\omega)\cdot\varepsilon_0\cdot\vec{E} \tag{5.9}$$

$\varepsilon^*(\omega)$ designates the complex dielectric function of the sample and ε_0 the dielectric permittivity of the vacuum ($\varepsilon_0 = 8.854\cdot10^{-12}$ $A^2\cdot s^4\cdot kg^{-1}\cdot m^{-3}$). It has to be pointed out, that $\varepsilon^*(\omega)$ in-

cludes, in real polymers, the effects from time-dependent orientation polarisation of permanent dipoles and time-dependent charge transport (hopping) as well. Hence, DES cannot discriminate between these two mechanisms but this does not matter in the context of this study because we are interested in a macroscopic quantity that couples to the average processes of polymer mobility in the sample, like $\varepsilon^*(\omega)$.

The complex dielectric function determines the capacitance $C^*(\omega)$ of a plate capacitor with the area of the overlap of the two plate electrodes, A, and the separation between the plate, d:

$$C^*(\omega) = \varepsilon^*(\omega) \cdot \varepsilon_0 \cdot \frac{A}{d} \tag{5.10}$$

For the metal-adhesive joints, A is given by the bonded area and $d = d_P$.
The complex dielectric function is given by

$$\varepsilon^*(\omega) = \varepsilon'(\omega) - i \cdot \varepsilon''(\omega) \tag{5.11}$$

The real part $\varepsilon'(\omega)$ represents the reversibly stored electric energy whereas the imaginary part $\varepsilon''(\omega)$ describes dissipated energy. Both parts depend on the angular frequency ω, with $\omega = 2 \cdot \pi \cdot f$ (where f is the measuring frequency).

The dielectric function $\varepsilon^*(\omega)$ of the sample is calculated from the measured impedance Z by combining the equations (5.8) and (5.10).

For the investigated amorphous polyurethane, three main mechanisms affect the dielectric function $\varepsilon^*(\omega)$: Orientation polarisation, conductivity and electrode polarisation.
The interpretation of these effects will be resumed throughout the discussion of the measured dielectric spectra.

5.4.1.2. Experimental set-up

A calibrated dielectric broadband spectrometer from NOVOCONTROL Technologies GmbH & Co. KG is used for all tests. This spectrometer allows measurements in a temperature range from -160 ° C to 500 ° C and covers a frequency range from 3 µHz to 10 MHz. The setup consists of the Broadband Dielectric Converter and the Alpha High Resolution Dielectric Analyser, which enable the impedance measurement by using the frequency response analyser and current-to-voltage converter. Furthermore, the device includes a Quatro Cryosystem (see Figure 5-26), which controls the sample temperature. This system contains a cryostat with the sample cell and a vaporisation device for liquid nitrogen. A heater evaporates the liquid nitrogen (-196 °C) inside of a Dewar vessel and a pressure sensor controls the gaseous nitrogen flow. The gaseous nitrogen is heated up to the desired temperature and flows through the sample cell. With this assembly, maximum heating rates of up to 8 K / min can be achieved. The entire electronics are controlled by computer via the measuring and control software WinDETA [199].

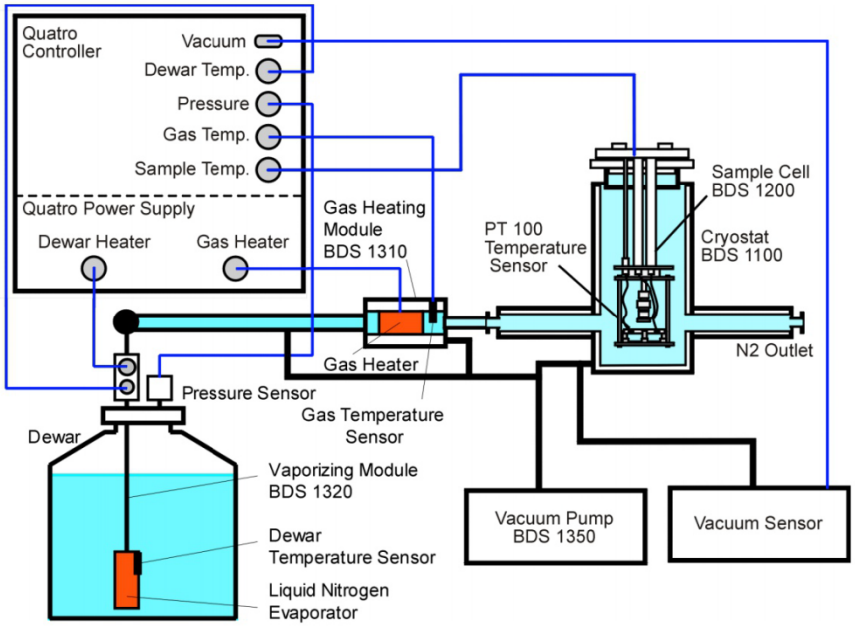

Figure 5-26: Experimental set-up of the dielectric spectrometer with the Quatro Cryosystem and the integrated Sample cell BDS 1200 [200]

5.4.1.3. Approach

Similar to the investigations with DMA and DSC, the same adhesive joints with different d_P and different metal substrates (PVD deposited Au, Cu and Al) are analysed with DES by temperature scans (from about -100 °C to +100 °C) with 8 K / min, for different frequencies (1, 10, 10^2, 10^3, 10^4, 10^5, 10^6 Hz) to detect and characterise possible interphases.

By varying the sample thickness d_P, the magnitude E of the external electric field between the capacitor plates of the sample cell is also changed for a given voltage U:

$$E = \frac{U}{d_P} \tag{5.12}$$

Above a particular electric field, the dielectric (i. e. the sample) in the capacitor becomes conductive. The voltage at which this occurs is called the breakdown voltage. Therefore, it is necessary to ensure that the applied voltage during the experiment does not exceed the breakdown voltage. Moreover, U has to be set small enough for the given d_P that the resulting E (eg. eq. (5.12)) meets the linear response presumed by eq. (5.9). The condition of linear response is met when the measured $\varepsilon'(\omega)$ and $\varepsilon''(\omega)$ do not depend on magnitude the applied electric field.

To determine the lowest possible magnitude of the electric field for the measurements, a polyurethane bulk sample is characterised with three different voltages: 0.1, 0.5 and 1 V – Figure 5-27. Bulk samples are prepared in a similar way as described in section 3.2.1. Pieces of the casted polyurethane adhesive plate are coated (after post-curing of the adhesive) with gold by PVD. Samples with 1 cm diameter are then die cut from these pieces, so that there is no metal on the edges of the samples.

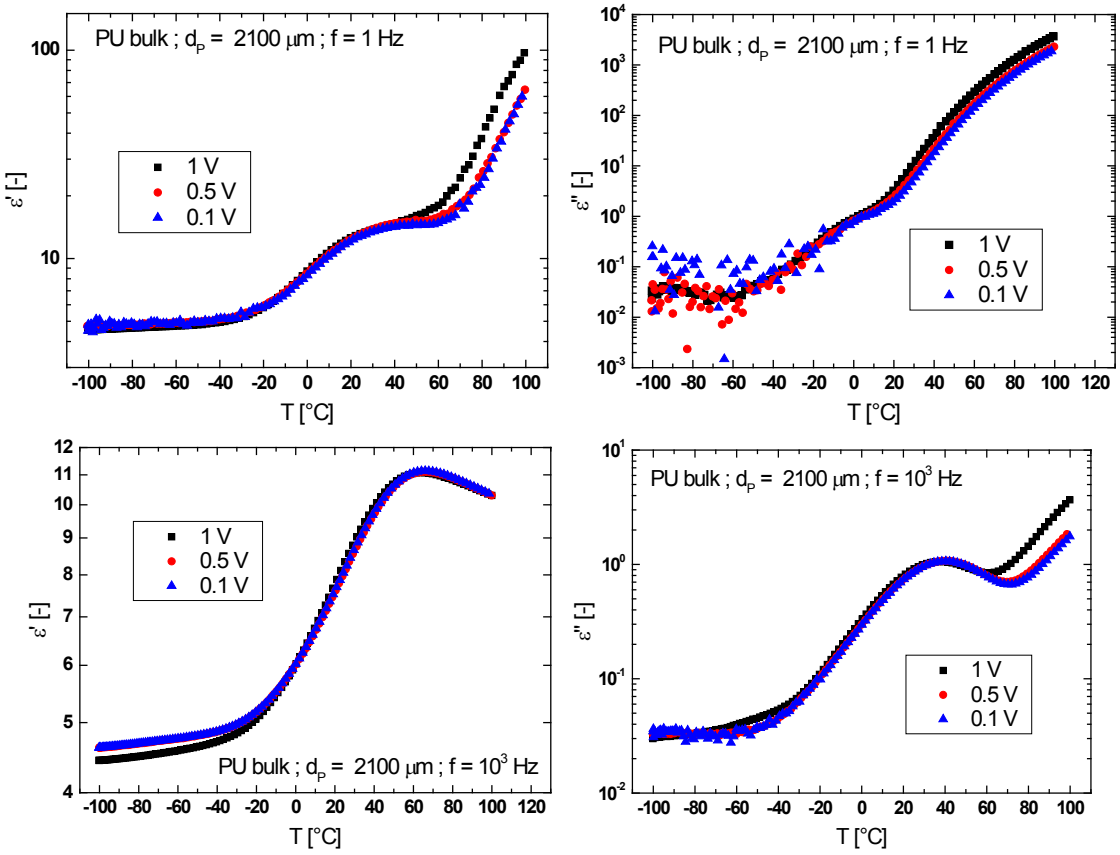

Figure 5-27: Real (ε', left) and imaginary (ε'', right) parts of the dielectric function of a polyurethane bulk sample ($d_P \approx 2100$ µm) measured at different voltages (0.1, 0.5 and 1 V) and different frequencies (1 Hz , top and 10^3 Hz, bottom) as a function of the temperature

Figure 5-27 shows a strong deviation of the results obtained with 1 V from those for the other voltages. Hence, a voltage of 1 V is not within the linear response range of the sample and is thus not adapted for the measurements. At low temperature, measurements are disrupted for measuring voltages of 0.1 and 0.5 V, especially for the imaginary parts of the dielectric function, ε''. The scatter of the values grows with decreasing electric field strength. However, the values in the major electric relaxation range (step in ε' and maximum in ε'') do not seem to be influenced by this effect.

The voltages 0.1 V and 0.5 V correspond to electric field strengths of 47.6 and 238.1 $V \cdot m^{-1}$ respectively for the bulk sample. Since the two measuring curves overlap, both voltage parameters can also be considered for the measurements for thick samples. However, as shown by the equation (5.12), the influence of the magnitude of the electric field is inversely proportion-

al to the sample thickness. Therefore measurements with the thinnest adhesive joint are performed at different frequencies as well to determine the maximal measuring voltage – Figure 5-28.

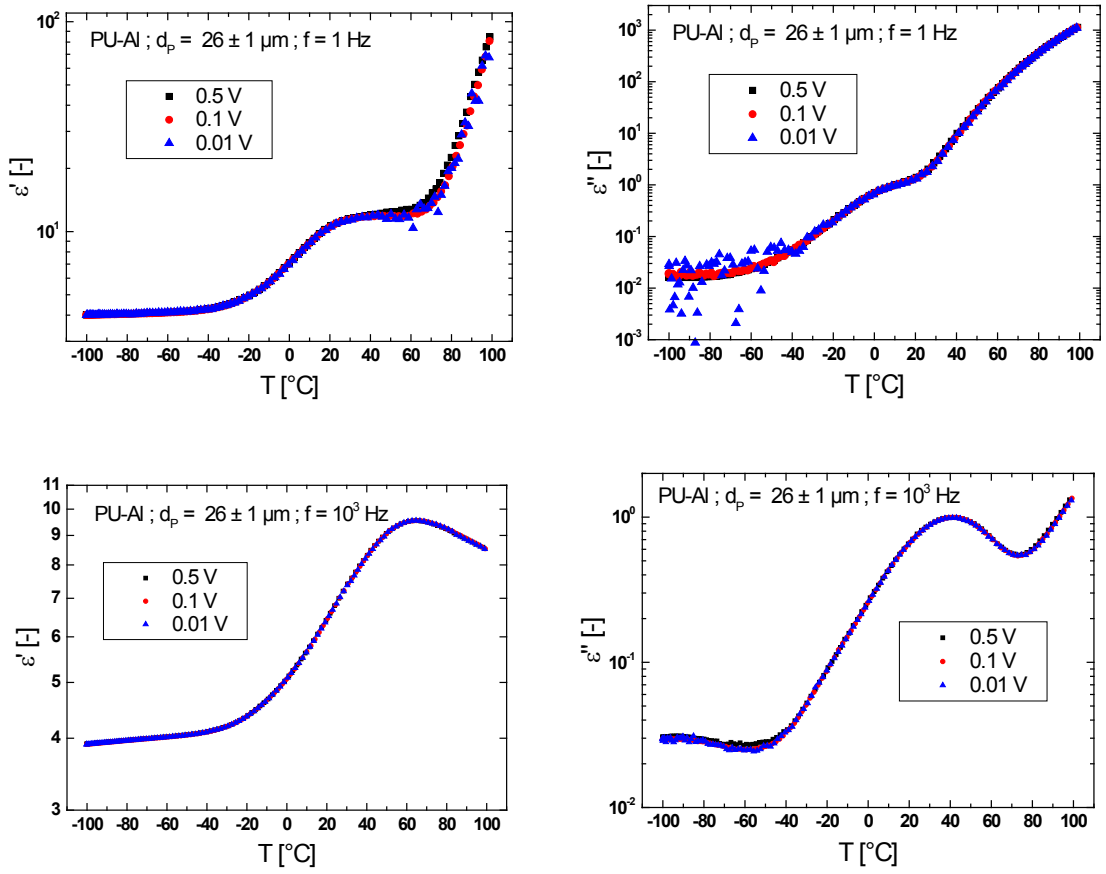

Figure 5-28: Real (ε', left) and imaginary (ε'', right) parts of the dielectric function of a PVD aluminium - polyurethane adhesive joint ($d_P \approx 26 \pm 1$ µm) measured at different voltages (0.01, 0.1 and 0.5 V) and different frequencies (1 Hz , top and 10^3 Hz, bottom) as a function of the temperature

For a sample with a $d_P \approx 26 \pm 1$ µm, a voltage of 0.01 V corresponds to an electric field strength of about 384.6 $V \cdot m^{-1}$ which is in the same order of magnitude than the value obtained with 0.5 V for the bulk sample. Nevertheless, the experimental curves at low measuring frequencies are scattered – Figure 5-28.

The results obtained with a voltage of 0.1 V – i. e. electric field strength of 3846.2 $V \cdot m^{-1}$ – cannot be distinguished from those obtained with 0.01 V. Therefore, all the following DES experiments, presented in this work, are performed with a voltage of 0.1 V regardless of the sample thickness. The results illustrated in Figure 5-27 and Figure 5-28 demonstrate that the electric field strength, obtained with a voltage of 0.1 V, does not influence the results within the sample thickness, temperature and frequency range.

5.4.2. **Results**

The temperature and frequency dependent dielectric function $\varepsilon^* = \varepsilon' - i \cdot \varepsilon''$ of a 26 µm aluminium-polyurethane adhesive joint is shown in Figure 5-29. The plots represent a major electric relaxation in the amorphous PU-network. In the glassy state of the adhesive, most of the motions in the polymer chains are blocked and the orientation of the dipoles and charge hopping processes are limited. The real part, ε', and the imaginary part, ε'', are relatively low and slowly increase with increasing temperature as the number of thermally activated motions grows. Similarly to the DMA experiments, the relaxation processes are shifted to higher temperature with increasing measuring frequency. This indicates that the major electric relaxation observed in the same temperature range can be associated with the co-operative mobility of the polymer chain segments (average over d_P) and thus, with the dynamic glass transition of the polyurethane adhesive. This major electric relaxation process is characterised by a peak in ε'' and a step-like increase of ε' versus temperature at each given frequency. After the major relaxation in the sample with $d_P = 26$ µm, a new relaxation appears at high temperatures in ε' and ε''. Since it is only visible at low f (1 , 10 Hz), there must be a very slow process behind it. There could be two reasons for this:

- severely impaired cooperative mobility in interphase
  or
- electrode polarisation: the accumulation of charge carriers at the surface of the electrode plates can cause an increase in ε' and ε'' at high temperatures and low frequency. This so-called electrode polarisation (interface polarisation)

Because of this secondary relaxation the end of the glass transition and sometimes even the glass transition temperature cannot be evaluated for these frequencies.

Another interesting feature for $f \geq 10^2$ Hz in these curves, which is also visible in Figure 5-30, is that ε' does not run into a plateau after the step-like relaxation as prescribed for dielectric relaxation in textbooks, but ε' falls off again. This already shows that not only dipole polarisation is involved here but also charge hopping.

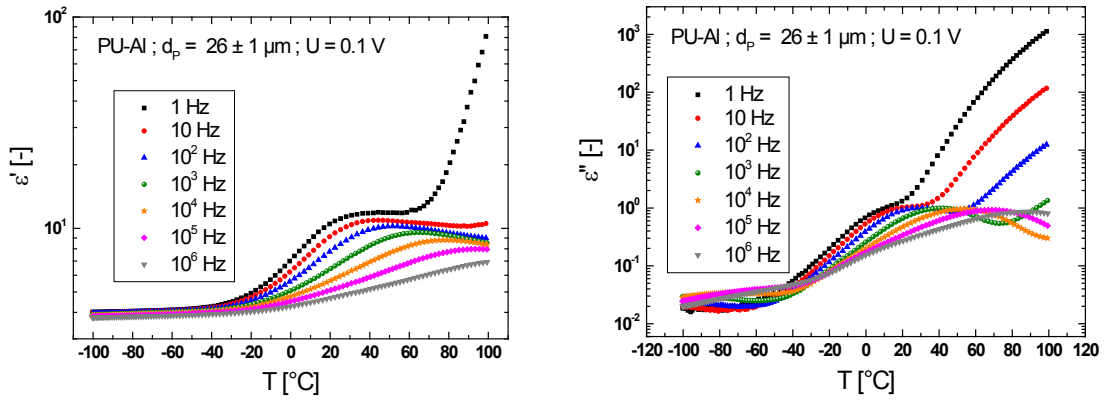

Figure 5-29: Real (ε', left) and imaginary (ε'', right) parts of the dielectric function of a PVD aluminium - polyurethane adhesive joint ($d_P \approx 26 \pm 1$ µm) measured at different frequencies as a function of the temperature

As for the results obtained with DMA and the different DSC techniques, only one glass transition can be observed in Figure 5-30. Consequently the measured plots represent the effective dielectric response of the adhesive layer. The plots in Figure 5-30 illustrate the influence of d_P on the dielectric properties of the adhesive joints. In the glassy state of the adhesive, the measurements depict no systematic bond line thickness dependence of the dielectric function[27].

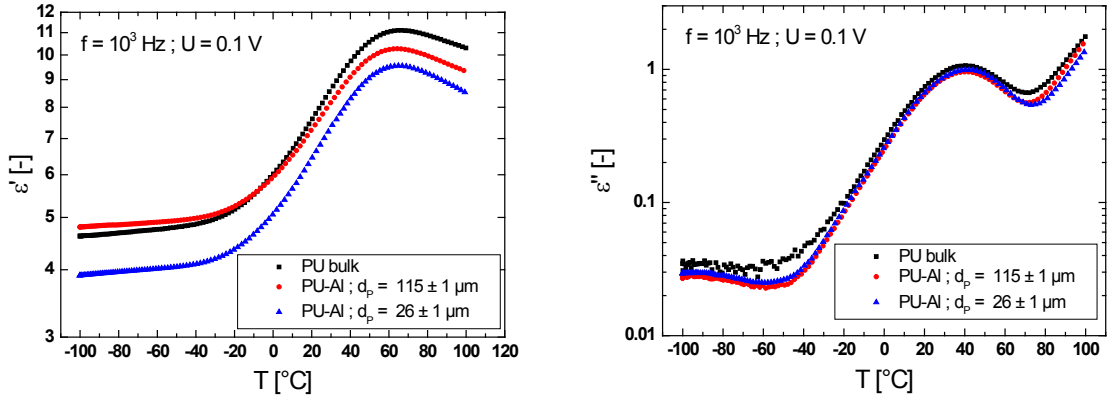

Figure 5-30: Real (ε' , left) and imaginary (ε″ , right) parts of the dielectric function of PVD aluminium - polyurethane adhesive joints with different d_P and polyurethane adhesive bulk measured at 10^3 Hz as a function of the temperature

Using the 1st derivative of ε' and ε″, the temperature for the inflection point in ε' and the temperature for the ε″-maximum are taken as the dynamic glass transition temperature, respectively $T_g^{dyn,\varepsilon'}$ and $T_g^{dyn,\varepsilon''}$ for the measured frequencies. The thickness dependence of $T_g^{dyn,\varepsilon'}$ (top) and $T_g^{dyn,\varepsilon''}$ (bottom) for Al-PU adhesive joints is shown in Figure 5-31.

[27] Note that the dielectric function was not calibrated for this study. Hence, neither ε′- nor ε″-data should be compared on a quantitative basis for different samples.

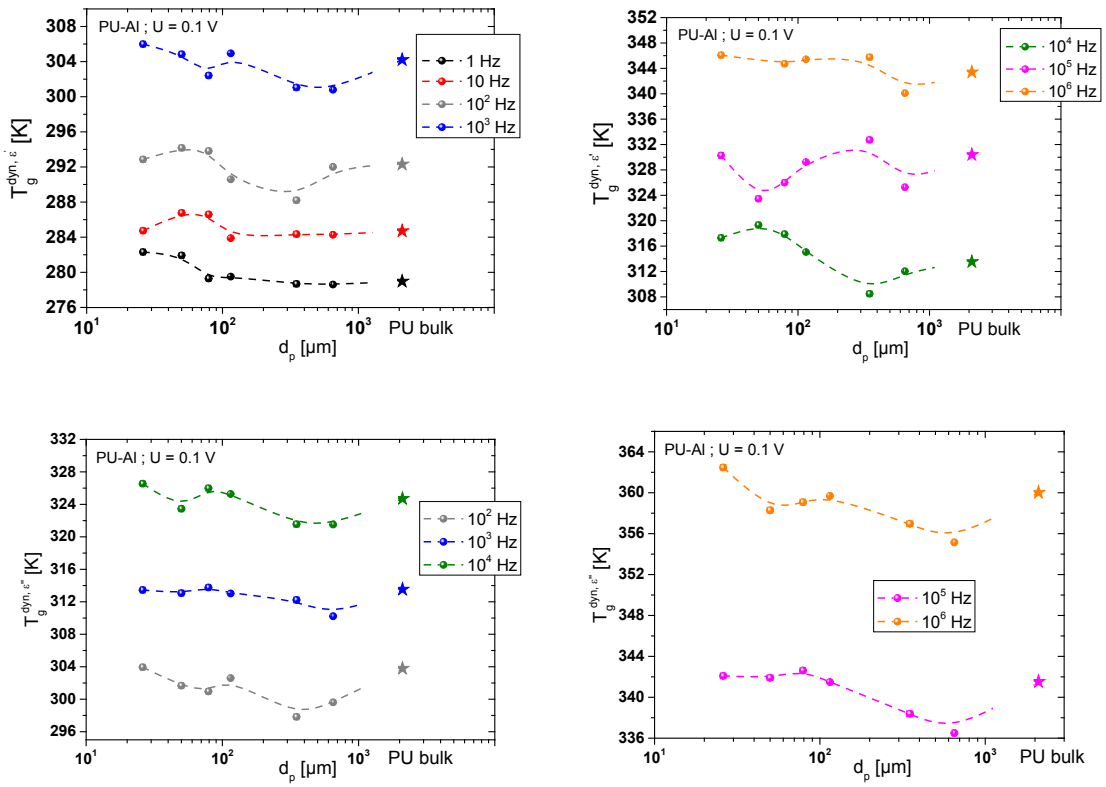

Figure 5-31: Dynamic glass transition temperatures, $T_g^{dyn,\varepsilon'}$ (top) and $T_g^{dyn,\varepsilon''}$ (bottom) as function of bond line thickness, d_P in Al-PU adhesive joints for different frequencies ("★" symbols represent the values measured for PU bulk)

By considering only the results obtained for the Al-PU adhesive joints, the glass transition temperatures $T_g^{dyn,\varepsilon'}$ and $T_g^{dyn,\varepsilon''}$ tend to decrease with increasing adhesive thickness for most of the measured frequencies. However, the maximal difference between the glass transition temperatures of the thinnest and the thickest adhesive joints is only about 6 K. Because of these small variations in T_g, an influence of d_P in the dielectric properties of the adhesive joints cannot be clearly identified. Nevertheless, similarities in the evolution of T_g with the results obtained with TM-flash-DSC can be noticed – Figure 5-23. The analysis of the glass transition temperature for frequencies 1 and 10 Hz is especially influenced by the secondary relaxation observed at high temperatures. This raises question the reliability of these results.

Although the same polyurethane batch has been used for the preparation of the adhesive joints and the bulk samples, the glass transition temperature of the bulk adhesive is relatively high in comparison with the adhesive joints. This effect could be also caused by a secondary electric relaxation.

The analysis of the width of the glass transition is limited to its lower half; between the beginning of the glass transition $T_{g,begin}^{dyn}(d_P)$ and the glass transition temperature $T_g^{dyn}(d_P)$. Figure 5-32 illustrates the adhesive thickness dependence of the lower half width of the dynamic glass transition in Al-PU adhesive joints measured with 10^4 Hz for ε' and ε". Although the

results display a trend to decrease with increasing adhesive thickness, the value of $T_g^{dyn,\varepsilon'}(d_P) - T_{g,begin}^{dyn,\varepsilon'}(d_P)$, measured for the bulk sample with the ε' curve does not reflect this effect. Regardless of the value obtained for the bulk adhesive, a decreasing lower half width of the glass transition with increasing d_P would indicate a larger dipole mobility within the interphase region. This result somehow contradicts the observation made in Figure 5-31 and those obtained with the mechanical testing methods. The different nature of the interphase, characterised by DES, could explain this difference.

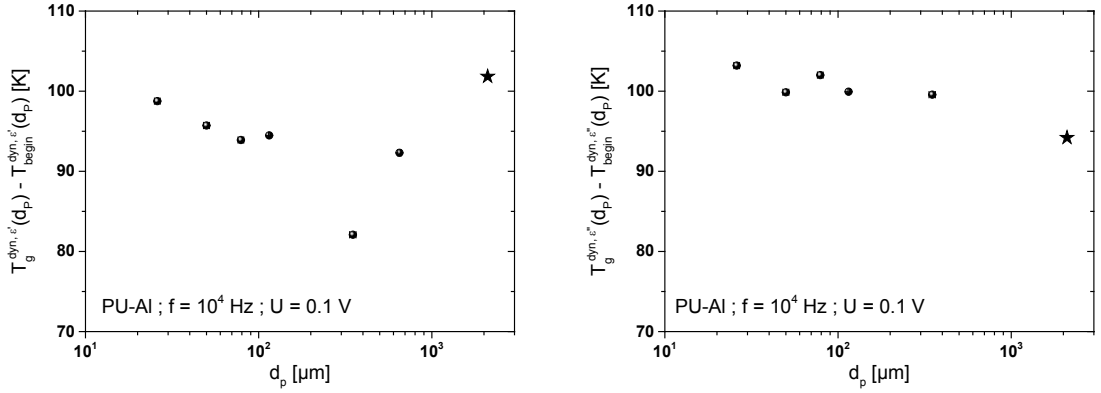

Figure 5-32: Lower half width of the dynamic glass transition in Al-PU adhesive joints, measured with 10^4 Hz ("★" symbols represent the values measured for PU bulk)

The same experiments have been carried out with PU-Cu and PU-Au adhesive joints to identify a possible influence of the metal substrate on the dielectric properties of the assumed interphase. However, no dependence could be detected as illustrated in Figure 5-33. The glass transition temperature of the three types of adhesive joints shows a trend to decrease with increasing adhesive thickness but the non-systematic variation of d_P for all the measuring frequencies weakens the interpretation of this effect.

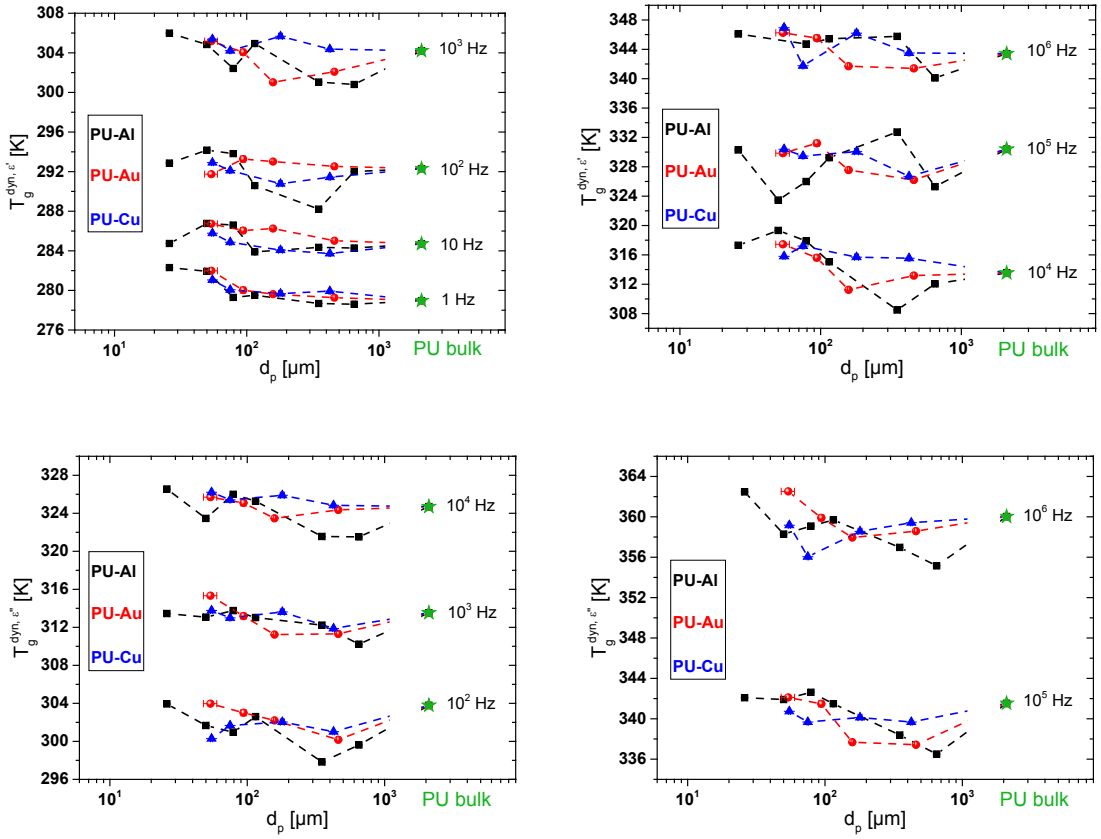

Figure 5-33: Dynamic glass transition temperatures, $T_g^{dyn,\varepsilon'}$ (top) and $T_g^{dyn,\varepsilon''}$ (bottom) as function of bond line thickness, d_P in PU-Al, PU-Au and PU-Cu adhesive joints for different frequencies ("★" symbols represent the values measured for PU bulk)

5.4.3. **Conclusions**

Although the experimental conditions should allow comparing the results of different adhesive thickness to each other, no clearly defined influence of d_P and the metal substrate on the dielectric properties could be identified in the investigated samples. The results show that the observed electric relaxations originate not only from dipole polarisation but also from charge hopping transport. The major electric transition can be related to the glass transition of the adhesive. The glass transition temperature of Al-, Au-, and Cu-PU adhesive joints tends to decrease with increasing d_P. This would corroborate the results obtained with mechanical testing and DSC methods whereby it indicates an interphase in terms of cooperative mobility in the polyurethane adhesive at the contact with the metal surface. A secondary electric relaxation could be observed at high temperature for low frequencies. The nature of this relaxation remains to be determined whether it originates from a strongly hindered co-operative mobility in the interphase or from electrode polarisation.

6. Conclusions and outlook

6.1. Conclusions

This work focuses on demonstrating the existence of interphases in polymer-metal adhesive bonds. Since the definition of interphase is directly related to the nature of the excitation, this problem has been limited, for a major part of this work, to the identification of mechanical interphases in adhesive joints. In order to identify and characterise potential mechanical interphases, it is first necessary to understand the complex mechanical behaviour of crosslinked polymers. Such polymer networks show a viscoelastic response, which depends on time and temperature. These effects are particularly evident in the (mechanical) glass transition range, also called transition region. It is important to note that under certain conditions, the behaviour of such polymers is often considered elastic. Two kinds of "elasticity" can be distinguished in polymer networks: entropy (or rubber-like) elasticity and energy elasticity (glassy state). However, these observations are only due to the limitation of the experimental conditions (i. e.: device resolution, temperature and measurement time). Regardless of the experimental conditions, a crosslinked polymer always exhibits viscoelastic behaviour.

In order to detect the influence of the interphases, PU-AlMg3 and stainless steel-PU adhesive joints having adhesive thicknesses from about 130 µm to circa 2 mm were mechanically tested with:

- Shear tests at constant shear rates
- Creep experiments at constant shear stress
- Stress relaxation experiments at constant shear strain.

All these tests were carried out in the linear viscoelastic region of the adhesive. By considering the analytical solutions of simple and one-dimensional constitutive models (Zener and generalised Maxwell model), the mechanical parameters, specific to the adhesive, can be obtained from the experimental results. These parameters are then used to calculate the relaxation and retardation time spectra which define the viscoelastic properties of the adhesive in the bonding. With these spectra it is finally possible to calculate the other viscoelastic functions. Thanks to this method, it is not only possible to compare and verify the experimental results with each other but also to quantify the mechanical properties of the adhesive bonds for a given temperature and thickness.

In this work, the adhesive layer is considered to be a homogeneous continuum. Of course, this consideration is an aberration and contradicts the concept of interphase but, since local gradients in the mechanical properties of such bonds remain difficult to measure in situ to date, this strategy still allows the detection of interphases. Indeed, if such interphases exist, then the properties of the bond should depend on the adhesive thickness: the influence of interphases is predominant in adhesive bonds with a thin adhesive layer, whereas the properties of the bulk

adhesive are expected to rule the mechanical behaviour of thick adhesive bonds. This approach can be applied for the identification of other interphase types as well. It is thus possible to indirectly (ex situ) characterise the gradients in the physical properties of such adhesive bonds.

Although the method described above may seem simple, defined and precise experimental conditions are necessary for its implementation.
Particular attention was paid to the preparation of the adhesive, the surface treatment of the substrates and finally the bonding of the substrates to ensure that the samples have the same initial conditions. Thus the results obtained from the different samples can be quantitatively compared with each other. Following a strict preparation protocol and monitoring the environmental conditions of the samples proved to be decisive in achieving this goal. The investigated adhesive is a fully cured thermoset, amorphous polyurethane. The glass transition of the bulk material ranges from 213 K to 303 K (measured by DSC at 10 K/min) and the glass transition temperature is $T_g^{DSC,bulk} = 266 \pm 1$ K.
Another challenge was the design and construction of experimental devices reliable and accurate enough to be able to characterise the thermomechanical behaviour of bonded joints. One of the greatest challenges was the elimination of environmental factors (variations in ambient temperature and humidity, vibrations and temperature dependence of the force and displacement sensors) that affected the experimental measurements. Accurate temperature control of samples and installations over a long period of time is indeed necessary for the precise determination of the thermomechanical properties of polymers.
The disturbing effects outlined above have been detected and greatly limited through preliminary tests and the development of an approach that allows reproducible experimental conditions. The chemical, thermal and mechanical stability of the adhesive (joints) was also monitored to ensure that the samples remained unchanged throughout the experiments.

The temperature dependence of the mechanical properties of PU-AlMg3 and PU-stainless steel bonds was characterised in a temperature range from about 268 K to ca. 353 K. The experimental results of the isothermal shear test at constant shear rate, creep and stress relaxation experiments have shown that the relaxed elastic properties (equilibrium moduli) of the polymer and their temperature dependence can be extrapolated from the entropy “elasticity” to the transition region. It proves that the moduli in the relaxed viscoelastic state are dominated by the entropic restoring forces. The resulting linear increase of the equilibrium moduli with increasing temperature is then valid in the transition region and leads to a good approximation of the thermomechanical behaviour of the polyurethane adhesive in the investigated temperature region. Moreover the determination of the retardation time spectra allows a quantitative analysis of the viscoelastic properties of the adhesive joints and their temperature dependence.

Mechanical tests conducted on PU-AlMg3 and PU-stainless steel bonds reveal a bond line thickness dependence of both relaxed "elastic" and viscoelastic properties in a thickness range from about 130 µm to about 2000 µm. The analysis of the results of shear, creep and stress relaxation tests shows the same effect: as the adhesive thickness decreases, the stiffness of the bonded joint increases. Moreover, the retardation time spectra, which are material-specific viscoelastic functions, depend clearly on the bondline thickness. These effects are interpreted

as the formation of interphases in the polyurethane adhesive in contact with the metal substrates. These mechanical interphases appear stiffer or less compliant than the bulk adhesive. The results show that these interphases influence the effective mechanical properties of the adhesive joints up to a bond line thickness of about 1.5 mm.
Due to the experimental conditions (finite measurement time and temperature range), only part of the viscoelastic properties of bonded joints can be measured. In order to find out whether the measured data are sufficient to represent the adhesive dynamics fairly accurately, the interrelations between the different viscoelastic functions are used. This method allows not only to calculate viscoelastic functions from others but also to check the quality of the experimental measurements by comparing them with data calculated from other mechanical tests. The agreement of the measured viscoelastic functions with those calculated shows that the experimental data are sufficient to give a good approximation of the thermomechanical behaviour of bonded joints. From an isothermal creep curve, it is thus possible to calculate the corresponding retardation and relaxation time spectra, the stress relaxation modulus as well as the shear modulus for different constant shear rates.

To complement these calculations, an attempt to predict the mechanical behaviour of adhesive joints by implementing both temperature and adhesive thickness dependence to the calculations has been suggested. Although the evaluation of the retardation time spectra reveals complex thermorheological behaviour of the viscoelastic functions in the adhesive joints, the time-temperature equivalence, as described by Williams, Landel and Ferry, provides a good approximation of the thermomechanical behaviour of a bonded joint for given adhesive thickness. Based on this finding, similar consideration as for the time-temperature equivalence has been attempted to describe the bond line thickness dependence of the viscoelastic properties in adhesive joints: a vertical shift of the retardation spectra is implemented to simulate the bond line thickness dependence. However a bigger experimental database is necessary to discuss the quality and the limitations of this bondline thickness - time equivalence, the first results lead to the conclusion that the mechanical interphase exhibits different mechanical properties from those of the adhesive bulk.

To investigate the (dynamical) mechanical properties of metal-polymer sandwich samples down to some few μm thickness, the suitability of dynamical mechanical analysis (DMA) has been confirmed. The thickness dependence of the mechanical properties of Au-PU and Al-PU adhesive joints are interpreted as proof for a dynamic mechanical interphase between the polyurethane adhesive and the metal substrate. This interphase possesses a higher crosslink density and, therefore, a higher glass transition temperature implying less cooperative mobility than in the PU bulk. Moreover the interphase network structure should be more uniform than in bulk PU as the glass transition range is getting narrower with respect to temperature.
In order to identify the possible influence of this interphase on further physical properties, the same sample types as those used for DMA have been investigated with different methods namely differential scanning calorimetry (DSC) and dielectric spectroscopy (DES).
The caloric results only indicate the existence of interphases in a thickness range up to 50 μm in the adhesive joints. These results should be complemented with further investigations.

The same applies for the results obtained with DES which show that no clearly defined influence of the adhesive thickness on the dielectric properties could be identified.
These results illustrate that the interphase influences the physical properties of the bonds to different extents and that knowledge of the processes triggering the formation of such interphases is necessary to better understand the adhesion mechanisms.

6.2. Outlook

The existence of mechanical interphase in adhesive joints could be proved and their influence on the mechanical properties as a function of the temperature and bond line thickness has been quantitatively characterised by shear, creep and relaxation tests as well as dynamic mechanical analysis. The method used in this work for the quantitative analysis of viscoelastic properties is based on simple one-dimensional constitutive models. By using more complex rheological models, which are more appropriate to describe the behaviour of polymer networks, a higher resolution in the experimental range can be expected.
Although the cubic polynomial function gives a fairly good approximation of the continuous retardation time spectrum in this work, a function such as a truncated and inversed "Lennard-Jones potential" function seems more appropriate to physically describe the evolution of such a spectrum, especially if the number of known data pairs $\left\{\tau_i; L^*\left(\tau_i\right)\right\}$ is large.

Nevertheless, the experimental data pool from this work can be used as a basis for the development and verification of a numerical model to predict the thermomechanical behaviour of bonded joints considering the bond line thickness. Such a model is also necessary to separate the contributions of the interphase from that of the adhesive bulk in the mechanical response of bonded joints.

The formation of internal stresses during the cure of the adhesive in contact with the substrate could be an explanation for the existence of mechanical interphases in bonded joint. A dedicated study on this topic would help to improve the understanding of the formation of such interphases and thus the adhesion mechanisms in general.

A. List of acronyms

a_T	Horizontal shift factor in time – temperature equivalence
b_τ	Horizontal shift factor in bond line thickness – time equivalence
b_L	Vertical shift factor in bond line thickness – time equivalence
BE	Backscattered electrons
DES	Dielectric spectroscopy
DMA	Dynamic mechanical analysis
d_P	Bond line thickness / Adhesive layer thickness
DSC	Differential scanning calorimetry
EDX	Energy-dispersive X-ray spectroscopy
FIB	Focused ion beam
γ	Shear strain
G(t)	Relaxation shear modulus / relaxation function
G_∞	Equilibrium shear modulus / Relaxed shear modulus
$H(\tau)$	Continuous relaxation time spectrum
$H^*(\tau)$	Discrete relaxation time spectrum
J(t)	Creep compliance / creep function
J_∞	Equilibrium creep compliance / Relaxed creep compliance
$L(\tau)$	Continuous retardation time spectrum
$L^*(\tau)$	Discrete retardation time spectrum
μ	Hyperelastic shear modulus
M	Dynamic shear modulus
MDI	Methylene diphenyl diisocyanate
PU	Polyurethane
PTFE	Polytetrafluoroethylene
SE	Secondary electrons
SEM	Scanning electron microscopy
SFM	Scanning force microscopy
τ	Retardation time / Relaxation time
T_g	Glass transition temperature
T_{12}	Shear stress
TGA	Thermogravimetric analysis
WLF	Williams–Landel–Ferry (equation)
WLI	White light interferometry

B. References

[1] J. Batal,
Charakterisierung der mechanischen Grenzschicht in Polymer-Metall-Klebungen,
PhD thesis, Universitaet des Saarlandes, Saarbruecken, **2012**.

[2] W. Possart,
Adhesion - Current Research and Applications,
Wiley-VCH Verlag, Weinheim, **2005**, ISBN 978-3-527-31263-4.

[3] L. H. Sharpe,
The Interphase in Adhesion,
Journal of Adhesion **1972**, *4* (1), p. 51-64.

[4] D. Arayasantiparb, S. McKnight, M. Libera,
Compositional variation within the epoxy/adherend interphase,
Journal of Adhesion Science and Technology **2001**, *15* (12), p. 1463-1484.

[5] M. Aufray, A. A. Roche,
Properties of the Interphase Epoxy-Amine/Metal: Influences from the Nature of the Amine and the Metal,
W. Possart (Ed.),
Adhesion - Current Research and Applications, Chapter 7,
Wiley-VCH, Weinheim, 2005, ISBN 3-527-31263-3, p. 89-102.

[6] M. Aufray, A. A. Roche,
Epoxy-amine/metal interphases: Influences from sharp needle-like crystal formation,
International Journal of Adhesion and Adhesives **2007**, *27* (5), p. 387-393.

[7] M. G. Barthés-Labrousse,
Mechanisms of Formation of the Interphase in Epoxy-Amine/Aluminium Joints,
The Journal of Adhesion **2012**, *88* (8), p. 699-719.

[8] A. Meiser,
Vernetzung und Alterung eines Epoxidklebstoffs im Kontakt mit Atmosphären und Metallen,
PhD thesis, Universität des Saarlandes, Saarbrücken, **2010**.

[9] W. Possart, J. K. Krüger, C. Wehlack, U. Müller, C. Petersen, R. Bactavatchalou, A. Meiser,
Formation and structure of epoxy network interphases at the contact to native metal surfaces,
Comptes Rendus Chimie **2006**, *9* (1), p. 60-79.

[10] C. Wehlack, W. Possart,
Chemical Structure Formation and Morphology in Ultrathin Polyurethane Films on Metals,
W.Possart (Ed.),
Adhesion - Current Research and Applications, 6,
WILEY-VCH, Weinheim, 2005, ISBN 3-527-31263-3, p. 71-87.

[11] C. Wehlack,
Chemische Struktur und ihre Entstehung in dünnen Epoxid- und Polyurethanschichten auf Metallen,
PhD thesis, Universitaet des Saarlandes, Saarbruecken, **2008**.

[12] C. Wehlack, W. Possart,
Characterization of the epoxy-metal interphase: FTIR-ERAS and spectra calculation for ultra-thin films,
Macromolecular. Symposia. **2004**, *205* (1), p. 251-262.

[13] C. Wehlack, W. Possart, J. K. Krüger, U. Müller,
Epoxy and Polyurethane Networks in Thin Films On Metals - Formation, Structure, Properties,
Soft Materials **2007**, *5* (2&3), p. 87-134.
[14] C. Wehlack, W. Possart,
Formation, structure and morphology of polyurethane-metal interphases,
IOP Conference Series: Materials Science and Engineering, **2009**.
[15] C. Wehlack, H. Ehbing, D. J. Dijkstra, W. Possart,
How Do Metal Adherends Infuence the Chemical Structure Formation of Thin Polyurethane Films?,
Conference Proceedings, *4th World Congress on Adhesion and Related Phenomena (WCARP2010)*, Arcachon, France, September 26-30, **2010**.
[16] C. Wehlack, E. Mallandain, H. Ehbing, D. J. Dijkstra, W. Possart,
How Does Air Moisture Affect the Chemical Structure Formation in Thin Polyurethane Films on Metals?,
Conference Proceedings, *4th World Congress on Adhesion and Related Phenomena (WCARP2010)*, Arcachon, France, September 26-30, **2010**.
[17] C. Wehlack, S. Bodin, H. Ehbing, D. J. Dijkstra, W. Possart,
Properties of Thin Polyurethane Films on Metals at the Glass Transition,
Conference Proceedings, *4th World Congress on Adhesion and Related Phenomena (WCARP2010)*, Arcachon, France, September 26-30, **2011**.
[18] A. Meiser, C. Kübel, H. Schäfer, W. Possart,
Electron microscopic studies on the diffusion of metal ions in epoxy-metal interphases,
International Journal of Adhesion and Adhesives **2009**, *30* (3), p. 170-177.
[19] R. G. Dillingham, F. J. Boerio,
Interphase Composition in Aluminum/Epoxy Adhesive Joints,
Journal of Adhesion **1987**, *24* (2-4), p. 315-335.
[20] S. G. Hong, T. C. Wang,
The effect of copper oxides on the curing of brominated epoxy resins,
Thermochimica Acta **1994**, *237* (2), p. 305-316.
[21] C. Bockenheimer, B. Valeske, W. Possart,
Network structure in epoxy aluminium bonds after mechanical treatment,
International Journal of Adhesion and Adhesives **2002**, *22* (5), p. 349-356.
[22] W. Brockmann, O. D. Hennemann, H. Kollek, C. Matz,
Adhesion in bonded aluminium joints for aircraft construction,
International Journal of Adhesion and Adhesives **1986**, *6* (3), p. 115-143.
[23] P. Montois, V. Nassiet, J. A. Petit, Y. Baziard,
Viscosity effect on epoxy-diamine/metal interphases: Part I: Thermal and thermomechanical behaviour,
International Journal of Adhesion and Adhesives **2006**, *26* (6), p. 391-399.
[24] M. Aufray, A. A. Roche,
Residual Stresses and Practical Adhesion: Effect of Organo-metallic Complex Formation and Crystallization,
Journal of Adhesion Science and Technology **2006**, *20* (16), p. 1889-1903.
[25] S. Bentadjine, R. Petiaud, A. A. Roche, V. Massardier,
Organo-metallic complex characterization formed when liquid epoxy-diamine mixtures are applied onto metallic substrates,
Polymer **2001**, *42* (14), p. 6271-6282.

[26] J. Bouchet, A. A. Roche,
Internal stresses, Young's modulus and practical adhesion of organic coatings applied onto 5754 aluminium alloy,
Thin Solid Films **1999**, *355-356*, p. 270-276.
[27] J. Bouchet, A. A. Roche, E. Jacquelin,
Determination of residual stresses in coated metallic substrates,
Journal of Adhesion Science and Technology **2001**, *15* (3), p. 321-343.
[28] J. Bouchet, A. A. Roche, E. Jacquelin,
The role of the polymer/metal interphase and its residual stresses in the critical strain energy release rate (Gc) determined using a three-point flexure test,
2001, *15* (3), p. 345-369.
[29] H. Bourahla, J. Lenoir, M. Romand, J. Chauchard,
Influence de l'epaisseur de l'adhésif et du vieillissement sur les propriétés mécaniques dynamiques d'un assemblage: Adhésif structural/acier inoxydable,
Die Angewandte Makromolekulare Chemie **1990**, *178* (1), p. 47-62.
[30] D. Fata, C. Bockenheimer, W. Possart,
Epoxies on Stainless Steel - Curing and Aging,
W.Possart (Ed.),
Adhesion - Current Research and Applications, 30,
WILEY-VCH, Weinheim, 2005, ISBN 3-527-31263-3, p. 479-505.
[31] A. A. Roche, J. Guillemenet,
Mechanical and chemical properties of organic coatings applied to metallic sheet substrates,
Thin Solid Films **1999**, *342* (1-2), p. 52-60.
[32] R. Sanctuary, J. Baller, J. K. Krüger, D. Schaefer, R. Bactavatchalou, B. Wetzel, W. Possart, P. Alnot,
Complex specific heat capacity of two nanocomposite systems,
Thermochimica Acta **2006**, *445-6* (2), p. 111-115.
[33] D. Fata,
Epoxidsysteme im Verbund mit rostfreien Stählen - Vernetzung und Alterung,
PhD thesis, Universität des Saarlandes, Saarbrücken, **2005**.
[34] R. Häßler, E. zur Mühlen,
An introduction to μ-TA^{TM} and its application to the study of interfaces,
Thermochimica Acta **2000**, *361* (1-2), p. 113-120.
[35] A. Meiser, A. J. Karst, K. Willstrand, W. Possart,
Curing and chemical ageing in epoxies: a local study of the interphase to metals,
8th European Adhesion Conference EURADH 2008 and 10th International Conference on the Science & Technology of Adhesion and Adhesives ADHESION '08, **2008**, p. 341-342.
[36] C. Bockenheimer, D. Fata, W. Possart,
New aspects of aging in epoxy networks. I. Thermal aging,
Journal of Applied Polymer Science **2004**, *91* (1), p. 361-368.
[37] A. Meiser, K. Willstrand, P. Fehling, W. Possart,
Chemical Aging in Epoxies: A Local Study of the Interphases to Air and to Metals,
Journal of Adhesion **2008**, *84* (4), p. 299-321.
[38] A. Meiser, K. Willstrand, W. Possart,
Influence of Composition, Humidity, and Temperature on Chemical Aging in Epoxies: A Local Study of the Interphase with Air,
The Journal of Adhesion **2010**, *86*, p. 222-243.

[39] A. Meiser, W. Possart,
Epoxy-Metal Interphases: Chemical and Mechanical Aging,
Journal of Adhesion **2011**, *87* (11), p. 313-330.
[40] A. Meiser, C. Wehlack, W. Possart,
Chemical Processes in Ultra-thin Epoxy Films on Metals During Ageing,
W. Possart (Ed.),
Adhesion - Current Research and Applications, Chapter 28,
Wiley-VCH, Weinheim, 2005, ISBN 3-527-31263-3, p. 445-463.
[41] C. Sperandio, J. Bardon, A. Laachachi, H. Aubriet, D. Ruch,
Influence of plasma surface treatment on bond strength behaviour of an adhesively bonded aluminium-epoxy system,
International Journal of Adhesion and Adhesives **2010**, *30* (8), p. 720-728.
[42] J. K. Krüger, U. Müller, R. Bactavatchalou, D. Liebschner, M. Sander, W. Possart, C. Wehlack, J. Baller, D. Rouxel,
Mechanical Interphases in Epoxies as seen by Nondestructive High-Performance Brillouin Microscopy,
Adhesion: Current Research and Applications,
WILEY-VCH Verlag GmbH & Co. KGaA, Weinheim, 2006, p. 125-142.
[43] P. Montois, V. Nassiet, J. Alain Petit, D. Adrian,
Viscosity effect on epoxy-diamine/metal interphases-Part II: Mechanical resistance and durability,
International Journal of Adhesion and Adhesives **2007**, *27* (2), p. 145-155.
[44] K. Shimizu, M. L. Abel, C. Phanopoulos, S. Holvoet, J. F. Watts,
The characterisation of the interfacial chemistry of adhesion of rigid polyurethane foam to aluminium,
Journal of Materials Science **2012**, *47* (2), p. 902-918.
[45] D. Castagnetti, A. Spaggiari, E. Dragoni,
Effect of Bondline Thickness on the Static Strength of Structural Adhesives Under Nearly-Homogeneous Shear Stresses,
The Journal of Adhesion **2011**, *87* (7-8), p. 780-803.
[46] L. F. M. da Silva, T. N. S. S. Rodrigues, M. A. V. Figueiredo, M. F. S. F. de Moura, J. A. G. Chousal,
Effect of Adhesive Type and Thickness on the Lap Shear Strength,
The Journal of Adhesion **2006**, *82* (11), p. 1091-1115.
[47] M. Johlitz, S. Diebels, J. Batal, H. &. P. W. Steeb,
Size effects in polyurethane bonds: experiments, modelling and parameter identification,
Journal of Materials Science **2008**, *43* (14), p. 4768-4779.
[48] A. Moradi, D. Leguillon, N. Carrère,
Influence of the adhesive thickness on a debonding - An asymptotic model,
Engineering Fracture Mechanics **2013**, *114*, p. 55-68.
[49] A. A. Roche, J. Bouchet, S. Bentadjine,
Formation of epoxy-diamine/metal interphases,
International Journal of Adhesion and Adhesives **2002**, *22* (6), p. 431-441.
[50] M. Schlimmer,
Der Zugscherversuch Fuer Metallklebstoffe. Neue Untersuchungsmethoden und Ergebnisse,
Materialwissenschaft und Werkstofftechnik **1988**, *19* (6), p. 182-190.
[51] W. Xu, H. Yu, C. Tao,
Damage and stress evolution in the bondlines of metallic adhesively bonded joints accompanied by bondline thickness effect,
International Journal of Adhesion and Adhesives **2015**, *59*, p. 86-97.

[52] J. Chung,
Nanoscale Characterization of Epoxy Interphase on Copper Microstructures,
Dissertation, Technische Universität Berlin, Berlin, **2006**.
[53] J. Chung, M. Munz, H. Sturm,
Stiffness variation in the interphase of amine-cured epoxy adjacent to copper microstructures,
Surface and Interface Analysis **2007**, *39* (7), p. 624-633.
[54] Z. Chen, S. Diebels, N. J. Peter,
Identification of Finite Viscoelasticity and Adhesion Effects in Nanoindentation of a Soft Polymer by Inverse Method,
Comput. Mater. Sci. **2013**, *72 %6*, p. 127-139.
[55] Z. Chen,
Nanoindentation testing of soft polymers: Computation, experiments and parameters identification,
Dissertation, Universität des Saarlandes, Saarbruecken, **2014**.
[56] Z. Chen,
Nanoindentation of Soft Polymers: Modeling, Experiments and Parameter Identification,
Technische Mechanik **2014**, *34*, p. 166-189.
[57] G. Possart,
Mechanical Interphases in Adhesives - Experiments, Modelling and Simulation,
Dissertation, Friedrich-Alexander-Universität Erlangen-Nürnberg, Erlangen, **2014**.
[58] P. L. Geiss, M. Schumann,
Investigation of the Mechanical Properties of Interphases in Adhesively Bonded Epoxy-Aluminum Joints by Localized Micro Extensometry,
The Journal of Adhesion **2012**, *88* (11-12), p. 941-955.
[59] M. Presser,
Entwicklung einer Methodik zur mechanischen Analyse der grenzschichtbeeinflussten Polymereigenschaften in Klebverbunden mit Epoxidharzklebstoffen,
PhD Thesis, TU Kaiserslautern, Kaiserslautern, **2011**.
[60] J. K. Krüger, W. Possart, R. Bactavatchalou, U. Müller, T. Britz, R. Sanctuary, P. Alnot,
Gradient of the Mechanical Modulus in Glass-Epoxy-Metal Joints as Measured by Brillouin Microscopy,
Journal of Adhesion **2004**, *80* (7), p. 585-599.
[61] M. Hossain, G. Possart, P. Steinmann,
A small-strain model to simulate the curing of thermosets,
Computational Mechanics **2009**, *43* (6), p. 769-779.
[62] M. Hossain, G. Possart, P. Steinmann,
A finite strain framework for the simulation of polymer curing. Part I: Elasticity,
Computational Mechanics **2009**, *44* (5), p. 621-630.
[63] M. Hossain, G. Possart, P. Steinmann,
A finite strain framework for the simulation of polymer curing. Part II. viscoelasticity and shrinkage,
Computational Mechanics **2010**, *46* (3), p. 363-375.
[64] M. Hossain, P. Steinmann,
Modelling and simulation of the curing process of polymers by a modified formulation of the Arruda-Boyce model,
Archives of Mechanics **2011**, *63* (5-6), p. 621-633.
[65] M. Hossain, P. Steinmann,
Degree of cure-dependent modelling for polymer curing processes at small-strain. Part I: Consistent reformulation,
Computational Mechanics **2014**, *53* (4), p. 777-787.

[66] J. Mergheim, G. Possart, P. Steinmann,
Modelling and computation of curing and damage of thermosets,
Computational Materials Science **2012**, *53* (1), p. 359-367.
[67] G. Marckmann, E. Verron,
Comparison of Hyperelastic Models for Rubber-Like Materials,
Rubber Chemistry and Technology **2006**, *79* (5), p. 835-858.
[68] M. Mooney,
A theory of large elastic deformation,
Journal of Applied Physics **1940**, *11*, p. 582-592.
[69] R. W. Ogden,
Elastic Deformations of Rubberlike Solids,
Mechanics of Solids **1982**, *The Rodney Hill 60th Anniversary Volume*, p. 499-537.
[70] P. J. Flory,
Statistical thermodynamics of random networks,
Proceedings of the Royal Society of London. A. Mathematical and Physical Sciences **1976**, *351* (1666), p. 351ff.
[71] L. R. G. Treloar,
Mechanics of rubber elasticity,
J. polym. sci. , C Polym. symp. **1974**, *48*, p. 107-123.
[72] M. Johlitz,
Experimentelle Untersuchung und Modellierung von Maßstabseffekten in Klebungen,
PhD thesis, Universitaet des Saarlandes, Saarbruecken, **2008**.
[73] M. Johlitz, S. Diebels, W. Possart,
Investigation of the thermoviscoelastic material behaviour of adhesive bonds close to the glass transition temperature,
Archive of Applied Mechanics **2012**, *82* (8), p. 1089-1102.
[74] L. Boltzmann,
Zur Theorie der elastischen Nachwirkung,
Annalen der Physik **1878**, *241* (11), p. 430-432.
[75] M. T. Shaw, W. J. MacKnight,
Introduction to Polymer Viscoelasticity,
Wiley, **2005**, ISBN 9780471741824.
[76] S. Etienne, L. David,
Introduction a la physique des polymeres - 2ed,
Dunod, **2012**, ISBN 9782100585779.
[77] Y. Huang, D. R. Paul,
Physical aging of thin glassy polymer films monitored by gas permeability,
Polymer **2004**, *45* (25), p. 8377-8393.
[78] A. V. Tobolsky,
Properties and structure of polymers,
Wiley, **1960**.
[79] L. R. G. Treloar,
The Physics of Rubber Elasticity,
3rd Edition, Oxford University Press, New York, **1995**, ISBN 978-0-19-857027-1.
[80] P. J. Flory, C. A. J. Hoeve, A. Ciferri,
Influence of bond angle restrictions on polymer elasticity,
Journal of Polymer Science **1959**, *34* (127), p. 337-347.
[81] E. Guth, H. Mark,
Zur innermolekularen, Statistik, insbesondere bei Kettenmolekiilen I,
Monatshefte fuer Chemie und verwandte Teile anderer Wissenschaften **1934**, *65* (1), p. 93-121.

[82] W. Kuhn,
Über die Gestalt fadenförmiger Moleküle in Lösungen,
Kolloid-Zeitschrift **1934**, *68* (1), p. 2-15.
[83] M. V. Volkenstein,
The configurational statistics of polymeric chains,
Journal of Polymer Science **1958**, *29* (120), p. 441-454.
[84] E. M. Arruda, M. C. Boyce,
A three-dimensional constitutive model for the large stretch behavior of rubber elastic materials,
Journal of the Mechanics and Physics of Solids **1993**, *41* (2), p. 389-412.
[85] G. T. Houlsby, A. M. Puzrin,
Thermodynamics,
G. T. Houlsby, A. M. Puzrin (Eds.),
Principles of Hyperplasticity: An Approach to Plasticity Theory Based on Thermodynamic Principles,
Springer London, London, 2007, ISBN 978-1-84628-240-9, p. 35-51.
[86] F. R. Schwarzl,
Polymermechanik : Struktur und mechanisches Verhalten von Polymeren,
Berlin : Springer, **1990**, ISBN 3540519653.
[87] R. S. Rivlin,
Large Elastic Deformations of Isotropic Materials: Fundamental Concepts,
Philosophical Transactions of the Royal Society A **1948**, *240*, p. 459-490.
[88] P. E. Rouse,
A Theory of the Linear Viscoelastic Properties of Dilute Solutions of Coiling Polymers,
The Journal of Chemical Physics **1953**, *21* (7), p. 1272-1280.
[89] J. D. Ferry,
Viscoelastic Properties of Polymers,
John Wiley & Sons, New York, **1980**, ISBN 0-471-04894-1.
[90] R. Lakes,
Viscoelastic Materials,
Cambridge University Press, Cambridge, **2009**, ISBN 9780521885683.
[91] A. S. Nowick, B. S. BERRY,
Anelastic relaxation in crystalline solids,
New York (N.Y.) : Academic press, **1972**, ISBN 0125226500.
[92] S. Bernstein,
Sur les fonctions absolument monotones,
Acta Math. **1929**, *52*, p. 1-66.
[93] A. Schmitt,
Viskoelastische Funktionen - Modellierung für Klebungen,
Master thesis, Universität des Saarlandes, Saarbruecken, **2013**.
[94] B. Gross,
Mathematical Structure of the Theories of Viscoelasticity,
Hermann et Cie, **1953**.
[95] T. L. Smith,
Approximate Equations for Interconverting the Various Mechanical Properties of Linear Viscoelastic Materials,
Transactions of the society of rheology **1958**, *2* (1), p. 131-151.
[96] M. Ionescu,
Chemistry and Technology of Polyols for Polyurethanes,
Rapra Technology Limited, **2005**, ISBN 978-1-84735-035-0.

[97] M. S. Sánchez-Adsuar, E. Papon, J. J. Villenave,
Influence of the synthesis conditions on the properties of thermoplastic polyurethane elastomers,
Journal of Applied Polymer Science **2000**, *76* (10), p. 1590-1595.
[98] M. S. Sànchez-Adsuar, E. Papon, J. J. Villenave,
Rheological characterization of thermoplastic polyurethane elastomers,
Polymer International **2000**, *49* (6), p. 591-598.
[99] K. P. Somani, S. S. Kansara, N. K. Patel, A. K. Rakshit,
Castor oil based polyurethane adhesives for wood-to-wood bonding,
International Journal of Adhesion and Adhesives **2003**, *23* (4), p. 269-275.
[100] *Desmodur® VP.PU 1806*,
Sicherheitsdatenblatt, Bayer MaterialScience AG, Leverkusen, **2006**.
[101] P. Thomas, C. Varron, P. Ardaud, J.-M. Bernard, M. Cowley, T. Jeanette, J. Maxted, G. Rayner, B. Storer, A. Shields, N. Wheat,
Waterborne & Solvent Based Surface Coating Resins and their Applications: Volume III - Polyurethanes,
John Wiley & Sons, Chichester, New York, **1998**, ISBN 0-471-97886-8.
[102] J. Dodge,
Polyurethanes and Polyureas,
Synthetic Methods in Step-Growth Polymers,
John Wiley & Sons, Inc., 2003, ISBN 9780471220527, p. 197-263.
[103] M. Szycher,
Szycher's Handbook of Polyurethanes,
CRC Press, London, **1999**, ISBN 0-8493-0602-7.
[104] C. Hepburn,
Polyurethane Elastomers,
2nd Edition, Elsevier Applied Science, London, **1992**, ISBN 1-85166-589-7.
[105] H. Ulrich,
2-Carbon Cumulenes,
Cumulenes in Click Reactions,
John Wiley & Sons, Ltd, 2009, ISBN 9780470747957, p. 45-241.
[106] M. F. Sonnenschein,
Polyurethanes: Science, Technology, Markets, and Trends,
John Wiley & Sons, Inc, **2014**, ISBN 9781118901274.
[107] *Baygal® K 55*,
Produktdatenblatt, Bayer MaterialScience AG, Leverkusen, **2006**.
[108] *Desmophen® 3600Z*,
Produktdatenblatt, Bayer MaterialScience AG, Leverkusen, **2007**.
[109] O. Bayer,
Das Di-Isocyanat-Polyadditionsverfahren (Polyurethane),
Angewandte Chemie **1947**, *59* (9), p. 257-272.
[110] G. Borkent,
Kinetics and Mechanism of Urethane and Urea Formation,
G. Borkent, J. J. Van Ardsten (Eds.),
Advances in Urethane Science and Technology, Vol. 3,
Technomic Publishing Co., Westport, Conn., 1974, p. 1-13.
[111] A. Farkas, G. A. Mills,
Catalytic Effects in Isocyanate Reactions,
Advances in Catalysis **1962**, *13*, p. 393-446.

[112] N. Luo, D.-N. Wang, S.-K. Ying,
Effect of Urea Groups on Reaction Kinetics of Polyurethane Formation,
Journal of Applied Polymer Science **1996**, *61* (2), p. 367-370.
[113] G. Oertel, G. W. Becker, D. Braun,
Polyurethane (Kunststoff-Handbuch 7),
3. Auflage, Carl Hanser Verlag, München, **1993**, ISBN 3-446-16263-1.
[114] D. Joel, R. Becker,
Zum Verhalten chemischer Sekundärbindungen in Polyurethanen,
Proceedings, *Polyurethanes World Congress*, Aachen, Germany, September 29 - October 02, **1987**, p. 671-676.
[115] M. F. Sonnenschein, W. Koonce,
Polyurethanes,
Encyclopedia of Polymer Science and Technology,
John Wiley & Sons, Inc., 2002, ISBN 9780471440260.
[116] K. Dušek,
Theory of network formation by additional crosslinking of polyurethanes due to biuret and allophanate formation,
Polymer Bulletin **1987**, *17* (5), p. 481-488.
[117] K. Dušek, M. Špírková, M. Ilavský,
Network formation in polyurethanes due to allophanate and biuret formation: Gel fraction and equilibrium modulus,
Makromolekulare Chemie. Macromolecular Symposia **1991**, *45* (1), p. 87-95.
[118] E. Yilgör, I. Yilgör, E. Yurtsever,
Hydrogen bonding and polyurethane morphology. I. Quantum mechanical calculations of hydrogen bond energies and vibrational spectroscopy of model compounds,
Polymer **2002**, *43* (24), p. 6551-6559.
[119] E. Yilgör, E. Yurtsever, I. Yilgör,
Hydrogen bonding and polyurethane morphology. II. Spectroscopic, thermal and crystallization behaviour of polyether blends with 1,3-dimethylurea and a model urethane compound,
Polymer **2002**, *43* (24), p. 6561-6568.
[120] Z. S. Petrovic, I. Javni, V. Divjakovic,
Structure and Physical Properties of Segmented Polyurethane Elastomers Containing Chemical Crosslinks in the Hard Segment,
Journal of Polymer Science Part B: Polymer Physics **1998**, *36* (2), p. 221-235.
[121] C. P. Christenson, M. A. Harthcock, M. D. Meadows, H. L. Spell, W. L. Howard, M. W. Creswick, R. E. Guerra, R. B. Turner,
Model MDI/Butanediol Polyurethanes: Molecular Structure, Morphology, Physical and Mechanical Properties,
Journal of Polymer Science Part B: Polymer Physics **1986**, *24* (7), p. 1401-1439.
[122] K. K. S. Hwang, G. Wu, S. B. Lin,
Synthesis and Characterization of MDI-Butanediol Urethane Model Compounds,
Journal of Polymer Science: Polymer Chemistry Edition **1984**, *22* (7), p. 1677-1697.
[123] H. Janik, B. Palys, Z. S. Petrovic,
Multiphase-Separated Polyurethanes Studied by Micro-Raman Spectroscopy,
Macromolecular Rapid Communications **2003**, *24* (3), p. 265-268.
[124] T. E. Lipatova, V. V. Shilov, N. N. Minenko,
The Heterogeneous Structure of Polyurethane Networks,
Die Angewandte Makromolekulare Chemie **1981**, *100* (1), p. 99-115.

[125] D. J. Martin, G. F. Meijs, G. M. Renwick, S. J. McCarthy, P. A. Gunatillake,
The Effect of Average Soft Segment Length on Morphology and Properties of a Series of Polyurethane Elastomers. I. Characterization of the Series,
Journal of Applied Polymer Science **1996**, *62* (9), p. 1377-1386.
[126] D. J. Martin, G. F. Meijs, P. A. Gunatillake, S. J. McCarthy, G. M. Renwick,
The Effect of Average Soft Segment Length on Morphology and Properties of a Series of Polyurethane Elastomers. II. SAXS-DSC Annealing Study,
Journal of Applied Polymer Science **1996**, *64* (4), p. 803-817.
[127] European commitee for standardization,
Aluminium and aluminium alloys — Chemical composition and form of wrought products — Part 3: Chemical composition and form of products,
Standard, EN 573-3:2019, **2019**.
[128] H. G. F. WILSDORF,
Structure of Amorphous Aluminium Oxide Films,
Nature **1951**, *168* (4275), p. 600-601.
[129] S. Wernick, R. Pinner, E. Zurbrügg,
Die Oberflächenbehandlung von Aluminium,
6, Eugen G. Leuze Verlag, **1978**.
[130] T. Iwata, T. Matsumoto, S. Terakawa, H. Kobayashi,
Fabrication of Al2O3/Al structure by nitric acid oxidation at room temperature,
Open Physics **2010**, *8* (6), p. 1015-1020.
[131] P. Hariharan,
Optical Interferometry,
2nd Edition, Academic Press, London, **2003**.
[132] P. Hariharan,
Basics of Interferometry,
2nd Edition, Academic Press, London, **2006**, ISBN 978-0-12-373589-8.
[133] P. de Groot, L. Deck,
Three-dimensional imaging by sub-Nyquist sampling of white-light interferograms,
Optics Letters **1993**, *18* (17), p. 1462-1464.
[134] H. D. Baehr, S. Kabelac,
Thermodynamik, Grundlagen und technische Anwendung,
Springer Verlag, Berlin, **2006**.
[135] L. Depollier,
Thermomechanische Eigenschaften von Metall-Klebungen mit vernetztem Polyurethan,
Diplomarbeit, Universität des Saarlandes, Saarbrücken, **2012**.
[136] M. Haïdopoulos,
Etude expérimentale d'optimisation de procédés de modifications de surface de l'acier inoxydable 316 pour application aux dispositifs endovasculaires,
PhD thesis, Université Laval, Québec, **2005**.
[137] C. C. Irving,
Electropolishing stainless steel implants,
ASTM Special Technical Publications **1985**, *859*, p. 136-143.
[138] S.-J. Lee, J.-J. Lai,
The effects of electropolishing (EP) process parameters on corrosion resistance of 316L stainless steel,
Journal of Materials Processing Technology **2003**, *140*, p. 206-210.
[139] E. J. Sutow, S. R. Pollack, E. Korostoff,
An in vitro investigation of the anodic polarization and capacitance behavior of 316L stainless steel,
Journal of Biomedical Materials Research **1976**, *10*, p. 671-693.

[140] E. J. Sutow,
The influence of electropolishing on the corrosion resistance of 316L stainless steel,
Journal of Biomedical Materials Research **1980**, *14*, p. 587-595.
[141] D. Vogt,
Durability of Adhesively Bonded Stainless Steel Joints under Accelerated Ageing Conditions,
PhD thesis, Technische Universität Kaiserslautern, Kaiserslautern, **2009**.
[142] E.-S. Lee,
Machining characteristics of the electropolishing of stainless steel (STS316L),
The International Journal of Advanced Manufacturing Technology **2000**, *16*, p. 591-599.
[143] Kosmac,A. Elektropolieren nichtrostender Stähle. *Euro Inox,* Reihe Werkstoff und Anwendungen. (2010). **11**.
[144] D. Landolt,
Review article - Fundamental aspects of electropolishing,
Electrochimica Acta **1987**, *32* (1), p. 1-11.
[145] D. B. Macdonald,
Passivity - The key to our metals-based civilization,
Pure and Applied Chemistry **1999**, *71* (6), p. 951-978.
[146] M. Matlosz,
Modeling of impedance mechanisms in electropolishing,
Electrochimica Acta **1995**, *40* (4), p. 393-401.
[147] A. A. Minakov, C. Schick,
Ultrafast thermal processing and nanocalorimetry at heating and cooling rates up to 1MK/s,
Review of Scientific Instruments **2007**, *78* (7), p. 073902ff.
[148] C.-O. A. Olsson, D. Landolt,
Passive films on stainless steels - chemistry, structure and growth,
Electrochimica Acta **2003**, *48*, p. 1093-1104.
[149] G. Petzow,
Metallographic Etching - 2nd Edition,
ASM International, **1999**.
[150] D. Wallinder, J. Pan, C. Leygraf, A. Delblanc-Bauer,
EIS and XPS study of surface modification of 316LVM stainless steel after passivation,
Corrosion Science **1999**, *41*, p. 275-289.
[151] ISO - International Organization for Standardization,
Adhesives -- Determination of shear behaviour of structural adhesives -- Part 2: Tensile test method using thick adherends,
Standard, ISO 11003-2:2019, **2019**.
[152] ISO - International Organization for Standardization,
Adhesives -- Determination of shear strength of adhesive bonds between rigid substrates by the block-shear method,
Standard, ISO 13445:2003, **2003**.
[153] ISO - International Organization for Standardization,
Adhesives -- Determination of tensile lap-shear strength of rigid-to-rigid bonded assemblies,
Standard, ISO 4587:2003, **2003**.
[154] O. Volkersen,
Die Nietkraftverteilung in zugbeanspruchten Nietverbindungen mit konstanten Laschenquerschnitten,
Luftfahrtforschung **1938**, *15* (1/2), p. 41-47.

[155] R. D. Adams, J. Comyn, W. C. Wake,
Structural Adhesive Joints in Engineering,
Second Edition, Chapman & Hall, London, **1997**, ISBN 0-412-70920-1.
[156] Dr Johannes HEIDENHAIN GmbH,
Length gauges,
http://www.heidenhain.de/fileadmin/pdb/media/img/208945-2G_Length_Gauges_en.pdf, **2017**.
[157] C. Schmitt,
Mechanische Interphase in PU-AlMg3-Klebungen,
Masterarbeit, Universität des Saarlandes, Saarbrücken, **2015**.
[158] M. Schwarz,
Mechanische Eigenschaften von PU-Al-Klebungen – Einfluss der Interphase,
Masterarbeit, Universität des Saarlandes, Saarbrücken, **2014**.
[159] ZwickRoell GmbH & Co.KG. Electromechanical Creep Testing Machine Kappa DS - Product information. (PI_ 88_951_07.2016):(2016).
[160] ZwickRoell GmbH & Co.KG. Materialpruefmaschine Kappa 20 DS: Ein Handbuch. Ulm (2011).
[161] ZwickRoell GmbH & Co.KG,
videoXtens - Hochgenau ganz ohne Kontakt! - Produkinformation,
Journal of Thermal Analysis and Calorimetry **2015**, *49* (2), p. 1081-1088.
[162] J. D. Menczel, R. D. Prime,
Thermal Analysis of Polymers: Fundamentals and Applications,
John Wiley & Sons, Hoboken, NJ, USA, **2009**, ISBN 978-0-471-76917-0.
[163] C. M. Earnest,
Compositional Analysis by Thermogravimetry,
Proceedings of the Symposium on Compositional Analysis by Thermogravimetry, *Symposium on Compositional Analysis by Thermogravimetry*, Philadelphia, **1988**.
[164] Y. J. Yu, K. Hearon, T. S. Wilson, D. J. Maitland,
The effect of moisture absorption on the physical properties of polyurethane shape memory polymer foams,
Smart materials & structures **2011**, *20* (8), p. 085010ff.
[165] E. Bosset,
Thermomechanisches Verhalten von Polyurethan-Aluminium Klebungen,
Diplomarbeit, Universität des Saarlandes, Saarbrücken, **2013**.
[166] J. J. Aklonis, W. J. MacKnight, M. Shen,
Introduction to polymer viscoelasticity,
Wiley-Interscience, New York, **1972**, ISBN 0471018600 9780471018605.
[167] L. Krogh, J. E. K. Schawe, W. Possart,
Dynamic mechanical properties of very thin adhesive joints,
Journal of Applied Polymer Science **2015**, *132* (24).
[168] F. Fug,
Chemische Adhäsionswechselwirkungen zwischen Isocyanaten und Metallsubstraten,
Diplomarbeit, Universität des Saarlandes, Saarbrücken, **2011**.
[169] F. Fug, C. Nies, W. Possart,
in situ FTIR study of adhesive interactions of 4,4â€²-methylene diphenyl diisocyanate and native metals,
International Journal of Adhesion and Adhesives **2014**, *52* (0), p. 66-76.
[170] F. Fug, K. Rohe, J. Vargas, C. Nies, M. Springborg,
4,40-methylene diphenyl diisocyanate e Conformational space, normal vibrations and infrared spectra,
Polymer **2016**, *99* (16), p. 671-683.

[171] C. Nies,
Chemische Adhäsionswechselwirkungen zwischen Polyurethan-Monomeren und Metallsubstraten,
Diplomarbeit, Universität des Saarlandes, Saarbrücken, **2010**.
[172] C. Nies, C. Wehlack, H. Ehbing, D. J. Dijkstra, W. Possart,
Adhesive Interactions of Polyurethane Monomers with Native Metal Surfaces,
The Journal of Adhesion **2012**, *88* (8), p. 665-683.
[173] C. Nies, F. Fug, C. Otto, W. Possart,
Adhesion of polyurethanes on native metal surfaces - stability and the role of urea-like species,
International Journal of Adhesion and Adhesives **2014**, *52* (0), p. 19-25.
[174] H. Jost,
Molekulare Schichten von Polyurethan und seinen Monomeren auf Metallen – Gasphasenabscheidung und Charakterisierung,
Masterarbeit, Universität des Saarlandes, Saarbrücken, **2015**.
[175] H. Leaderman,
Elastic and creep properties of filamentous materials,
Phd thesis, Massachusetts Institute of Technology, Dept. of Mechanical Engineering, **1941**.
[176] E. R. Pierik, W. J. B. Grouve, M. van Drongelen, R. Akkerman,
The influence of physical ageing on the in-plane shear creep compliance of 5HS C/PPS,
Mechanics of Time-Dependent Materials **2019**.
[177] M. L. Williams, R. F. Landel, J. D. Ferry,
The Temperature Dependence of Relaxation Mechanisms in Amorphous Polymers and Other Glass-forming Liquids,
Journal of the American Chemical Society **1955**, *77* (14), p. 3701-3707.
[178] W. I. Griffith,
The accelerated characterization of viscoelastic composite materials,
PhD thesis, Virginia Polytechnic Institute and State University, **1980**.
[179] U. Mueller, M. Philipp, M. Thomassey, R. Sanctuary, J. K. Krueger,
Temperature modulated optical refractometry: A quasi-isothermal method to determine the dynamic volume expansion coefficient,
Thermochimica Acta **2013**, *555*, p. 17-22.
[180] G. Binnig, C. F. Quate, C. Gerber,
Atomic Force Microscope,
Physical Review Letters **1986**, *56* (9), p. 930-933.
[181] G. Binnig,
Force microscopy,
Ultramicroscopy **1992**, *42-44* (Part 1), p. 7-15.
[182] H. Okamoto, D. J. Chakrabarti, D. E. Laughlin, T. B. Massalski,
The Au-Cu (Gold-Copper) system,
Journal of Phase Equilibria **1987**, *8* (5), p. 454ff.
[183] N. Causse, L. Quiroga Cortes, E. Dantras, C. Tonon, M. Chevalier, H. Combes, P. Guigue, C. Lacabanne,
New bonded assembly configuration for dynamic mechanical analysis of adhesives,
International Journal of Adhesion and Adhesives **2013**, *46*, p. 1-6.
[184] S. Diebels, A. Geringer,
Modelling Inhomogeneous Mechanical Properties in Adhesive Bonds,
The Journal of Adhesion **2012**, *88* (11-12), p. 924-940.

[185] A. T. DiBenedetto,
Prediction of the glass transition temperature of polymers: A model based on the principle of corresponding states,
Journal of Polymer Science Part B: Polymer Physics **1987**, *25* (9), p. 1949-1969.
[186] A. V. Tobolsky,
Mechanische Eigenschaften und Struktur von Polymeren,
Berliner Union, Stuttgart, **1967**.
[187] M. Bäker, H. Harders, J. Rösler,
Mechanisches Verhalten der Polymere,
J. Rösler, H. Harders, M. Bäker (Eds.),
Mechanisches Verhalten der Werkstoffe,
Springer Fachmedien, Wiesbaden, 2012, ISBN 978-3-8348-2241-3, p. 257-293.
[188] J. Chen, J. Xu, X. Wang, D. Zhou, P. Sun, G. Xue,
Thickness Dependence of Glass Transitions Measured by AC-Chip Calorimetry in Films with Controlled Interface,
Macromolecules **2013**, *46* (17), p. 7006-7011.
[189] M. Y. Efremov, E. A. Olson, M. Zhang, Z. Zhang, L. H. Allen,
Glass Transition in Ultrathin Polymer Films: Calorimetric Study,
Physical Review Letters **2003**, *91* (8), p. 085703ff.
[190] H. Huth, A. A. Minakov, A. Serghei, F. Kremer, C. Schick,
Differential AC-chip calorimeter for glass transition measurements in ultra thin polymeric films,
The European Physical Journal Special Topics **2007**, *141* (1), p. 153-160.
[191] C. Schick,
Glass transition under confinement-what can be learned from calorimetry,
The European Physical Journal Special Topics **2010**, *189* (1), p. 3-36.
[192] D. Zhou, H. Huth, Y. Gao, G. Xue, C. Schick,
Calorimetric Glass Transition of Poly(2,6-dimethyl-1,5-phenylene oxide) Thin Films,
Macromolecules **2008**, *41* (20), p. 7662-7666.
[193] E. Zhuravlev, C. Schick,
Fast scanning power compensated differential scanning nano-calorimeter: 1. The device,
Thermochimica Acta **2010**, *505* (1-2), p. 1-13.
[194] E. Zhuravlev, C. Schick,
Fast scanning power compensated differential scanning nano-calorimeter: 2. Heat capacity analysis,
Thermochimica Acta **2010**, *505* (1-2), p. 14-21.
[195] S. Adamovsky, C. Schick,
Ultra-fast isothermal calorimetry using thin film sensors,
Thermochimica Acta **2004**, *415* (1-2), p. 1-7.
[196] F. Kremer,
Broadband Dielectric Spectroscopy,
1. Auflage, Springer-Verlag, Berlin Heidelberg New York, **2003**, ISBN 3-540-43407-0.
[197] H. Neurohr,
Molekulare Dynamik in dünnen Polymerschichten auf Metallen: Vernetzung, Netzwerkzustand und Alterung,
Dissertation, Universität des Saarlandes, Saarbrücken, **2006**.
[198] NOVOCONTROL GmbH. Novocontrol Broadband Dielectric Converter (BDC), Owner's manual. (1996).
[199] NOVOCONTROL Technologies GmbH & Co.KG. WinDETA. (2017).
[200] NOVOCONTROL Technologies GmbH & Co.KG. Quatro Cryosystem. (2017).